Monitoring of the quality of marine waters in French Guiana by remote sensing and in-situ measurements

Manh Tran Duy

Thèse de Doctorat

Mention: Sciences Agronomiques et Écologiques

Spécialité: Sciences de la Mer - Océanographie physique

présentée à ***l'Ecole Doctorale en Sciences Technologie et Santé (ED 585)***

de l'Université du Littoral Côte d'Opale

par

Manh Duy TRAN

pour obtenir le grade de Docteur de l'Université du Littoral Côte d'Opale

Surveillance de la qualité des eaux marines de Guyane par télédétection et mesures in-situ

Soutenue le 30/06/2023, après avis des rapporteurs, devant le jury d'examen:

M. Milton KAMPEL, Directeur de recherche, INPE	**Rapporteur**
M. David DOXARAN, Chargé de recherche, LOV	**Rapporteur**
M^me^ Lucile DUFORET-GAURIER, Maîtresse de conférences, ULCO	**Examinateur**
M^me^ Marine HERRMANN, Directrice de recherche, LEGOS	**Examinateur**
M. Hubert LOISEL, Professeur, ULCO, LOG	**Directeur de thèse**
M. Vincent VANTREPOTTE, Chargé de recherche, LOG	**Co-encadrant**

PhD Thesis

Major: Agricultural and Ecological Sciences

Speciality: Marine Sciences - Physical Oceanography

presented at the ***Doctoral School of Science, Technology and Health (ED 585)***

of the Université du Littoral Côte d'Opale

by

Manh Duy TRAN

To obtain the degree of Doctor of the Université du Littoral Côte d'Opale

Monitoring of the quality of marine waters in French Guiana by remote sensing and in-situ measurements

Defended on the 30/06/2023 after approval of the reviewers, in front of the jury:

Mr. Milton KAMPEL, Research Director, INPE	**Reviewer**
Mr. David DOXARAN, Researcher, LOV	**Reviewer**
Mrs. Lucile DUFORET-GAURIER, Associate Professor, ULCO	**Examiner**
Mrs. Marine HERRMANN, Research Director, LEGOS	**Examiner**
Mr. Hubert LOISEL, Professor, ULCO, LOG	**Thesis supervisor**
Mr. Vincent VANTREPOTTE, Researcher, LOG	**Co-supervisor**

Acknowledgements

As I reach the final steps of my PhD journey, I would like to extend my profound gratitude to those who have supported and guided me throughout this endeavor:

First and foremost, my deepest appreciation goes to my primary supervisor, Vincent Vantrepotte, whose constant support has been absolutely indispensable. I sincerely doubt I could have achieved this milestone without him. His constructive criticism and uplifting encouragement have taught me valuable lessons and greatly contributed to my growth.

I am also immensely grateful to my co-supervisor, Hubert Loisel, for his astute ideas, constructive feedback on my thesis and the paper, and for granting me the opportunities to complete both my Master's and PhD degrees under his guidance. I hold him in the highest regard.

My sincerest thanks go to the Office Français de la Biodiversité (OFB), DEAL, Office de l'Eau Guyane, and the Laboratoire d'Océanologie et de Géosciences (LOG) for generously providing financial support and hosting throughout my research.

I would like to express my gratitude to the jury members, Milton Kampel, David Doxaran, Lucile Duforêt-Gaurier, and Marine Herrmann, who kindly undertook the responsibility of evaluating my work.

I also appreciate the efforts of committee members Cédric Jamet and Antoine Gardel, who diligently monitored and provided valuable advice on the progress of my PhD.

My former Master's supervisor, Charles Verpoorter, deserves special recognition for his guidance, his positive impact on my journey, and for connecting me with Vincent.

I am grateful for the assistance of my colleagues and friends, including Elena and her family, Daniel, Son, Gabi, Hieu, Carina, Kien, Yang, Corentin, Ikram, Sara, Cuong, Lucas, and Sayoob. Their support and friendship have made my three years of PhD study truly unforgettable.

To my parents, I owe an enormous debt of gratitude for their unwavering emotional support, faith, and pride in my accomplishments.

Lastly, I would like to express my love and appreciation to my incredible wife, Linh, who has always stood by me with positive encouragement, trust, and love. And to our precious little one, Bach, who has brought immeasurable joy to our lives.

Table of contents

Table of contents

Table of contents

Table of contents

List of Symbols

Parameters	Description	Unit
λ	Wavelength	nm
$a_{CDOM}(\lambda)$	Colored dissolved organic matter absorption	m^{-1}
$a_p(\lambda)$	Particulate absorption coefficient	m^{-1}
$a_{ph}(\lambda)$	Absorption coefficient of pigments of living phytoplankton	m^{-1}
$a_w(\lambda)$	Absorption coefficient of pure water	m^{-1}
$b_{bp}(\lambda)$	Particulate backscattering coefficient	m^{-1}
$c_p(\lambda)$	Particulate attenuation coefficient	m^{-1}
Chl-a	Chlorophyll-a concentration	$mg.m^{-3}$
DOC	Dissolved Organic Carbon	$\mu mol.L^{-1}$
$E_d(0^+,\lambda)$	Above water down-welling irradiance	$W.m^{-2}$
$K_d(\lambda)$	Diffuse attenuation coefficient	m^{-1}
$K_w(\lambda)$	Diffuse attenuation coefficient for pure seawater	m^{-1}
$L_u(0^-,l)$	Upwelling radiance below sea surface	$W.m^{-2}.sr^{-1}$
$R_{rs}(\lambda)$	Remote sensing reflectance	Sr^{-1}
POC	Particulate organic carbon	$mg.m^{-3}$
SPM	Suspended particulate matter	$g.m^{-3}$
SSS	Sea surface salinity	PSU
SST	Sea surface temperature	°C

List of Figures

List of Figures

List of Figures

List of Tables

List of Tables

Résumé

Milieux essentiels à l'équilibre écologique et au bien-être de l'homme, les écosystèmes côtiers fonctionnent comme des puits de "carbone bleu", qui capturent et stockent le dioxyde de carbone atmosphérique, jouant ainsi un rôle crucial dans la régulation du climat. En outre, ces zones de transition sont des zones cruciales pour la biodiversité, offrant des habitats à une série d'espèces aquatiques cruciales y compris pour les espèces clés pour la pêche ance. Elles contribuent donc de manière significative aux économies locales et sont d’une haute importance écologique.

Pourtant, la résilience et la stabilité à long terme de ces écosystèmes sont de plus en plus menacées par toute une série de facteurs environnementaux qui peuvent être impactés par les forçages anthropiques. En Guyane française, la nécessité de disposer d'outils de surveillance avancés devient encore plus urgente compte tenu de la croissance démographique prévue, où le nombre de résidents devrait doubler d'ici 2025. Ces outils sont essentiels pour évaluer les impacts potentiels futurs sur le domaine côtier, en particulier dans le contexte actuel d'augmentation des forçages anthropiques tels que l'extraction de l'or, la déforestation et l’érosion côtière. Ces activités, ainsi que les influences naturelles telles que les bancs de vase et les apports des rivières locales, contribuent à la dynamique biogéochimique complexe de la région. Cependant, les contributions relatives de ces éléments restent floues en raison de l'insuffisance des mesures in situ.

Les recherches antérieures menées localement en Guyane française se sont principalement concentrées sur deux paramètres classiques, à savoir les particules en suspension (« Suspended Particulate Matter » SPM) et la chlorophylle-a (« Chlorophyll-a » Chl-a), qui sont généralement associés à la migration des bancs de vase et aux tourbillons du courant nord-brésilien (« North Brazil Current » NBC). Bien que ces paramètres soient indéniablement importants, ils peuvent ne pas rendre compte de la complexité de la dynamique biogéochimique présente dans la zone d'étude. Par exemple, il reste une lacune notable dans notre compréhension des facteurs localisés, tels que l'exportation de matière organique à partir des écosystèmes de mangrove et l'influence des modulations de marée. C'est pourquoi des paramètres supplémentaires, tels que le carbone organique particulaire (« Particulate Organic Carbon » POC) et le carbone organique dissous (« Dissolved Organic Carbon » DOC), sont également essentiels pour une compréhension plus complète de la qualité des eaux côtières guyanaises. En outre, la turbidité élevée due aux charges sédimentaires transportées par le fleuve Amazone et la présence d'un reflet solaire permanent

compliquent encore la complexité optique des eaux de la région pour des observations à distance efficaces. Par conséquent, une méthodologie plus adaptée est nécessaire pour utiliser suffisamment les données satellitaires afin d'améliorer la surveillance de la qualité de l'eau dans les eaux côtières de la Guyane française.

Compte tenu de ces défis et des lacunes dans les connaissances actuelles, cette recherche doctorale est structurée en cinq chapitres distincts. Chaque chapitre a un but spécifique aligné sur les objectifs principaux de l'étude : 1) Le premier objectif primaire est le développement d'une série temporelle complète de produits de couleur de l'océan clés (Chl-a, SPM, l'absorption de matières organiques dissoutes colorées (« Absorption of Colored Dissolved Organic Matter » a_{CDOM}), ainsi que POC et DOC). Ces paramètres sont reconnus comme des indicateurs importants pour le suivi de la qualité de l'eau dans les régions côtières. 2) Le second objectif est de décrire la dynamique biogéochimique temporelle à l'échelle régionale. Il s'agit d'identifier les principaux facteurs de variabilité biogéochimique et de proposer des descripteurs biogéochimiques pertinents pour le suivi de la qualité de l'eau. Les tendances à long terme seront également analysées afin d'évaluer l'influence des variations induites par les forçages environnementaux au cours des 20 dernières années. 3) Le troisième et dernier objectif principal de cette recherche est de proposer une partition plus efficace des masses d'eau en utilisant des méthodes statistiques robustes. Ceci contribuera à la mise en place de politiques de surveillance localisées, améliorant ainsi la gestion durable des écosystèmes côtiers de la Guyane française.

Le chapitre 1 sert d'introduction à cette recherche et pose les bases en fournissant des informations générales essentielles. Il expose les principales raisons de l'étude, en soulignant l'importance des écosystèmes côtiers pour l'équilibre écologique, les contributions économiques et le bien-être de la société. Ce chapitre identifie les défis actuels auxquels ces écosystèmes sont confrontés, tels que la dégradation de l'environnement et l'augmentation des activités humaines, soulignant ainsi les lacunes de la recherche existante. En présentant ces problèmes, le chapitre 1 établit le contexte et articule les questions et les objectifs scientifiques que cette recherche vise à aborder.

Le chapitre 2 se concentre sur les aspects méthodologiques de la recherche, en détaillant spécifiquement les ensembles de données et les approches statistiques utilisées dans cette étude doctorale. Il donne un aperçu des types de données utilisées, y compris les données satellitaires et les mesures sur le terrain, en expliquant leurs rôles respectifs dans l'amélioration de la

compréhension des écosystèmes côtiers. En outre, ce chapitre détaille les méthodes statistiques utilisées pour l'interprétation et l'analyse des données, y compris les techniques d'examen des tendances à long terme et de catégorisation des types d'eau, entre autres.

Le chapitre 3 s'appuie sur les connaissances fondamentales discutées dans le chapitre 1, en particulier sur la nécessité de disposer de plus de modèles bio-optiques d'inversion pour comprendre la dynamique biogéochimique des eaux de la Guyane française. Bien que des études antérieures en Guyane française aient utilisé des modèles bio-optiques dans une certaine mesure, une évaluation critique de leur applicabilité à l'échelle régionale a été largement absente, sauf dans le cas du SPM. Compte tenu de la complexité optique des conditions des eaux côtières dans la zone d'étude, le chapitre donne la priorité à l'adaptation régionale de différents algorithmes d'inversion pour dériver des informations quantitatives sur les paramètres biogéochimiques à partir de données satellitaires.

Le chapitre est divisé en deux sections principales. La première partie est consacrée à une évaluation localisée de plusieurs variables, y compris SPM, POC, et $a_{CDOM}(412)$, en prenant comme référence les bandes centrales MERIS (Medium Resolution Imaging Spectrometer) dans le domaine visible. D'autre part, la dernière partie propose un examen plus détaillé du Chl-a, un paramètre crucial largement reconnu comme un descripteur essentiel dans la surveillance de la qualité de l'eau. Cette section s'appuie sur un ensemble complet de données in situ recueillies dans divers environnements côtiers à travers le monde, et les résultats ont été valorisés par une présentation orale lors d'une conférence internationale et par la publication de travaux de recherche.

Pour ce faire, nous avons adopté une approche basée sur les classes comme cadre d'évaluation des formulations historiques pour dériver la concentration des paramètres considérés. Afin d'éviter toute redondance, une sélection préliminaire a été effectuée pour identifier les modèles suffisamment distincts, ce qui a permis de concentrer l'examen sur les plus pertinents. Les versions originales et adaptées à la région de ces modèles ont été évaluées en comparant leur performance dans l'extraction de la concentration biogéochimique à partir de la réflectance de l'eau dans divers types d'eau optique (« Optical Water Types » OWTs) présents dans les eaux marines de la Guyane française.

En termes de résultats, l'examen de l'estimation de la SPM a révélé que la majorité des algorithmes testés ont donné des résultats satisfaisants. Notamment, l'algorithme BingHan16 est

apparu comme le plus précis pour l'estimation du SPM. Dans le cas du POC, la combinaison de deux modèles distincts a permis d'obtenir des résultats optimaux : Le17 et KienTran19. Ces modèles ont été appliqués sélectivement à des types d'eau optiques spécifiques afin de maximiser la précision de l'estimation du POC. Pour l'estimation de l'a_{CDOM}, le modèle Cao18, basé sur une méthode de régression multivariée, a été jugé le plus approprié parmi les algorithmes candidats pour capturer efficacement la relation entre la réflectance de l'eau et l'a_{CDOM}.

En outre, ce chapitre explore en profondeur les défis associés à l'estimation de la Chl-a dans diverses conditions d'eau et présente des solutions fiables jusqu'à un certain niveau de turbidité. Dans les environnements très turbides avec la présence de constituants coexistants tels que CDOM et SPM (eaux du cas 2), les algorithmes conventionnels de rapport de bande bleu/vert présentent des limites dans l'obtention d'informations précises sur le Chl-a. Ceci est particulièrement évident dans la zone côtière, où les eaux de surface et les eaux souterraines ont un rapport de bande bleu/vert élevé. Ceci est particulièrement évident dans la zone côtière de la Guyane française, où la complexité optique est accrue en raison des niveaux importants de sédiments en suspension. Les modèles d'inversion existants pour la Chl-a ont démontré une précision insuffisante dans ce domaine spécifique. En réponse à ce problème, un ensemble complet de données a été utilisé pour formuler deux algorithmes distincts : l'un conçu pour les eaux claires à moyennement turbides utilisant des rapports de bandes visibles, à savoir l'algorithme Multiple Band Ratio (MuBR), et l'autre pour les eaux très turbides avec un niveau élevé de Chl-a utilisant un modèle Rouge-NIR adapté basé sur l'indice de différence normalisé de la chlorophylle-a (basé sur « Normalized Difference Chlorophyll-a Index » NDCI). Ces algorithmes ont ensuite été intégrés dans un cadre de classification optique pour une application plus large. Les performances de ces nouveaux algorithmes ont ensuite été évaluées à l'aide de données d'observation provenant de Sentinel2-MSI et de Sentinel3-OLCI. Les résultats montrent que le traitement POLYMER s'est avéré le plus approprié pour dériver des estimations de Chl-a à partir de cette approche intégrée, bien qu'une validation supplémentaire soit nécessaire pour des conditions de turbidité et de Chl-a extrêmes. Bien que la méthodologie soit potentiellement transférable à d'autres capteurs satellitaires, des recherches supplémentaires sont impératives, en particulier pour les capteurs comme MODIS (Moderate Resolution Imaging Spectroradiometer) qui offrent des informations limitées dans le domaine du proche infrarouge. L'étude souligne également les limites des approches actuelles pour récupérer des informations sur la biomasse du phytoplancton dans des environnements ultra-turbides, soulignant la nécessité de développer des

approches spécialisées, potentiellement en tirant parti des capacités des futures missions hyperspectrales.

Le chapitre 4 vise à combler les lacunes existantes dans notre compréhension de la dynamique spatio-temporelle des descripteurs biogéochimiques clés dans les eaux de la Guyane française. Alors que la recherche historique s'est largement concentrée sur la dynamique sédimentaire, en particulier celle des bancs de vase, et dans une moindre mesure sur les échanges de carbone entre les domaines terrestres et océaniques, il y a un manque notable d'observations régionales globales et à long terme. L'objectif principal de ce chapitre est de caractériser la variabilité temporelle des variables biogéochimiques. Ces variables sont estimées à partir de l'espace à l'aide d'algorithmes adaptés à la région, qui ont été détaillés au chapitre 3. Divers ensembles de données sur la couleur de l'océan, y compris des archives satellitaires à moyenne et haute résolution spatiale, sont utilisés à cette fin. Des outils statistiques spécialisés, tels que la méthode de décomposition des séries temporelles Census X-11, sont utilisés pour analyser ces ensembles de données. Cette approche permet de mieux comprendre les variations des concentrations en surface des particules et des matières dissoutes. Une attention particulière est accordée à la côte de la Guyane française, où des données provenant de capteurs plus récents sont également prises en compte. Un autre objectif de ce chapitre est d'identifier les principaux facteurs environnementaux influençant ces variations biogéochimiques, en se concentrant sur différentes régions des eaux de la Guyane française. D'autres facteurs, tels que la température et la salinité de la surface de la mer, ainsi que les débits des fleuves, sont également pris en compte et comparés à d'autres paramètres pour soutenir cet objectif. Le chapitre conclut en proposant un ensemble d'indicateurs clés qui peuvent servir de base pour mieux catégoriser les masses d'eau en termes de représentativité biogéochimique et de qualité de l'eau.

Les résultats obtenus révèlent que les charges sédimentaires près du fleuve Oiapoque sont substantiellement plus élevées que celles près de l'embouchure du fleuve Maroni, avec une différence de SPM allant de 5 à 10 $g.m^{-3}$. Ceci suggère une influence plus prononcée du fleuve Amazone dans les régions orientales de la côte guyanaise.

Dans les zones off-shore, des variations saisonnières significatives ont été observées à des latitudes comprises entre 5°N et 7°N et des longitudes comprises entre 52,5°W et 51°W, à plus de 50 km de l'estuaire de l'Oiapoque. Ces variations confirment un cycle annuel de flux rétrofléchi, particulièrement évident en saison sèche sous l'effet des alizés du sud-est. Le contenu

biogéochimique s'étend également vers l'ouest pendant la saison humide, peut-être sous l'influence de la bathymétrie et des changements de direction des vents. Bien que ces processus affectent toutes les variables biogéochimiques, l'amplitude des variations des substances dissoutes et particulaires est relativement plus faible dans l'extension off-shore occidentale, ce qui indique des conditions plus stables. Les régions SPM irrégulières dans le domaine off-shore à l'ouest de la zone de rétroflexion peuvent être liées à la formation d'tourbillons anticycloniques du courant nord-brésilien (NBC), qui se produisent 5 à 6 fois par an et ont un impact plus prononcé sur le SPM que sur d'autres paramètres.

Dans les zones côtières, des tendances distinctes ont été observées sur le plateau continental, illustrant la migration vers le nord-ouest des bancs de vase dérivés de l'Amazone à une vitesse moyenne de 1 à 2 km/an. Les fluctuations saisonnières du SPM soulignent le rôle des alizés du nord-est dans la modulation de l'accrétion et de l'érosion des bancs de vase. Le contenu organique des rivières locales semble être plus important que le total des solides en suspension, comme le montre une corrélation plus élevée entre le POC et le débit de la rivière Maroni. La modulation périodique du NBC sur le plateau intérieur peut être liée à une ceinture saisonnière de SPM apparaissant 1 à 2 mois après que la rétroflexion ait atteint sa position la plus septentrionale. Les variations opposées de Chl-a dans cette ceinture peuvent être dues à la disponibilité de la lumière pour la croissance du phytoplancton pendant la saison sèche. Les fluctuations du POC et de l'$a_{CDOM}(412)$ montrent de fortes variations irrégulières, potentiellement dues au carbone organique provenant des mangroves et des sédiments du fleuve Amazone, influencés par les changements saisonniers de la direction du vent. Les facteurs de marée peuvent également contribuer à la variabilité du bassin de carbone organique dans cette région.

Les données à long terme de MERIS couvrant la période 2002-2012 ne montrent pas de changements significatifs, à l'exception de la migration des bancs de vase, ce qui suggère un impact anthropique minime. Les vents alizés sont identifiés comme étant cruciaux pour gouverner la dynamique biogéochimique, en particulier pour les matériaux particulaires dans le domaine côtier. Les tests de co-variation entre les paramètres biogéochimiques soulignent l'importance du POC et du SPM dans la compréhension des impacts hydrodynamiques et environnementaux sur la qualité de l'eau. Le rapport POC/SPM pourrait servir d'indicateur potentiel pour le suivi de la qualité de l'eau et de la variabilité biogéochimique dans l'écosystème côtier de la Guyane française.

Compte tenu des incertitudes liées à la dynamique biogéochimique, des mesures in situ supplémentaires et l'inclusion d'autres facteurs tels que le vent et la direction du courant sont essentielles pour une compréhension plus complète. Des questions restent sans réponse, comme la proportion de composants organiques d'origine locale par rapport à ceux provenant de l'Amazone, la raison de l'extension vers l'ouest de tous les paramètres biogéochimiques et l'impact plus visible des tourbillons NBC sur les variations de SPM. Par conséquent, un cadre efficace est nécessaire pour se concentrer sur des zones ou des types d'eau spécifiques en vue d'un échantillonnage efficace.

Chapitre 5 est consacré à la tâche cruciale de définir la condition "standard" des eaux marines en Guyane française. Cette norme sert de référence essentielle pour les parties prenantes engagées dans la surveillance biogéochimique et pour les décideurs politiques qui façonnent les stratégies environnementales régionales. L'objectif principal de ce chapitre est d'examiner plusieurs approches de classification pour partitionner les masses d'eau marines en Guyane française, basées sur les propriétés optiques, les variations temporelles et les proxies de la composition particulaire (« Proxy of Particulate Component » PPC, rapports POC/SPM). En appliquant ces méthodes de classification à des ensembles de données satellitaires à résolution moyenne et élevée, le chapitre vise à réaliser une analyse complète pour élucider les caractéristiques biogéochimiques associées à chaque type classifié d'eau marine dans la région.

En ce qui concerne la classification optique, nous analysons les spectres de réflectance pour distinguer les motifs pouvant indiquer des attributs spécifiques de l'eau, tels que la présence de particules en suspension, de matière organique et inorganique dissoute, et de différents types de phytoplancton. D'autre part, la classification POC/SPM se concentre sur la segmentation des masses d'eau en catégories spécifiques allant de celles riches en matières organiques à celles mixtes et enfin à celles dominées par les minéraux. Ce cadre de classification est essentiel pour faire progresser notre connaissance sur la distribution spatiale des substances organiques et inorganiques à travers différents types d'eau. De plus, la classification temporelle, qui utilise des techniques de cartes auto-organisatrices (« Self-Organizing Map » SOM), est utilisée pour regrouper des régions ou des pixels présentant une variabilité temporelle analogue. Cette approche est particulièrement efficace pour représenter la distribution spatiale des variables biogéochimiques au fil du temps et identifier les facteurs environnementaux pouvant être attribués à ces variations. Ces méthodes de partitionnement ont été examinées puis synthétisées pour fournir une évaluation plus large des propriétés de l'eau sur différentes régions.

L'intégration de ces approches distinctes devrait être un outil essentiel pour la planification et l'exécution d'études sur le terrain qui surveillent la qualité de l'eau dans divers environnements marins, tant côtiers qu'au large.

Un autre objectif clé de ce chapitre est de définir une stratégie d'échantillonnage bien définie basée sur les schémas de classification précédemment discutés et qui servira de cadre structurel pour la conduite de programmes de surveillance régionaux. Ces programmes ne se contenteront pas de suivre l'état actuel des propriétés de l'eau, mais évalueront également comment ces propriétés pourraient être impactées par les changements environnementaux au fil du temps. Compte tenu de l'absence de changements substantiels à long terme dans les eaux marines de la Guyane française, comme révélé dans le chapitre 4, un autre objectif clé de ce chapitre est de définir une condition de base fondamentale. Cette base sera formulée en utilisant des mesures dérivées de satellites et servira de référence critique pour identifier les anomalies ou les changements inattendus au sein de l'écosystème marin. L'établissement de cet état de référence est d'une importance capitale pour la conservation et la gestion marines, fournissant des informations essentielles requises pour mener des stratégies non seulement efficaces mais aussi réactives contre les problèmes émergents dans l'environnement marin.

Dans ce chapitre, les résultats confirment l'efficacité de la classification optique pour segmenter les eaux marines de la Guyane française en quatre types d'eau optique uniques. L'alignement entre les données spectrales acquises au sol et par satellite souligne la fiabilité de l'utilisation des mesures de couleur de l'océan pour cette classification. Les données à haute résolution du Sentinel-2 ont mis en évidence des changements saisonniers dans les OWTs autour de la rivière Maroni, surtout pendant les périodes de fortes précipitations. À l'inverse, la région de la rivière Oyapock a montré un manque de variation saisonnière significative, indiquant la nécessité potentielle d'autres méthodes ou de mesures in situ supplémentaires pour une classification précise.

En utilisant la technique de la SOM pour effectuer la classification temporelle, en se concentrant spécifiquement sur les valeurs de POC/SPM, ce chapitre renforce les conclusions présentées au Chapitre 4. Cette méthodologie offre une analyse complète qui explore l'impact de l'Amazone sur les eaux au large. Elle prend en compte divers facteurs tels que la présence d'tourbillons NBC, la rétroflexion NBC et l'extension vers l'ouest de paramètres biogéochimiques clés. Cette approche multifacette améliore notre compréhension des interactions complexes dans

l'environnement marin. Cependant, il est important de souligner que la fiabilité et la robustesse de cette technique dépendent en partie de l'accès à une série temporelle étendue de données pour une interprétation plus précise et nuancée.

Le processus de catégorisation basé sur les rapports POC/SPM a donné trois conditions d'eau distinctes : dominées par les minéraux, mixtes et dominées par l'organique. Cette classification consolide considérablement notre compréhension de la manière dont la distribution de la matière organique en suspension varie saisonnièrement dans les zones côtières. Plus précisément, nous avons observé que pendant les périodes de fort débit, les fractions organiques dans ces régions ont tendance à se contracter spatialement. Cette contraction est probablement due à l'effet de dilution causé par l'afflux de grands volumes de décharge d'eau. Fait important, la gamme de valeurs de POC/SPM que nous avons obtenues pour différents types d'eau optique OWTs était en forte concordance avec les mesures de terrain existantes. Cette cohérence ajoute une couche supplémentaire de validation à nos conclusions et souligne la fiabilité de l'utilisation des rapports POC/SPM comme paramètre clé pour comprendre la dynamique biogéochimique des différentes masses d'eau en Guyane française.

En utilisant des informations PPC, nous avons sélectionné et fusionné les techniques de partitionnement les plus efficaces pour classer les masses d'eau dans les régions côtières et au large de la Guyane française. Cette méthode intégrée sert de vue d'ensemble complète pour la délimitation des masses d'eau, offrant un niveau de fiabilité statistique qui pourrait potentiellement surmonter les limites des systèmes de classification conventionnels. Pour mettre ces conclusions en pratique, nous avons ensuite décrit une stratégie de mesure sur le terrain, comportant 12 stations stratégiquement placées à travers différents types d'eau, chacune conçue pour capturer les caractéristiques les plus significatives des masses d'eau à travers plusieurs régions de la zone d'étude. En particulier, les variations biogéochimiques dans le domaine au large sont plus susceptibles d'être caractérisées par des motifs temporels (saisonniers et irréguliers). Alors que les eaux mixtes et dominées par les minéraux associées à la manifestation de la banque de vase sont plus prononcées dans le domaine côtier de la Guyane française.

Les propriétés biogéochimiques liées à chaque OWT ont montré des variations saisonnières uniques, offrant des informations précieuses sur la saisonnalité des paramètres étudiés. Des valeurs de référence ont été établies pour ces paramètres à travers les quatre OWT pour servir de base à l'identification d'événements exceptionnels. Par exemple, un événement de précipitation

inhabituellement élevé en septembre 2021 a été détecté par des valeurs élevées de POC/SPM, probablement en raison de la dilution due à des précipitations intenses. Enfin, nous avons également envisagé la possibilité d'incorporer un large éventail de variables à la fois biogéochimiques et physiques dans la technique SOM. Cela nous permettrait d'attribuer une importance pondérée à chaque paramètre d'entrée, révélant ainsi l'importance relative de chaque variable pour différents types d'eau. Cette approche pourrait ainsi fournir une compréhension plus complète de l'écosystème marin. Plus précisément, elle pourrait être essentielle pour découvrir les interactions entre les variables biogéochimiques et leur impact sur des habitats écologiques spécifiques dans le milieu marin.

Bien que l'étude ait produit des conclusions informatives, plusieurs questions cruciales restent sans réponse, ce qui nécessite des investigations supplémentaires pour identifier les principaux moteurs affectant divers processus, tels que la présence du courant de la Guyane et l'extension vers l'ouest des variables biogéochimiques pendant la saison humide (venteuse). Des recherches supplémentaires sont nécessaires pour élucider les variations irrégulières de SPM potentiellement associées aux tourbillons du NBC. Des méthodologies capables de différencier entre les contributions locales (par exemple, les apports fluviaux, les échanges organiques des mangroves, les influences anthropiques) et régionales (par exemple, l'influence du fleuve Amazone) à la dynamique biogéochimique sont essentielles. Les futures recherches devraient privilégier des mesures in situ robustes, guidées par la stratégie d'échantillonnage proposée ici, et incorporer des paramètres physiques supplémentaires (par exemple, la dynamique du vent et du courant). Des données satellitaires mises à jour avec une résolution spatiale élevée et moyenne sont également recommandées pour les analyses temporelles, en particulier dans les régions côtières.

Les cadres de classification développés dans cette étude, englobant les classifications optiques, temporelles et PPC, ont démontré une applicabilité à d'autres environnements aquatiques géographiquement similaires. La stratégie d'échantillonnage proposée dans cette étude est considérée comme utile pour déployer efficacement des programmes de surveillance in situ et fournir également une analyse complète des fluctuations biogéochimiques, y compris l'identification des anomalies et les modulations de motifs saisonniers dans les eaux marines de la Guyane française. De plus, l'application de la classification SOM sur un ensemble de données multi-variables, englobant à la fois des variables biogéochimiques (POC, SPM, Chl-a, a_{CDOM}) et physiques (« Sea Surface Temperature » SST, « Sea Surface Salinity » SSS, « Mixed Layer

Depth » MLD, dynamique du vent et des vagues), offre la possibilité de définir les paramètres significatifs en évaluant leurs poids. Cette approche multi-métrique pourrait apporter des éclairages sur les aspects structurels et fonctionnels de l'écosystème marin, tels que la définition de niches écologiques et la dynamique des niveaux trophiques supérieurs.

INTRODUCTION

Coastal ecosystems provide manyfold benefits to human lives and hold enormous importance as they encompass diverse inter-connected aspects that are intricately related to ecological services, sociocultural factors, and economic development. These transitional regions play a significant role in "blue carbon" systems, serve as carbon sinks by capturing and storing carbon dioxide from the atmosphere, thus helping to regulate Earth's temperature (Nellemann & Corcoran, 2009). The marine vegetated habitats typically associated with coastal environment (e.g., mangroves, salt marshes, seagrasses and kelp forests, see **Figure 0.1**) occupy approximately 0.2% of the ocean surface but account for 50% of carbon storage in ocean sediments, and contribute 10% of net primary production in the ocean (Duarte et al., 2013). The coastal plant communities also serve as substantial elements for littoral protection by dissipating wave energy and reducing their impact on the shorelines. Moreover, coastal ecosystems serve as the living environments for various fish, shellfish, and other aquatic species that are harvested for consumption and commercial purposes. These resources contribute significantly to coastal economies as well as income for millions of individuals (Jänes et al., 2020; Theuerkauf et al., 2021). Monitoring the water quality and the associated biogeochemical mechanisms over coastal marine environment is therefore essential to facilitate the establishment of sustainable environmental policies and coastal management.

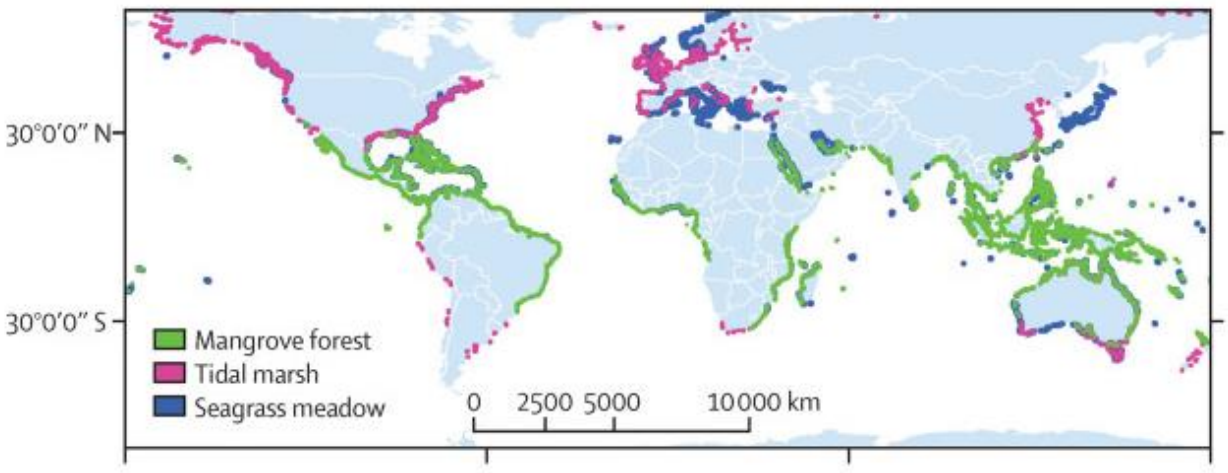

Figure 0.1. *The global distribution of Blue Carbon Ecosystems (BCE) with data derived from the UN Environment World Conservation Monitoring Centre (Adyel & Macreadie, 2022).*

Evaluation of environmental impacts on coastal regions appears to be a difficult task due to the involvement of multiple forcing variables. These drivers encompass the climate induced

variations of ocean/atmosphere properties and human activities which influence the biogeochemical dynamics of the water body in different ways. For example, changes in temperature and wind can alter the horizontal and vertical structures of water masses, which can have implications for nutrient availability and biological productivity (Gjelstrup et al., 2022; Loisel et al., 2017). Whereas, changes in precipitation can affect the land/ocean interactions, such as freshwater input and sediment transport, which can influence the salinity, turbidity and biogeochemistry of coastal waters (Harley et al., 2006; Loisel et al., 2014; Milliman & Kao, 2005; Vantrepotte et al., 2013). At the same time, anthropogenic impacts have increasingly left noticeable evidence on coastal waters through various activities such as dam construction, deforestation, intensive agriculture, and urbanization. These forcings have led to visible disturbance in the natural circulation of water constituents (i.e., nutrients, sediments, and organic carbon) over the land/ocean continuum (Milliman & Kao, 2005; Syvitski et al., 2005). In addition to these modifications, human-induced alterations of marine habitats, such as the destruction of wetlands and mangroves, have further exacerbated the impact on coastal ecosystems (Alongi, 2002). More specifically, overfishing has prompted shifts in food web structures, resulting in negative consequences for marine biodiversity and ecosystem function (Jackson et al., 2001; Pauly et al., 2002). Indeed, sustainable management of coastal ecosystems often requires our ability to provide reliable information through the implementation of appropriate numerical tools which can capture accurately the spatial and temporal dynamics of marine waters. This also supports facilitating the evaluation of the preservation or deterioration of coastal ocean environments, while serving as a useful tool to understand the relative contribution of natural and anthropogenic processes to the alteration in the water biogeochemical properties. For instance, Gallay et al. (2018) highlighted the effects of gold mining on sediment dynamics in the Maroni River by conducting a long-term study using MODIS data. Their research identified signs of human interference, as they observed a rising trend in suspended sediments that did not correspond with water discharge levels. However, undertaking such an analysis is challenging without baseline data like a reference state or the area's climatic conditions.

Although traditional in-situ observations offer precise information of the water properties, this approach typically presents certain disadvantages in terms of space, time, and cost as the acquisition of field measurements can be labor-intensive, time-consuming, and restricted to specific locations and timeframes. While Ocean Color Radiometry (OCR) serve as a valuable

and cost-effective tool for monitoring coastal water quality by providing insights into key biogeochemical parameters such as phytoplankton biomass, particulate and dissolved matter, and associated organic carbon stock (Mannino et al., 2008; Mélin & Vantrepotte, 2015; Platt & Sathyendranath, 2008). The integration of satellite archives from both medium-resolution sensors such as MERIS (Medium Resolution Imaging Spectrometer), MODIS (Moderate Resolution Imaging Spectroradiometer), and Sentinel-3/OLCI (Ocean and Land Colour Instrument) and high-resolution sensors such as Landsat-8/OLI (Operational Land Imager) and Sentinel-2/MSI (Multispectral Instrument) has enabled the collection of long-term observational data as well as fine details with a focus on specific local regions. Considering the offered advantageous benefits, remote sensing techniques have garnered significant attention as a valuable tool for supporting international environmental policies (i.e., EU Water Framework Directive (WFD), https://environment.ec.europa.eu/topics/water/water-framework-directive_en). Besides the mentioned advantages of remote sensing application, such approach also presents several inherent limitations including uncertainties in estimated products, information is confined to the surface layer, and susceptibility to cloud coverage interference. However, these limitations are largely compensated by its ability to provide an extensive spatio-temporal coverage (Gholizadeh et al., 2016), allowing a comprehensive view of the water masses over investigated areas.

In order to maximize the potential of OCR data to monitor coastal ocean waters, it is essential to address several methodological challenges that currently exist in the field. The first challenge arises from the optical complexity of coastal ecosystems, which necessitates the improvement of inversion algorithms for accurately estimating biogeochemical parameters from water color signals (Remote sensing reflectance, R_{rs}) (Groom et al., 2019; IOCCG, 2000, 2006). Case 1 waters are usually found in open ocean environments and are characterized by optical properties primarily influenced by phytoplankton and associated organic materials. In contrast, Case 2 waters are commonly located in coastal regions and exhibit optical properties shaped by a diverse range of constituents. These include not only phytoplankton but also mineral particles and various dissolved substances, whose concentrations can fluctuate independently (Gordon & Morel, 1983). Owing to the homogeneity in water constituents of Case-1 environments, existing inversion algorithms have proven to be effective in retrieving information on water properties in these regions. However, the estimation of biogeochemical parameter concentrations in coastal waters which are typically related to Case-2 waters, presents a more significant difficulty due to the increased optical complexity stemming from the co-existence of multiple components such as

suspended sediments, dissolved organic matter, and various optically active constituents (Dierssen & Karl, 2010). An additional remarkable obstacle in the implementation of remote sensing technique for monitoring coastal waters involves correction of atmospheric noises under the presence of aerosols, water vapor, and other atmospheric constituents. These elements can cause scattering and absorption of light, distorting the water-leaving optical signals before detected by satellite sensors (Gordon, 1997). As a matter of fact, accurate atmospheric correction is crucial, as any inaccuracies in the satellite-derived R_{rs} can lead to uncertainties in retrieving the information on biogeochemical descriptors. Considering the hydrodynamical complexity of transitional zone between land and ocean due to various processes, it is also necessary to develop a set of pertinent statistical methods to extract reliable information regarding the quality and characteristics of the water body (Loisel et al., 2013).

The coastal waters of French Guiana encompass distinct and highly vulnerable environments and habitats. In particular, the hydrological cycle and the nutrient availability in the region's marine ecosystem are significantly influenced by the seasonal shifts of the Intertropical Convergence Zone (ITCZ) which creates different patterns of precipitation, winds, and ocean currents between wet and dry seasons (Chevalier et al., 2008; Waliser & Gautier, 1993). Moreover, the shore-fringing mangroves colonizing on highly mobile mudbanks, substantially contribute to the "blue carbon" storage (Taillardat et al., 2018) and exchanges due to high above-ground tree biomass (Fromard et al., 1998; Walcker et al., 2018) and litter fall rates (Betoulle et al., 2001). The climate condition and presence of mangrove forests serve as crucial factors in regulating biogeochemical dynamics as well as habitats for various fish species (Nagelkerken et al., 2008), thus, impacting commercial and subsistence fisheries in French Guiana (Sanz et al., 2017).

The existing knowledge gap and the absence of a long-term in-situ data in French Guiana coastal waters present a challenge in understanding and managing coastal ecosystems effectively. In addition, a substantial amount of sediment supply originating from the Amazon River plume also elevates the optical complexity of the aquatic environments (Eisma et al., 1991; IOCCG, 2000), which necessitates the development of more adapted statistical tools and accurate ocean color products.

Until the current time, investigations dedicated to monitoring biogeochemical variability in the study area, exploiting ocean color observation, were mainly conducted with the focus on

SPM (i.e., Abascal-Zorrilla et al., 2020; Gardel & Gratiot, 2005; Vantrepotte et al., 2013) and Chlorophyll-a (Chl-a) (Lampert et al., 2015). Recent studies, which attempt at examining the spatio-temporal dynamics at regional scale, was conducted by Institut Français de Recherche pour l'Exploitation de la Mer (IFREMER) through 4 annual reports (Akopian & Lampert, 2018; Lampert et al., 2015, 2016, 2017). However, the bio-optical inversion algorithms used to derive the concentration of these two parameters (Gohin et al., 2002, 2020) have not been regionally adapted since these models were initially designed based on the dataset gathered in French waters (i.e., Réseau d'Observation et de Surveillance du Phytoplancton et des Phycotoxines REPHY). Hence, to obtain a comprehensive understanding of coastal water quality, it is essential to consider the local adaptation of inversion models for estimating other innovative biogeochemical indicators, such as Particulate Organic Carbon (POC), Colored Dissolved Organic Matter (a_{CDOM}), and Dissolved Organic Carbon (DOC). Another obstacle to monitor the French Guiana's coastal waters is the presence of sun glint effect that appears consistently in tropical regions (Abascal-Zorrilla et al., 2019) under a condition of solar incidence angles and relatively low wind velocities (Harmel & Chami, 2013; Tavares et al., 2021).

Indeed, biogeochemical dynamics play a crucial role in shaping marine ecosystem services, including fisheries as these processes regulates nutrient cycling, primary productivity, and the availability of resources for higher trophic levels (Cloern, 2001; Conley et al., 2009). The partition of the water masses taking into account the biogeochemical dynamics also supports developing effective regional monitoring policies. In this attempt, the delimitation proposed by IFREMER was established in the consideration of 4 zones corresponding to different fishing areas as well as the heterogeneity of coastal water body (Akopian & Lampert, 2018). However, this partitioning method for the French Guiana marine waters can still be improved through the incorporation of more rigorous statistical approaches.

Considering the fact that former satellite-based studies at regional scales have not been optimally adapted to exploit fully the potential offered by ocean color remote sensing observation, the present dissertation consists of five Chapters aiming at answering arose scientific questions:

1) What are the most suitable inversion algorithms to generate pertinent satellite ocean color products for monitoring the dynamics of biogeochemical parameters in French Guiana?

2) What is the description of the biogeochemical variability at the regional scales and the associated driving factors? Are there any long-term changes in the coastal water composition in the region?

3) Which parameters can serve as the key descriptors to follow for monitoring French Guiana's coastal water quality?

4) How to better partition the water masses in order to support the development of regional monitoring policies?

5) What is the reference state of the French Guiana's coastal waters?

Chapter 1 of this work presents essential background information, establishing the context and motivation of the research. This introductory chapter describes the research problem, outlines the objectives, and highlights the significance of the study.

In Chapter 2, a comprehensive overview of the datasets employed and the statistical methodologies utilized throughout this PhD research is provided. This chapter offers a detailed account of the data sources, including their acquisition, processing, and quality control measures.

Chapter 3 focuses on the methodologies to regional adaptation of inversion algorithms. The chapter discusses the development and selection of the most bio-optical models for estimating various biogeochemical parameters at a local scale, taking into account the unique environmental conditions of the study area.

Chapter 4 examines the biogeochemical variability at regional scales, along with the associated driving factors, and any potential long-term shifts in French Guiana's coastal water composition. This chapter discusses the connections between biogeochemical parameters and their possible origins, including environmental factors such as river outflow, tidal influence, and ocean currents, etc. This has been done through the temporal analysis performed on medium-spatial-resolution satellite archives. Additionally, the chapter aims to point out the crucial parameters that could function as effective descriptors for monitoring the coastal water quality of French Guiana.

Chapter 5 aims to facilitate the establishment of regional monitoring policies by analyzing the effectiveness and robustness of different partitioning methods considering the adoption of both medium and high-spatial resolution data. Furthermore, the chapter highlights the benefits of the proposed classification scheme, emphasizing its potential for providing a more

comprehensive insight into the biogeochemical dynamics and water properties of French Guiana's marine environment compared to the traditional approach. Attempts to establish a reference state of the water body considering multiple water quality indicators will also be suggested to detect exceptional events.

CHAPTER 1: STATE OF THE ART

French Guiana's coastal waters present unique and fragile ecosystems and habitats. The hydrological cycle and nutrient availability in the region are typically regulated by the Intertropical Convergence Zone's (ITCZ) seasonal oscillations, resulting in varied precipitation, wind, and ocean current patterns during wet and dry seasons (Chevalier et al., 2008; Waliser & Gautier, 1993). In addition, the mobile mudbanks along the shoreline supporting the growth of mangroves, which play a significant role in "blue carbon" storage (Taillardat et al., 2018) and exchange due to their contribution of above-ground tree biomass (Fromard et al., 1998; Walcker et al., 2018) and litterfall rates (Betoulle et al., 2001).

The scarcity of in-situ data in French Guiana's marine ecosystem poses a challenge in assessing biogeochemical variability, which is also crucial for regional monitoring strategies. Despite their potential as powerful tools for monitoring coastal water quality, the application of remote sensing techniques to French Guiana’s coastal waters might encounter several obstacles. The high turbidity resulting from significant sediment influx from the Amazon River (Eisma et al., 1991) increases the optical complexity of the water body. Consequently, quantifying biogeochemical concentration becomes a difficult task due to the presence of various colored water constituents, for instance, phytoplankton, suspended particulate matter (SPM), and colored dissolved organic matter (CDOM) which simultaneously affect the optical signals (IOCCG, 2000; Mouw et al., 2015; Werdell et al., 2018). Additionally, the persistent sun glint effect in the study area further complicates the observations of biogeochemical dynamics from space (Abascal-Zorrilla et al., 2019).

Until now, research aimed at monitoring biogeochemical variability in French Guiana's coastal waters have primarily concentrated on SPM and Chl-a (Abascal-Zorrilla et al., 2020; Akopian & Lampert, 2018; Gardel & Gratiot, 2005; Lampert et al., 2015, 2016, 2017; Vantrepotte et al., 2013). Nonetheless, the bio-optical inversion algorithms employed for determining the concentrations of these parameters have not been sufficiently adapted to the region. Thus, to achieve a more in-depth understanding of coastal water quality, it is essential to tune these inversion models as well as incorporate additional biogeochemical indicators such as POC and DOC. Moreover, the previous delimitation approach of the water masses used for the study area was not built from a robust statistical method.

Taking into account that previous satellite-based studies at regional scales did not fully harness the capabilities of ocean color remote sensing observations, this thesis aims to: 1) develop a collection of ocean color products (Chl-a, SPM, CDOM, POC, and DOC) for monitoring coastal water quality in French Guiana as well as offering comprehensive time series to local stakeholders; 2) describe the biogeochemical dynamics at the regional level and evaluate the related factors leading to the variability of considered parameters; 4) identify the essential biogeochemical descriptors and examine the presence of long-term changes; and 5) suggest a comprehensive classification scheme for partitioning water masses to facilitate the establishment of local monitoring policies and define the reference state that is beneficial to detect exceptional events.

1.1. Study area

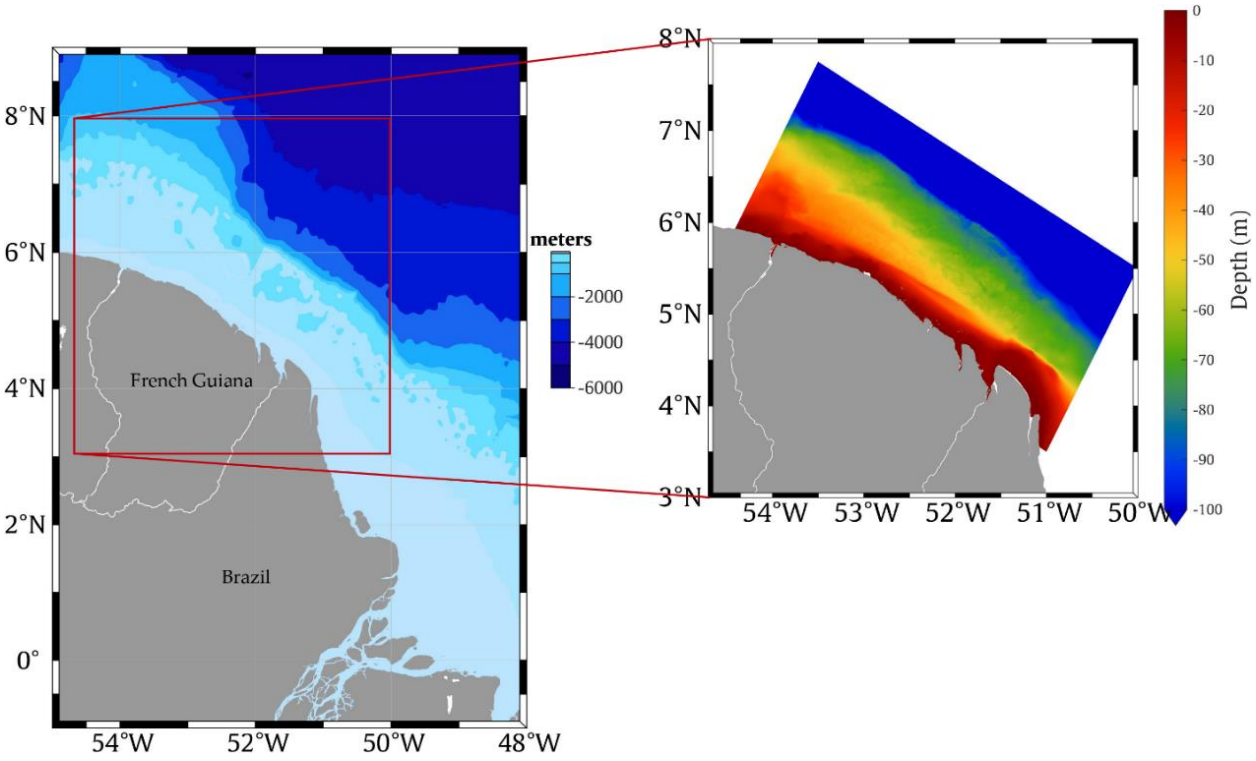

Figure 1.1. *Illustration of the French Guiana's coastal geomorphology with bathymetry and its location with respect to the Amazon River mouth (MNT Bathymétrique de Façade de La Guyane).*

The primary drivers affecting French Guiana coastal water quality encompass Amazonian mud inputs originating from the Amazon River mouth (**Figure 1.1**) and local hydrodynamic mechanisms (e.g., seasonal fluctuations, resuspension phenomena, etc.,). These drivers are

typically regulated by different environmental forcings and physical processes (e.g., wind, current, tides factors, and/or seafloor morphology) which significantly contribute to the biogeochemical dynamics and overall ecological state of the study area.

1.1.1. Climatological condition

French Guiana's coast is situated between latitudes 4º and 6º N and is predominantly influenced by equatorial climate. Its geographical location is responsible for the hot weather and high humidity throughout the year. Precipitation in this region is primarily characterized by the presence and displacement of the Intertropical Convergence Zone (ITCZ) from North to South, causing seasonal fluctuations defined by two periods of wet and dry seasons (Chevalier et al., 2004). More specifically, a short-wet season is usually observed from December to January as in response to the northward shifts of ITCZ, and a long one occurred between April to July with rain deposits intensity above 300 millimeters per month over St. Laurent du Maroni region. For the rest of the year, French Guiana experiences two dry seasons (short between February and March and long between August and November) with rainfall below 100 millimeters per month (French Guiana Climate: Average Weather, Temperature, Precipitation). The highest temperature of the year is also observed during this dry period typically in October. In fact, seasonal alteration in precipitation regulates the intensity of discharge flow in local rivers and thus impact on the biogeochemical dynamics over marine waters, for instance, increase in nutrient loads and phytoplankton productivity (Ray et al., 2018). Movement of ITCZ further leads to changes in the direction and intensity of Tradewinds, generating different environmental conditions inducing multiple hydrological processes such as sediment resuspension and strength of oceanic currents acting on Guiana Shield.

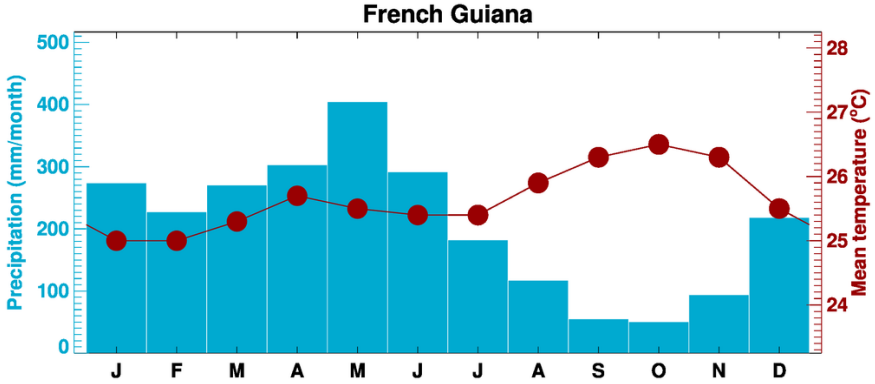

Figure 1.2. *Precipitation and Temperature in French Guiana (1961-1990)*

(Source : https://crudata.uea.ac.uk/~timo/climgen/national/web/FrenchGuiana/obs.htm)

1.1.2. Hydro-dynamic processes

1.1.2.1. Waves and Winds

Trade winds blowing towards the coast of the Guianas have been documented to be a crucial factor for coastal regime at different scales (Augustinus, 2004). The strongest winds have been recorded from January to April (from 6 m/s to 9 m/s) blowing from NE to SW direction leading to high energic waves approaching the French Guiana coastline. During dry period between June and November, manifested South-East Tradewinds alters ocean current direction thus causes seasonal impacts on biogeochemical dynamics. The seasonal presence of Tradewinds in relation to other physical processes (i.e., ITCZ position, current, local river discharge) is depicted in Tradewinds are also responsible for high rainfall during the wet season between December and July with a short interruption of a dry month in March (Anthony et al., 2010). The wave conditions are subject to these winds and directly act on the coastal dynamics. This has been especially documented at regional scale for mudbanks dynamics emphasizing the significant impact of trade winds direction and intensity of on erosion/deposition processed and thus on migration rate of the mudbanks (Abascal-Zorrilla, 2019; Abascal-Zorrilla et al., 2018; Augustinus, 2004; Augustinus et al., 1989; Eisma et al., 1991; Gratiot et al., 2007).

	Dec.	Jan.	Feb.	Mar.	Apr.	May	Jun.	Jul.	Aug.	Sep.	Oct.	Nov.	Dec.
Season	Rainy season			Little dry season	Rainy season				Dry season				
ITCZ position	Oscillated			2°S–2°N	Oscillated				8°N				
Amazon liquid discharge					Max. = 0.25 Sv					Min. = 0.08 Sv			
Local rivers liquid discharge					Max.								Min.
Wind	North-East Tradewinds							South-East Tradewinds					
Current	North Brazil current							North Brazil current and retroflection					

Figure 1.3. *Summary of the major environmental physical constraints on the French Guiana continental shelf (Chevalier et al., 2004).*

Waves in the French Guiana coastal domain come from an east-to-northeast direction, which is primarily in response to the direction and oscillation of trade winds (Gratiot et al., 2007). Significant period (T_s) and significant offshore height (H_s) of waves are observed to be in the range of 6 to 10 s and 1 to 2 m respectively **Figure 1.4**. Interestingly, the strongest trade-wind waves have been recorded from December to April and swell waves, however, are usually observed in autumn and winter (dry season) (Anthony et al., 2010).

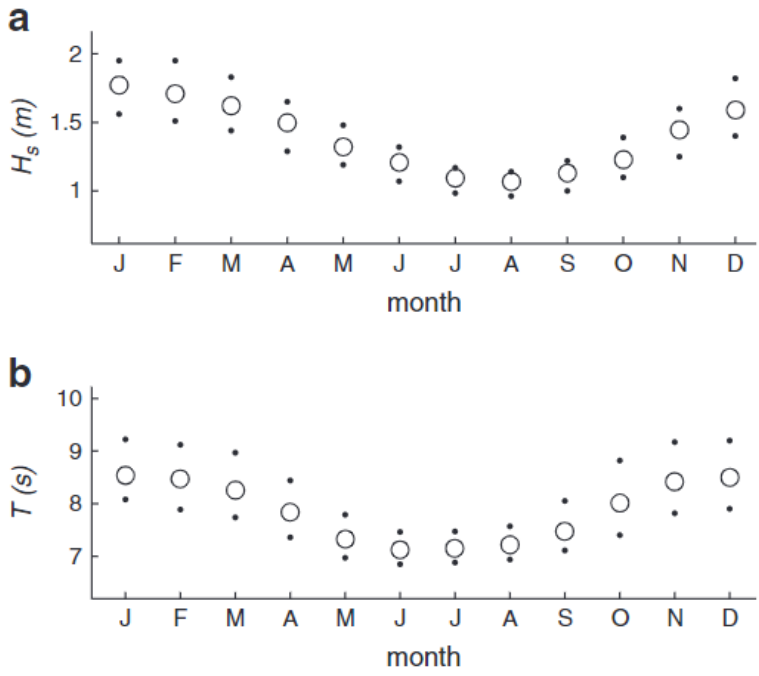

Figure 1.4. a) *Significant wave high (H_s) and* ***b)*** *wave period (T_s) estimated from ERA40 (European Reanalysis) wave dataset within 44 years (1960 - 2004) deployed by the European Centre for Medium-Range Weather Forecasts (ECMWF) at the location of 5° N, 52° W. (Gratiot et al., 2007)*

1.1.2.2. North Brazil Current rings and retroflection

North Brazil Current (NBC) has been known as a major western boundary current in the tropical Atlantic Ocean. This current conveys warm and rich-nutrient waters from the South Atlantic to the North Atlantic (Arnault et al., 1999; Schott et al., 1995). The seasonal transport of NBC was documented to be tightly connected to wind stress, which normally reaches its maximum from July to August (36 Sv) and minimum from April to May (13 Sv) near 4°N (Baklouti et al., 1998). From July to December, the NBC bifurcates and deflects from the South American coastline and curves back on itself (retroflects) at 6°N - 8°N to feed the North Equatorial Counter Current (NECC), the remaining portion of NBC follows the coast to join Guiana current (Baklouti et al., 1998, 2007; Fratantoni & Glickson, 2002). During this process, anti-cyclonic rings detach from the retroflection and move in the northwest direction as known as NBC rings with a mean diameter of approximately 390 km and a speed of propagation of 12.4 km/day (Garzoli et al., 2003; Johns et al., 1990). The manifestation of NBC retroflection as well as NBC rings play a vital role in spreading Amazon plume encompassing nutrient supply over French Guiana continental shelf. These warm-core vortices are detected with a frequency of 5 to

6 times per year and dissipate in the vicinity of the Lesser Antilles as a result of interactions with abrupt topography after 3-4 months of propagation (Fratantoni & Glickson, 2002; Goni & Johns, 2001).

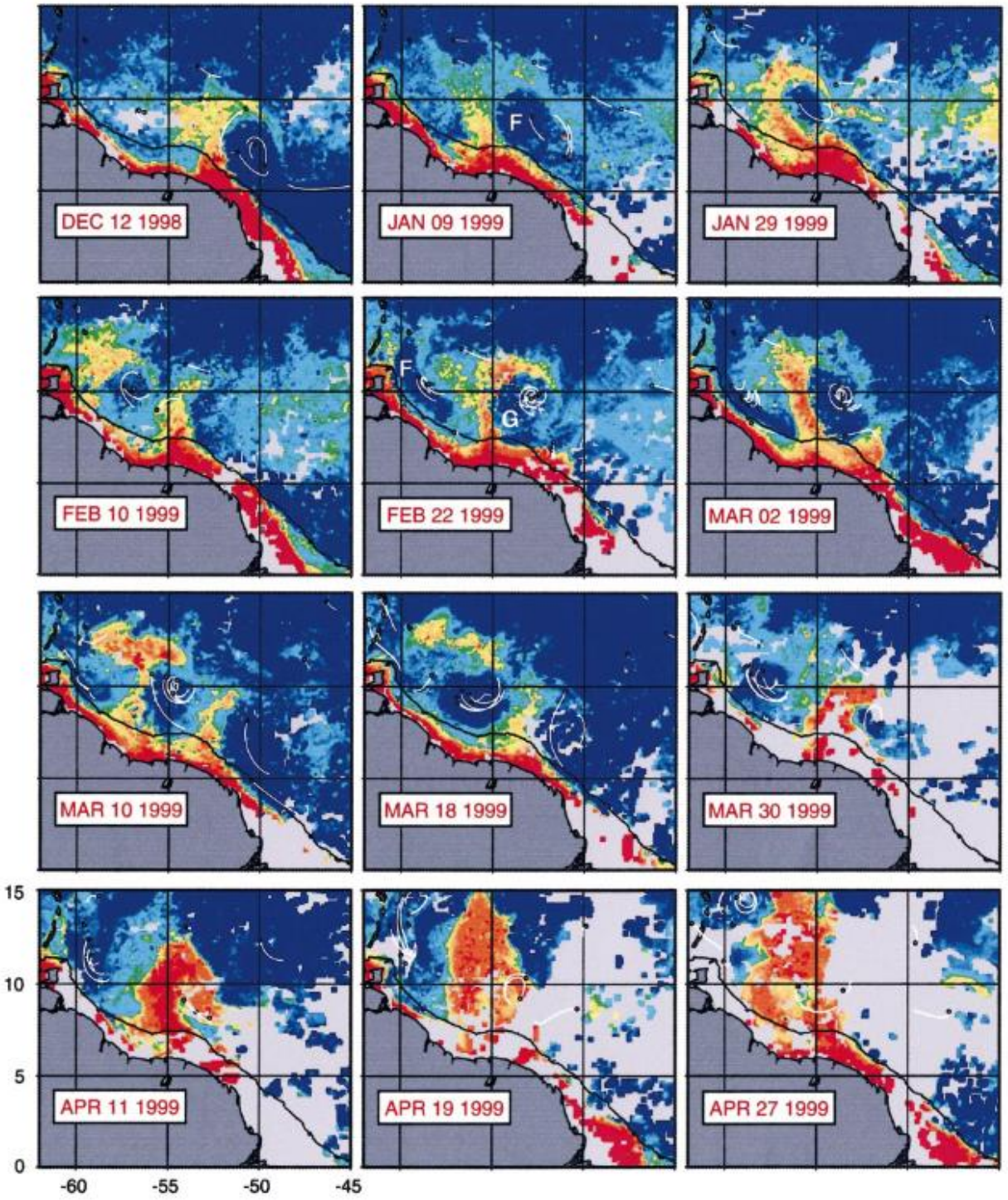

Figure 1.5. *Time series of composite SeaWiFS images depicting the evolution of 2 NBC Rings through Chlorophyll-a concentration. (Fratantoni & Glickson, 2002)*

1.1.2.3. Mudbank migration

The French Guiana coastline contributes to the world's longest muddy coast stretching between the Amazon's mouth and the Orinoco River delta (1500 km). As known as the largest river system on earth, the Amazon occupies a drainage basin of 6.1×10^6 km^2 and represents 20% of the freshwater discharge to the ocean (Moura et al., 2016). The fine-grained sediments forming muddy deposits originate from the Amazon River plume, which are transported northwestward along the coast of Guianas with an approximate volume of 1.5×10^8 tons every year (Eisma et al., 1991). Due to its special characteristics, the Amazon system generates a large area of plumes up to 1.3×10^6 km^2.

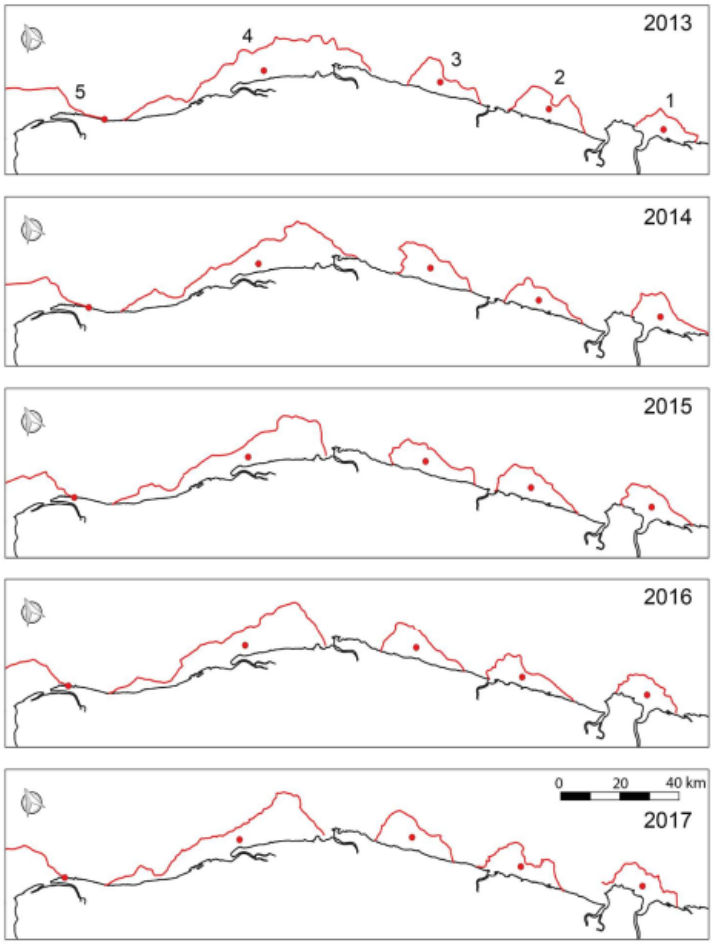

Figure 1.6. *Location and migration of existing mud banks on the French Guianese coastal between the dry seasons of 2013 and 2017. The red line corresponds to the footprint delimitation using the SPM values method, and the red circle corresponds to the barycenter of each mud bank for each year (Abascal-Zorrilla et al., 2018).*

The migration of mudbanks along the coastline of Guiana Shield is based on mud recycling which is principally driven by wind-generated waves acting on the liquefaction process (Allison & Lee, 2004; Chevalier et al., 2004, 2008; Gratiot et al., 2007; Rodriguez et al., 2001). The back of the bank is made up of solidified mud and is typically populated with beachfront mangroves. The mobilized sediment is subsequently transferred to the leading edge of the bank, causing a displacement of the mud bank along the coastline in the direction of the longshore drift directed northwestward (Allison & Lee, 2004). For this reason, the accretion and erosion of mudbanks are vital processes leading to thereof transportation. Eisma et al., (1991) with an implementation of a series of air photographs in the time period of 1947 - 1984, discovered that the mud deposition along the Guianese coast is principally linked to the intensity and direction of the northeasterly trade winds and does not rely on the severity of sediment loads delivered from the Amazon River.

In fact, SPM can be referred to as total suspended solids (TSS) or total suspended matter (TSM) and is constituted of all particulate materials that pass through a preweighted filter with a nominal pore size of 0.7 µm (Neukermans et al., 2012). Therefore, SPM encompasses organic (autotrophic and heterotrophic plankton, bacteria, viruses, and detritus) and mineral particles existing in the water column (Stramski et al., 2004). Due to this particular property and the special process of mud drifts, SPM has been considered as an indicator to monitor the mud bank dynamics using ocean color radiometry archives over French Guiana coastal waters. According to Gardel & Gratiot, (2005), the optical SPOT (Satellite Pour l'Observation de la Terre) imagery with a spatial resolution of 20 m has enabled the discovery of the migration rate of mud banks which was recorded to be higher than those reported in earlier studies. In particular, the average velocity of the Kourou–Cayenne mud bank was witnessed to be 1.4 km/year in the period of 1991-2002, meanwhile, the mean velocity of this bank was recorded to be 0.8 km/year from 1979 to 1984 by the investigation of Froidefond et al., (1988). The latter observations were performed by Vantrepotte et al., (2011, 2013) with a specific focus on the variability of TSM. More specifically, this study estimates TSM by an adoption of a generic single band algorithm proposed by Nechad et al., (2010) with the parameterization of the reflectance at 678 nm which corresponds to the red spectral band of the MODIS satellite sensor. The temporal variation of TSM was then analyzed based on the Census X-11 time series decomposition and the detection of monotonic change (Gilbert, 1988; Pezzulli et al., 2005). The findings over a period of eight years demonstrate that mud mobilization is predominantly related to trade winds season and has

an average speed of approximately 2 km/year with strong interannual fluctuation in SPM reaching up to 6 %/year. The evidence for the migration of mud banks is depicted in **Figure 1.7** and **Figure 1.8** through SPM concentration estimated over two transects crossing two adjacent mud banks in Kourou and Cayenne.

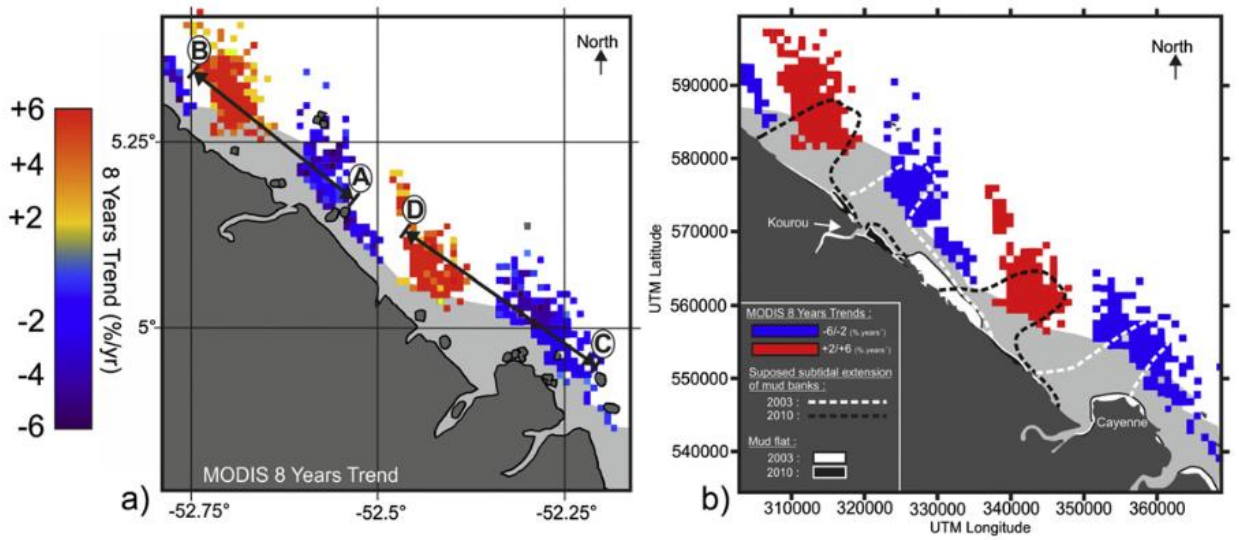

Figure 1.7. (a) *Significant trends in SPM detected over French Guiana coast from the 8-year MODIS time series (in %/year) and* ***(b)*** *comparison with the mud banks estimated position and morphology (Vantrepotte et al., 2013)*

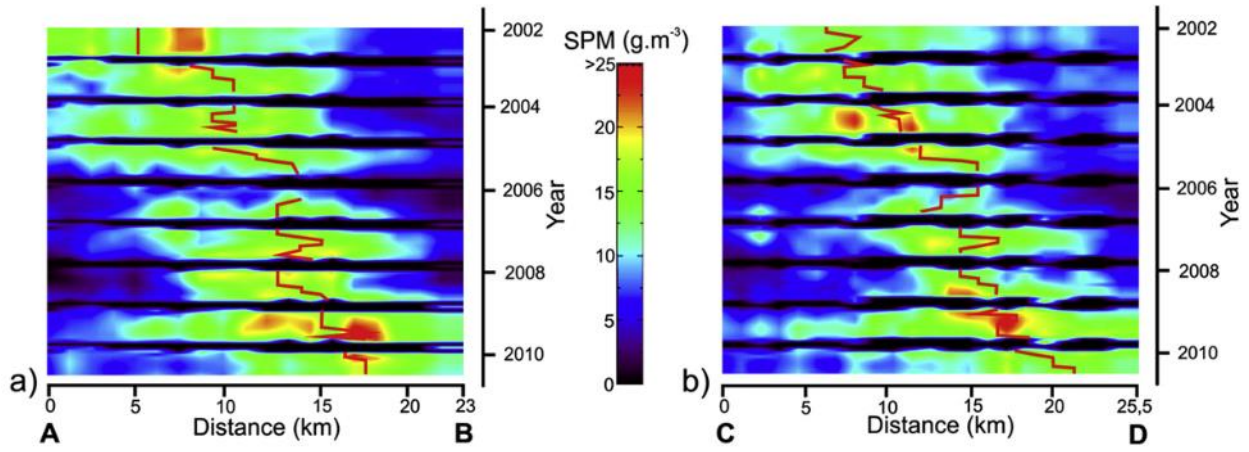

Figure 1.8*. Time space diagrams computed over two along-shore transects crossing the areas presenting significant 2002-2010 trends in SPM in the Kourou* ***(a)*** *and Cayenne* ***(b)*** *coastal regions (from points A to B and C to D, respectively, see* ***Figure 1.7****) (Vantrepotte et al., 2013)*

The formulation as well as the manifestation of mudbanks were further highlighted by Gensac et al., (2016) in which the migration of mudbanks has been confirmed to be tightly linked

to the massive supply of sediments from the Amazon River. Mudbank detection using high resolution satellite sensor (i.e., Landsat8/OLI) with the specific focus on French Guiana coastal domain was performed by the recent work of (Abascal-Zorrilla et al., 2018). Five mudbanks, which might differ in shapes, were identified over the inner shelf with migration rates (averaged value of 2. km/year) slightly higher when comparing with previous records **Figure 1.6**.

Aller & Blair, (2006) pointed out the impacts of mudbanks on the available organic content in the inner shelf and the involved chemical and physical processes. In particular, the synthesis of tides, wind-induced waves, and coastal currents contribute to the reoxidation of fluid muds as well as the remineralization of organic matter along the Amazon–Guianas coastline. Throughout the transportation process, sedimentary organic carbon undergoes depletion, causing marine sources to predominantly serve as the remineralization substrate. However, this does not appear in regions situated near mangrove shorelines.

1.1.2.4. Local rivers and mangrove ecosystems

Part of the "blue carbon" stock in the ocean is stored by mangroves which contribute large amounts of organic matter to the surrounding aquatic environment. This organic content consists of both particulate and dissolved materials stemming from decomposition and leaching products of leaf litter leaves through different physical processes (i.e., resuspension, tidal pumping) contribute substantially to the overall productivity of the ecosystem, thus impacting the water quality (Kristensen et al., 2008). In particular, mangroves present a crucial function in the biogeochemical cycling of carbon and nutrients (Adame & Lovelock, 2011) as they preserve the organic carbon thereby providing energy sources for aquatic species (Kristensen et al., 2008).

The development of mangroves in relation to the mudbank drifts along the coastline of French Guiana has been documented by various historical studies. In particular, at the back of the mudbank, erosion occurs and collapses the presence of mangroves. Meanwhile, the accretion phase at the front of the mud flat contributes to the establishment of mangrove areas (Berlamont et al., 1993; Gardel & Gratiot, 2005). The process of mudbank accretion leading to the development of mangroves is described in **Figure 1.9**.

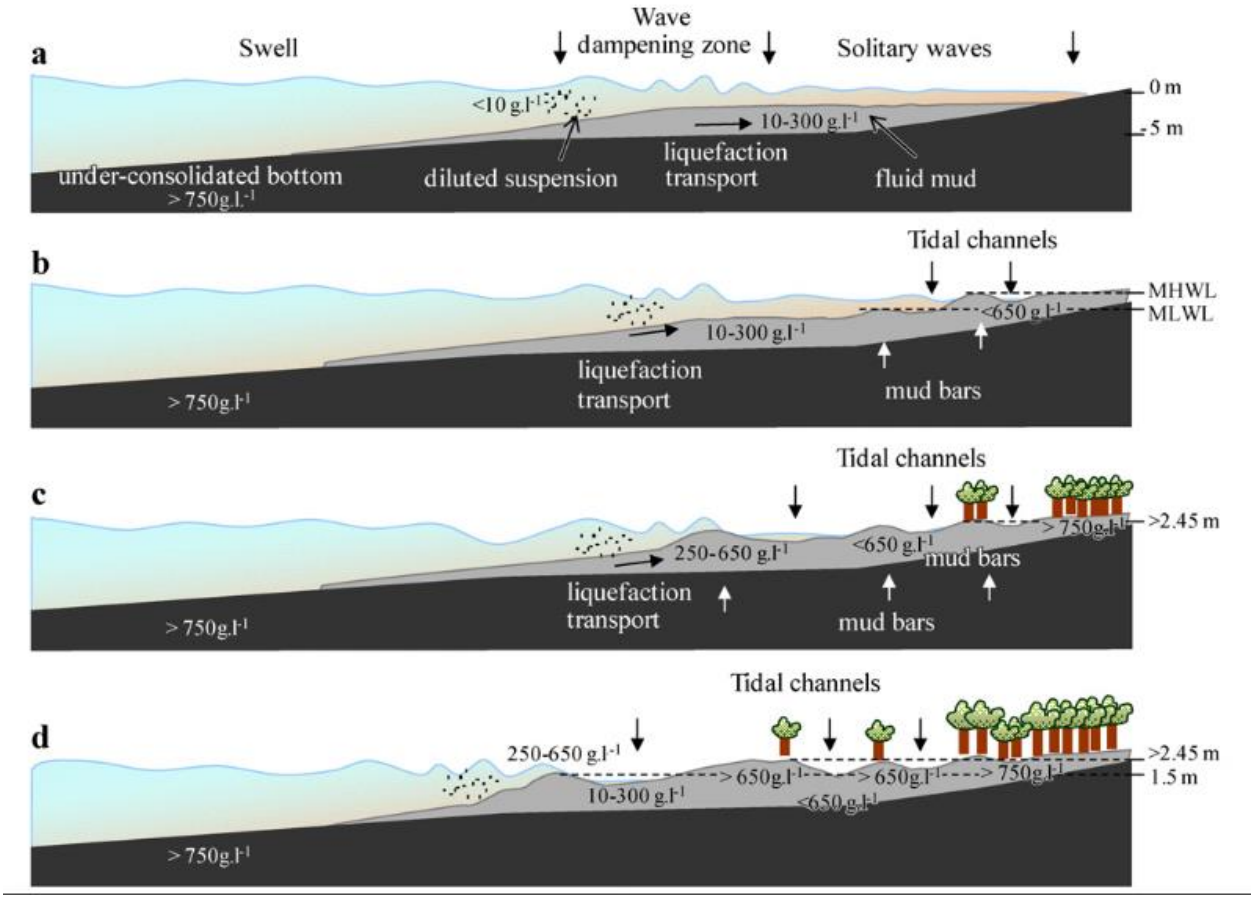

Figure 1.9. *Stages in the formulation of mud bars by waves with the evolution of mangrove forests (Gardel et al., 2011).*

Coastal waters in French Guiana are partly governed by freshwaters influence originating from the outlets of local rivers located along the shorelines (**Figure 1.2**). This river system is established by eight small rivers (Mana, Counamama, Sinnamary, Kourou, Montsinery, Mahury, Kaw, and Approuague,) and two main rivers (Maroni and Oiapoque). Furthermore, the Maroni River and Oiapoque River form the border of French Guiana, separating its territory from Surinam (in the west) and Brazil (in the east), respectively. In French Guiana, the variation of river discharge exhibits a seasonal pattern as a consequence of rainfall alternation. For instance, the averaged discharge flow rate recorded in Maroni River can reach up to approximately 5000 m^3/s during high flow period and remain below 1000 m^3/s throughout dry season particularly from September to November.

The contribution of the French Guiana local rivers to the coastal sedimentation is insignificant which occupies approximately 1% of the suspended loads transported along the shore with a suspended sediment concentration of 0.1-10 $mg.L^{-1}$ (Lambs et al., 2007; Prost,

1989). During the wet season, the French Guiana rivers can supply a significant amount of fresh water to the coast, which reduces the salinity in this area (Lambs et al., 2007). The contribution of total organic matter from the two Guiana Shield basins (the Maroni and Oiapoque Rivers) was recorded to show maximum concentrations in high water stages as a result of organic matter accumulated in soils flushed out by rainfall. In contrast, Chl-a exhibited lower concentrations during this period which might be attributed to the weakly mineralized waters (Gallay, Mora, et al., 2018; Sondag et al., 2010).

In addition to this, the seasonal variation of discharge flow in local rivers play a vital role in regulating organic pool over the estuarine vicinity as high surface runoff introduces more mangrove-derived POC and DOC encompassing the involvement of freshwater phytoplankton (Ray et al., 2018). In French Guiana estuarine ecosystem, substantial associations are present between intertidal mangrove habitats and estuarine environments in relation to carbon export and exchange through diverse mechanisms. These processes formulate a complex system with the presence of litter leaching, pore water drainage, sediment erosion, sediment resuspension, remineralization, lateral CO_2 transport, and methanotrophy.

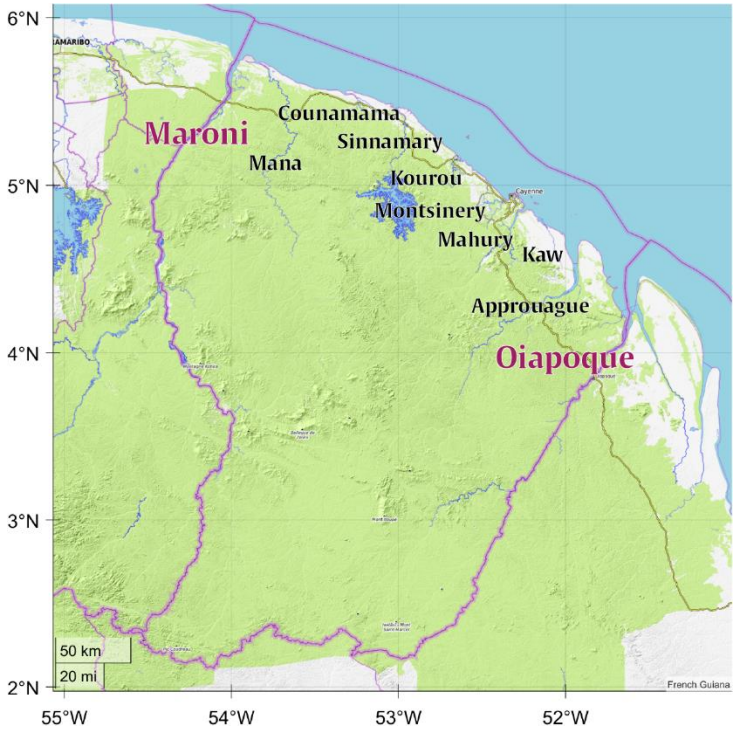

Figure 1.10. *Locations of main rivers along the French Guiana coast*

1.1.2.5. Tide

The tide in French Guiana is recognized as a combination of two daily low and high tides with different amplitudes (Service Hydrographique et Océanographique de la Marine, 1975). The tidal currents are assumed to not significantly impact the current direction in the outer shelf domain, which present as a weak flow of 0.05 - 0.1 m/s during the neap-spring cycle (Bourret et al., 2008). However, in the inner shelf, it is witnessed that the tidal currents exhibit a stronger influence and can reach up to the velocity of 0.55 m/s in front of the Sinnamary river mouth. For this reason, although the erosion and deposition of the mudbanks are predominantly regulated by waves, the littoral current and tide modulate these processes (Chevalier et al., 2008).

1.2. Ocean color observation as a tool for monitoring coastal waters

1.2.1. Remote sensing technique for monitoring biogeochemical variability

1.2.1.1. General considerations

Conventionally, indicators for water quality including physical, chemical, and biological parameters are measured by deploying field measurements in sampling sites and then evaluating the samples in the laboratory. This traditional sampling method typically requires manual work and is limited in determining the spatial and temporal variability of the biogeochemical variables. Ocean color data have been considered as a mean to overcome the addressed issues and facilitate the assessment of optically significant constituents in the water bodies (Alparslan et al., 2007; Brando & Dekker, 2003; Gholizadeh et al., 2016; Gordon & Morel, 1983; Saad El-Din et al., 2013).

However, the application of remote sensing technique encounters some challenges in optically complex waters (Case-2 waters) where the co-occurring water constituents are present. This is mainly due to the fact that these components interact with light in different ways leading to difficulties to differentiate their respective optical signals. The overlapping absorption, scattering spectra, and reflectance also leads to obstacles to directly relate them to one substance (IOCCG, 2000). Further challenges were addressed by Loisel et al., (2013) that optical signals in coastal waters are potentially influenced by the environmental characteristics encompassing presence of clouds, resuspension process in shallow waters, bubbles induced from waves, etc. Therefore, the estimation of biogeochemical parameters usually requires more complex and sophisticated inversion algorithms than those designed for clear waters (Case-1 water).

The accuracy of ocean color data can also be impacted by atmospheric disturbances caused by different factors including aerosols, Rayleigh scattering, water vapor absorption, and sun glint. Therefore, atmospheric correction processing also plays an important role in retrieving accurately radiometric signals. The necessity of noise removal from Top Of Atmosphere (TOA) radiance is due to the fact that qualitative and quantitative information about the bio-optical components within the water body derived from inversions algorithm strongly relies on the reliability of obtained reflectance (Loisel et al., 2013).

1.2.1.2. Challenges in Monitoring Coastal Water Quality in French Guiana

Historical satellite-based studies conducted over the French Guiana coastal domain have confirmed the potential of remotely sensed data assimilation to better understand the hydro-sedimentary as well as hydro-dynamics in this area through research dedicated to investigation of the mudbank manifestation, winds stress, and ocean currents (Fratantoni & Glickson, 2002; J.-M. Froidefond et al., 2002; Gardel & Gratiot, 2005; Vantrepotte et al., 2013). The monitoring work dedicated to coastal water quality based on the adoption of satellite imagery in French Guiana has been mainly carried out by IFREMER (Lampert et al., 2015) with a focus on the analysis of two conventional parameters, SPM and Chl-a, which were derived from OC5 algorithm developed by Gohin et al., (2002). This algorithm is a modified version of OC4 model proposed by The National Aeronautics and Space Administration (NASA) with a correction of the effect of SPM at the wavelength of 412 nm and 555 nm. The model was initially designed for the dataset collected in French waters through Réseau d'Observation et de Surveillance du Phytoplancton et des Phycotoxines (REPHY). In addition, the match-up validation to verify the performance of the OC5 model in the study area presents a limitation due to the constrained number of in-situ measurements. Hence, to obtain an encompassing understanding about the biogeochemical dynamics as well as the coastal water quality in the study area, it is necessary to take into account other indicators, in addition to Chl-a and SPM, such as POC, DOC, and CDOM with a set of corresponding inversion algorithms adapted regionally using in-situ data collected in French Guiana coastal domain.

French Guiana coastal ecosystem represents a substantial influence from the Amazon River mouth, thus significantly enhancing the optical contrast of the water body through the presence of high suspended sediment loads. In other words, the French Guiana coastal waters are representative for Case-2 waters where the optical properties of co-existing components are

regularly overlapped. For instance, despite its importance as a critical water quality indicator, chlorophyll-a (Chl-a) estimates in optically complex waters are often considered unreliable, particularly at low concentrations, due to the minimal contribution of phytoplankton absorption in such conditions. As discussed in Section 1.2.1.1, this distinct feature further complicated the retrieval of bio-optical parameters in the study area. For this reason, an adapted Chl-a model, accompanied with a scheme to to assess the reliability of Chl-a estimates at various turbidity levels, is of significant importance.

French Guiana marine waters appears to be highly impacted by permanent sun glint effects as a consequence of geographical location, leading to substantial missing data in terms of ocean color observations (Abascal-Zorrilla et al., 2019). This is due to the fact that tropical regions are frequently subject to sun glint contamination when sunlight reflects off the surface of the water at a certain angle, creating a bright, reflective spot on the water's surface (Kay et al., 2009; Mobley, 2015). As a consequence, the sunglint-contaminated pixels typically exhibit an overestimation in the reflectance and are usually masked during atmospheric correction process. An example depicting the loss of information due to sun glint effects is shown in **Figure 1.11**. Hence, utilizing satellite-based techniques to study biogeochemical dynamics in French Guiana requires the implementation of a suitable atmospheric correction scheme capable of dealing with sun glint effects.

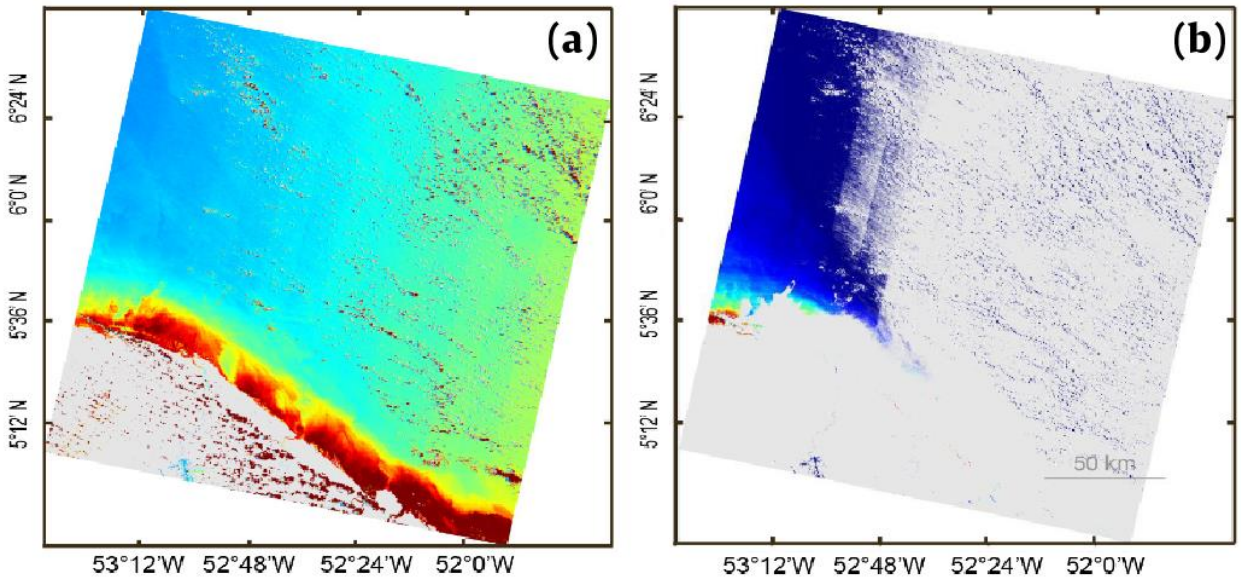

Figure 1.11. *Illustration of sun glint effects in French Guiana coastal domain through a Landsat8-OLI image.* ***a)*** *TOA reflectance at the wavelength of 665 nm,* ***b)*** *atmospherically corrected image with contaminated pixels masked in gray (Abascal-Zorrilla et al., 2019).*

1.2.2. Water Quality significance and partition of the water masses

1.2.2.1. Coastal water quality context

Coastal water quality is a critical issue that can be influenced by a complex and interrelated set of sources including pollution from land-based sources (e.g., agricultural runoff, industrial and sewage discharges), nutrient enrichment (e.g., nitrogen and phosphorus), physical factors (e.g.: temperature, salinity, and pH), and biological factors (e.g., harmful algal bloom). With the aim of protection, management, and improvement of the water resources, the Water Framework Directive (WFD) was established by different nations in the European Union. The WFD is considered as a regulation to apply to all types of water bodies comprising of rivers, lakes, groundwater, and coastal waters, which aims to maintain the EU waters to be in a good quality and meet the ecological and chemical criteria (European Commission, 2018). Accordingly, the EQR (Ecological Quality Ratio) was proposed in Annex V of WFD to assess the ecological status of the water body based on a combination of biological, chemical, and physical data. The percentage difference between the observed value and the reference values is calculated for each water quality indicator and these percentages are then combined to provide a general EQR depending on the type of water body WFD (2000/60/EC) **Figure 1.12**. Nevertheless, the assessment of water quality considering WFD as a standard may encounter potential challenges.

For example, the information about the reference values is often limited and the degree of deviation from reference conditions defining the boundaries between ecological statuses remains unclear (Santos et al., 2021).

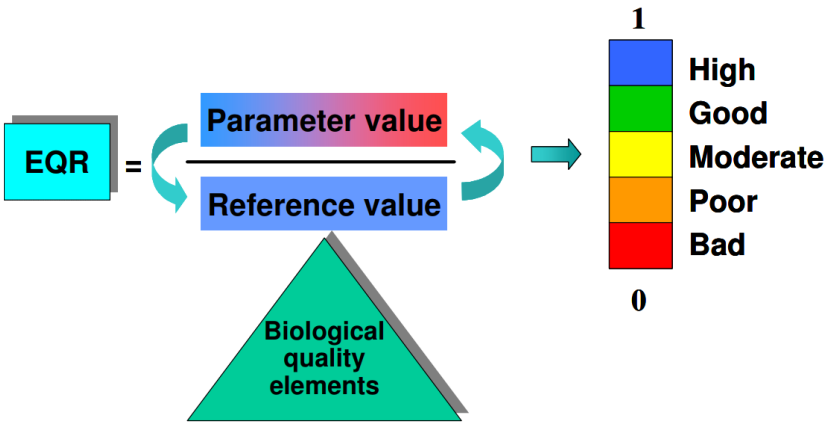

Figure 1.12. *The calculation of EQR (Ecological Quality Ratio)*

Evaluating the quality of water in coastal environments is a complicated task that typically involves multiple indicators including physical, biological, and chemical parameters (Gupta et al., 2003; Jha et al., 2015; Ma et al., 2020). The Water Quality Index (WQI) is often used to convey an overall evaluation of the water. Th et al., (2013) highlighted the importance of defining the weight of each considered indicator to determine coastal water quality index (WQI), which includes four essential elements: First, selecting appropriate water quality variables is crucial, as WQI values depend on the chosen parameters, which can vary based on the study area. Second, assigning weights to each indicator is important to determine the relative significance of each parameter. Third, transforming raw data into an index enables comparison of water quality across locations and time periods. Lastly, aggregating all parameters into a single value represents overall water quality.

In an attempt to define the ecological status of French coastal waters, the study of Gohin et al., (2008) adopted the P90 values of Chl-a concentration derived from ocean color data to determine different thresholds corresponding to 5 categories of EQR (Bad, Poor, Moderate, Good, and High). Such classification scheme, however, might present some limitations due to the accuracy and reliability of the data as well as the complexity of the link between Chl-a and ecological status.

1.2.2.2. Current knowledge in French Guiana

In the circumstance of French Guiana, knowledge about the quality of coastal waters is still limited as the appropriate parameters and their importance have not been defined yet. Indeed, the selection of the relevant parameters from remote sensing observation is challenging because the water quality involves a variety of elements that might not be directly measured or quantified from optical signals.

As a matter of fact, the major advantage of partitioning the water masses is to facilitate the monitoring process of an aquatic environment spatially and temporally, which supports regional policies. The traditional classification method performed on French Guiana coastal waters was proposed by IFREMER, which aims to split the coastal domain into four regions based on a combination of fishing areas and coast-to-coast sectors. The spatial extensions of these four regions are shown in **Figure 1.13**. Such clustering approach was chosen as these 4 zones are associated with historical fishing data since the 1980s that might be useful for the interpretation of ocean color observations. Accordingly, zone 2 (in front of Cayenne) was defined to be the largest zone with a surface area of 1121 km^2 and the smallest zone is zone 4 with a 177 km^2 surface area. High turbidity and abundance in phytoplankton biomass are commonly found in zone 1 and zone 4 in which the averaged SPM and Chl-a values can reach up to 30 $mg.L^{-1}$ and 6 $mg.m^{-3}$, respectively. However, this partitioning approach can be improved using more robust statistics as it inherently encompasses some disadvantages. For instance, the delimitation of zone 4 leads to a compact coastal area, which potentially yields a low number of available pixels. Further, the delimitation of the four zones does not take into account the information about biogeochemical dynamics which play a crucial role in the region’s ecosystem.

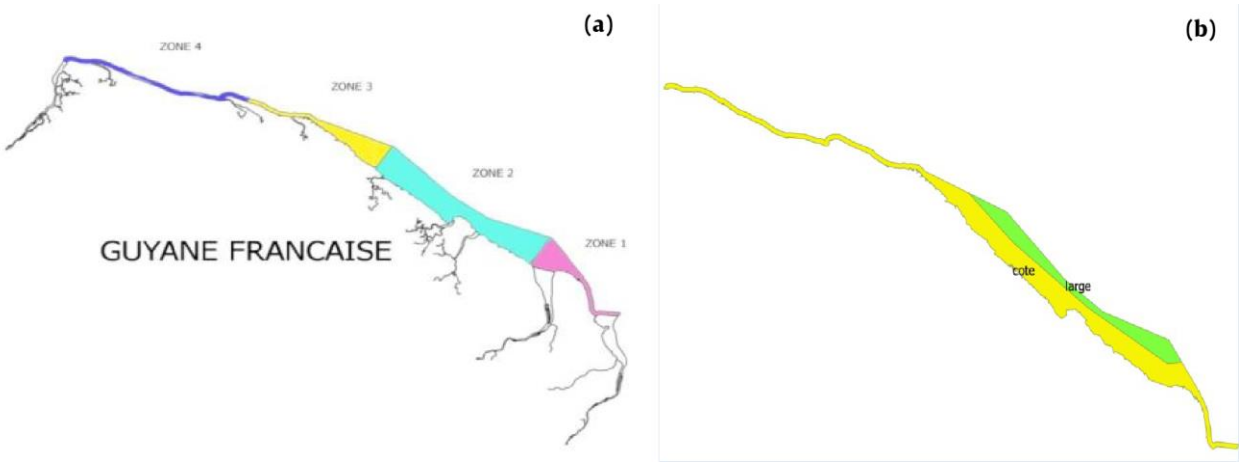

Figure 1.13. *Division of the French Guiana coastal water body into* ***a)*** *four zones considering fishing areas, and* ***b)*** *two regions considering coastal and offshore waters (Lampert et al., 2015)*

1.3. Conclusion

Given the pristine environmental conditions and the anticipated demographic growth in French Guiana, for which the predicted population could double by 2025 (Faatau, 2019), it is necessary to develop relevant observational tools to assess the potential future impacts on coastal domain. In addition to this, the French Guiana river basins have been subject to the influences stemming from increasing anthropogenic activities such as gold mining, deforestation, and removal soils (Gallay et al., 2018; Laperche et al., 2014). Moreover, changes in biogeochemical dynamics over coastal and offshore domains can also be attributed to the environmental factors including regional and local forcings (i.e., mudbanks as a consequence of Amazon influence, contribution of local river inputs) as well as climate modulations (i.e., waves, winds, and tides). The relative contribution to the biogeochemical regime of these elements remains unclear due to limited in-situ measurements leading to lack of information discovered in the region. Understanding the dynamics and state of the French Guiana marine ecosystem is therefore of paramount importance.

Previous research has primarily centered on the variability of SPM and Chl-a, which is basically dedicated to the mudbank migration and NBC rings. However, these parameters might not be adequate to comprehensively depict the biogeochemical dynamics occurring in the study area, for instance, elements related to local impacts such as contribution of local rivers, organic exports from mangroves, and tidal modulations. In addition to this, the investigation on

monitoring coastal water quality often requires the involvement of further parameters such as POC and DOC which present the organic content within the water masses. The high turbidity due to massive sediment loads from the Amazon River's plume leading to optical complexity of French Guiana coastal waters as well as the presence of permanent sun glint, necessitate a more sufficient approach to extensively exploit the potential of satellite data for evaluating the environmental and anthropogenic forcings.

Considering the addressed challenges and current knowledge, the first objective of this thesis is to generate a set of ocean color products, including Chl-a, SPM, CDOM, POC, and DOC, which will be adopted to better monitoring of coastal water quality in French Guiana. The temporal analysis based on these satellite archives will also provide comprehensive time series data to local stakeholders (i.e., Office Français de la Biodiversité (OFB), DEAL, Office de l'Eau Guyane) for supporting the development of regional monitoring programs. The second objective is to describe the biogeochemical dynamics at the regional scale over time, determining the primary factors causing variability and identifying the pertinent biogeochemical descriptors for monitoring coastal water quality in French Guiana. The long-term trend will also be addressed to evaluate the influence of existing environmental forcings. Finally, the present thesis aims to propose a more effective partition of the water masses utilizing robust statistical methods, which will contribute to the establishment of local monitoring policies.

CHAPTER 2: Materials and methods

2.1. Introduction

As introduced in Chapter 1, French Guiana coastal ecosystem is influenced by various environmental factors that contribute significantly to the biogeochemical dynamics over the study area in both off-shore and coastal regions. To further understand the variability of different water quality parameters and the forcings thereof driving alterations of water constituents within the water body, it is necessary to take into account the incorporation of multiple methodologies and tools.

The present Chapter illustrates the available in-situ dataset including radiometric and biogeochemical measurements collected in the French Guiana marine environments. Besides, satellite archives with medium and high spatial resolution capturing the dynamics of these coastal waters, are also presented.

Then, different methods for classifying the water masses and analyzing the time series generated in the frame of this PhD thesis to characterize the spatio-temporal pattern of biogeochemical variations and provide reliable information to support the establishment of regional monitoring programs will be described.

2.2. In-situ dataset

2.2.1. Classical in-situ cruises

In-situ measurements have been compiled from the data collected during 8 cruises conducted by LOG (Laboratoire d'Océanologie et de Géosciences) and LEEISA (Laboratoire Écologie, Évolution, Interactions des Systèmes Amazoniens) teams over French Guiana waters between 2006 and 2017. These sampling missions were deployed as part of diverse research projects (e.g., CNES TOSCA Coastal Waters, MODOC, HARDECOT, ANR GlobCoast, ESA S3VT) with the focus mainly on coastal waters, estuarine environments, and mudbank regions. The locations of these sampling points and deployment time thereof are presented in **Figure 2.1.a** and **Table 2.1.b**, respectively, where the sampling deployments were located < 40 m isobath.

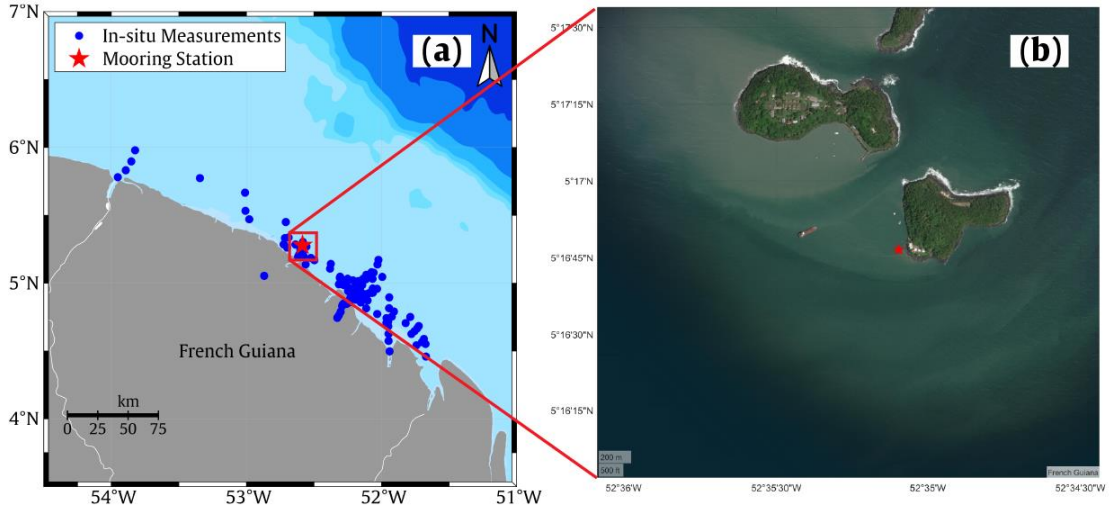

Figure 2.1. a) *The location of in-situ measurements and* ***b)*** *A focused view on the location of the mooring station.*

2.2.2. Autonomous platform

An autonomous station was conducted approximately 60 meters away from Insula Saint-Joseph Island (French Guiana) on 09/01/2020 in the frame of the "French Guiana water quality project", Office de l'eau Guyane, OFB, DEAL). In practice a buoy equipped using a YSI EXO2 probe (Multiparameter Water Quality, https://www.ysi.com/exo2), was deployed with the aim of measuring different variables including Chl-a, FDOM (fluorescence of dissolved organic matter), turbidity, temperature, and salinity every 15 minutes **Figure 2.1.b**. However, the deployment of this equipment was stopped on 25/08/2020 due to difficulties in setup conditions during the mission period. We however take the advantage of the in-situ dataset extracted from these high-frequency measurements as additional information for the implementation of the match-up exercise.

2.3. Radiometric measurements

In this study, 200 hyperspectral measurements of remote sensing reflectance (R_{rs}, sr^{-1}) in the visible domain of the spectrum ranging from 350 nm to 750 nm were deployed in French Guiana coastal waters using TriOS-Radiation Measurement Sensor with Enhanced Spectral resolution (RAMSES) radiometers (**Figure 2.2**).

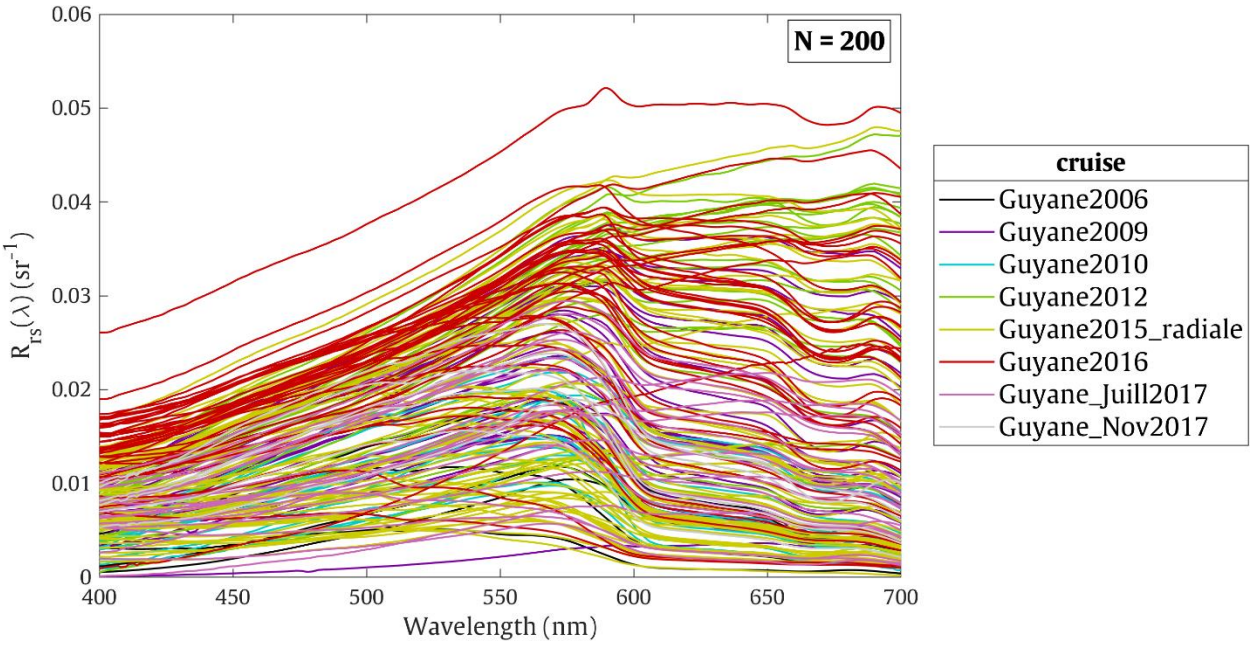

Figure 2.2. *Remote sensing reflectance ($R_{rs}(\lambda)$) of the in-situ dataset measured in French Guiana waters.*

The implementation of the reflectance consists of two principal steps in which the first radiometer was equipped on the deck to measure the above-surface downward irradiance, $E_d(0^+,\lambda)$. While the upward radiance, $L_u(z, \lambda)$, was recorded by the second radiometer. $R_{rs}(\lambda)$ was estimated following the standard principle of in-water and above-water radiometric measurements which can be expressed as in the formula below (Mueller, 2003):

$$R_{rs}(\lambda) = \frac{L_u(\lambda)}{E_d(0^+, \lambda)} \qquad 2.1$$

where λ indicates the wavelengths, $L_u(\lambda)$ is the up-welling radiance, and $E_d(0^+, \lambda)$ corresponds to down-welling irradiance. $R_{rs}(\lambda)$ is evaluated using the water-leaving radiance L_u and E_d in the air, just above the water surface as illustrated in **Figure 2.3**. It is worth mentioning that data points corresponding to unusual $R_{rs}(\lambda)$ shapes or negative values of reflectance were discarded from the in-situ dataset. This step is crucial as the biases in $R_{rs}(\lambda)$ might lead to unexpected results in the estimation of biogeochemical variables.

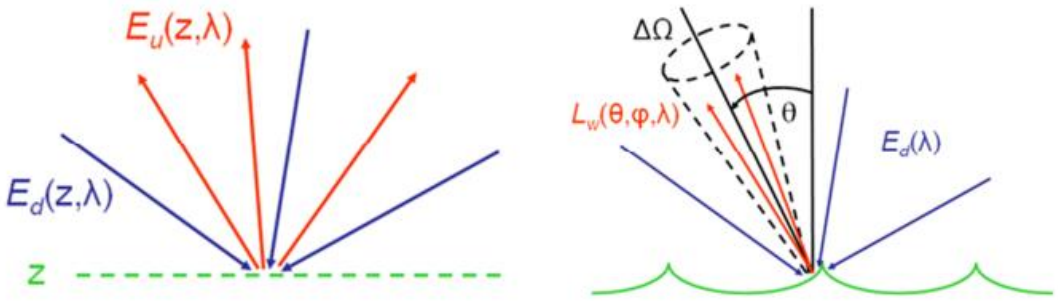

***Figure 2.3**. Illustration of light rays contributing to the irradiance reflectance R (left) and to the remote sensing reflectance (right) (Reflectances: Ocean Optics Web Book).*

2.4. Bio-optical and biogeochemical measurements

Various methods were employed to obtain a diverse range of surface water samples, ensuring comprehensive representation of the study area. Typically, samples were filtered on the research vessel immediately after collection to minimize contamination and maintain their integrity. Following filtration, samples were stored in suitable containers based on the specific analyte under examination. These containers were diligently labeled, sealed, and preserved under adapted conditions depending on the unique requirements of each analyte, such as temperature-controlled environments or darkness to avoid photodegradation. This systematic approach to sample collection, storage, and preservation ensures the accurate analysis of the studied samples. These discrete water sampling were performed to measure a suite of biogeochemical parameters including first analyses of the phytoplankton and particulate matter gathered from filtrations performed on GF/F filters over French Guiana marine waters and were used as the database of various studies (Bonelli et al., 2021; T. K. Tran et al., 2019; Vantrepotte et al., 2012, 2015). These samples were then analyzed in order to obtain information on:

- Suspended particulate matter concentration (SPM, $g.m^{-3}$). These measurements were performed following the SOMLIT protocol (https://www.somlit.fr) and briefly consist in measuring the weight of the particulates retained on a GF/F filter.
- Chlorophyll-a (Chl-a, $mg.m^{-3}$) was measured using a fluorometric technique (Holm-Hansen et al., 1965) samples gathered since 2014 were analyzed in French Guiana following the SOMLIT protocol (Salter et al., 2021).
- Particulate Organic Carbon concentrations (POC, $mg.m^{-3}$) is here considered as particulate carbon from organic origin particles with a diameter between 0.4 and 200 µm,

with pre-filtration usually performed following the SOMLIT protocol (Salter et al., 2021).

- Absorption of the colored dissolved organic matter (a_{CDOM}, m^{-1}). CDOM absorption spectra were measured on filtrates obtained after a filtration on 0.2 µm Millipore filters and were measured by spectrophotometry using 10 cm Quartz Cuve and following the standard protocol (Mitchell et al., 2003) as detailed in Vantrepotte et al., (2015).
- Dissolved Organic Carbon (DOC, $\mu mol.L^{-1}$) concentration was obtained from filtered seawater samples under gentle vacuum (< 5 mm Hg) through 0.7 µm pre-combusted 47 mm glass fiber membranes (Whatman GF/F) as documented in Vantrepotte et al., (2015). In addition, filtration aiming to collect information on the dissolved matter were also performed keeping and analyzing the filtrates in the laboratory.

It is worth noting that a quality control was performed on the raw dataset to exclude data points that are considered as outliers from relationship tests between each pair of biogeochemical variables (e.g., Chl-a and Chl-a fluorescence, SPM and Turbidity, SPM and $b_{bp}(665)$, etc.). The concentration range and available measurements of each parameter were compiled from eight distinct sampling missions conducted in the study area. A comprehensive graphical representation of the data, including the range of variability observed in French Guiana waters for the different parameters considered, is provided in **Figure 2.4**.

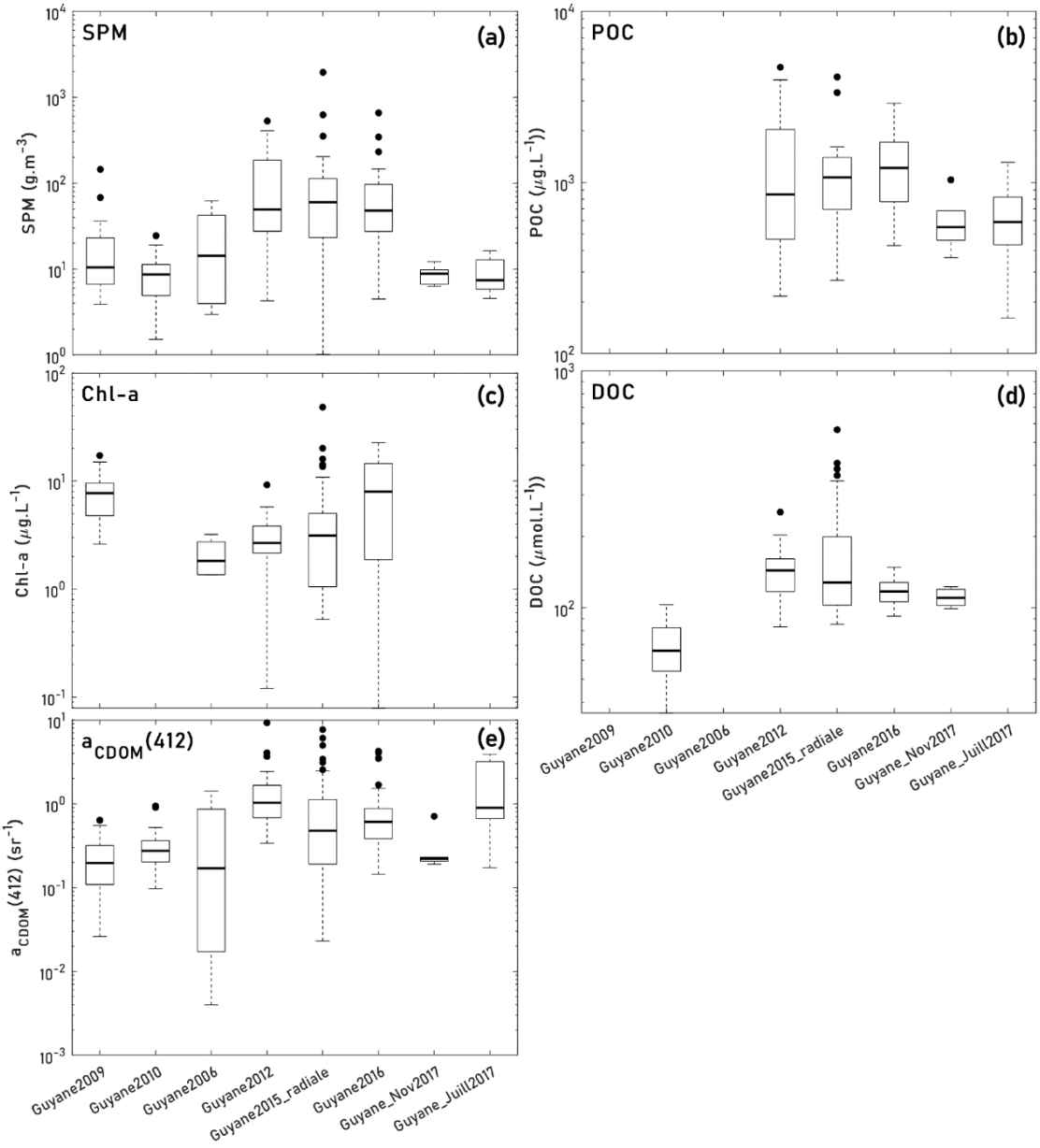

Figure 2.4. *The concentration range of* ***a)*** *SPM,* ***b)*** *POC,* ***c)*** *Chl-a,* ***d)*** *DOC,* ***e)*** $a_{CDOM}(412)$ *corresponds to 8 cruises conducted in French Guiana coastal waters.*

Table 2.1. *Number of measurements and deployment time of the cruises conducted over French Guiana waters.*

Parameters	N	Mean	Median	Min	Max	Stdv
SPM ($g.m^{-3}$)	174	70.90	24.33	1.02	1945.34	174.68
Chl-a ($mg.m^{-3}$)	119	6.27	3.74	0.08	48.32	6.68
aCDOM(412) (m^{-1})	193	0.94	0.54	0.00	9.24	1.29
POC ($mg.m^{-3}$)	92	1150.48	868.79	161.47	4705.48	912.96
DOC ($\mu mol.L^{-1}$)	118	137.65	116.92	35.99	564.08	79.04

2.5. Satellite Ocean Color Data

To detect the long-term changes in French Guiana marine waters, the merged products of the GlobColour data composed of different sensors such as SeaWiFS (Sea-Viewing Wide Field-of-View Sensor), MERIS, and VIIRS (Visible Infrared Imaging Radiometer Suite) and the GlobCoast data (MERIS) will be exploited as these satellite archives offer an extensive temporal coverage. Even though the MODIS satellite images allows for a relatively long time series of observation, the red band of this sensor, however, was found to be saturated due to the atmospheric failures in retrieving the reflectance at the wavelength of 667 nm in turbid environments. Such satellite products, therefore, are not considered in this study.

The spatio-temporal variability of biogeochemical parameters will be examined through the time series analysis conducted on MERIS data since this sensor provides a relevant time span with finer spatial details compared to the GlobColour products. Besides, Sentinel-2/MSI and Sentinel-3/OLCI data will also be used to obtain additional information for better understanding the biogeochemical dynamics in the region with the focus on estuarine areas.

As it is necessary to take into account the up-to-date information and the comprehensive spatial coverage of the entire coastal domain when defining a reference state, the Sentinel-3 was selected to establish a standard condition of the water masses. This data along with Sentinel-2, and MERIS archives will be adopted for different classification schemes based on their compatibility with the partitioning methods as well as their relevance with the objectives. The theorical application of these classification schemes will be further elaborated in the section 2.7.

Considering the permanent sun glint effect acting consistently over French Guiana marine waters. The POLYMER (POLYnomial-based algorithm applied to MERIS) atmospheric correction (AC) algorithm was performed for MERIS and Sentinel-2 data. This AC processor was initially developed for MERIS sensor with the advantage of sun-glint effect removal

(Steinmetz et al., 2011) and its performance has been widely validated for both open ocean and coastal waters in various studies (Bui et al., 2022; Mograne et al., 2019; Pereira-Sandoval et al., 2019; Soppa et al., 2021; Warren et al., 2019).

The assimilation of remotely sensed data is particularly described in **Figure 2.5** in the consideration of objectives previously mentioned. A general description of each satellite sensor is illustrated in **Table 2.2**.

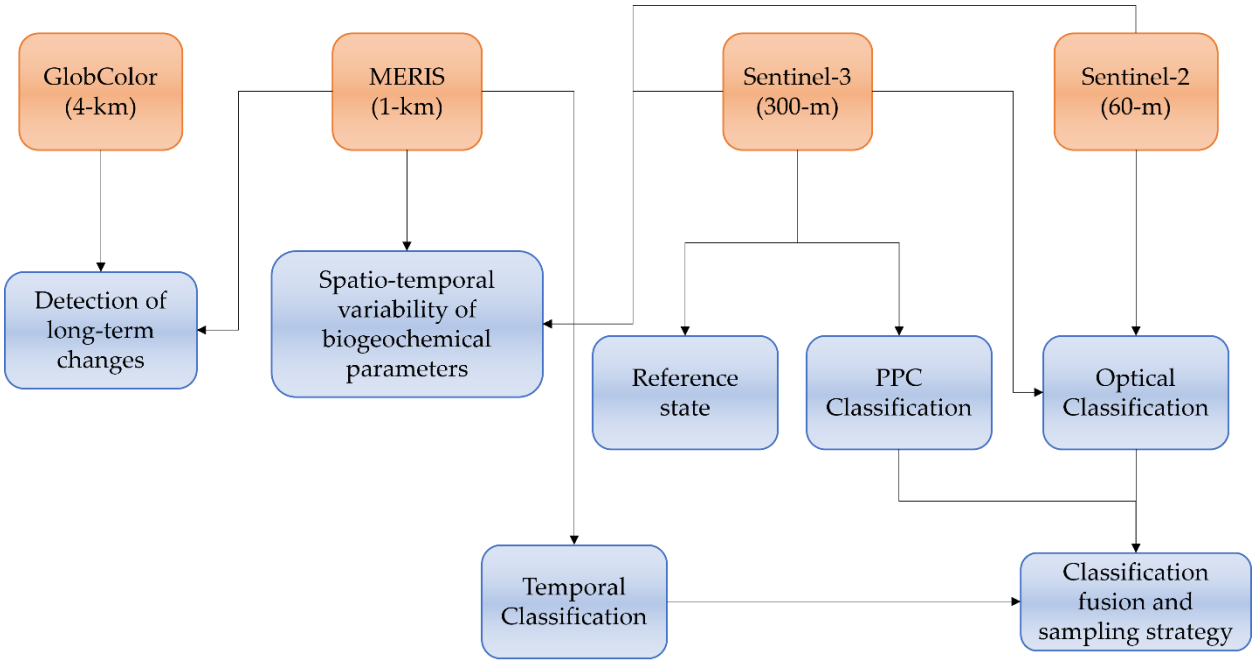

Figure 2.5. *Flow chart of satellite archives employment considering the objectives mentioned in Chapter 1.*

Table 2.2. *Description of 4 satellite products including Sentinel-2, Sentinel-3, MERIS (GlobCoast), and GlobColour (merged product) used for monitoring coastal water variability in French Guiana.*

		Sentinel-2		**MERIS (GlobCoast)**		**Sentinel-3**	**GlobColour (merged)**
		2A	2B	8-day	monthly	monthly	monthly
Spatial Resolution	10 m	✓	✓				
	20 m	✓	✓				
	30 m						
	60 m	✓	✓				
	300 m	✓				✓	
	1 km			✓	✓		
	4 km						✓

Visible Wavelengths (nm)	412			✓	✓	✓	✓
	443	✓	✓	✓	✓	✓	✓
	490	✓	✓	✓	✓	✓	✓
	510			✓	✓	✓	✓
	560	✓	✓	✓	✓	✓	✓
	665	✓	✓	✓	✓	✓	✓
Revisit Time		10 days	10 days	Daily		Daily	Daily
		5 days					
Sensor		MSI		MERIS		OLCI	Merged
Coverage		13 tiles		French Guiana		French Guiana	French Guiana
Number of images		2331	1705	458	121	80	283
		4036					
Storage		3.48 TB		4.3 GB	1.14 GB	10.5 GB	413 MB

2.5.1. Medium spatial resolution imagery

Daily MERIS satellite images (04/2002 - 04/2012) with the reduced spatial resolution (1 × 1 km^2 at nadir) covering the French Guiana coastal zone have been merged and reprojected to generate monthly composite data. These ocean color data were atmospherically corrected by a in the frame of GlobCoast project (11/2012 - 11/2015), funded by the French National Research Agency (ANR) with various ocean color parameters available such as SPM, Chlorophyll-a, a_{CDOM}, DOC, K_d, and b_{bp}. The description of the GlobCoast data can be found at https://archimer.ifremer.fr/doc/00357/46823/ (Loisel et al., 2017; M. D. Tran et al., 2023).

The GlobColour project started in 2005 as an ESA Data User Element (DUE) project to provide a continuous data set of merged L3 Ocean Colour products. From May 2015, these products also contribute to the Copernicus Marine Environment Monitoring Service (CMEMS). The GlobColour data (http://globcolour.info) used in this study has been developed, validated, and distributed by ACRI-ST, France. These satellite archives have been accessed in monthly format with 4-km spatial resolution spanning from 09/1997 to 03/2021.

Monthly reflectance Sentinel-3/OLCI products have been downloaded from CMEMS (https://marine.copernicus.eu/) data storage, which were subset to capture the French Guiana's marine regions. Such satellite archives were atmospherically corrected by EUMETSAT (European Organisation for the Exploitation of Meteorological Satellites) processing chain which implements BAC (Baseline Atmospheric Correction) and C2RCC (Case-2 Regional

CoastColour) atmospheric correction schemes for clear waters (Case-1) and optically complex waters (Case-2), respectively.

2.5.2. High spatial resolution imagery

The MSI (Multispectral Instrument) onboard Sentinel-2 satellites captures high-resolution optical images with a wide range of spectral bands. Sentinel-2 satellites consist of two identical units, Sentinel-2A and Sentinel-2B, operating simultaneously to ensure frequent revisit times and comprehensive global coverage. The Sentinel-2/MSI Level-1C images have been collected from Plateforme d'Exploitation des Produits Sentinel (PEPS: https://peps.cnes.fr/), a platform developed by the French space agency CNES with 13 tiles covering mainly the coastal domain of French Guiana (**Figure 2.6**).

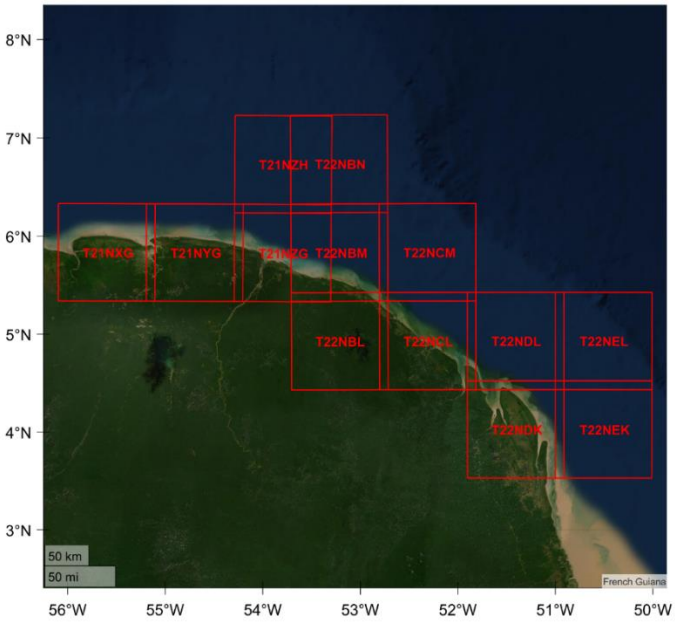

Figure 2.6. *Location of 13 Sentinel-2 tiles covering French Guiana's coastal domain.*

2.6. Ancillary data

In order to describe the dynamics of French Guiana waters taking into account modulation of the environmental conditions, several ancillary data (in-situ, satellite and model) were considered in addition to the previous in-situ and ocean color satellite data sets). Sea Surface Temperature (SST) and sea surface salinity (SSS) datasets have been downloaded from the available daily database distributed by HYCOM (Hybrid Coordinate Ocean Model) (https://www.hycom.org/). In particular, this is the global reanalysis database (GOFS 3.1) with a spatial resolution of 1/12° with 3-hour interval. HYCOM adopts NCODA 3DVAR model (Navy Coupled Ocean Data

Assimilation (NCODA) system, version 3) to simulate SST and SSS by the assimilation of the in-situ and satellite data, which is documented in Cummings & Smedstad, (2013). This database was processed using an arithmetic averaging method for producing monthly images and reprojected within a 1km-spatial-resolution grid to obtain a consistent format with GlobCoast data.

The flow rate of river discharge was collected from stationary stations located in 2 big rivers in French Guiana (Maroni and Oiapoque). This dataset was accessed on Service d'observation des ressources en eaux du bassin de l'Amazone (SO-HYBAM, https://hybam.obs-mip.fr/).

2.7. Algorithm tuning procedure

A first step of this PhD consisted of the adaptation of different models used for estimating key biogeochemical descriptors from the ocean color signals (i.e., R_{rs}) at regional scale, exploiting the in-situ data set described in the section 2.2. Theoretically, to generate inversion models estimating a certain water parameter from signals received from satellite sensors, the adequacy of in-situ measurements consisting of reflectance and concentration of the targeted water constituent plays an important role in the formulation and accuracy of the bio-optical algorithms. Therefore, the existing models proposed by different authors were tuned regionally by the modification of the coefficients thereof to match ideally the $R_{rs}(\lambda)$ values (predictors) and concentration of biogeochemical parameters (response variables) from the in-situ dataset collected directly in French Guiana waters. In other words, the meaning of model adaptation can be understood as the finding of the least square value. Least-squares (LS) problem has been known as one of the significant optimization problems in linear algebra. This problem can be expressed as the equation below:

$$Ax=b \tag{2.2}$$

where $A \in R^{m \times n}$ and $b \in R^{m \times 1}$. To solve this, we attempt to find x such that Ax=b, which can be simplified as:

$$\arg\min_{x} \|Ax-b\|_2 \tag{2.3}$$

The traditional solution to denote this problem is to transform the equation Ax=b into

$$x=(A^{T}A)^{-1}A^{T}b \quad (2.4)$$

However, the inverse of any matrix in numerical linear algebra should be avoided since its calculation usually requires many resources especially when a large matrix is involved. Therefore, QR decomposition of the matrix A was discovered to deal with the such issue:

$$A=QR \quad (2.5)$$

where Q is an orthogonal matrix and R is an upper-triangular matrix. The solution for the LS problem can be rewritten as:

$$(QR)^{T}(QR)x=(QR)^{T}b \quad (2.6)$$

$$R^{T}Q^{T}QRx=R^{T}Q^{T}b \quad (2.7)$$

$$R^{T}Rx=R^{T}Q^{T}b \quad (2.8)$$

$$Rx=Q^{T}b \quad (2.9)$$

$$Rx=v \quad (2.10)$$

For this reason, the regional adaptation of bio-optical models especially constructed by one or multiple independent variables has been performed using QR decomposition. This technique is available as a function (fitlm) supported in MATLAB and adopted to obtain the relevant coefficients of the specified linear regression function that represents the optimal fit to the given dataset.

2.8. Partition of water masses

As introduced in the Chapter 1, one of the objectives of this PhD is to partition the water masses considering the lack of in-situ measurements conducted over French Guiana marine waters. The identification of different water types indeed facilitates the deployment of regional monitoring programs as it provides a comprehensive view into the water properties. For this reason, different classification schemes including optical, Proxy of Particulate Component (PPC), and temporal classification approaches will be examined to better explore their appropriateness to delimit the marine waters taking into account off-shore and coastal domains of the study area.

More specifically, 3 Optical Water Types (OWTs) will be utilized for the regional adaptation of inversion algorithms to estimate different biogeochemical parameters including SPM, POC, DOC, and $a_{CDOM}(412)$ from satellite data, considering the limited in-situ measurements deployed in French Guiana waters. Additionally, we use 5 OWTs for the development of a Chl-a model as such algorithm was established based on an extensive in-situ dataset gathered in various coastal ecosystems. Finally, 4 OWTs will be selected for partitioning the water masses in French Guiana since this number of OWTs shows the optimal delimitation of the reflectance.

2.8.1. Optical Classification and Optical Indices

2.8.1.1. Classification of in-situ Rrs(λ)

As a matter of fact, the optical signals acquired on satellite sensors are tightly linked to the reflectance value of a given object on the water surface. With this in mind, the raw R_{rs} were necessarily normalized to obtain a deeper view of the reflectance shape. In particular, the normalized R_{rs} subsets were determined by the ratio between their original value and the surface below the spectral shape following the formula:

$$R_{rs}^{norm} = \frac{R_{rs}(\lambda)}{\int_{\lambda_1}^{\lambda_2} R_{rs}(\lambda) d\lambda} \qquad 2.11$$

Since the measurements were established on a regional scale (French Guiana waters), the hyperspectral R_{rs} collected from in-situ were clustered into different homogeneous optical water types (OWTs) using unsupervised classification as described in Lubac & Loisel, (2007) and Vantrepotte et al., (2012). In particular, this step was conducted under the implementation of the hierarchical classification method of Ward, (1963) which was verified to be the most relevant hierarchical decision tree approach in most situations (Ferreira & Hitchcock, 2009). Regarding each OTW, a specific biogeochemical feature can be associated with different concentration ranges of water constituents.

2.8.1.2. Satellite Rrs(λ) labeling

The OWTs defined in the previous section were used for labelling the satellite R_{rs} spectra. This labelling consists in computing the OWT membership of an input R_{rs} spectrum (e.g., satellite R_{rs}) to each of the OWTs defined from the in-situ dataset which are characterized by specific mean (μ) and covariance (Σ) matrices (Mélin et al., 2011; Vantrepotte et al., 2012). The

Mahalanobis distance Δ^2 applied to the log-transformed R_{rs}^{norm} is then used to estimate the distance between input spectrum x and a given OWT i_c as follows:

$$\Delta_{ic}^2(x) = \left(x-\mu_{ic}\right)^T \Sigma_{ic}^{-1}(x-\mu_{ic}) \quad 2.12$$

where T indicates the matrix transpose.

The OWT membership of satellite pixels to each of the defined OWTs was then estimated as in Vantrepotte et al., (2012). The probability density function (PDF), corresponding to each targeted pixel associated with $x=\log(R_{rs})$, is calculated based on its Mahalanobis distance (Δ_M^2) to the distribution of OWT i_c and can be expressed as below:

$$P_{ic}(x)=\frac{1}{(2\pi)^{d/2}|\Sigma|^{1/2}}\exp\left[-\frac{1}{2}\Delta_{ic}^2(x)\right] \quad 2.13$$

The computed probability values are then normalized (p*) so that the sum of OWT memberships equals 1 by taking the ratio between P for ic OWT and the total P for all OWTs considering such as (Mélin & Vantrepotte, 2015):

$$p_{ic}^*=\frac{P_{ic}}{\sum_{ic=1}^{Nc} P_{ic}} \quad 2.14$$

2.8.2. Proxy of Particulate Composition (PPC) classification

SPM can be referred to total suspended solids (TSS) or total suspended matter (TSM) and is constituted of all particulate materials that pass through a preweighted filter with a nominal pore size of 0.7 µm (Neukermans et al., 2012). Therefore, SPM encompasses organic (autotrophic and heterotrophic plankton, bacteria, viruses, and detritus) and mineral particles existing in the water column (Stramski et al., 2004). Due to this particular property, SPM has been considered as an important indicator to investigate the sediment transport (e.g., through the manifestation of ocean currents, wave actions, and river discharge), and coastal geo-morphological processes (i.e., accretion, erosion, mudbank migration), thus supporting the evaluation of the impacts of anthropogenic activities as well as natural forcings (Abascal-Zorrilla et al., 2018; Douillet et al., 2001; Li et al., 2021; Loisel, et al., 2014; Vanhellemont & Ruddick, 2014; Vantrepotte et al., 2013).

POC, on the other hand, is one of the main pools of ocean organic carbon, which consists of living materials (heterotrophic bacteria, phytoplankton, zooplankton) and detritus (i.e., non-living cells, dead plant material, decomposing organisms, fecal matter) in suspension. The POC/SPM ratio, denoted as Proxy of Particulate Composition (PPC) (Loisel et al., 2023), has been typically adopted in various studies to examine the temporal variability in the composition and origin of the particulate matter pool (Coynel et al., 2005; Doxaran et al., 2012, 2015; Ehn et al., 2019; Emmerton et al., 2008). This variability is often associated with changes in regional environmental factors, such as water discharge and phytoplankton bloom. Additionally, the POC/SPM ratio allows to better interpret optical properties of in-situ measurements (Babin, Morel, et al., 2003; Doxaran et al., 2012; Loisel et al., 2007; Woźniak et al., 2011) and satellite ocean color radiometry (OCR) observations (Vantrepotte et al., 2011).

In the present thesis, the POC/SPM classification will be conducted according to the defined thresholds suggested in Loisel et al., (2023) (i.e., 0.08 and 0.2) in which the water body can be categorized as mineral-dominated, mixed, and organic-dominated waters. These threshold values were established based on a re-examination of those proposed by Woźniak et al., (2010) through the relationship between POC/SPM ratio and b_{bp}/c_p optical ratio performed on an extensive in-situ dataset (Loisel et al., 2023).

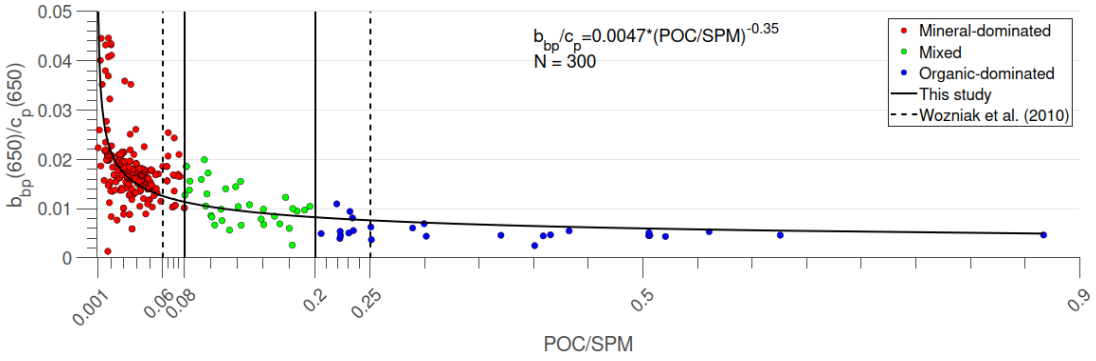

Figure 2.7. *Relationships between $b_{bp}/c_p(650)$ and POC/SPM. The black curve stands for the power regression. The vertical dashed lines represent the thresholds delimiting the water types according to* Woźniak et al., (2010). *The vertical solid lines show the new thresholds defined in Loisel et al., (2023).*

2.8.3. Neural Network Self-Organizing Map (SOM)

The Self-Organizing Map (SOM) is known as an unsupervised machine learning or more specifically a non-supervised clustering method developed by Kohonen, (1998), that attempts to

match the units (neurons or nodes) in a defined network map as closely as possible to the observations in the input dataset. The map of these neurons is typically established in the form of a hexagonal or rectangular 2-dimensional grid. The execution of SOM is based on competitive training. In other words, the Euclidean distances between all the nodes in the network and the targeted data point are recalculated after each training iteration to select the Best Matching Unit (BMU) which is the closest neuron to the point. The weight of the selected BMU is accordingly modified towards the input vector. However, the weights of surrounding neurons are adjusted as well since the neurons are connected with each other by a Gaussian function (neighborhood function) $\theta(u,v,s)$ with the peak corresponding to the location of BMU. The magnitude of the adjustment diminishes after each epoch according to the learning coefficient (learning rate) $\alpha(s)$. The updated weight vector $W_v(s)$ after step s that can be calculated as follow:

$$W_v(s+1)=W_v(s)+\theta(u,v,s)\times\alpha(s)\times[D(t)-W_v(s)] \quad 2.15$$

where s is the step index, $W_v(s)$ is the current weight vector, $\theta(u,v,s)$ is the neighborhood function representing the relationship between the BMU u and set of neurons v, $\alpha(s)$ is a monotonic decreasing learning coefficient which is conditioned by $0 \leq \alpha(s) \leq 1$, and D(t) is the considered data point. The neighborhood function $\theta(u,v,s)$ is expressed as below:

$$\theta(u,v,s)=\exp\left(-\frac{\|r_v-r_u\|^2}{2\sigma^2(s)}\right) \quad 2.16$$

where r_v, r_u are the vectorial locations on the defined grid, and σ is called the radius or the width of the neighborhood function which also decreases over time. Eventually, the initial SOM network is adjusted to cover the data as much as possible and each neuron is representative of a number of data points which refers to the principle of unsupervised classification. In the case of multivariate distribution, SOM has also been known as a sufficient method to perform dimensionality reduction. In this thesis, the SOM was adopted to partition the time series of water masses derived from a specified water quality parameter.

2.9. Timeseries analysis

2.9.1. Census X-11 time series decomposition

With the aim of analyzing the time series to have a better insight into the biogeochemical variability, the Census X-11 time series decomposition method was selected and applied

individually to each pixel that is associated with its corresponding time series. This approach was initially developed by Julius Shiskin et al., (1967) and colleagues at the U.S Bureau of the Census as a result of its various versions previously discovered. Theoretically, once X-11 is implemented, it splits a targeted signal (X(t) into three core components (Trend term Tt, Seasonal term St, Irregular term It) through an application of moving average calculations such as:

$$X(t)=S(t)+T(t)+I(t) \quad 2.17$$

It is worth noting that the preparation of the input data should be necessarily taken into account to avoid the incorrect estimates potentially generated by the absence of satellite coverage due to clouds and/or glint effects. In particular, if the number of available temporal data values of a considered pixel corresponding to a given month is less than 50% of the year, the pixel is omitted from the procedure. Otherwise, the missing data is inter/extrapolated according to the eigenvectors filtering method represented in Ibanez & Conversi, (2002). In this thesis, the execution of X-11 was performed following the procedure specifically documented in Vantrepotte & Mélin, (2011), which can be described in three fundamental steps:

- **Step 1 (Initial Trend and Seasonal estimates):**

(a) First-estimated Trend series

The first estimate of the trend component was conducted using a centered moving average with periodicity (p) applied to the input signal (X(t). In this case, p is chosen to correspond to the number of months in a year (12 months) since it will be utilized for monthly composite data of MERIS sensors. Therefore, the first calculation of the trend-cycle term of the time series X(t) at the time step t is expressed as below:

$$T_1(t)=MA_{2\times12}\left(X(t)\right)$$
$$=\left[X\left(t-\frac{p}{2}\right)+2X\left(t-\frac{p}{2}-1\right)+\ldots+2X(t)+\ldots2X\left(t+\frac{p}{2}-1\right)+X\left(t+\frac{p}{2}\right)\right] \quad 2.18$$
$$=[X(t-6)+2X(t-5)+\ldots+2X(t)+\ldots2X(t+5)+X(t+6)]$$

(a) First-estimated Seasonal series

The trend-adjusted series, $X_{t\text{-adjusted1}}(t)$, is then derived by the subtraction between the initial time series, X(t), and the first-estimated trend series, $T_1(t)$: $T_{t\text{-adjusted1}}(t)=X(t)-T_1(t)$.

Subsequently, we performed the moving average on $X_{t\text{-}adjusted1}(t)$ with p=2 to obtain the first estimated $S_1(t)$.

$$S_1(t)=MA_{2\times2}\left(X_{t\text{-}adjusted}(t)\right) \\ =[X(t-6)+2X(t-5)+\ldots+2X(t)+\ldots2X(t+5)+X(t+6)] \quad 2.19$$

Once $S_1(t)$ series is acquired, the first seasonal-adjusted series can be estimated as: $X_{s\text{-}adjusted1}(t)=X(t)-S_1(t)$.

- **Step 2 (Refined Trend and final Seasonal estimates):**

(a) To retrieve the refined trend-cycle component $T_2(t)$, we repeat the operation in Step 1.a on the seasonal-adjusted series using annual-centered with a trend filter proposed by Henderson, (1916). The advantage of this filter application is that it provides an improvement in the trend series with a smoother fluctuation.

(b) The final seasonal component S(t) is computed by redoing step 1.b on the second trend-adjusted series $X_{t\text{-}adjusted2}(t)=X(t)-T_2(t)$. The second seasonal-adjusted series is formulated as: $X_{s\text{-}adjusted2}(t)=X(t)-S(t)$.

- **Step 3 (Final Trend and Irregular estimates):**

(a) The final estimate of trend term T(t) is derived from the repetition of step 2.a on the second seasonal-adjusted series $X_{s\text{-}adjusted2}(t)$.

(b) The residual of the subtraction between the input time series and the sum of the final trend and seasonal components are identified as the Irregular term:

$$I(t)=X(t)-T(t)-S(t) \quad 2.20$$

One of the valuable features of the X-11 procedure is that the seasonal component is deduced locally by different filters. Hence, the values computed for a certain year are not influenced or biased by events occurring at other times. To assess and potentially map the significance of each X-11 component on a given time series, the relative contribution ρ_z^2 corresponding to the targeted component z (where z = S, T, or I) is expressed as:

$$\rho_z^2=\frac{\sigma z^2}{\sigma X^2}\times100\% \quad 2.21$$

where σX^2 represents total variance and can be computed following the formula below:

$$\text{Var-X(t)}^2=\text{Var-S(t)}^2+\text{Var-T(t)}^2+\text{Var-I(t)}^2+2\text{cov(S(t),T(t),I(t))} \quad 2.22$$

where Var-S(t)^2, Var-T(t)^2, and Var-I(t)^2 are the variance associated with seasonal, trend, and irregular terms respectively.

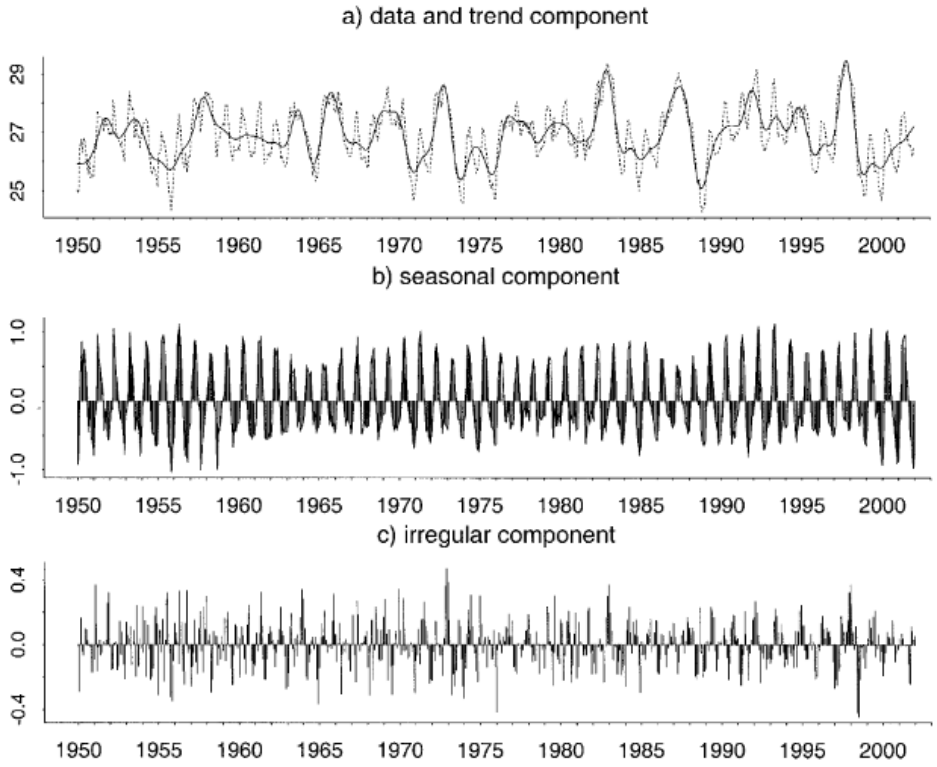

Figure 2.8. *The X-11 decomposition of the Nino-3.4 SST time series:* ***a)*** *original series (dashed) and X-11 trend component (solid);* ***b)*** *X-11 seasonal component;* ***c)*** *Irregular component. (Pezzulli et al., 2005)*

2.9.2. Trend Detection

The detection of monotonic trends in the time series has been derived from an application of the seasonal Mann-Kendall (MK) statistic test on the initial signal. Specifically, the principle of this test is to recognize whether the time series presents an upward or downward tendency based on the null hypothesis (H_0) and alternative hypothesis (H_a) corresponding to the absence and presence of the monotonic trend. (Hirsch et al., 1982) have indicated that the MK test is appropriate where changes are significant. In this thesis, the MK test has been conducted according to (Gilbert, 1988) as follows:

$$S_m = \sum_{i=1}^{nm-1} \sum_{j=i+1}^{nm} \mathrm{sgn}(x_{jm}-x_{im}) \quad 2.23$$

Where nm presents the number of valid data for the month m and the computation of $\mathrm{sgn}(x_{jm}-x_{im})$ can be described as:

$$\mathrm{sgn}(x_{jm}-x_{im}) = \begin{cases} 1 \text{ if } x_{jm}-x_{im}>0 \\ 0 \text{ if } x_{jm}-x_{im}=0 \text{ or the sign of } x_{jm}-x_{im} \text{ can not be determined} \\ -1 \text{ if } x_{jm}-x_{im}<0 \end{cases} \quad 2.24$$

The final test result S is defined by the sum of the monthly statistic: $S=\sum_{m=1}^{p} S_m$. Then, the variance of Var(S) is computed as below:

$$\mathrm{Var}(S)=\frac{1}{18}[n(n-1)(2n+5)-\sum_{p-1}^{g} t_p(t_p-1)(2t_p+5)] \quad 2.25$$

Where g is the number of tied groups (number of values that are duplicated in the sequence) and t_p is the number of observations in the p^{th} group (number of repeated times). Then, the denoted Z, which is the standardized value of S, is calculated using the root mean squared of Var(S):

$$Z=\begin{cases} \frac{S-1}{\sqrt{\mathrm{Var}(S)}} \text{ if } S<0 \\ 0 \text{ if } S=0 \\ \frac{S+1}{\sqrt{\mathrm{Var}(S)}} \text{ if } S>0 \end{cases} \quad 2.26$$

If Z presents a positive value, the series has a tendency to increase with time. Meanwhile, a negative value of Z indicates a decreasing trend of the signal. At this point, a type one error rate α ($0<\alpha< 0.5$) is adopted to perform the decision on the hypothesis. In particular, H_0 is rejected and H_a is accepted if $|Z|\geq Z_{1-\alpha/2}$ where $Z_{1-\alpha/2}$ is the $100(1-\alpha/2)^{th}$ percentile of the standard normal distribution. We used Sen's slope (β in % yr^{-1}) which is a robust method developed by Sen, (1968) to evaluate the magnitude of the detected trend. The computation of β is based on the median of individual slopes b_{mij} of all pairs (X_{mj}, X_{mi}):

$$b_{mij}=\left[\frac{X_{mj}-X_{mi}}{j-i}\right] \quad 2.27$$

With m = 1, 2, …, p and $1 \leq i < j \leq nm$.

2.10. Statistic Indicators

The performance evaluation of candidate algorithms is based on different statistical metrics including RMSD (Root Mean Square Deviation), MAPD (Mean Absolute Percentage Difference), MRAD (Mean Relative Absolute Difference), MB (Mean Bias), Slope, and R^2 (Determination Coefficient). These statistic indicators are computed from the model-derived and in-situ concentration of biogeochemical parameters which were transformed into a logarithmic scale as the bio-optical variability in the ocean is usually considered to be log-normally distributed (Campbell, 1995):

$$RMSD=\left\{\sum_{i=1}^{N}\frac{\left[\log_{10}\left(C_i^{mod}\right)-\log_{10}\left(C_i^{obs}\right)\right]^2}{N}\right\}^{\frac{1}{2}} \quad 2.28$$

$$MAPD=\text{median}\left[\frac{\left|\log_{10}\left(C_i^{mod}\right)-\log_{10}\left(C_i^{obs}\right)\right|}{\log_{10}\left(C_i^{obs}\right)}\right]\times 100\% \quad 2.29$$

$$MRAD=\frac{1}{N}\times\sum_{i=1}^{N}\frac{\left|C_i^{mod}-C_i^{obs}\right|}{C_i^{obs}}\times 100\% \quad 2.30$$

$$MB=\frac{1}{N}\times\sum_{i=1}^{N}\left|\log_{10}\left(C_i^{mod}\right)-\log_{10}\left(C_i^{obs}\right)\right| \quad 2.31$$

$$\log_{10}\left(C^{mod}\right)=m\times\log_{10}\left(C^{obs}\right)+c \quad 2.32$$

where C^{obs} represents the in-situ observations and C^{mod} is the Rrs-based estimates.

In addition, a linear regression between C^{obs} and C^{mod} was performed for each considered model leading to the estimation of a Slope and coefficient of determination (R^2) as additional statistical descriptors.

Radar charts have been further used to compare the performance of the inversion algorithms. This graphical display allows the representation of multiple statistical parameters summarized in the form of a two-dimensional chart (T. K. Tran et al., 2019). Here an overview of the normalized MAPD, RMSD, MRAD, MB, Slope, and R^2 (Equations 2.28 – 2.32) is provided, the normalization is computed as follows:

$$RMSD^{norm}(j)=\frac{RMSD(j)}{\max(RMSD(j),j=1,k)} \quad 2.33$$

$$MAPD^{norm}(j)=\frac{MAPD(j)}{\max(MAPD(j),j=1,k)} \quad 2.34$$

$$MRAD^{norm}(j)=\frac{MRAD(j)}{\max(MRAD(j),j=1,k)} \quad 2.35$$

$$MB^{norm}(j)=\frac{MB(j)}{\max(MB(j),j=1,k)} \quad 2.36$$

$$Slope^{norm}(j)=\frac{|1-Slope(j)|}{\max(|1-Slope(j)|,j=1,k)} \quad 2.37$$

$$R^{2\,norm}(j)=\frac{\min(R^2(j),j=1,k)}{R^2(j)} \quad 2.38$$

where j represents each individual model considered in a defined inter-comparison exercise.

Besides a synthetic visual examination, radar plots were also used to compute a unique statistical indicator outlining the general performance of the considered inversion methods. This consists in practice to compute the area associated with the polygons linking the normalized indicators indicated from Equations 2.33 to 2.38 as below:

$$Area=\frac{1}{2}\times\frac{\pi}{6}\times[RMSD^{norm}(j)\times MAPD^{norm}(j)+MAPD^{norm}(j)\times MRAD^{norm}(j)+MRAD^{norm}(j)\times MB^{norm}(j)+MB^{norm}(j)\times Slope^{norm}(j)+Slope^{norm}(j)\times R^{2\,norm}(j)+R^{2\,norm}(j)\times RMSD^{norm}(j)] \quad 2.39$$

CHAPTER 3: Regional adaptation and Selection of Bio-optical algorithms for French Guiana coastal waters

3.1. Introduction

As illustrated in the Chapter 1, latter studies, which focus on the biogeochemical dynamics of the French Guiana waters, partly exploited bio-optical models without specifically evaluated at regional scale (Lampert et al., 2015, i.e., Chl-a and Turbidity estimated by default from the OC5 model, Gohin et al., 2002). SPM was the only parameters which was evaluated specifically for recent former regional studies (Gallay et al., 2019; Vantrepotte et al., 2013; Vantrepotte, Loisel, et al., 2011). The reliability of the satellite-derived information for describing French Guiana waters is however critical considering the optical complexity of these waters gathering ultra-turbid environments (Vantrepotte et al., 2011, Vantrepotte, et al., 2012, Abascal-Zorrilla, et al., 2019).

The general objective of this chapter was therefore to define a set of bio-optical algorithms which are the most adapted to estimate key biogeochemical variables from ocean color observation over the water masses of French Guiana. This includes estimates of the near-surface concentration of conventional variables, such as SPM and Chl-a, but also of indicators, such as POC, a_{CDOM}, DOC, and POC/SPM ratio, which have been estimated more recently from space, allowing to gain a more comprehensive understanding of the observation of water quality variability. To fulfill this general objective, the general frame of the bio-optical models evaluation consisted first at considering formulations already documented for estimating the mentioned parameters of interest from the marine reflectance. These candidate algorithms have been preselected considering models that are generally similar to avoid redundancy in the evaluation process and to focus on the most pertinent models. These candidate models were in practice evaluated considering both their original versions as well as versions tuned at regional scales. Further, the evaluation frame was based on the consideration of the different optical water types (OWTs) composing the French Guiana waters in order to evaluate: 1) What is the relative performance of the different inversion methods according to the optical properties of the water masses? 2) What is the interest of combining the models most adapted for the different OWT in order to optimize the satellite estimates at regional scale? This evaluation was performed

considering the different sensors of interest of this work including MERIS, Sentinel3 OLCI, Sentinel2-MSI, GlobColour merged products (See section 2.3).

In the first part of this chapter, the regional evaluation of the SPM, POC, $a_{CDOM}(412)$ and POC/SPM inversion methods will be presented focusing on the regional data set described in section 2.2 focusing on the results obtained for MERIS sensor (a comprehensive detail of the models selected for all the considered is provided at the end of this chapter).

In the second part of this chapter, results related to the evaluation of the Chl-a for S2 and S3 will be more specifically detailed. Indeed, the evaluation of this parameter which is often used as the main descriptor in the coastal environment was particularly important. For that purpose, an extended global in-situ data set was considered. This work was presented at the Ocean Optics 2022 conference through an oral presentation (M. D. Tran et al., 2022) and was also valorized through a publication (M. D. Tran et al., 2023) with the full-text version described in Annex section.

The tuned models according to available $R_{rs}(\lambda)$ of MERIS central bands have been used as a frame to perform the evaluation of different inversion algorithms as well as the selection of the most suitable bio-optical models. This is due to the fact that MERIS's visible bands and those of the majority of satellite sensors are generally similar (e.g., OLCI, MSI, and SeaWiFS). In addition, the selected algorithm regarding each biogeochemical variable will be adapted considering satellite sensors introduced in section 2.3. Combining different remote sensing archives can be advantageous for long-term observations as it offers a wider range of the temporal coverage available for analysis, thereby enabling a more comprehensive understanding of temporal trends and patterns.

CHAPTER 3 – PART I

3.2. Optical Water Types (OWTs) definition

In order to evaluate the performance of different inversion models, 3 optical water types (OWTs) have been defined from the in-situ $R_{rs}(\lambda)$ data set gathered in French Guiana (see section 2.2) following the method described in the section 2.2.1 (Vantrepotte et al., 2012, Mélin and Vantrepotte, 2015). The illustration of the 3 OWTs is shown in **Figure 3.1** where the corresponding shapes of the normalized $R_{rs}(\lambda)$ are presented. As the OWTs exhibit an increasing pattern in the normalized $R_{rs}(\lambda)$ values toward the red part of the spectrum (from OWT 1 to 3), the optical characteristics of each OWT can provide a rough information about the turbidity level within the water masses. Indeed, an OWT can be representative for specific conditions of the water body that can be seen from **Table 3.1**. For example, the OWT 3, with a significant $R_{rs}(\lambda)$ peak in the red domain, corresponds to the water mass that is strongly influenced by terrestrial inputs with the highest average concentration of SPM (129.56 $g.m^{-3}$), POC (1050.13 $mg.m^{-3}$), DOC (179.16 $\mu mol.L^{-1}$), $a_{CDOM}(412)$ (1.59 m^{-1}) and Chl-a (7.82 $mg.m^{-3}$) recorded among the three OWTs. The OWT 2 can be referred to a mixed situation with a remarkable contribution of POC, evidenced by the highest POC/SPM ratio value of 0.12. The OWT 1, with the lowest concentration of all variables, is more likely related to clear waters as presenting a significant peak in the blue of the reflectance curve. The partitioned water types along with their associated characteristics will be elaborated in the Chapter 5 where the in-situ $R_{rs}(\lambda)$ data is classified into 4 OWTs. In the present examination, these unique optical features associated to the 3 defined OWTs have been adopted as a general frame with the focus of assessing the accuracy to retrieve the concentration of the considered biogeochemical parameters in French Guiana coastal waters.

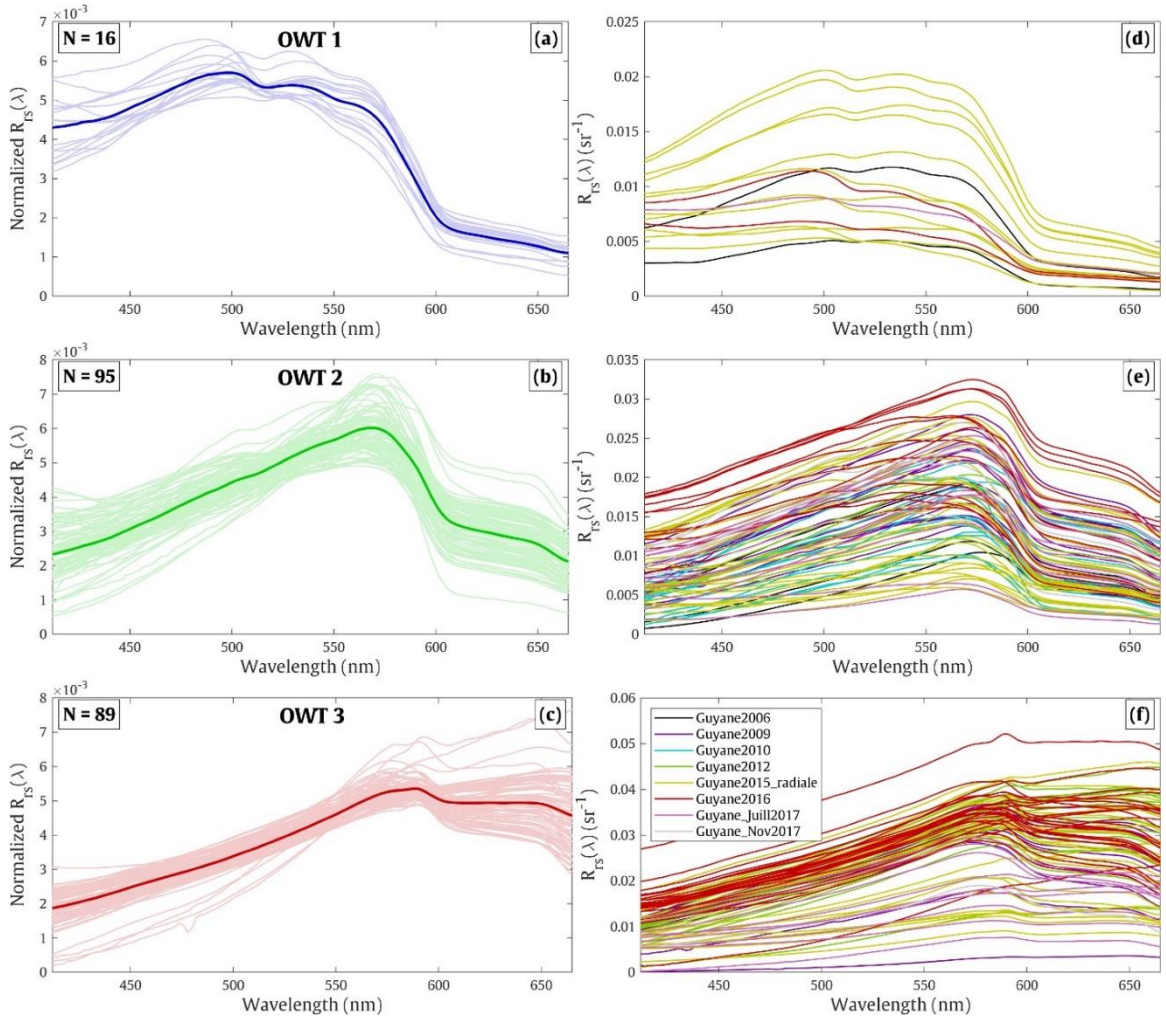

Figure 3.1. *The left panels (a-c) show the normalized reflectance associated with the 3 OWTs defined from the in-situ dataset. The solid bold lines present the mean of the normalized $R_{rs}(\lambda)$. The right panels (d-f) show the raw reflectance for the corresponding OWTs with the colors indicate conducted missions.*

Table 3.1. *Statistics of the biogeochemical parameters associated with three OWTs defined from the in-situ dataset of French Guiana coastal waters.*

	Parameters	N	min	max	mean	median	stdv
OWT 1	SPM ($g.m^{-3}$)	6	2.30	17.75	6.22	4.39	5.76
	Chl-a ($mg.m^{-3}$)	7	0.42	4.47	2.14	1.36	1.42
	POC ($mg.m^{-3}$)	5	161.47	1381.09	758.18	729.65	484.02
	a_{CDOM} (412) (m^{-1})	12	0.00	0.26	0.11	0.09	0.09
	DOC ($\mu mol.L^{-1}$)	11	88.92	126.80	102.48	98.27	12.76
	POC/SPM	2	0.03	0.16	0.10	0.10	0.09
	Chl-a/POC	4	0.001	0.003	0.002	0.002	0.001
	$a_{ph}(400)/a_p(400)$	7	0.73	0.86	0.81	0.79	0.04
	$a_{CDOM}(400)/(a_{CDOM}(400)+a_p(400))$	5	0.32	0.84	0.57	0.57	0.22
OWT 2	SPM ($g.m^{-3}$)	71	1.15	44.03	11.03	8.87	8.71
	Chl-a($mg.m^{-3}$)	45	0.83	20.09	4.61	3.10	4.43
	POC($mg.m^{-3}$)	35	215.97	1368.54	679.60	583.61	319.09
	a_{CDOM}(412) (m^{-1})	92	0.03	1.61	0.41	0.28	0.33
	DOC ($\mu mol.L^{-1}$)	59	35.99	361.82	110.44	102.22	61.20
	POC/SPM	26	0.02	1.17	0.12	0.05	0.22
	Chl-a/POC	19	0.001	0.013	0.005	0.004	0.003
	$a_{ph}(400)/a_p(400)$	45	0.77	0.96	0.85	0.84	0.05
	$a_{CDOM}(400)/(a_{CDOM}(400)+a_p(400))$	42	0.09	0.92	0.63	0.66	0.22
OWT 3	SPM ($g.m^{-3}$)	76	5.93	1945.34	129.56	49.96	250.37
	Chl-a($mg.m^{-3}$)	67	0.08	48.32	7.82	5.75	7.77
	POC($mg.m^{-3}$)	52	268.03	4705.48	1505.13	1249.85	1051.41
	a_{CDOM}(412) (m^{-1})	89	0.14	9.24	1.59	0.88	1.65
	DOC ($\mu mol.L^{-1}$)	48	83.18	564.08	179.16	156.94	88.97
	POC/SPM	48	0.01	0.14	0.03	0.03	0.03
	Chl-a/POC	43	0.0001	0.016	0.006	0.005	0.004
	$a_{ph}(400)/a_p(400)$	67	0.65	1.02	0.86	0.88	0.08
	$a_{CDOM}(400)/(a_{CDOM}(400)+a_p(400))$	67	0.29	1.00	0.78	0.82	0.17
Overall	SPM ($g.m^{-3}$)	153	1.15	1945.34	69.72	16.67	185.80
	Chl-a ($mg.m^{-3}$)	119	0.08	48.32	6.27	3.74	6.68
	POC ($mg.m^{-3}$)	92	161.47	4705.48	1150.48	868.79	912.96
	a_{CDOM}(412) (m^{-1})	193	0.00	9.24	0.94	0.54	1.29
	DOC ($\mu mol.L^{-1}$)	118	35.99	564.08	137.65	116.92	79.04
	POC/SPM	76	0.01	1.17	0.06	0.03	0.14
	Chl-a/POC	66	0.0001	0.016	0.005	0.004	0.004
	$a_{ph}(400)/a_p(400)$	119	0.65	1.02	0.85	0.85	0.07
	$a_{CDOM}(400)/(a_{CDOM}(400)+a_p(400))$	114	0.09	1.00	0.71	0.75	0.21

3.3. Suspended particulate matter (SPM)

3.3.1. Description of candidate SPM models

Five historical SPM algorithms including empirical and semi-analytical approaches were selected for evaluation in French Guiana coastal waters. Recent machine-learning-based models (e.g., Pahlevan et al., 2020), which adopt all information in the visible and NIR regions, were not considered in this examination due to the availability of spectral bands offered by GlobCoast and GlobColour data as well as the time-consuming computation they might cause. Empirical models, such as those introduced by Doxaran et al., (2002), Ngoc et al., (2020), and Siswanto et al., (2011), were typically developed based on the statistical relationship between nLw (normalized water Leaving radiance) or $R_{rs}(\lambda)$ (remote sensing reflectance) and the in-situ SPM concentration. While semi-analytical algorithms such as Han et al., (2016); Nechad et al., (2010) indirectly estimate SPM by primarily analyzing the connection between $R_{rs}(\lambda)$ and IOPs (Inherent Optical Properties) of an aquatic environment such as absorption and backscattering coefficients. The description of the tested algorithms is shown in **Table 3.2**.

Table 3.2. *Description of existing SPM models that are selected in the performance evaluation*

Model	Type/Function	SPM range ($g.m^{-3}$)	Study Area	Reference
Doxaran02	Empirical/ Power-law	35 - 2072	Gironde estuary (France)	(Doxaran et al., 2002)
Siswanto11	Empirical/ Multivariable	0.04 - 340	Yellow and East China Seas (China)	(Siswanto et al., 2011)
DatDN20	Empirical/ cubic polynomial	0.47 - 240.14	Vietnamese coastal zone & Tonle Sap lake (Cambodia)	(Ngoc et al., 2020)
Nechad10	Semi-Analytical	1.2 - 110.3	Southern North Sea	(Nechad et al., 2010)
BingHan16	Semi-Analytical	0.154 - 2627	Global Dataset	(Han et al., 2016)

(1) Doxaran02

The model Doxaran02 is developed by Doxaran et al., (2002) using an in-situ dataset collected in the Gironde estuary located in southwest France with the SPM concentration ranging from 35 $g.m^{-3}$ to 2072 $g.m^{-3}$. This location is known as a good example of case-2 water due to the high turbidity observed within the water body. The model used the ratio between the reflectance in the Near InfraRed (NIR) and in the green part of the spectrum as the input for an index number of a power law function.

$$SPM=\exp(\frac{X+0.9614}{0.3193}) \quad 3.1$$

where

$$X_1=\frac{R_{rs}(865)}{R_{rs}(555)} \quad 3.2$$

(2) Nechad10

Nechad et al., (2010) proposed a semi-analytical model for estimating SPM through a relationship test for a continuous range of wavelengths from 520 nm to 885 nm. This algorithm (see Equation 3.3) takes the advantage of the red band where a significant correlation was found between the signal on this particular band and the measured SPM within a range of 1.24 $mg.L^{-1}$ and 110.27 $mg.L^{-1}$.

$$SPM=\frac{A^{\rho}\rho_w(670)}{1-\frac{\rho_w(670)}{C^{\rho}}}+B^{\rho} \quad 3.3$$

where A^{ρ} is assumed as the ratio of non-particle absorption (a_{np}) to specific particulate backscattering coefficient (b^*_{bp}), C^{ρ} corresponds to the ratio between b^*_{bp} and specific particulate absorption coefficient (a^*_p), B^{ρ} the coefficient represents the errors of measurement and model. ρ_w is the water-leaving reflectance which can be calculated from R_{rs}: $\rho_w(\lambda)=\pi R_{rs}(\lambda)$.

(3) Siswanto11

The model Siswanto11 is designed for the Yellow and East China Seas where the concentration of TSM can reach 340.07 $g.m^{-3}$ in Spring (Siswanto et al., 2011). The such empirical algorithm is developed as a regional adapted version of (Tassan, 1994) which takes into account two input variables X_1, X_2 and can be expressed as the equation below:

$$\log_{10}(SPM)=0.649+25.623X_1+0.646X_2 \quad 3.4$$

where

$$X_1=R_{rs}(555)+R_{rs}(670) \quad 3.5$$

$$X_2=\frac{R_{rs}(490)}{R_{rs}(555)} \quad 3.6$$

(4) BingHan16

BingHan16 (Han et al., 2016) is a Semi-Analytical Algorithm (SAA) developed based on a global dataset gathered from different sampling sites in Europe, French Guiana, Vietnam, North Canada, and China within a variety of aquatic conditions (*i.e.*, river run-off, sediment resuspension, phytoplankton bloom, *etc.*). Generally, this model aims to blend two versions of Nechad10 model with tuned coefficients by using a weighting function to optimize the retrieval of SPM taking into account low to medium turbid waters and highly turbid waters. In practice, the model uses thresholds of $R_{rs}(\lambda)$ in the red part of the spectrum (0.03 sr^{-1} and 0.04 sr^{-1}) to classify the water into low and high SPM conditions (see **Figure 3.7.c,d**). Next, a switching method, which is applied to combine the two algorithms corresponding to two defined water types to obtain a unique estimation of SPM, is expressed in Equation 3.7.e. Such procedure is explained by the following equations:

$$SPM_L=\frac{A^{\rho}_L.\rho_w(\lambda_0)}{1-\frac{\rho_w(\lambda_0)}{C^{\rho}_L}} \quad 3.7.a$$

$$SPM_H=\frac{A^{\rho}_H.\rho_w(\lambda_0)}{1-\frac{\rho_w(\lambda_0)}{C^{\rho}_H}} \quad 3.7.b$$

$$W_L=\begin{cases}1, \text{ if } R_{rs}(\lambda_0)\le 0.03 \text{ sr}^{-1}\\ 0, \text{ if } R_{rs}(\lambda_0)\ge 0.04 \text{ sr}^{-1}\\ \log_{10}(0.04)-\log_{10}[R_{rs}(\lambda_0)], \text{ otherwise}\end{cases} \quad 3.7.c$$

$$W_H=\begin{cases}0, \text{ if } R_{rs}(\lambda_0)\le 0.03 \text{ sr}^{-1}\\ 1, \text{ if } R_{rs}(\lambda_0)\ge 0.04 \text{ sr}^{-1}\\ \log_{10}[R_{rs}(\lambda_0)]-\log_{10}(0.03), \text{ otherwise}\end{cases} \quad 3.7.d$$

$$SPM=\frac{W_L.SPM_{L+}W_H.SPM_H}{W_{L+}W_H} \quad 3.7.e$$

This model was defined for SeaWiFS, MODIS, MERIS/OLCI/MSI, VIIRS, and OLI sensors; the coefficients specific to each satellite are documented in Han et al., 2016 and not recalled here.

(1) DatDN20-1 & DatDN20-2

In this thesis, two versions of Ngoc et al., (2020) (DatDN20-1 Equation 3.8 and DatDN20-2 Equation 3.9) were tested along with other historical models in the performance examination. These two versions are developed using the available spectral bands in the green and red domain of VNREDSat-1 which bands are similar to Landsat-8 sensor. The algorithm was validated on the in-situ dataset gathered in the Vietnamese coastal zone and Tonlesap River in Cambodia (Ngoc et al., 2020). The formulation of this model is constructed by a cubic polynomial function and can be expressed as below:

$$\log_{10}(SPM)=0.281\log_{10}^{3}R_{rs}(655)+2.48\log_{10}^{2}R_{rs}(655)+7.94\log_{10}R_{rs}(655)+9.35 \quad 3.8$$

$$\log_{10}(SPM)=0.663\log_{10}^{3}\frac{R_{rs}(655)}{R_{rs}(565)}+1.48\log_{10}^{2}\frac{R_{rs}(655)}{R_{rs}(565)}+2.57\log_{10}\frac{R_{rs}(655)}{R_{rs}(565)}+1.59 \quad 3.9$$

3.3.2. Selection of the most pertinent SPM model

The tested models have been tuned regionally using in-situ measurements collected in French Guiana coastal waters. This dataset is clustered into three Optical Water Types (OWTs) based on the normalization of measured hyperspectral $R_{rs}(\lambda)$. **Figure 3.2** depicts the better version of each inversion algorithm, where the original forms possibly outperform the tuned ones. This might be due to the difference in the SPM range of the development dataset that potentially causes a slight discrepancy in the statistics. The DatDN20-1 model, which uses the $R_{rs}(\lambda)$ in the red as an independent variable, exhibits better performance than DatDN20-2 with an R^2 of 0.77 and RMSE of 0.29 $g.m^{-3}$ to rank the second position among the five models after being adapted **Figure 3.2.e,f**. This result emphasizes a greater correlation between SPM and $R_{rs}(665)$ compared to the ratio of $R_{rs}(560)$/ $R_{rs}(665)$ considering the French Guiana dataset. The Doxaran02 model presents a fairly good accuracy in retrieving SPM for highly turbid waters (OWT 3), however, such an algorithm tends to overestimate SPM concentration in the low to moderate range **Figure 3.2.d**. This is understandable since Doxaran02 was initially developed for aquatic conditions containing SPM levels more than 35 $g.m^{-3}$. The optimized version of the Siswanto11 algorithm, originally designed for SPM values ranging between 0.33 and 340 $g.m^{-3}$, shows a relatively good SPM prediction illustrated by MAPD of 18.06% and RMSE of 0.32 $g.m^{-3}$. However, the general performance of this model is lower than that of the semi-analytical approach Nechad10. The model Nechad10 exhibits outstanding SPM retrieval, as evidenced by the maximum R^2 and RMSD of 0.78 and 0.28 $g.m^{-3}$, respectively, despite being built for a narrow range of SPM

between 1.2 and 110.3 $g.m^{-3}$. The use of a constant offset (B^{ρ}) in this model, however, raises the possibility of an overestimation of SPM at low concentrations (Han et al., 2016). For this reason, the model BingHan16 was proposed using a Nechad10-based core, but without taking the aforementioned constant offset into consideration. In addition, the use of a weighting approach performed in its formulation presents the best accuracy of SPM estimation in the present dataset with the optimal Slope of 0.87 and smallest area of 0.489 in the radar plot **Figure 3.2.a,g**. According to the obtained results, the original version of the BingHan16 model was adopted to derive SPM concentration in French Guiana coastal waters.

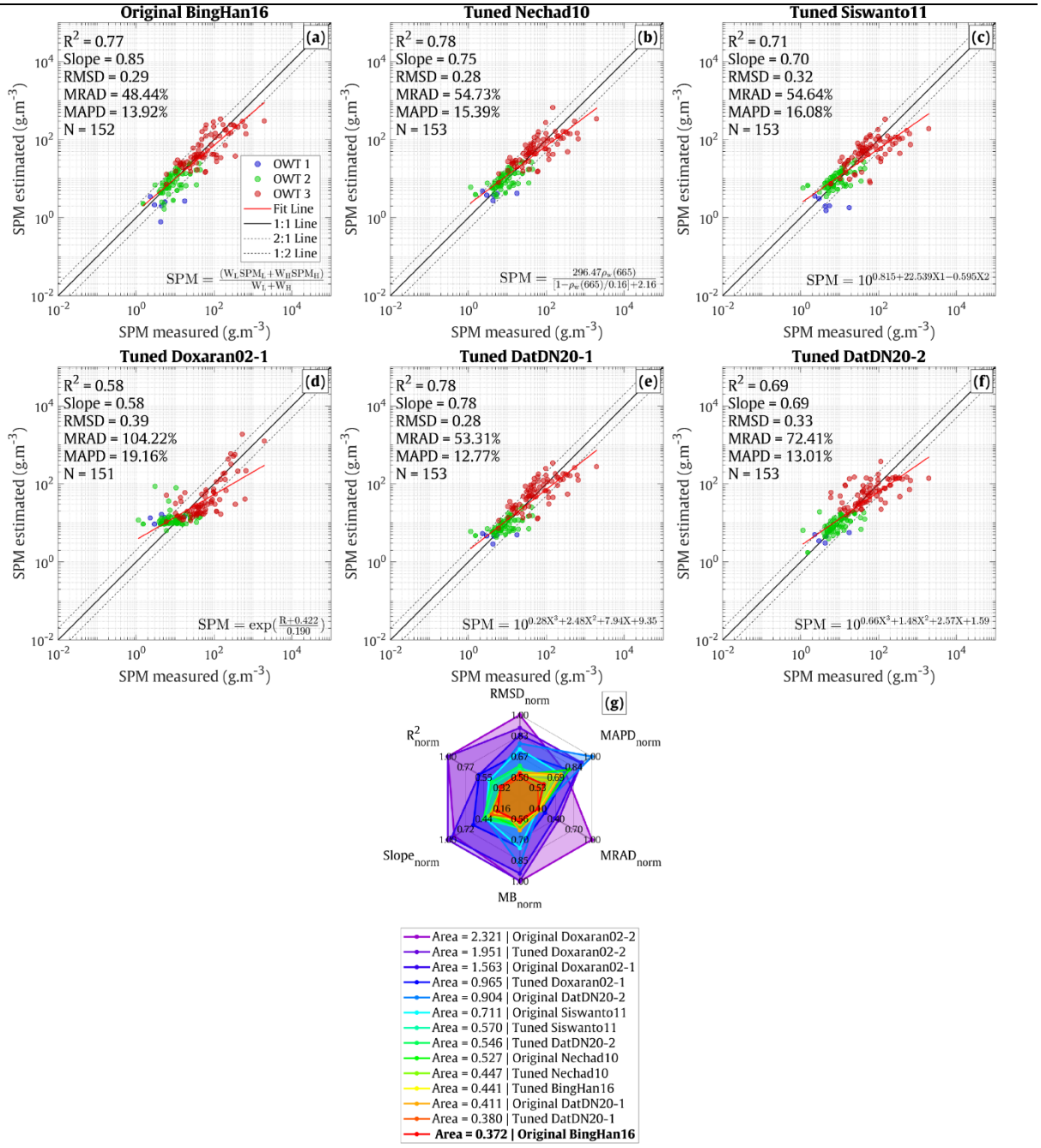

Figure 3.2. *Inter-comparison considering MERIS sensor of measured and model-derived SPM concentration when the model* ***a)*** *Original BingHan16;* ***b)*** *Tuned Nechad10;* ***c)*** *Tuned Siswanto11;* ***d)*** *Doxaran02-1;* ***e)*** *Tuned DatDN20-1;* ***f)*** *Tuned DatDN20-2 are applied to the in-situ dataset collected in French Guiana coastal waters. Blue, Green, and Red correspond to OWT 1, OWT 2, and OWT 3, respectively. The overall comparison described by statistical indicators is illustrated in panel* ***g)****.*

3.4. Particulate Organic Carbon (POC)

3.4.1. Description of POC candidate algorithms

In open ocean waters, POC has been historically estimated using relationships based on the backscattering coefficient, for instance, (Loisel et al., 2007) with a satisfying accuracy. Specific models for estimating POC in optically complex environments have been developed more recently through dedicated studies in coastal or river-dominated domains (Le et al., 2017; T. K. Tran et al., 2019). Here, the evaluation of the performance of the POC concentration by using remote sensing observations was performed considering five empirical algorithms which are Stramski08 (Stramski et al., 2008), Woźniak16 (Woźniak et al., 2016), Le17 (Le et al., 2017) , Le18 (Le et al., 2018) , and KienTran19 (T. K. Tran et al., 2019). These models, which rely on empirical relationships between measured different spectral bands and POC concentration (**Table 3.3**), have been considered as the candidate algorithms as they are developed from a variety of aquatic conditions including both Case-1 and Case-2 waters.

Table 3.3. *Description of existing POC models that are selected in the performance evaluation*

Model	Type/Function	POC range ($mg.m^{-3}$)	Study Area	Reference
Stramski08	Empirical/ Power-law	10 - 270	Eastern South Pacific	(Stramski et al., 2008)
Woźniak16	Empirical/ Power-law	145 – 2370	Baltic Sea Gulf of Gdansk (Poland)	(Woźniak et al., 2016)
Le17	Empirical/ Multivariable	11.5 - 230	Louisiana & Mobile Bay (Gulf of Mexico)	(Le et al., 2017)
Le18	Empirical/ Power-law	52.6 – 375.2	Global Dataset	(Le et al., 2018)
KienTran19	Empirical/ Power-law	45.37 - 5744	Global Dataset	(T. K. Tran et al., 2019)

(1) Stramski08

The model Stramski08 (Stramski et al., 2008) is an empirical algorithm which uses the band ratios between green and blue of $R_{rs}(\lambda)$ to estimate POC concentration for open ocean waters. The in-situ dataset to develop this model was collected within oligotrophic and upwelling waters of the Eastern South Pacific Ocean with a POC range between 10 $mg.m^{-3}$ and 270 $mg.m^{-3}$. The blue-to-green ratio was adopted to be an input variable for a power-law function formulating the model.

$$POC=203.2\frac{R_{rs}(443)^{-1.034}}{R_{rs}(555)} \quad 3.10$$

$$POC=308.3\frac{R_{rs}(490)^{-1.639}}{R_{rs}(555)} \quad 3.11$$

(2) Woźniak16

(Woźniak et al., 2016) developed a POC algorithm established from the 75 measurements sampled in the Gulf of Gdansk (Poland) representing a wide range of POC from 145 $mg.m^{-3}$ to 2370 $mg.m^{-3}$. Similar to Stramski08, Woźniak16 is formulated using a power-law function based on a band ratio in the green part of the visible spectrum as described in the following equation:

$$POC=0.814\frac{R_{rs}(555)^{-4.42}}{R_{rs}(589)} \quad 3.12$$

(3) Le17

The Le17 model (Le et al., 2017) is based on a multiband function initially developed for MODIS and SeaWiFS sensors. This model was designed to be suitable for aquatic environments characterized by river-dominated estuaries in the Gulf of Mexico with an upper limit of POC concentration of 230 $mg.m^{-3}$.

$$POC=\exp[-126.22R_{rs}(488)-120.74R_{rs}(531)+245.42R_{rs}(547) -493.54R_{rs}(667)+489.3R_{rs}(678)-0.59] \quad 3.13$$

$$POC=\exp(-115.69R_{rs}(490)-53.64R_{rs}(510)+172.13R_{rs}(555)-40.06R_{rs}(670)-0.54) \quad 3.14$$

(4) Le18

Le et al., (2018) proposed a POC inversion model using a color index CI_{POC}. This indexis computed from $R_{rs}(\lambda)$ of three spectral bands centered at 490 nm, 555 nm, and 670 nm. The relationship between the in-situ POC of a global dataset (POC in the range of 10-1000 $mg.m^{-3}$) and the index CI_{POC} was, then, determined by a power-law function which was designed in regard to the values of CI_{POC}.

$$CI_{POC}=R_{rs}(555)-\left\{R_{rs}(490)+\frac{555-490}{670-490}[R_{rs}(670)-R_{rs}(490)]\right\} \quad 3.15.a$$

$$CI_{POC} \leq -0.0005 : POC = 10^{185.72 CI_{POC} + 1.97} \quad 3.15.b$$

$$CI_{POC} \geq -0.0005 : POC = 10^{485.19 CI_{POC} + 2.1} \quad 3.15.c$$

(5) KienTran19

T. K. Tran et al., (2019) examined different existing empirical POC algorithms and deployed the inter-comparison to assess their performance based on a global data set gathered in coastal environments. The authors also developed an inversion model based on the MBR (Maximum Band Ratio) approach tested on a global dataset composed of the in-situ measurements conducted in the Baltic Sea, Bay of Biscay, Beaufort Sea Arctic Ocean, Vietnamese East Sea, English Channel, French Guiana, North Sea, and South Pacific Ocean with the POC ranging between 45.37 and 5744 $mg.m^{-3}$. This model can be simplified as below:

$$POC = 10^{0.928X + 2.875} \quad 3.16$$

with

$$X = \log_{10}\left\{\max\left[\frac{R_{rs}(665)}{R_{rs}(490)}, \frac{R_{rs}(665)}{R_{rs}(510)}, \frac{R_{rs}(665)}{R_{rs}(555)}\right]\right\} \quad 3.17$$

3.4.2. Selection of the most pertinent POC model

The inter-comparison of tested POC models was conducted on 92 data points for which both R_{rs} and POC measurements were available in French Guiana. Similar to SPM, the better version of selected algorithms for retrieving POC is shown in **Figure 3.3**. Due to the inherent limitation and sensitivity of the Stramski08-BR3 and KienTran19 models which is probably related to the highly turbid condition, both original and adapted versions of these two models fail to predict POC in French Guiana coastal waters. Clear evidence of this issue can be found in **Figure 3.3.d,e** where the poor correlation between estimated and measured POC values is demonstrated. This is not unexpected given that the Stramski08-BR3 models only allow for a maximum POC concentration of 270 $mg.m^{-3}$, respectively, which is approximately 13 times lower than the highest value of POC reported in the French Guiana dataset (4705.5 $mg.m^{-3}$). The Le18 model shows a clear saturation to estimate the POC concentration that can be seen from the **Figure 3.3.e**. A similar propensity can be found in the performance of the Woźniak16 model presenting a low correlation between the log-transformed in-situ and model-derived POC (R^2 = 0.23) and high dispersion from the 1:1 line. The multiband model Le17 exhibits the most satisfying

accuracy among the five investigated models in retrieving POC over French Guiana coastal waters. By displaying a distribution of the data points, especially those belonging to OWT 3 close to the 1:1 line, such model proves its reliability to estimate POC concentration in turbid environments with RMSD of 0.23 mg.m^{-3} and MAPD of 5.16%.

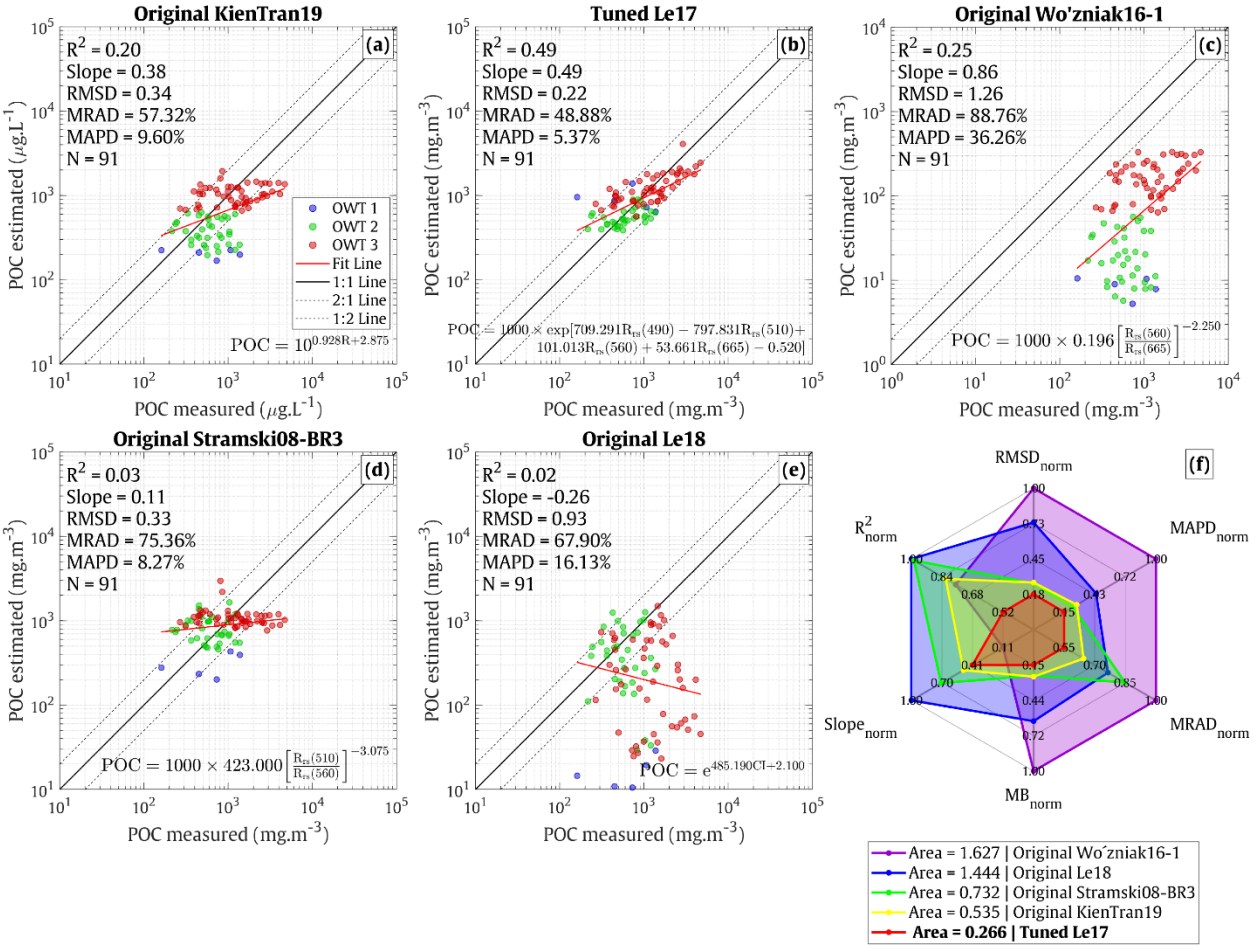

Figure 3.3. *Inter-comparison of measured and model-derived POC concentration when the model* ***a)*** *Tuned KienTran19;* ***b)*** *Tuned Le17;* ***c)*** *Tuned Woźniak16;* ***d)*** *Tuned Stramski08;* ***e)*** *Tuned Le18 are applied to the in-situ dataset collected in French Guiana coastal waters. Blue, Green, and Red correspond to OWT 1, OWT 2, and OWT 3, respectively. The overall comparison described by statistical indicators is illustrated in panel* ***f)****.*

Even though the model Le17 globally outperforms the other algorithms from the analysis carried out on our in-situ dataset, it fails to estimate POC properly over clear environments. This is here underlined by a few points gathered for offshore waters in **Figure 3.2.b** where we can observe an overestimation of POC value for the OWT 1. Although this pattern is here supported by a very limited number of data points, it is clearly illustrated when applying Le17 to satellite-

images where no dynamic is found in the offshore waters (not shown here). As an alternative, we therefore suggest combining the models KienTran19 and Le17 using a blending strategy as a solution to the data coverage limitation (D'Alimonte et al., 2003; Mélin et al., 2011 Vantrepotte et al., 2012). Since the model Le17 has shown its reliability to estimate POC for medium to turbid waters, the probability values belonging to OWT 3 has been used as the blending coefficient of this model. Meanwhile, the model KienTran19 is applied to data points corresponding to OWTs 1 and 2 representing clear waters as documented in T. K. Tran et al., (2019) and as confirmed here. The performance of this combined model (KienTran19-Le17) is shown in **Figure 3.4** where the Slope reaches 0.6 and MAPD between measured and estimated POC is 6.98%.

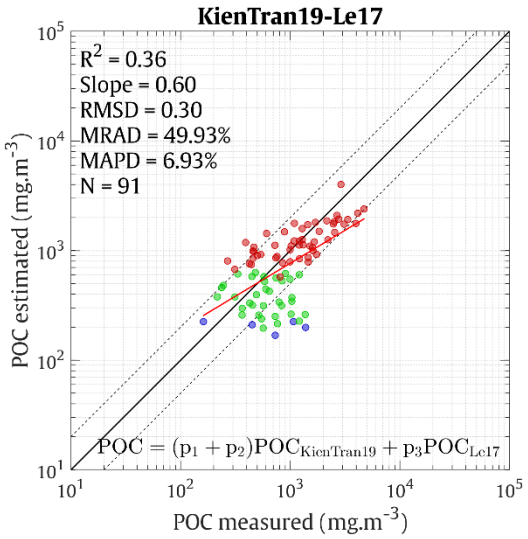

Figure 3.4. *Scatter plot between in-situ and model-derived POC from the combination of KienTran19 and Le17 models. The dash lines represent 2:1 and 1:2 lines, respectively. The solid black line is the 1:1 line. The solid line in red corresponds to the fit line. Blue, Green, and Red are OWT 1, OWT 2, and OWT 3, respectively.*

3.5. Absorption of Colored Dissolved Organic Matter (a_{CDOM})

In this section, five inversion algorithms for estimating $a_{CDOM}(412)$ have been evaluated. It is worth mentioning that some of the considered formulations were initially developed for estimating $a_{CDOM}(443)$ and $a_{CDOM}(420)$, for instance, (D'sa et al., 2006; Kutser et al., 2005). These models have been adapted to estimate the CDOM absorption at 412 nm using the in-situ data collected in French Guiana waters. **Table 3.4** illustrates the description of a_{CDOM} models considered in this regional intercomparison exercise.

Table 3.4. *Description of existing a_{CDOM} models that are selected in the performance evaluation*

Model	Type/Function	a_{CDOM} range (m^{-1})	Study Area	Reference
Kutser05	Empirical/ Power-law	0.68 – 11.13	Swedish Lake	(Kutser et al., 2005)
D'sa06	Empirical/ Power-law	0.07 – 0.20	Northern Gulf of Mexico	(D'sa et al., 2006)
Cao18	Empirical/ Multivariable	0.2 – 37	Chesapeake Bay, Delaware Bay, Gulf of Mexico	(Cao, Tzortziou, Hu, Mannino, Fichot, del Vecchio, et al., 2018)
Son-B2R	Empirical/ Power-law	0.004 – 6.06	Global Dataset	(In prep)
Loisel14	Neural Network	0.04 – 3.65	Synthetic Dataset, European & French Guiana coast, NOMAD Global Dataset	(Jamet et al., 2012; Loisel et al., 2018; Loisel et al., 2014)

3.5.1. Description of a_{CDOM} candidate algorithms

(1) Kutser05

The model Kutser05 developed by Kutser et al., (2005) was aimed to retrieve CDOM in 13 lakes located in southern Finland and in 21 lakes situated in southern Sweden. This inversion model is based on an empirical approach taking into account the ratio of $R_{rs}(565)/R_{rs}(660)$ and is designed to be suitable for a_{CDOM} range of 0.68 – 11.13 m^{-1}.

$$a_{CDOM}(420)=5.13\left[\frac{R_{rs}(565)}{R_{rs}(660)}\right]^{-2.67} \quad 3.18$$

(2) D'Sa06

Another empirical model, D'Sa06 likewise based on a power-law function of a band ratio, but involving other wavelengths, was suggested by D'sa et al., (2006). In particular, this algorithm considers the ratio of $R_{rs}(510)/R_{rs}(555)$ as the independent variable to estimate $a_{CDOM}(412)$ between 0.04 and 1.2 m^{-1} on the Louisiana shelf in the Northern Gulf of Mexico.

$$a_{CDOM}(412)=0.227\frac{R_{rs}(510)^{-2.022}}{R_{rs}(555)} \quad 3.19$$

(3) Cao18

The empirical algorithm Cao18 was formulated based on an exponential function of multiple linear regression (MLR) with independent variables corresponding to $R_{rs}(\lambda)$ at different spectral

channels of MODIS and MERIS sensors. The authors note that although this model was first created to obtain a_{CDOM} at 300 nm and 350 nm, it also yields a similar result at 412 nm with a MAPD of 26.9 % Cao et al., (2018). The approach produces estimation of a_{CDOM} over more than two orders of magnitude (for example, $a_{CDOM}(300)$ in the range of 0.2 to 0.37 m^{-1}).

$$\ln\left(a_{CDOM}(412)\right) = -0.0206\ln\left(R_{rs}(443)\right) - 0.6128\ln\left(R_{rs}(448)\right) - 0.007\ln\left(R_{rs}(531)\right) - 0.4944\ln\left(R_{rs}(555)\right) + 0.9362\ln\left(R_{rs}(667)\right) + 0.9666 \quad (3.20)$$

(4) Son-B2R

Son-B2R is an abbreviation of a Blue-to-Red-ratio model developed by Son Nguyen Vu who is currently a PhD candidate at LOG (Laboratoire d'Océanologie et de Géosciences). Such a model examined the relationship between the ratio of $R_{rs}(483)/R_{rs}(655)$ and the in-situ $a_{CDOM}(412)$ gathered globally in different sites. The nature of this relationship is expressed in the form of a polynomial function of the fourth order. The $a_{CDOM}(412)$ estimated by the model Son-B2R is represented in the following equation:

$$\log_{10}\left(a_{CDOM}(412)\right) = 0.001823\left(\frac{R_{rs}(483)}{R_{rs}(655)}\right)^4 - 0.05377\left(\frac{R_{rs}(483)}{R_{rs}(655)}\right)^3 + 0.05442\left(\frac{R_{rs}(483)}{R_{rs}(655)}\right)^2 - 0.8855\frac{R_{rs}(483)}{R_{rs}(655)} - 0.2649 \quad (3.21)$$

(5) Loisel14

The estimation of $a_{CDOM}(412)$ by the model Loisel14 was designed by a machine learning approach with to two principal steps. More specifically, the first step refers to the establishment of a neural network model proposed by Jamet et al., (2012) to retrieve the spectral diffuse attenuation coefficient $K_d(\lambda)$. Such a model considers the inputs of $R_{rs}(\lambda)$ at all standard bands in the visible spectral range of satellite ocean color sensors. The refinement of this machine learning algorithm is documented in Loisel et al., (2018) and its operation relies on a network of two hidden layers with five neurons in each layer. The second step is related to the estimation $a_{CDOM}(412)$ from the log-transformed parameter X computed by the difference values between the diffuse attenuation coefficient, $K_d(\lambda)$, and the diffuse attenuation coefficient for pure seawater, $K_w(\lambda)$, at two spectral bands of 412 nm and 555nm with a consideration of the impact of the particulate fraction $\Delta_p(410)$-$\Delta_p(555)$. The initial formulation was developed for

$a_{CDOM}(410)$ values ranging from 0.04 to 3.65 m^{-1} using a quadratic function (Loisel et al., 2014) and can be expressed as below:

$$\log_{10}\left(a_{CDOM}(410)\right)=0.1548[\log_{10}(X)]^2+1.1939\log_{10}(X)+0.0689 \quad 3.22$$

where

$$X=\left(K_d(410)-K_w(410)\right)-\left(K_d(555)-K_w(555)\right)-\left(\Delta_p(410)-\Delta_p(555)\right) \quad 3.23$$

3.5.2. Selection of the most pertinent a_{CDOM} model

The inter-comparison results performed on the five bio-optical models including Cao18, Son-B2R, Kutser05, D'sa06, and Loisel14 introduced in section 3.5.1 and based on a total of 193 $a_{CDOM}(412)$-$R_{rs}(\lambda)$ measurements are presented in **Figure 3.4**. In most cases, the adapted versions of the models under consideration perform significantly better than those in the original form. It is apparent that the model D'Sa06 fails to derive $a_{CDOM}(412)$, especially for turbid waters, as evidenced by a low slope of 0.15 and a deviation of the red points from the 1:1 line. This is not surprising as the development of this model is constrained to a maximum $a_{CDOM}(412)$ value of 0.2 m^{-1}. The model Loisel14, which is based on a semi-analytical approach, shows a relatively relevant performance with a Slope of 0.61. However, the information on CDOM extracted from this algorithm is not optimal, which is represented by a high value of MAPD (73.36%) as well as a scattering pattern in the distribution of the data points around the 1:1 line. The two models Son-B2R and Kutser05 both display a comparable accuracy and tend to overestimate $a_{CDOM}(412)$ in highly turbid environments (**Figure 3.5.b,c**). The areas calculated from the radar plot associated with these two algorithms further demonstrate their relatively comparable performance (**Figure 3.5.f**, $area_{Son\text{-}B2R}$ = 0.735 and $area_{Kutser05}$ = 0.707). The modified version of the model suggested by Cao et al., (2018) presents the best performance among the models evaluated, as for instance indicated by the lowest statistical area value (*i.e.,* $area_{Cao18}$ = 0.377) found for this algorithm among all the formulations evaluated. Therefore, the adapted version of the models of Cao et al., (2018) has been chosen as the appropriate inversion model to estimate $a_{CDOM}(412)$ in the coastal waters of French Guiana.

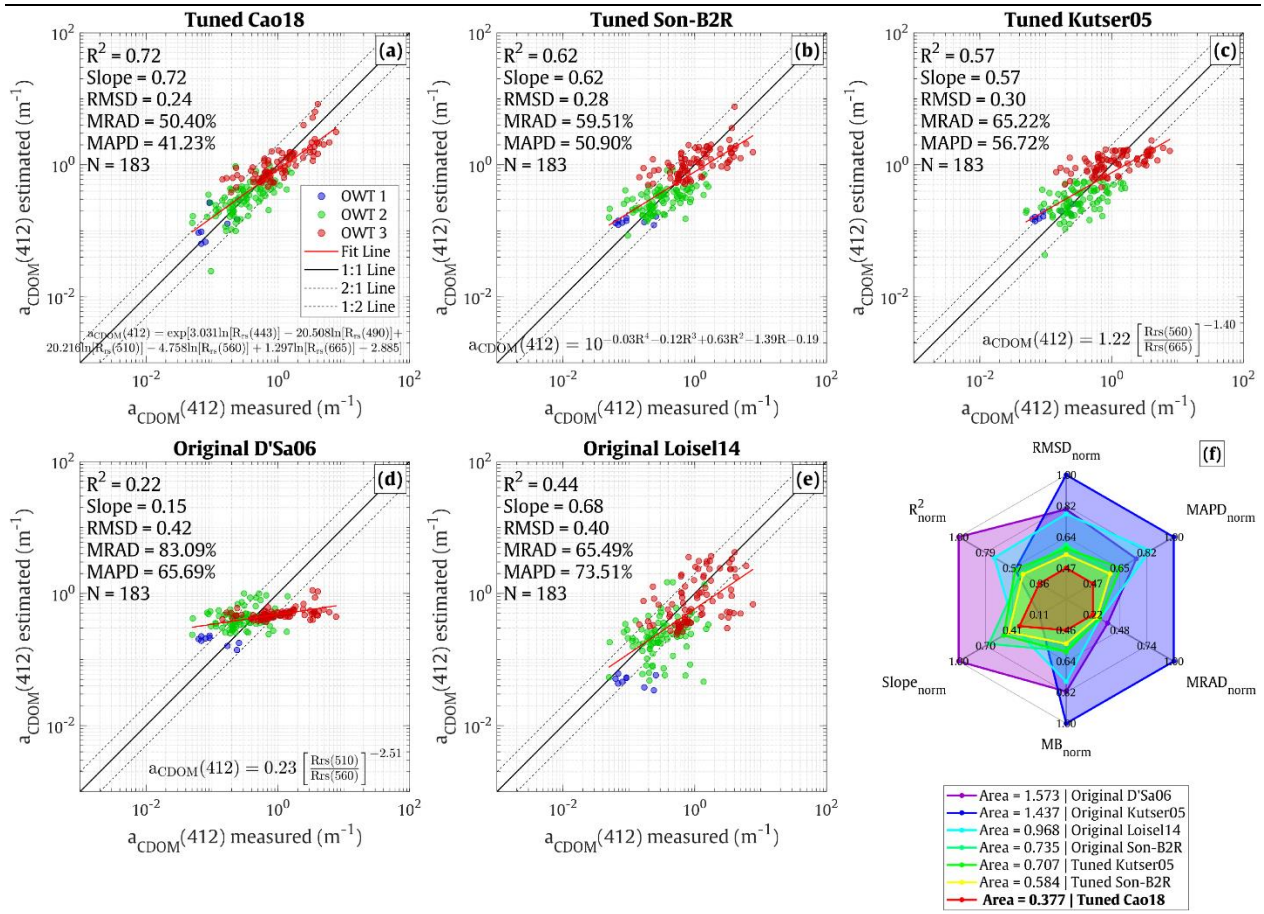

Figure 3.5. *Inter-comparison considering MERIS sensor of measured and model-derived $a_{CDOM}(412)$ concentration when the model* ***a)*** *Tuned Cao18,* ***b)*** *Tuned Son-B2R,* ***c)****Tuned Kutser05,* ***d)*** *Original D'Sa06,* ***e)*** *Original Loisel14 applied to the in-situ dataset collected in French Guiana coastal waters. Blue, Green, and Red correspond to OWT 1, OWT 2, and OWT 3, respectively;* ***f)*** *The overall comparison described by statistical indicators.*

3.6. Dissolved Organic Carbon (DOC)

3.6.1. Description of original versions of DOC algorithms

Remote-sensing-based retrievals of dissolved organic carbon (DOC) over optically contrasted environments remain scarce. This parameter can be estimated from exploiting linear relationships between a_{CDOM} and DOC in coastal waters influenced by terrestrial inputs, where CDOM and DOC follow the same dilution gradient (Joshi et al., 2017; Le et al., 2013, Mannino et al., 2008). However, such relationships have shown clear limitations related to the fact that they strongly vary at seasonal scale for a defined coastal site but also from one coastal area to another. To overcome these issues different approaches have been proposed focusing mainly on

the relationship between the information of the CDOM absorption spectra slopes in the UV domain ($S_{275\text{-}295}$) and the specific absorption coefficient ($a^*_{CDOM}(\lambda) = a_{CDOM}(\lambda)/DOC$) (Helms et al., 2008, Fichot and Benner., 2011, Valerio et al., 2018). A simplified general relationships was proposed by Vantrepotte et al., (2015) (Vantrepotte15) in order to estimate directly $a_{CDOM}(\lambda)/DOC$ from $a_{CDOM}(412)$ on a variety of coastal sites including some samples of French Guiana. Here we simply illustrate the performance of this model taking into account the most recent samples gathered at regional scale. This algorithm is described by the following equations:

$$a^*_{CDOM}(412) = 10^{0.7109\log_{10}(a_{CDOM}(412))-2.1722} \quad 3.24$$

where

$$a^*_{CDOM}(412) = \frac{a_{CDOM}(412)}{DOC} \quad 3.25$$

Vantrepotte et al., (2015) also suggested another approach to estimate $a^*_{CDOM}(412)$ from the spectral slope in the range from 275 nm to 295 nm ($S_{275\text{-}295}$), as the tight relationship between these two parameters has been examined on a gathered dataset. Therefore, this algorithm has also been tested to derive $a^*_{CDOM}(412)$ in the present study and is expressed in the equation below:

$$a^*_{CDOM}(412)=a\left(e^{(b.S_{275\text{-}295})}-e^{(c.S_{275\text{-}295})}\right)+d \quad 3.26$$

where a = 12.4761; b = -553.17; c = 0.01097; and d = 12.48124698.

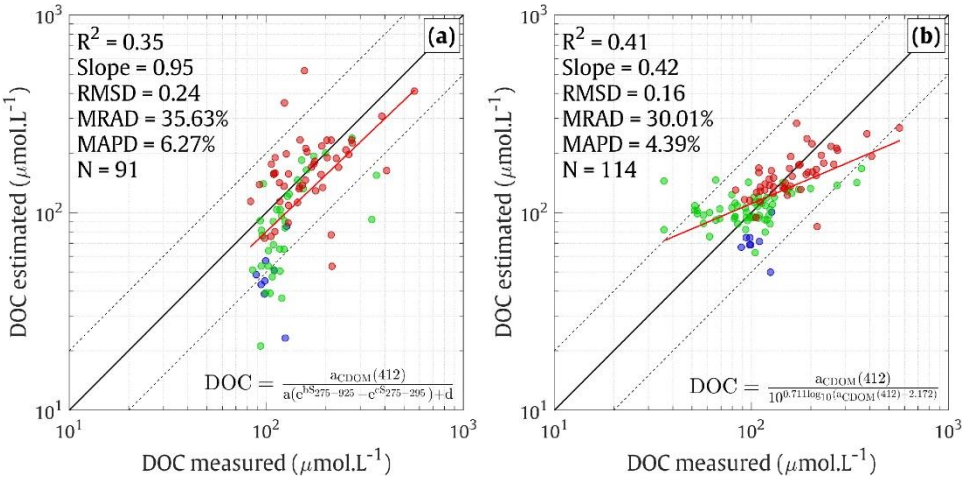

Figure 3.6. *Illustration of the performance of the DOC inversion model by proposed by Vantrepotte et al. (2015) with* ***a)*** *from $S_{275\text{-}295}$ approach and* ***b)*** *from $a_{CDOM}(412)$.*

Considering the fact that the hyperspectral data is more suitable to derive DOC from $S_{275-295}$ approach as it offers continuous information of the electromagnetic spectrum, DOC will be estimated directly from $a_{CDOM}(412)$ in this thesis.

3.7. POC/SPM ratio

The ratio of particulate organic matter to suspended particulate matter (POC/SPM) can provide information on the amount of the particulate matter pool providing an estimate of the relative contribution of organic particles to the total suspended solids (Woźniak et al., 2010). Here, we examined two approaches to derive the value of POC/SPM including an estimation of the POC/SPM considering the approaches selected for estimating individually these two parameters at regional scale (see Sections 3.3.2 and 3.4.2, respectively) and a Neural-Network (NN) based model recently developed at LOG (Loisel et al., 2023). In practice, this latter model estimates the POC/SPM ratio directly from the parameterization of $R_{rs}(\lambda)$ at four different wavelengths in the visible part of the spectrum (412, 490, 510, 560 nm). This algorithm was developed based on a neural network with three hidden layers. The performances of the two methods are depicted in **Figure 3.7.**

The POC/SPM-direct approach shows the overall best statistics among the two approaches evaluated (**Figure 3.6**, e.g., MAPD = 46.71% vs 106.5% for the direct and NN methods, respectively) although an overestimation of the POC/SPM values in clear waters associated with OWT 1 and OWT 2, where the contribution of POC to the SPM is relatively substantial. Meanwhile, such deviation pattern is less pronounced in the POC/SPM prediction of the Neural-Network model **Figure 3.7.b**. This should however be confirmed using a larger data set in these clear environments. The performance of the regional direct approach is clearly more reliable when compared to the Neural-Network one in turbid waters where the later model tends to provide negative estimates in some cases. In this thesis, the regional direct approach for estimating POC/SPM has been therefore selected for further application in French Guiana waters.

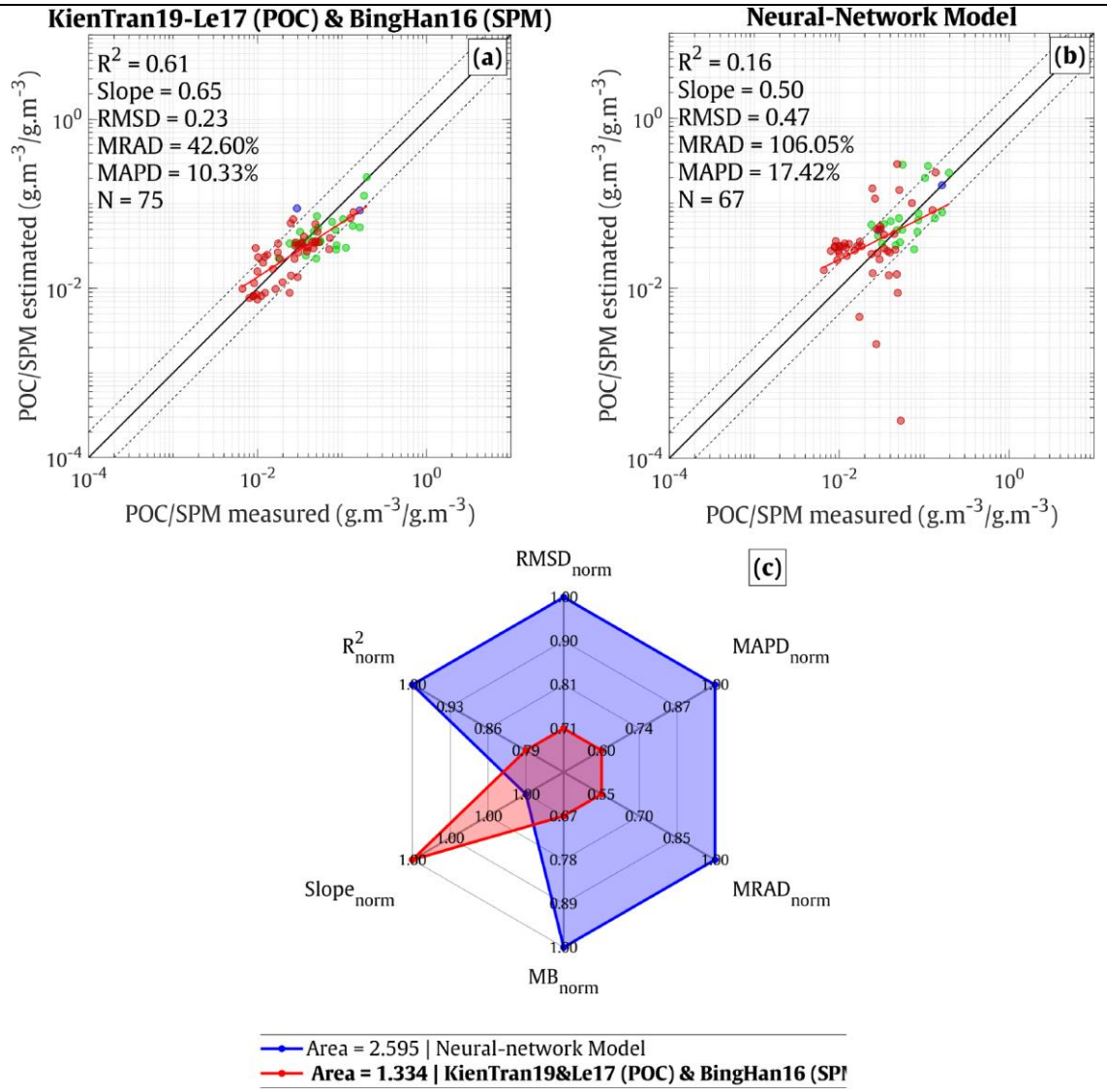

Figure 3.7. *Inter-comparison of measured and model-derived DOC concentration when the model* ***a)*** *KienTran19-Le17 & BingHan16;* ***b)*** *Neural-Network Model applied to the in-situ dataset collected in French Guiana coastal waters. Blue, Green, and Red correspond to OWT 1, OWT 2, and OWT 3, respectively. The overall comparison described by statistical indicators is illustrated in panel* ***c)****.*

CHAPTER 3 – PART II

3.8. Chlorophyll-a (Chl-a)

In fact, the optical signal of Chl-a is significantly influenced by the co-occurrence of other constituents (i.e., CDOM, SPM) in highly turbid waters (Case-2 waters) where the typical Blue/Green band-ratio algorithms tend to fail in retrieving Chl-a information (Groom et al., 2019; Lavigne et al., 2021; Mélin & Vantrepotte, 2015). The massive amount of suspended sediment transported to French Guiana coastal zone makes this area becomes representative for an optically complex environment (Eisma et al., 1991). Due to this signature feature, none of the inversion Chl-a models is fully successful to estimate accurately Chl-a over French Guiana coastal domain (which will be elaborated in the following sections). Therefore, a global dataset was used to develop two algorithms corresponding to clear to medium turbid and turbid/ high Chl-a waters. Such models were then combined using an optical classification scheme as a frame for global applications. This approach was valorized through a publication of (M. D. Tran et al., 2023).

3.8.1. Introduction

The Ocean Color (OC) chlorophyll-a models and related offspring algorithms (O'Reilly et al., 1998; O'Reilly & Werdell, 2019), which are based on the use of a Maximum Band Ratio in the Blue-Green domain of the visible spectrum, have been especially widely validated over clear environments and are now operationally used for deriving Chl-a in open ocean waters (Ford & Barciela, 2017; Garnesson et al., 2019; Xi et al., 2020). Estimating Chl-a from space still however represents a challenging task in coastal waters (Case-2 waters) (Groom et al., 2019; Lavigne et al., 2021). This is related to the high optical diversity of these environments (Mélin & Vantrepotte, 2015) where water optical properties are diversely driven, by a variable contribution of phytoplankton, suspended particulate matter (SPM), and colored dissolved organic matter (CDOM). In high CDOM and/or SPM, phytoplankton impact on the reflectance signal at the shortest wavelengths of the visible range. This feature tends to impair the performance of classical Blue/Green ratio based empirical Chl-a inversion models (Henderikx Freitas & Dierssen, 2019; Loisel et al., 2017; Yang et al., 2018).

Specific Chl-a algorithms have been developed taking advantage of the impact of the phytoplankton on the water optical properties in the Red and NIR regions of the electromagnetic

spectrum. Such Red-NIR models rely on the negligible impact of CDOM and SPM absorption while exploiting the optical signature of phytoplankton absorption or chlorophyll fluorescence on the reflectance spectra over the two latter spectral domains (Gilerson et al., 2010; J. Gower et al., 2005; S. T. Gower et al., 1999; Gurlin et al., 2011). These Red-NIR-based approaches are however failing in clear waters, where the phytoplankton signal can be masked in relationships to the high contribution of pure water absorption at higher wavelengths (Gons et al., 2008; Odermatt et al., 2012).

An extensive study by Neil et al., (2019) has further illustrated the interest in an adaptive framework for dynamically selecting and optimizing Chl-a inversion models in inland waters based on optical water types (OWTs). With the main objective to provide ocean color data users a simple way to evaluate the reliability of the Chl-a estimates derived from Blue/Green and Red/NIR inversion models, (Lavigne et al., 2021) developed quality control tests for improving MERIS (OLCI) Chl-a estimates in coastal waters. Besides these recent studies, new alternative approaches based on machine-learning-based methods, which may be more computing time-consuming than standard reflectance ratios, are now developed for deriving Chl-a over a large range of Chl-a contents and considering a variety of bio-optical regimes in inland and coastal waters (Pahlevan et al., 2020). Although numerous efforts performed during the last decades for accurately estimating Chl-a concentration from the remote sensing reflectance using adapted inversion, there is still no consensus on the algorithm or the set of algorithms to be applied for deriving Chl-a for large-scale applications in coastal waters.

Considering the addressed challenges in applicability of historical Chl-a models regarding different aquatic environments as well as the potential obstacles in the algorithm combination, this study represents a contribution to the continuous efforts for optimizing Chl-a retrieval from ocean color observation in coastal waters. More specifically, this work aims at evaluating the combination of different band-ratio-based models for estimating Chl-a in contrasted coastal waters from Sentinel-2 and Sentinel-3 data. For this purpose, a global in-situ R_{rs}-Chl-a in-situ dataset (N=1244) gathering samples collected over contrasted coastal environments was exploited to define the current band ratios methods the most adapted to derive Chl-a from clear to highly-turbid coastal environments and illustrate the current limitation associated with such approaches.

3.8.2. Materials and Methods

3.8.2.1. In-situ dataset

The in-situ dataset (DS-W, N = 1244, Mean Chl-a = 12.14 $mg.m^{-3}$) combines concomitant measurements of Chl-a and remote sensing reflectance (R_{rs}) collected between 1997 and 2016 in the frame of diverse worldwide distributed field campaigns in contrasted coastal areas (European coastal waters (Babin, Stramski, et al., 2003; Lubac et al., 2008; Lubac & Loisel, 2007; Neukermans et al., 2012), French Guiana (Vantrepotte et al., 2012, 2015), Eastern Viet Nam Sea (Loisel et al., 2017; Loisel, et al., 2014), South Shetland islands, the US coastal waters, The Sea of Japan (Werdell & Bailey, 2005), Beaufort Sea North Canada (Be et al., 2008), and Brazil (Guanabara Bay, Rio de Janeiro) (E. N. Oliveira et al., 2016) (**Figure 3.8**). This dataset covers a wide range of Chl-a concentrations with values ranging over 4 orders of magnitude (0.03 – 555.99 μgL^{-1}, **Table 3.5**) from oligotrophic waters (e.g., Mediterranean Sea, clear polar waters) to ultra-eutrophic environments such as Guanabara Bay, Rio de Janeiro (E. N. Oliveira et al., 2016). The DS-W was further randomly split into a development dataset (DS-D, N = 831, Mean Chl-a = 13.63 $mg.m^{-3}$) and a validation dataset (DS-V, N = 356, Mean Chl-a = 9.45 $mg.m^{-3}$), representing 70 and 30 % of DS-W, respectively, these three datasets follow a similar distribution (**Figure 3.9**). It is worth noting that the proportion of DS-D/DS-V partition was performed excluding the points corresponding to OWT5 (N= 57), for which no band-ratio-based model development has been performed (see section 3.8.3.2.1 and 3.8.3.3.1).

The Chl-a/SPM ratio has been calculated for the whole dataset for providing rough information on the relative importance of the Chl-a signal associated with the different water masses considered in this study. Considering that the SPM concentration was not available for all the in-situ samples in DS-W, SPM was estimated from the $R_{rs}(665)$ using the model by Han et al., (2016) which reliable performance has been illustrated from various former studies in contrasted coastal waters (Gensac et al., 2016; Zorrilla et al., 2019).

Table 3.5. *Description of the in-situ dataset of Chl-a ($mg.m^{-3}$) considered in the frame of this study: number of samples (N), minimum (Min), maximum (Max), mean (Mean), and standard deviation (StdDev).*

Region	Temporal coverage	N	Min	Max	Mean	StdDev	Reference
Vietnam	2011-2014	43	0.66	17.45	4.63	3.75	(Loisel et al., 2017; Loisel, et al., 2014)

French Guiana	2006-2016	108	0.41	22.65	6.40	5.45	(Vantrepotte et al., 2012, 2015)
Guanabara Bay (Brazil)	2012-2015	161	1.03	555.99	76.06	101.46	(E. N. Oliveira et al., 2016)
Beaufort Sea	2014	40	0.03	3.52	0.32	0.64	(Bélanger et al., 2008)
Sea of Japan	1999-2001	41	0.13	2.89	0.73	0.64	(Werdell & Bailey, 2005)
USA	1999-2007	498	0.08	28.46	1.71	2.79	(Werdell & Bailey, 2005)
South Shetland islands	2000-2007	82	0.03	4.01	0.86	0.81	(Werdell & Bailey, 2005)
Europe	1997-2012	271	0.05	33.33	3.69	5.42	(Babin, Stramski, et al., 2003; Lubac et al., 2008; Lubac & Loisel, 2007; Neukermans et al., 2012)
Total	1997-2016	1244	0.03	555.99	12.14	44.13	

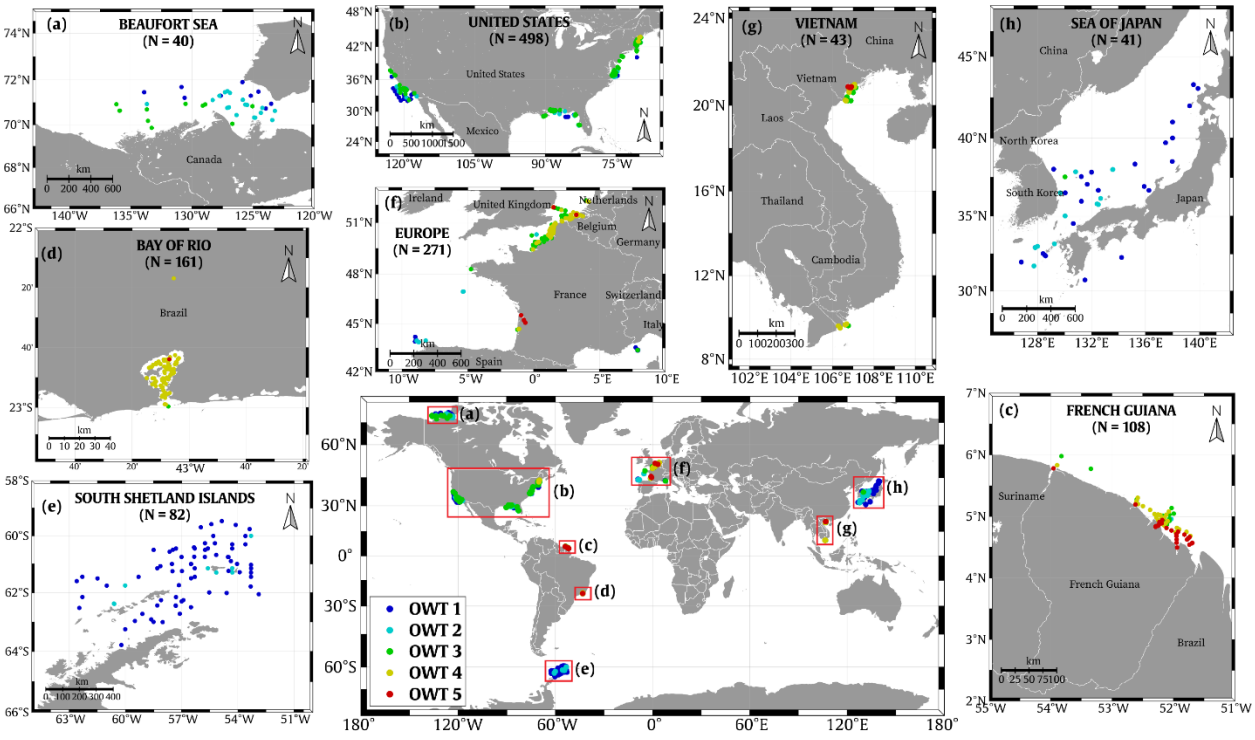

Figure 3.8. *Spatial distribution of in-situ Rrs-Chl-a measurements gathered within the DS-W dataset (N = 1244), colors indicate the optical water types to which each in-situ sample is associated with (see section 3.8.2.1).*

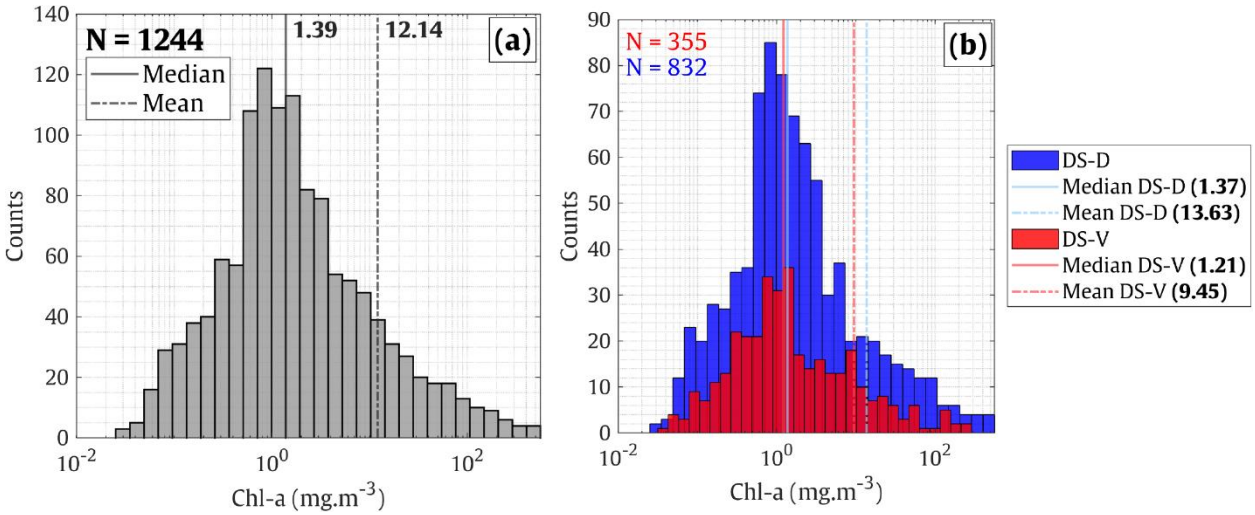

Figure 3.9. *Chl-a absolute frequency distribution for* ***a)*** *the whole in-situ dataset DS-W (N = 1244),* ***b)*** *the development dataset (DS-D, N = 832) and the validation dataset (DS-V, N = 355). The number of data points corresponding to OWT 5 has been excluded in the DS-D and DS-V.*

3.8.2.2. Satellite and Match-up Dataset

Data in DS-W have been acquired before the S2 and S3 time period (from June 2015 and February 2016 respectively). An external and independent in-situ dataset, which encompasses only Chl-a measurements, has been therefore considered in addition to DS-W for validation purposes (**Figure 3.10**). In practice, Chl-a samples collected along the French coast are in the frame of the SOMLIT (Coastal Environment Observation Service, https://www.somlit.fr/) and REPHY (Observation and Monitoring Network for Phytoplankton and Hydrology in coastal waters, https://www.seanoe.org/data/00361/47248/) French national survey programs. These long-lasting in-situ datasets (e.g., continuous monthly data since 1997 for SOMLIT) present the advantage of being acquired following a standardized protocol.

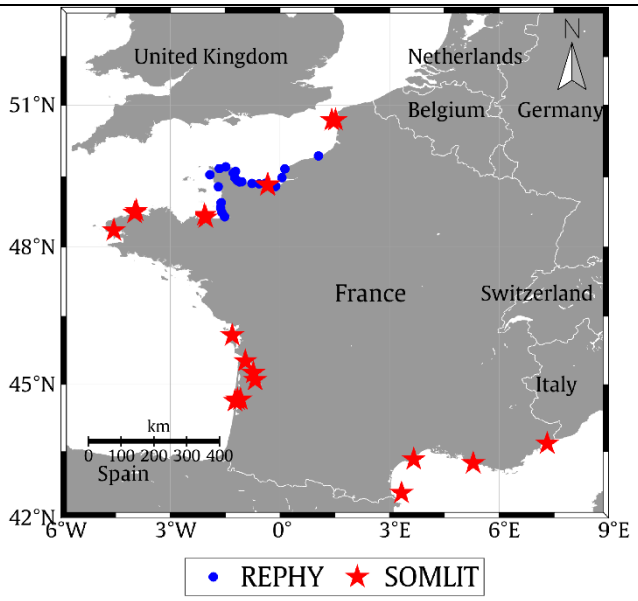

Figure 3.10. *Distribution of the REPHY and SOMLIT stations considered in the matchup dataset DS-M.*

In practice, Satellite Sentinel2-MSI A/B (60 m resolution) and Sentinel3-OLCI A/B (300 m resolution) R_{rs} data have been extracted for both SOMLIT and REPHY Chl-a samples over the time period 7/09/2015 – 19/03/2021 and 24/05/2016 – 07/04/2021 for MSI and OLCI respectively). Specifically, top-of-atmosphere Level 1 products have been processed considering three atmospheric correction schemes including POLYMER version 4.13 (Steinmetz et al., 2011), C2RCC (Brockmann et al., 2016), and ACOLITE (Vanhellemont, 2019). The matchup extraction was performed considering a 3×3 window around each in-situ sampling point. Several quality control criteria have been then applied (Werdell et al., 2009) considering: (1) the number of valid pixels (at least 5 valid pixels among the 9 pixels extracted), (2) the spatial homogeneity of the matchup subsets assessed from the variation coefficient within the subset window (CV = standard deviation/mean × 100 < 30%) and (3) the time difference between in-situ and satellite measurements (lower than 3 hours).

After the application of all these criteria, the final matchup dataset (DS-M) is then composed of a maximal number of 194 matchup points for MSI and 362 for OLCI with Chl-a concentrations ranging between 0.19 and 34.12 $mg.m^{-3}$ (mean = 2.48 $mg.m^{-3}$, standard deviation = 3.79 $mg.m^{-3}$) and 0.05 and 52.93 $mg.m^{-3}$ (mean = 2.52 $mg.m^{-3}$, standard deviation = 3.7 $mg.m^{-3}$), respectively. The Chl-a statistics of the DS-M is further illustrated in **Figure 3.11**.

In addition to the Sentinel-2 and Sentinel-3 matchup dataset, the global MERIS GlobCoast dataset (monthly 1-km spatial resolution) (Loisel et al., 2017; Loisel et al., 2014) was further considered for illustrating and discussing the potential applicability of the models selected with the frame of this study with a global scale perspective.

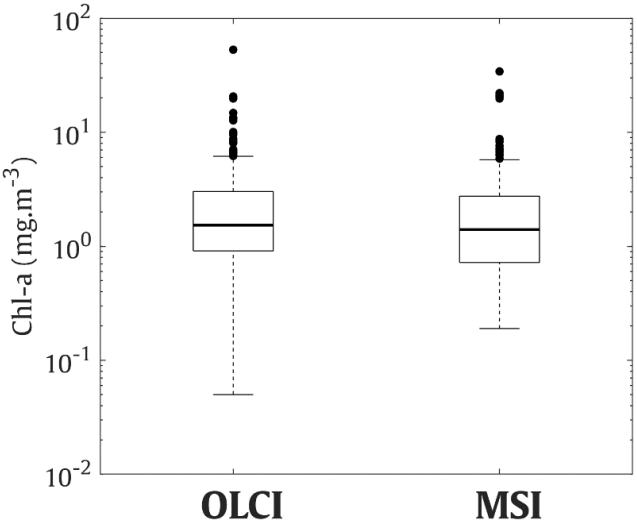

Figure 3.11. *Box plot showing Chl-a range of the final matchup dataset (DS-M) regarding OLCI and MSI sensors.*

3.8.2.3. Optical classification

Optical Water Types (OWT) were defined using the procedure defined in Mélin & Vantrepotte, 2015) applied to the DS-W R_{rs} dataset. In practice, normalized R_{rs} data were considered to cluster the reflectance data focusing on the shape of the spectra. The normalization was applied to multispectral R_{rs} data considering 6 wavelengths in the visible part of the spectrum (412, 443, 490, 510, 560, and 665 nm) centered on the OLCI bands. The normalized R_{rs} was determined by the ratio between its original value and the surface below the spectral shape as follows:

$$R_{rs}^{norm} = \frac{R_{rs}(\lambda)}{\int_{\lambda_1}^{\lambda_2} R_{rs}(\lambda)d\lambda} \qquad 3.27$$

where R_{rs}^{norm} represents the normalized remote sensing reflectance.

An unsupervised classification was then applied to the R_{rs}^{norm}dataset using Ward's clustering method (Ward, 1963) which presents the advantage of being less sensitive to outliers compared to other approaches (Vantrepotte et al., 2012). Then, satellite pixel OWT labelling and OWT

membership calculation have been performed using the procedure defined in Mélin & Vantrepotte, (2015) as described in section 2.8.1.

This classification led to the definition of 5 optical water types showing different R_{rs} spectral shapes (**Figure 3.12.a**). OWTs 1 and 2 (N = 269 and 185, respectively) are associated with clear oligotrophic to mesotrophic waters (mean Chl-a = 0.38 ± 0.36 and 0.96 ± 0.74 $mg.m^{-3}$, respectively) with R_{rs} spectra typically peaking in the blue part of the visible spectrum. OWT 3 samples are corresponding to mesotrophic waters characterized by high R_{rs} in the green part of the visible spectrum with a R_{rs} plateau ranging between 490 and 560 nm (N= 426, mean Chl-a = 2.33 ± 3.09 $mg.m^{-3}$). The Chl-a/SPM ratio for these 3 OWTs is increasing from the OWT 1 (2.25 × 10^{-3}) to the OWT 3 (4.04 × 10^{-3}).

OWTs 4 and 5 are associated with highly turbid/eutrophic coastal waters. The OWT 4 corresponds to high Chl-a waters with a R_{rs} peak at 560 nm (N = 307, Mean Chl-a = 43.72 ± 80.89 $mg.m^{-3}$) and shows the maximal Chl-a/SPM ratio among the different OWTs (Chl-a/SPM = 13.10^{-3}) related to ultra-eutrophic for these samples. Conversely, OWT 5 samples (N = 57) are more likely associated with turbid waters showing a higher proportion of non-algal particles (sediments and detritus) when compared to OWT 4 as emphasized from the lower average Chl-a (7.15 ± 10.46 $mg.m^{-3}$) and the lowest Chl-a/SPM ratio (1.43 × 10^{-3}) found for these samples (**Figure 3.12.c**).

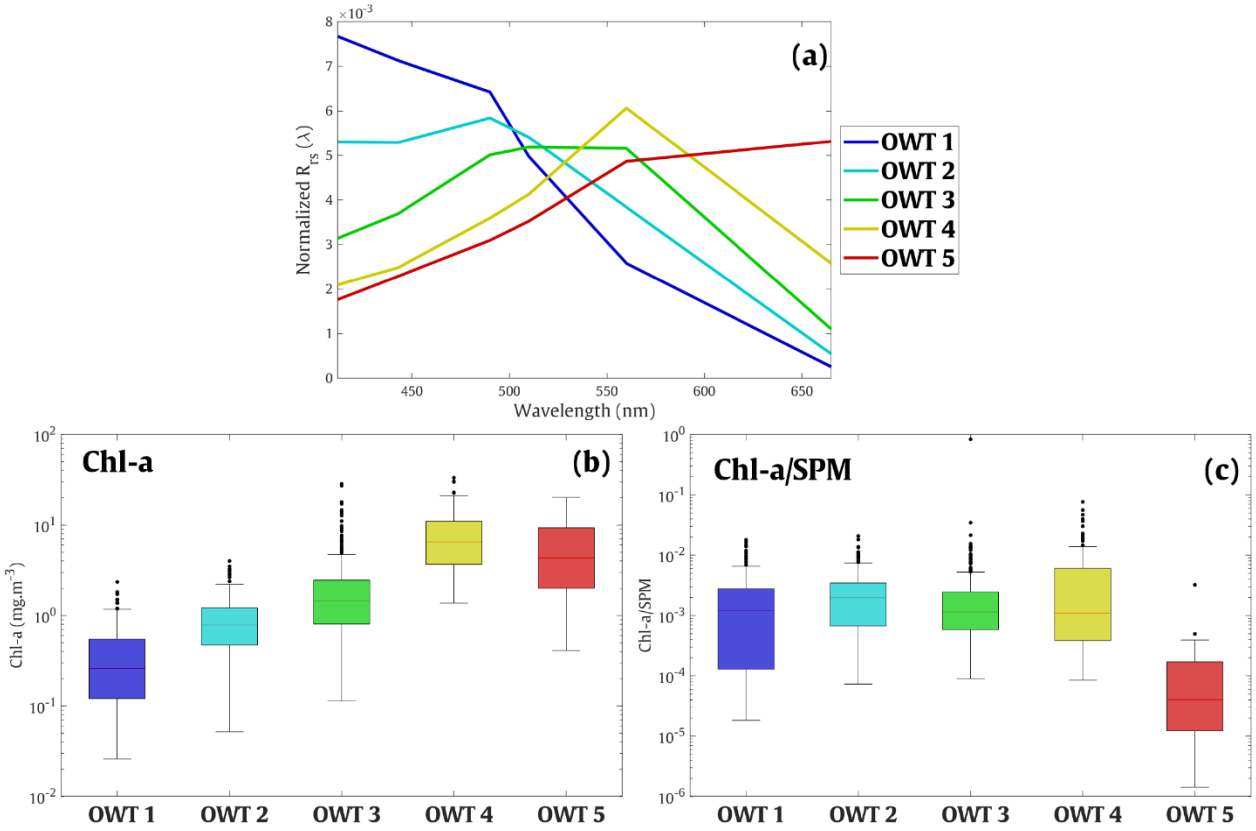

Figure 3.12. a) *Average R_{rs}^{norm} spectra corresponding to the optical water types defined from the DS-W dataset (N = 1244), boxplots illustrating the distribution of Chl-a* ***b)*** *and Chl-a/SPM ratio* ***c)*** *associated with each optical class. While all the samples considered in DS-W are available for all the visible wavelengths corresponding to Sentinel2-MSI and Sentinel3-OLCI bands, it is worth noticing that the spectral coverage of the R_{rs} in-situ dataset in the NIR part of the spectrum is unequal. For most of the samples associated with OWTs 1, 2, and 3, little information was available in the NIR (12.8% for OWTs 1, 2, and 3, respectively) while this information was present for most (98 %) of the samples associated with OWTs 4 and 5, for which Red and NIR algorithms are devoted (see section 3.8.2.4).*

3.8.2.4. Chl-a candidate inversion algorithms

A variety of empirical band-ratio-based bio-optical algorithms have been developed for estimating Chl-a concentration from satellite ocean remote sensing observation. Here a selection of "standard" models based on different input R_{rs} data and formulations have been performed among the number of different methods available considering models which performances have already been shown to be relevant to the diverse types of coastal environments taking into account results provided from recent extensive inter-comparison exercises (Neil et al., 2019). In

practice, historical models considered here can be split into two categories: Blue/Green (Red) ratio-based models more likely adapted to clear to moderately turbid waters (Gohin et al., 2002; O'Reilly & Werdell, 2019) and Red/NIR ratio-based methods specifically developed for turbid environments (Gilerson et al., 2010; Gons et al., 2008; Gurlin et al., 2011; Mishra & Mishra, 2012).

It is important to mention that all the considered models, except the model OC5 proposed by Gohin et al., (2002), have been considered in their original and tuned versions fitting the different formulations to the DS-D data corresponding to the optical water types they have been designed for (see sections 3.8.3.2 and 3.8.3.3). These coefficients are here provided for each original model.

3.8.2.4.1. Blue/Green(Red) band-ratio-based models

Considering the radiometric resolution of Sentinel2-MSI and Sentinel3-OLCI sensors two models have been selected for clear to medium turbid waters. These models correspond to the empirical NASA OC-family algorithms developed from the NOMAD dataset extensively used to produce standard Chl-a products from satellite observation.

(1) OC6

This recent algorithm OC6 (O'Reilly & Werdell, 2019) corresponds to an adaptation of the OC4 model (O'Reilly et al., 1998) which includes additional bands at 412 and 665 nm to extend the applicability of this approach, typically applied to open ocean waters, towards coastal waters. This model can be described as follow:

$$\text{Chl-a}=10^{a_0+a_1\times R+a_2\times R^2+a_3\times R^3+a_4\times R^4} \quad 3.28$$

where

$$R=\log_{10}\left\{\frac{\max\left[R_{rs}(412),R_{rs}(443),R_{rs}(490),R_{rs}(510)\right]}{\text{mean}[R_{rs}(560),R_{rs}(665)]}\right\} \quad 3.29$$

The original coefficients for this model are $a_0 = 0.2424$, $a_1 = -2.2146$, $a_2 = 1.5193$, $a_3 = -0.7702$, $a_4 = -0.4291$

(2) OC3

The main equation of the OC3 model to compute Chl-a remains the same as in Equation 3.28. However, this algorithm uses a different Blue/Green ratio input that is established by 3 spectral bands in the visible part of the spectrum (O'Reilly & Werdell, 2019). Such ratio can be expressed as below:

$$R=\log_{10}\left\{\frac{\max[R_{rs}(443),R_{rs}(490)]}{R_{rs}(560)]}\right\} \quad 3.30$$

and coefficients $a_0 = 0.41712$, $a_1 = -2.56402$, $a_2 = 1.22219$, $a_3 = 1.02751$, $a_4 = -1.56804$.

(3) OC5-Gohin

The five channels model by Gohin et al., (2002) was developed in order to correct the overestimation of the Chl-a estimated from the OC4 model in coastal waters presenting moderate turbidity levels and high CDOM loads. Based on sensor-specific LUTs empirically developed from an extensive in-situ dataset. It has been here considered using the LUTs defined for MERIS.

3.8.2.4.2. Red-NIR algorithms

(1) Gurlin11

The empirical model developed by Gurlin et al., (2011) consists of a second-order polynomial function based on the $R_{rs}(709)/R_{rs}(665)$ band ratio:

$$\text{Chl-a} = a\times\left[\frac{R_{rs}(709)}{R_{rs}(665)}\right]^2 + b\times\left[\frac{R_{rs}(709)}{R_{rs}(665)}\right] + c \quad 3.31$$

where a = 25.28; b = 14.85; c = −15.18

(2) Gilerson10

The model proposed for MERIS by Gilerson et al., (2010) is based on a linear relationship between in-situ Chl-a and the NIR/Red ratio of MERIS such as:

$$\text{Chl-a}=a\times\left[\frac{R_{rs}(709)}{R_{rs}(665)}\right] + b \quad 3.32$$

where a = 35.745; b = −19.295; c = 1.124

(3) Gons08

The Chl-a inversion algorithm developed by Gons et al., (2002) for turbid environments is a semi-analytical approach considering IOPs information along with the Red-NIR reflectance ratio and the reflectance at 779 nm. The version proposed in Gons et al., (2008) is considered here as is expressed as follows:

$$\text{Chl-a} = \frac{\left\{\left[\frac{R_{rs}(709)}{R_{rs}(665)}\right] \times \left[a_w(709)+b_b-a_w(665)-b_b^p\right]\right\}}{a^*_{phy}(665)} \quad 3.33$$

where $a_w(709)$ and $a_w(665)$, the water absorption coefficients at 709 nm and 665 nm were estimated as 0.7 m^{-1} and 0.4m^{-1}, respectively (Pope & Fry, 1997). $a^*_{phy}(665)$ is the chlorophyll-specific absorption that was defined as 0.016 $m^2.mg^{-1}$. The calculation of the back-scattering coefficient b_b is estimated from the water leaving reflectance at 779 nm as:

$$b_b = \frac{1.61 \times R_w(779)}{0.082-0.6R_w(779)} \quad 3.34$$

where R_w (779) is the water-leaving reflectance ($R_w = R_{rs} \times pi$)

Mishra12

The model proposed by Mishra & Mishra, (2012) is an empirical model developed for application in estuarine and coastal waters. It is based on the calculation of the Normalized Difference Chlorophyll Index (NDCI) as an input variable to derive Chl-a:

$$\text{NDCI} = \frac{R_{rs}(709)-R_{rs}(665)}{R_{rs}(709)+R_{rs}(665)} \quad 3.35$$

$$\text{Chl-a} = a + b \times \text{NDCI} + c \times \text{NDCI}^2 \quad 3.36$$

where a = 42.197; b = 236.5; c = 314.97

The performance of the considered Chl-a models was evaluated considering a set of statistical metrics described in section 2.10.

3.8.3. Results

3.8.3.1. Performances of historical models

The performance of the historical models described in section 3.8.2.4 in their original version was first illustrated considering the whole dataset (DS-W, **Figure 3.13** and **Figure 3.14**)

gathering a maximum of 1244 values considering the R_{rs} input wavelengths for the OC3, OC5, and OC6 models (i.e. R_{rs} at 412, 443, 490, 510, 560, 665 nm), and 470 values for the one used for in Gurlin11, Gilerson10, Mishra12; Gons08 (i.e. R_{rs} at 665, 709, 779 nm).

As already documented, models based on the use of the band ratios in the visible part of the spectrum (OC6, OC3, and OC5, **Figure 3.13.a-c**) provide reliable Chl-a estimates for clear to medium turbid waters (OWT 1, 2, 3) with R^2 values of 0.59, 0.61, and 0.57, respectively, **Figure 3.14**). The models however show limitations for estimating Chl-a in the most turbid environments (OWT 4 and 5) as illustrated by the high scattering found in **Figure 3.13** as well as by the low R^2 (< 0.28) found for the OWT 4 samples when applying these models (**Figure 3.14**). The OC-5 model which has been designed for moderately coastal waters providing a correction of the overestimation generally provided from the OC4 algorithm also shows clear limitations for the OWT 4 (**Figure 3.13**) in agreement with the previous studies (Gohin et al., 2019; Loisel et al., 2017). Loisel et al., (2017) for instance, documented an exponential increase in the uncertainties related to OC5-derived Chl-a with increasing turbidity (i.e. SPM concentration > 60 $mg.L^{-1}$). As expected, the OC3, OC4 and OC5 models (not based on the NIR band) are totally saturated over the whole range of Chl-a for the OWT 5 samples generating quasi-invariant Chl-a estimates.

Red-NIR-based approaches (Gurlin11, Gilerson10, Mishra12; Gons08, **Figure 3.13.d-g**) are conversely showing poor performances for OWTs 1, 2, and 3 samples with R^2 remaining below 0.1 (see **Figure 3.14**) for these waters whatever the model considered. These models have however not been developed for these waters with a relatively low level of turbidity. A general better performance is however found for Gilerson10, Gurlin11, Mishra12, and Gons08 models for the OWT 4 samples. This confirms the reliable applicability of the latter methods for estimating Chl-a over highly turbid and high Chl-a waters (Neil et al., 2019). These models, in their original formulations, still however show limitations, more likely related to the data range they have been developed. This is for instance emphasized by the saturation pattern found for the lower-end Chl-a values for Mishra12 (**Figure 3.13.f**) already pointed out by previous studies (Mishra & Mishra, 2012). The model of Gons08 while providing relatively good Chl-a estimates for high Chl-a values (>10 $g.L^{-1}$) tends to fail for low Chl-a for the OWT 4 samples, highly underestimating Chl-a value (**Figure 3.13.g**) and further generates negative Chl-a (N = 287 vs N = 299, 298 and 300 for Gurlin11, Gilerson10, and Mishra12, respectively) in agreement with former studies (Gons et al., 2008; Lavigne et al., 2021).

None of the Red-NIR models evaluated are able to produce reliable Chl-a estimates for the ultra-turbid waters represented by the OWT 5 samples, due to the very low impact of the Chl-a on the reflectance signal for these waters (Lavigne et al., 2021). A clear saturation is found for Gilerson10, Gurlin11, and Mishra12 (**Figure 3.13.d-f**) and low R^2 values obtained for these models (**Figure 3.14**), emphasizing the limitation of these Red-NIR-based methods towards ultra-turbid waters. The model by Gons et al., (2008) is globally able to reproduce the Chl-a gradient found in OWT 5 data although an overall high uncertainty level as illustrated by the scattering in **Figure 3.13.d** for these samples. As previously mentioned for the OWT 4 this model tends to produce negative Chl-a values as illustrated by the lower number of estimated Chl-a for Gons08 model when compared to Gurlin11, Gilerson10, and Mishra12 algorithms for OWT 5 (N = 35 and 57, 57, and 57, respectively).

These results are confirming the relative limitations of the different band ratio formulations usually considered for estimating Chl-a over contrasted coastal environments. Considering the performance of the considered models in their original formulations, an optimization of historical models as well a development of new formulation was further performed sub-setting the in-situ dataset into two groups: 1) one gathering oligotrophic to mesotrophic waters (OWTs 1, 2, 3) for which visible wavelengths have been considered, 2) one gathering highly turbid/high Chl-a samples corresponding to the OWT 4.

Further considering that all the band-ratio-based evaluated methods were failing for OWT 5 samples, no adaptation of these existing methods was performed for the corresponding samples.

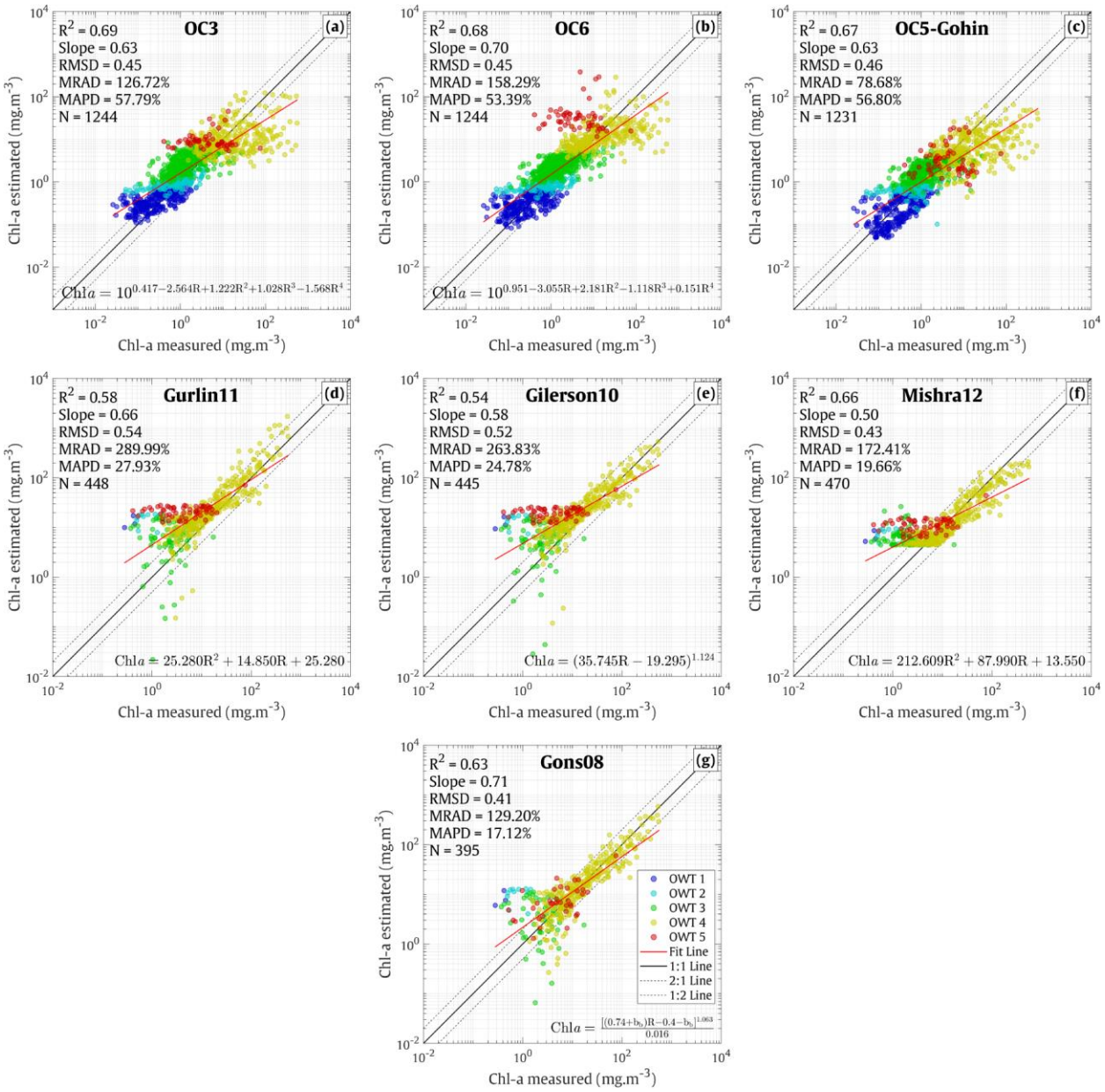

Figure 3.13. *Scatterplot (log-log scale) of the in-situ Chl-a (DS-W) vs the Chl-a estimated from the different historical band-ratio-based model considered in their original formulations (see section 3.8.2.4).*

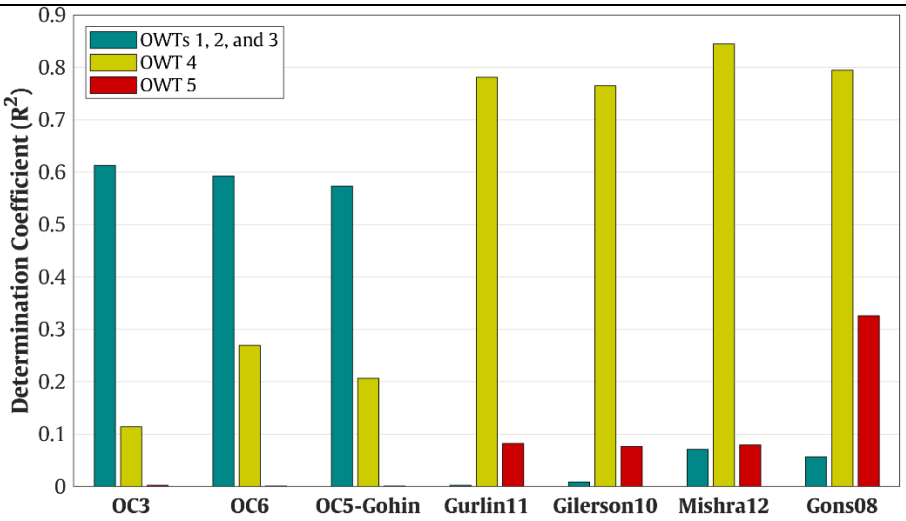

Figure 3.14. *Determination coefficient (R^2) of the linear relationships between the in-situ Chla and the estimated Chl-a corresponding to each OWT subset in DS-W (**Figure 3.13**) for the different band ratios based historical models considered in the frame of this study in their original versions (section 3.8.2.4).*

3.8.3.2. Chl-a estimates clear to medium turbid waters

3.8.3.2.1. Development of a new algorithm for OWTs 1, 2, and 3

Considering the previous results, OC3 and OC6 models (OC3-Tuned and OC6-Tuned) which are the most adapted for clear to medium turbid waters (OWTs 1, 2, and 3) have been optimized on the DS-D dataset (N = 617, Table 2) using the QR decomposition method where the design matrix of the regression problem into the orthogonal matrix (Q) and a triangular matrix (R). This optimization approach is available as "fitlm" function in Matlab.

Table 3.6. Coefficients of the OC3 and OC6 models adapted to the DS-D dataset for OWTs 1,2,3 (N = 617).

Models	Tuned Coefficients	Equations	R^2
OC3	$a_0 = 0.289$; $a_1 = -2.997$; $a_2 = 1.956$; $a_3 = 2.189$; $a_4 = -3.773$	3.28, 3.29	0.63
OC6	$a_0 = 0.931$; $a_1 = -2.710$; $a_2 = -2.715$; $a_3 = 8.873$; $a_4 = -5.340$	3.28, 3.30	0.60

In addition to these adapted historical formulations, an alternative model for oligotrophic to mesotrophic waters was developed by exploiting the DS-D dataset. This model named MUBR is based on a combination of multiple band ratios which have been shown to provide the best performance for estimating Chl-a from DS-D (**Figure 3.15**). It is worth noticing that the $R_{rs}(412)$ was not considered in the development of the MUBR model considering that this wavelength is not available for MSI and that this band is susceptible to be affected by large uncertainties

related to the atmospheric correction processes (Mograne et al., 2019). The MUBR algorithm is in practice based on the combination of three band ratios using four visible bands from the blue to the red available for both Sentinel2-MSI and Sentinel3-OLCI. This formulation is expressed as follows:

$$Chl_{MuBR}=10^{a_0+a_1R1+a_2R2+a_3R3} \quad 3.37$$

where

$$R1=\log_{10}\left[\frac{R_{rs}(490)}{R_{rs}(443)}\right] \quad 3.38$$

$$R2=\log_{10}\left[\frac{R_{rs}(560)}{R_{rs}(490)}\right] \quad 3.39$$

$$R3=\log_{10}\left[\frac{R_{rs}(665)}{R_{rs}(560)}\right] \quad 3.40$$

and where $a_0 = 0.665$, $a_1 = -3.506$, $a_2 = 3.590$, $a_3 = -0.019$

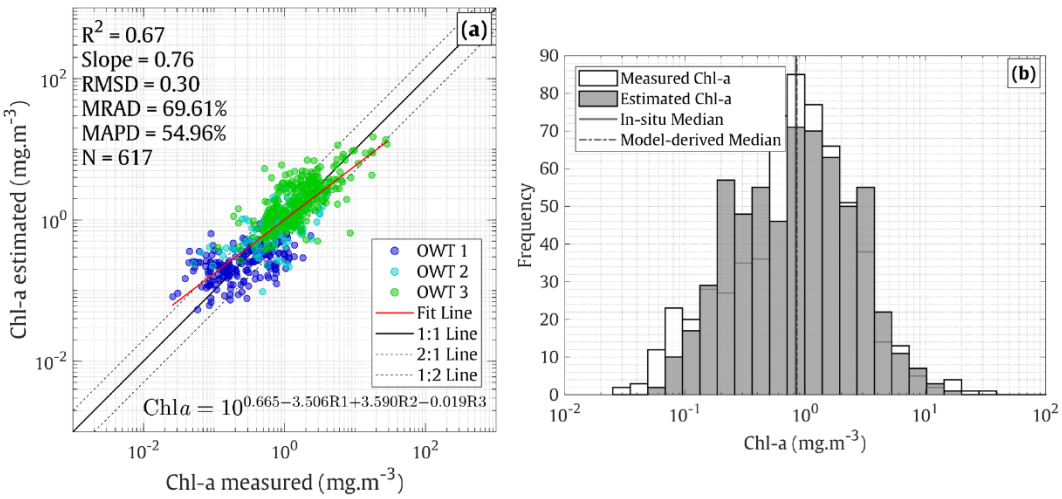

Figure 3.15. a) *Relationship between the in-situ vs estimated Chl-a from the MUBR model developed on the samples corresponding to OWTs 1, 2, 3 in the DS-D dataset (N = 617).* ***b)*** *Histograms of distribution of the Chl-a values corresponding to the OWTs 1, 2, and 3 samples in DS-D and for the Chl-a values estimated from the MUBR model.*

3.8.3.2.2. Model selection for clear to medium turbid waters

The intercomparison on the performance of the Chl-a estimates on clear to medium turbid waters (OWTs 1, 2, and 3) was performed on the independent validation dataset DS-V (N = 263)

considering in addition to MUBR, classical clear waters band ratio models adapted on DS-D (OC3-Tuned and OC6-Tuned) as well as considering the model OC5 in its original version. Results in **Figure 3.16.a-c** show that the MUBR model provides the best performance considering our validation dataset when compared to OC3-Tuned and OC6-Tuned models with an overall lower dispersion (e.g., MRAD = 66.72% vs 97.12 % and 86.24 % respectively) as well as with a general better estimation of Chl-a value over the whole range of Chl-a for the considered subset (e.g., Slope = 0.76 vs 0.69 and 0.64, respectively). We observed a similar performance of the OC5 original model on this such clear to medium turbid waters validation dataset (**Figure 3.16.c**) to that obtained for OC3 (e.g., area of 2.109. The better performance for the MUBR model is further underlined in the radar plot provided in **Figure 3.16.d** where the area found for MUBR, representing a summary of the statistical parameters considered, is lower (1.24) than that for the other three methods considering both their original and adapted versions (OC3-Tuned: 2.45 and 2.09, respectively, OC6-Tuned: 2.45 and 2.05, respectively). The lower performance of OC3 and OC6 methods on the DS-V subset for OWTs 1, 2, and 3 can be explained by an overestimation of the very low Chl-a values as well as by a saturation of the Chl-a estimated for the highest Chl-a values (**Figure 3.16**).

Our results, therefore, tend to indicate that the model MUBR represents a valuable alternative for estimating Chl-a focusing on the clear to moderate turbid waters gathered using the dataset considered in the frame of the present study (OWTs 1, 2, 3 data).

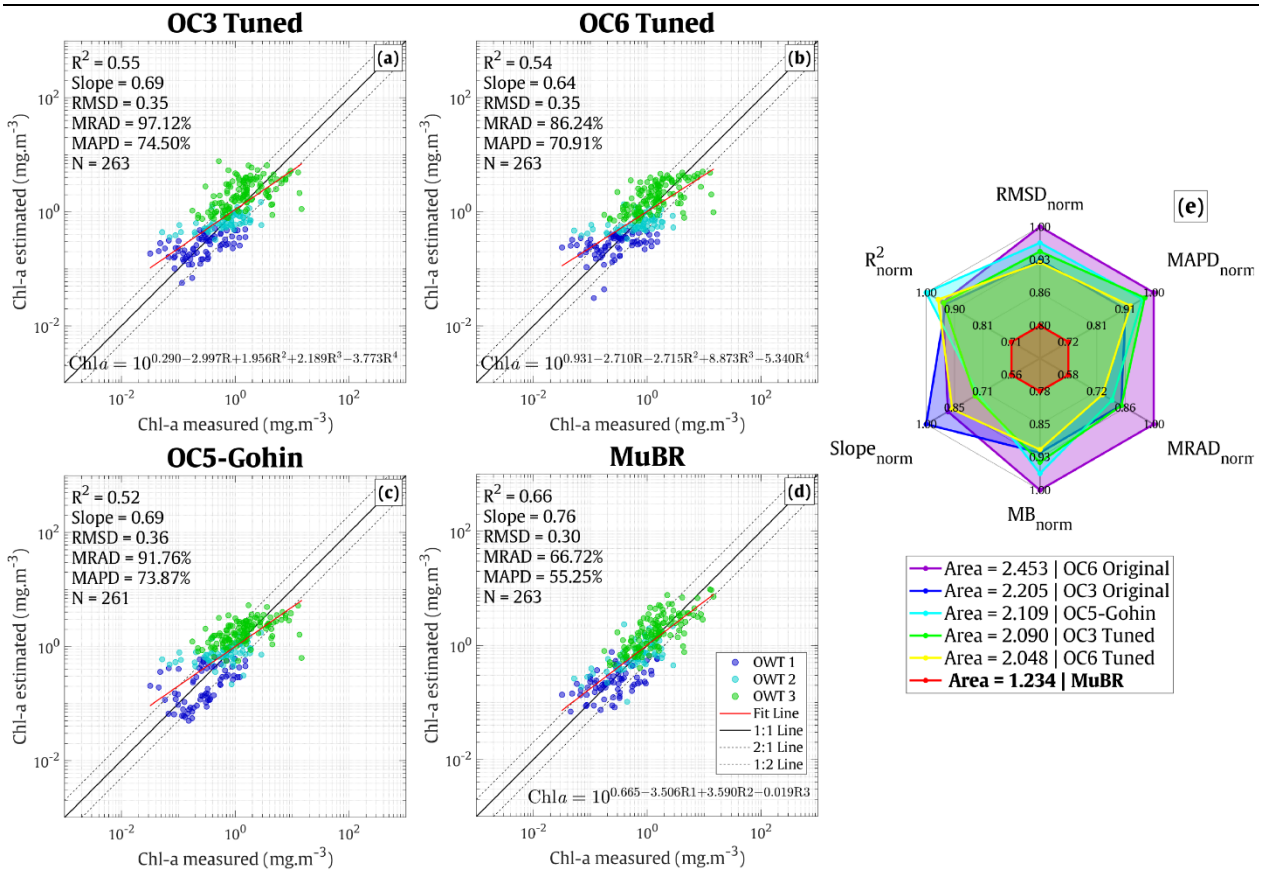

Figure 3.16. *Intercomparison of the performance of the Chl-a inversion models for the OWTs 1, 2, and 3 samples in the in-situ validation dataset DS-V (N = 263). Relationships between in-situ vs estimated Chl-a applying* ***a)***, ***b)***, *and* ***c)*** *the OC3, OC6, and OC5-Gohin models adapted to the development dataset DV-D and* ***d)*** *for the MUBR model* ***e)*** *summary of the performance of the Chl-a inversion models, the lowest area of the polygon associated with each model represented in the radar plot corresponds to the best model. Note that the statistics for the original versions of OC3 and OC6 are also shown for completeness.*

3.8.3.3. Chl-a estimation in turbid/high Chl-a waters (OWT 4)

3.8.3.3.1. Development of a new algorithm

Considering the results of the previous section, a focus was performed to define the model the most adapted for estimating Chl-a over highly turbid/high Chl-a waters corresponding to OWT 4 samples only considering that adapting the models considered was useless for the OWT 5 samples (not shown). In practice, the Red-NIR-based models by Gurlin11, Gilerson10, Mishra12, and Gons08 were adapted to our dataset defining new coefficients for each model refitting the corresponding formulation on the DS-D samples (not shown, Table 3).

Table 3.7. *The tuned coefficients for the Gurlin10, Gilerson11, Gons08, and Mishra12 models adapted to the DS-D dataset for OWT 4 (N= 210).*

Models	Tuned Coefficients	Equations	R^2
Gurlin11	a = 0.83; b = −11.398; c = 24.923	3.31	0.80
Gilerson10	a = 13.328; b = −6.373; c = 1.393	3.32	0.80
Gons08	$a^*_{phy}(665)$ = 0.0139; p = 1.0752	3.33, 3.34	0.79
Mishra12	a = 13.801; b = 111.673; c = 354.095	3.35, 3.36	0.82

In addition, a new formulation (referred as NDCI-based model) was developed for OWT 4 samples (**Figure 3.17**) considering the saturation pattern towards low Chl-a values already reported for models using the NDCI parameter as an input value (Bi et al., 2022; Mishra & Mishra, 2012; Neil et al., 2019) and is expressed as follows:

$$\text{Chl-a}=10^{a_0+a_1\text{NDCI}+a_2\text{NDCI}^2} \quad 3.41$$

where a_0 = 1.179, a_1 = 2.689, a_2 = −1.083

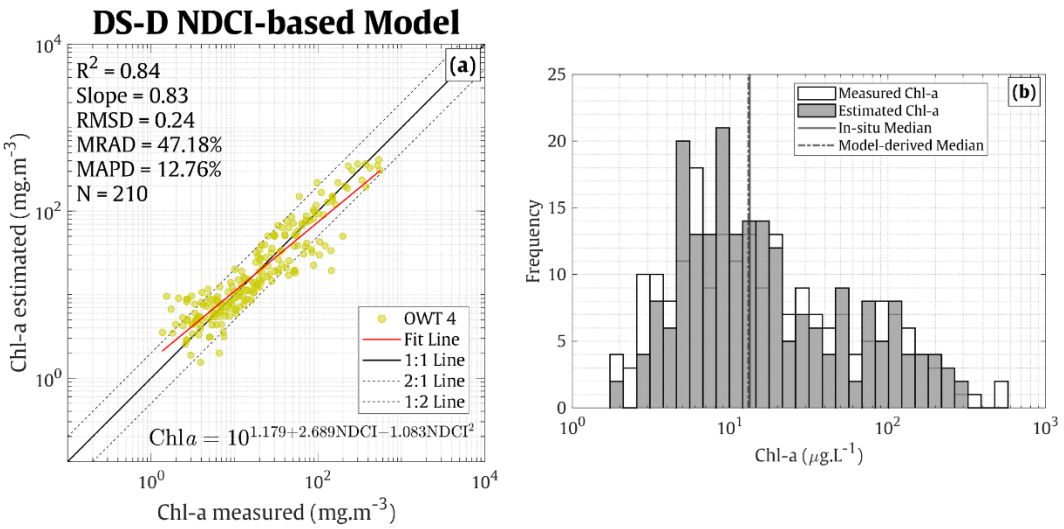

Figure 3.17. a) *Relationship between the in-situ vs estimated Chl-a from the NDCI-based model developed on the OWT 4 samples in the DS-D dataset (N = 210).* ***b)*** *Histograms of distribution of the OWT 4 Chl-a in DS-D and for the Chl-a values estimated from the NDCI-based model.*

3.8.3.3.2. Model selection for highly turbid/high Chl-a waters

The relative performances of these Red-NIR models were then evaluated on the DS-V dataset for OWT 4 (N_{max} = 90, **Figure 3.18**). Although very similar statistics are found for all the tuned versions of the models evaluated, the new NDCI-based model presents the best performances (area = 0.472, **Figure 3.18.f**). As previously pointed out from the DS-W dataset

(**Figure 3.13.g**) Gons08 tends to generate an underestimation of the lower-end Chl-a concentration (i.e. Chl-a < 5 $mg.m^{-3}$) in OWT 4 potentially conducting to the generation of negative values (**Figure 3.18.c**, N = 86 for the original and tuned versions vs N = 90 for the other models). It is worth mentioning that the tuned version of Gons08 does not provide better estimates than the original one probably related to the difference in the Chl-a range presented in our development dataset (1.37 - 556 $mg.m^{-3}$) and the one in Gons et al., (2008) (0.37 - 131 $mg.m^{-3}$) as the adapted coefficients and the performances corresponding to different inversion models in the DS-V might vary according to Chl-a level. The tuned versions of Gilerson10 and Gurlin11 (**Figure 3.18.a-b**) globally show satisfactory performances (area = 0.602 and 0.577, respectively), confirming the effectiveness of these models to derive Chl-a in turbid environments (Neil et al., 2019). Interestingly the tuned version of Mirshra12 (**Figure 3.18.d**) although exhibiting a generally reliable performance, still shows a saturation pattern towards the smallest Chl-a for the OWT 4 samples (< 5 $mg.m^{-3}$). Such saturation pattern is not found when applying the modification of this model corresponding to the NDCI-based formulation proposed here (**Figure 3.18.e**).

This intercomparison exercise thus suggests that the NDCI-based model represents the most adapted model for estimating Chl-a over highly turbid/high Chl-a (OWT 4) waters gathered in our in-situ dataset.

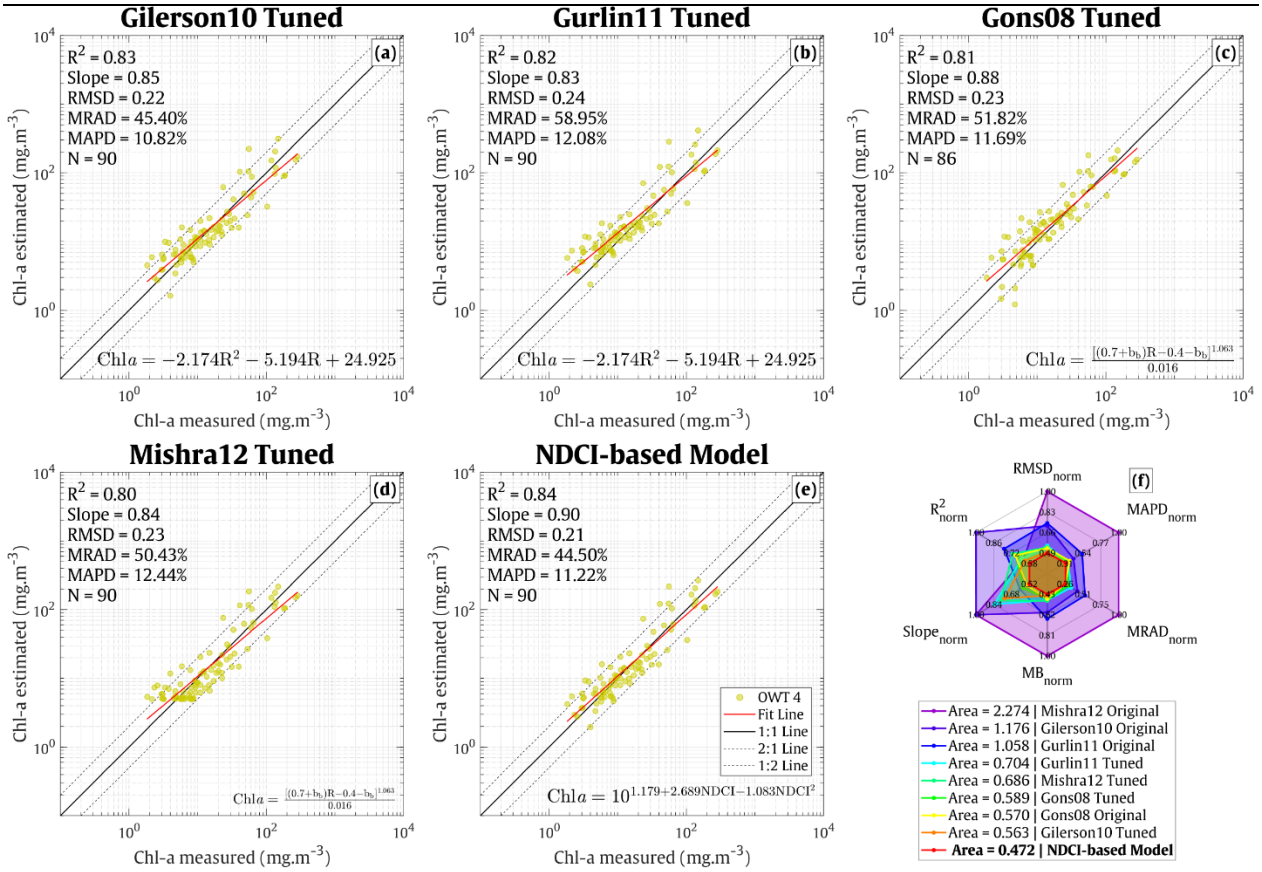

Figure 3.18. *Intercomparison of the performance of the adapted versions of Red-NIR model on highly turbid/high Chl-a validation data corresponding to the OWT 4 samples in DS-V (N = 90). Scatterplots of the in-situ Chl-a vs the Chl-a estimated from* ***a)*** *Gilerson10,* ***b)*** *Gurlin11,* ***c)*** *Gons08,* ***d)*** *Mishra12, and* ***e)*** *NDCI-based models. A summary of the performance of the considered model for estimating Chl-a is provided in the radar plot* ***f)*** *where the performance of both original and tuned versions of these 4 models is also provided for completeness.*

3.8.3.4. Class-based combination of multiple Chl-a models for OWT 1, 2, 3, and 4

The previous algorithms evaluation exercises clearly confirm the inability for a unique simple band ratio to deliver reliable estimates over the whole range of Chl-a values found in coastal waters (Lavigne et al., 2021; Loisel et al., 2017; Neil et al., 2019). We further illustrate that the use of two band ratio formulations considering a first model combining band ratios in the visible domain for clear to medium turbid waters (MUBR for OWTs 1, 2, 3) and a Red-NIR model (NDCI-based) for highly turbid/high Chla waters (OWT 4).

Different methods can be used for producing Chl-a maps by applying different bio-optical algorithms on a pixel-per-pixel basis. Diverse former studies have for instance illustrated the

interest of using a weighted average to provide smooth Chl-a gradients in transition areas between different inversion algorithms. Such weighting approaches were diversely based on the use of Chl-a values (Smith et al., 2018) or on the exploitation of the optical characteristics of the water masses provided from optical water types defined from the reflectance spectra (Hieronymi et al., 2017; Mélin et al., 2011; Neil et al., 2019).

Such optical-based weighted approach was considered in the frame of this study using weights based on the belonging probability of each sampling point (in-situ sample or satellite pixel) to each optical group of optical water types to which a specific Chl-a model should be applied (i.e., MUBR for OWTs 1, 2, 3, and Mishra12-Tuned for OWT 4). The combination of algorithms from 2 groups of OWTs was performed following the equation (Vantrepotte et al., 2012):

$$\text{Chl-a}=(p_1^*+p_2^*+p_3^*) \times \text{Chl-a}_{123}+ p_4^* \times \text{Chl-a}_4 \qquad 3.42$$

where:

p_1^*, p_2^*, p_3^*, and p_4^* correspond to the normalized probability for the OWTs 1, 2, 3, and 4 respectively (Mélin & Vantrepotte, 2015).

Chl-a_{123} is the Chl-a estimated from MuBR designed for OWTs 1, 2, and 3. Chl_4 is the Chl-a estimated by using Red/NIR models designed for OWT 4. The tuned coefficients for the calculation of Chl-a_{123} and Chl-a_4 (Equations 3.37 and 3.41).

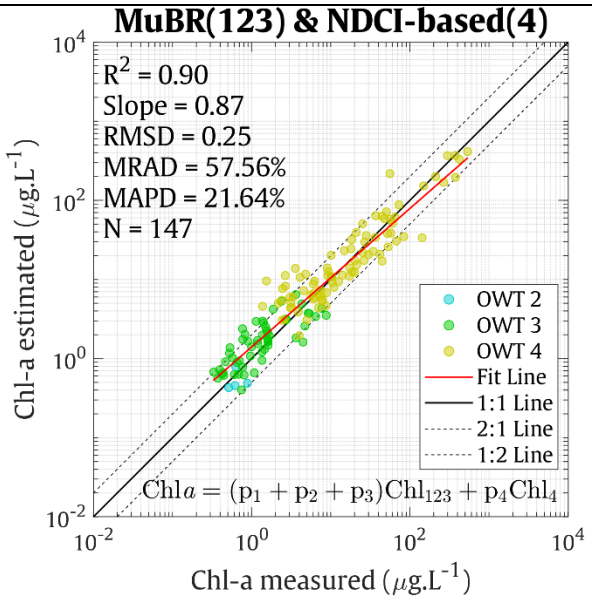

Figure 3.19. *Performance of the combination of the DS-V in-situ and estimated Chl-a combining the MUBR model for clear/moderate turbid waters (OWTs 1, 2, and 3) and the NDCI-based model (N = 147).*

The evaluation of this weighted combination is provided in **Figure 3.19**. It is worth mentioning that the number of points presented in **Figure 3.19** (N = 147) corresponds to the maximal number of points in DS-V with available information from the visible to the NIR for samples corresponding to OWTs 1, 2, 3, and 4. An overall good performance is found for the MUBR-NDCI-based combination (MAPD = 21.64 %, RMSD = 0.25).

3.8.3.5. Match-up exercise

The validation of the Chl-a estimates performed using the MUBR-NDCI-based combination proposed in this study was performed through a matchup exercise based on the DS-M dataset for both OLCI and MSI (section 3.8.2.2). Our results emphasize a general expected degradation in the accuracy of the Chl-a estimates for these two sensors (**Figure 3.20**) when compared to the performance of the Chla inversion performed using the in-situ validation dataset (**Figure 3.19**). Globally, the best performance is here found when applying the MUBR-NDCI-based combination using satellite $R_{rs}(\lambda)$ derived from the POLYMER processing for both sensors. The Chl-a derived with POLYMER yields the highest number of valid matchups for both OLCI (N = 358 vs N = 184 and 225 for ACOLITE and C2RCC, respectively) and MSI (N = 188 vs N = 138 and 143 for ACOLITE and C2RCC, respectively). This result is in agreement with former intercomparison exercises, for instance, (Pahlevan et al., 2021). Although an overall high

scattering level in the matchups, POLYMER globally provides better estimates from the clear to the highly turbid waters with a better performance found for OLCI when compared to MSI (**Figure 3.20.b** and **Figure 3.20.e**). For both sensors, ACOLITE processing tends to generate an overestimation of the retrieved Chl-a also found for C2RCC, especially for the OWT 4 samples, suggesting the probable need to improve atmospheric correction in the NIR domain. The patterns depicted in **Figure 3.19** remain globally valid when considering the common matchup points (not shown) for the three atmospheric correction schemes applied to both sensors. A general better performance in retrieving Chl-a is still found when applying the MUBR-NCDI-based combination to POLYMER data to OLCI (e.g., MAPD =114, 172, and 116 % for POLYMER, ACOLITE, and C2RCC, respectively, N = 214) and MSI (e.g., MAPD = 68, 149 and 148 % for POLYMER, ACOLITE, and C2RCC, respectively, N = 99) $R_{rs}(\lambda)$.

Our results therefore relatively differ from previous works (Pahlevan et al., 2021) where POLYMER was not found to provide the best performance when evaluating different atmospheric corrections schemes (and Chl-a models) for Landsat-8 and Sentinel-2 applications over lakes, rivers, and coastal waters. However, this better performance might be related to the general good performance of POLYMER when considering band ratios as illustrated from former studies in coastal waters (Mograne et al., 2019; Warren et al., 2019). This might be also explained by the fact that the current matchup dataset (DS-M) does not contain many very highly turbid or high Chl-a waters (max Chl-a = 34.12 $mg.m^{-3}$ and 52.93 $mg.m^{-3}$ for MSI and OLCI, respectively) underlining the need to perform additional matchup exercises on a larger dataset. Investigating more in detail the relative impact of the considered atmospheric correction schemes is out of the scope of this study considering that the matchup dataset DS-D contains Chl-a data only. However it should be mentioned that up to now no consensual atmospheric correction scheme is currently recommended for Sentinel2-MSI and Sentinel3-OLCI applications in coastal waters, the performance of the different approaches being susceptible to vary widely according to the wavelength as well as according to the water type considered (Bui et al., 2022; Mograne et al., 2019; Pahlevan et al., 2021).

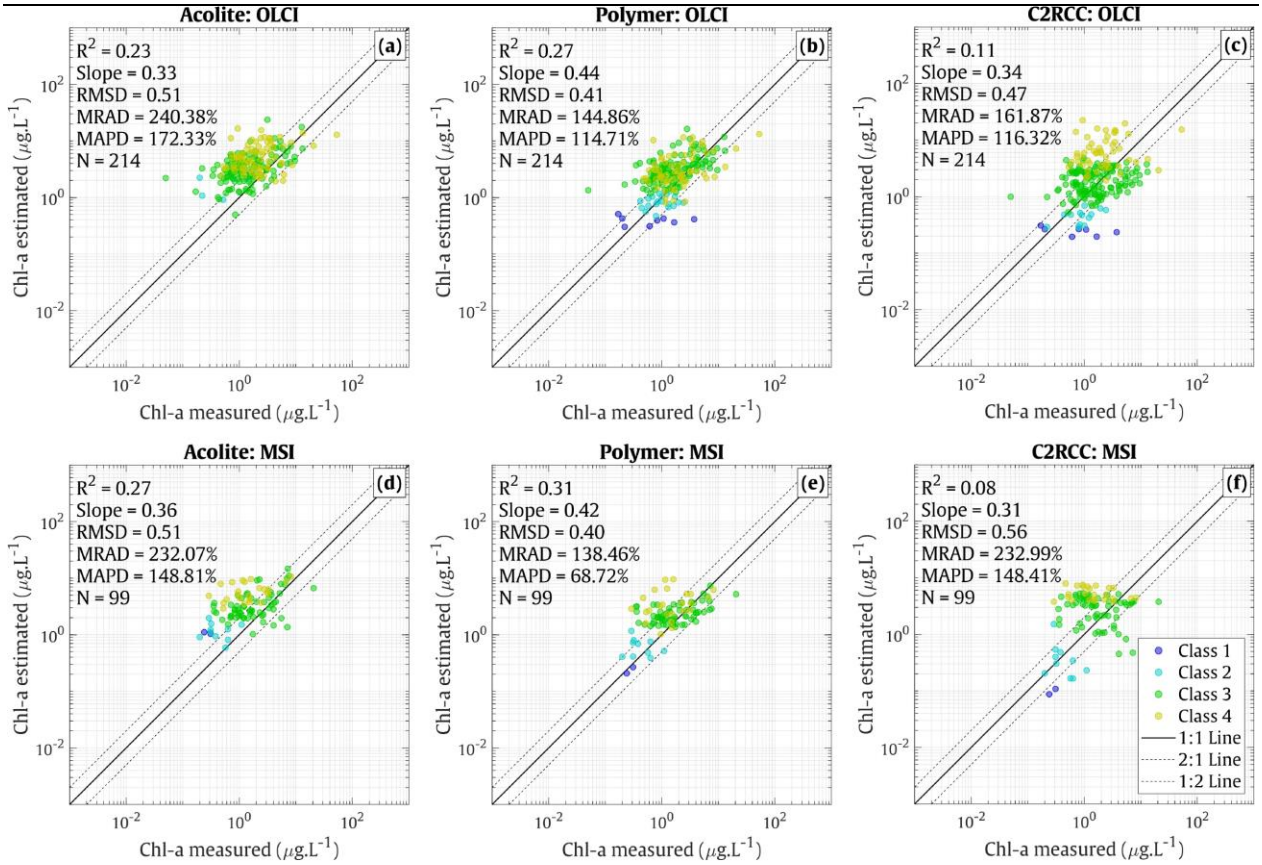

Figure 3.20. *Chl-a matchup validation (DS-M dataset, section 3.8.2.2) computed applying the MUBR-Mishra12-Tuned combination on the $R_{rs}(\lambda)$ generated applying three atmospheric corrections schemes (ACOLITE, POLYMER and C2RCC) for Sentinel3-OLCI* ***(a, b, c)*** *and Sentinel2-MSI* ***(d, e, f)****, respectively.3.1.*

3.8.4. Discussion

3.8.4.1. Chl-a algorithms combination

The results obtained in the previous sections have illustrated that the Red-NIR formulations globally demonstrated their ability to retrieve Chl-a value in highly turbid/high Chl-a waters with a satisfying accuracy (**Figure 3.19**). Our results further emphasize the necessity to consider compatible models when applying weighting approaches as the one depicted in section 3.8.3.4 taking care of the applicability of the approaches to be merged especially in transition areas. A limitation was for instance found for the formulation by Gons et al., (2008) which tends to generate negative Chl-a values for the low Chl-a levels (< 5 $mg.m^{-3}$) for the OWT-4 waters. Such limitations might represent an issue when merging multiple algorithms on a pixel-per-pixel basis. As a matter of fact, the application of a combination based on MUBR and Gons08 will lead to a

generation of bias or even create negative Chl-a in the transition area between OWT 3 and OWT 4 (not shown) where pixels can show relatively high-OWT membership values for both OWTs.

To avoid such issues, a possible way would consist in considering other approaches than the one based on the weighting methods based on pixel OWT membership (Equation 3.42) for combining multiple bio-optical models. Lavigne et al., (2021) for instance recently proposed pixel-per-pixel-based quality control tests (diversely based on the Chl-a as well as on thresholds applied on different MERIS R_{rs}) for selecting the most appropriate models for estimating Chl-a (Gohin et al., 2002; Gons et al., 2008; O'Reilly & Werdell, 2019). As mentioned by these authors the main objective of such quality control-based approach is more likely to provide to the users a way to evaluate the reliability of the models applied to a defined area. These authors further illustrate the possibility to use this selection procedure to eventually merge multiple algorithms although such approach might generate discontinuity in the Chl-a maps when switching from one algorithm to another.

The interest of using the OWT membership information to merge the two inversion models considered here was further illustrated from a Sentinel2-MSI map in the Vietnamese coastal waters close to the Mekong river and Nha Be river estuaries (East Vietnam Sea **Figure 3.21.a**) which shows contrasted water masses ranging from clear (OWT 2) to ultra-turbid (OWT-5) waters (**Figure 3.21.c**). The MUBR-NDCI-based combination was here applied considering for each pixel the best model according to the pixel OWT (i.e., without weighting the models, not shown) as well as applying the weighing approach described in Equation 3.42 (**Figure 3.21.d**). The need to consider the pixel OWT membership to combine MUBR and NDCI-based models is illustrated in **Figure 3.21.e** where the relative difference between the Chl-a map produced without and with a weighting function. It appears that the simple juxtaposition of the most pertinent model can generate significant discontinuities in the final Chl-a estimates. As a matter of fact, maximum differences reaching 10% are observed in the transition areas between OWTs 3 and 4. Such possible spatial artifact induced using an unweighted can represent a significant issue when using high spatial resolution data such as Sentinel2-MSI (or Landsat8-OLI) which are susceptible to capture fine-scale transition gradients in coastal waters (Lavigne et al., 2021; Vantrepotte et al., 2012).

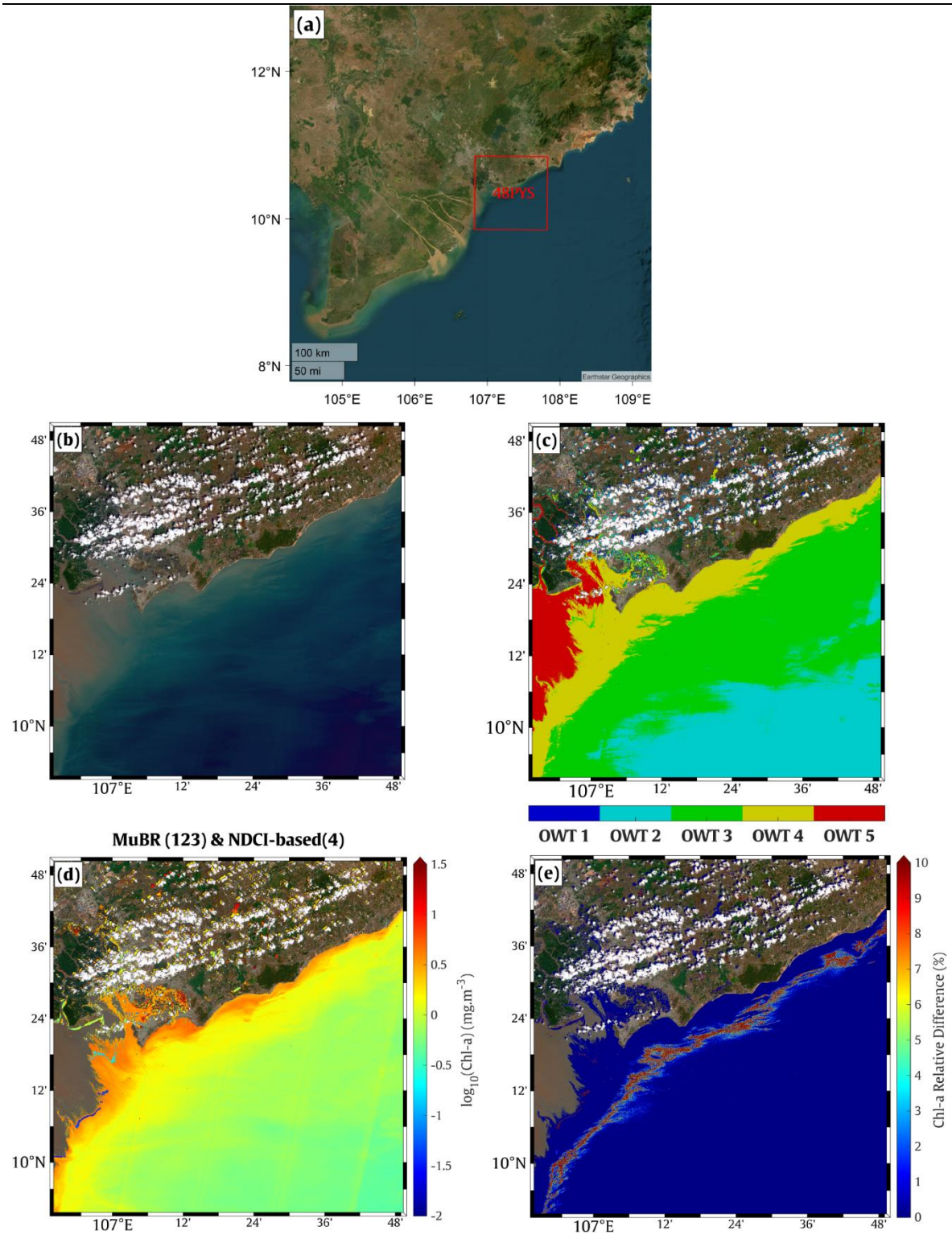

Figure 3.21. *Illustration of the interest of using a weighting function based on the OWT membership probability for blending multiple Chl-a from a Sentinel2-MSI (60 m, POLYMER processing) image gathered in the Vietnamese coastal waters.* ***a)*** *true color image,* ***b)*** *optical water types distribution* ***c)*** *Chl-a estimated from the MUBR-NDCI-based combination where*

masked grey areas are those belonging to OWT-5, ***d)*** *relative difference (%) in the Chl-a estimated from the MUBR-NDCI-based combination with and without using pixel OWT belonging probability as a weighting function (see Equation 3.42).*

3.8.4.2. Applicability of band-ratio-based Chl-a models at global scale and current limitations and perspectives.

To summarize the results developed in the previous sections regarding the relative performance of the different Chl-a inversion methods selected for the different optical OWTs defined in the frame of this study, global monthly MERIS 1km R_{rs} data were associated with the five optical OWTs defined in this work. **Figure 3.22** shows the most frequent OWT observed for each pixel over the MERIS time period. The coastal domain was here defined considering a global mask proposed by Mélin & Vantrepotte, (2015) for characterising the optical diversity of coastal waters which is based on the combination of criteria based on bathymetry and distance to the coast. It appears that pixels corresponding to OWTs 1, 2, and 3 represent 63, 21, and 14 % of the considered coastal domain, meaning that the MUBR model can be applied in the vast majority (98 %) of the considered waters. OWT 4 pixels where the use of Red/NIR models such as the NDCI-based model defined here are the most suitable represent only 2% of the whole domain being often corresponding to coastal margins impacted by the dilution of terrestrial inputs, including waters offshore river plume or mangrove areas for instance. The OWT 5 waters, for which none of the tested band-ratio-based Chl-a inversion methods provide accurate Chl-a estimates represent 1% of the global domain here considered. Focusing on moderate to ultra-turbid waters (OWTs 3, 4, and 5) our results indicate that Chl-a can be estimated with a satisfying accuracy (OWTs 3 and 4) over 94 % of the coastal margins and shelf waters.

The main limitations in estimating Chl-a from ocean color observation are therefore related to ultra turbid waters corresponding to the OWT 5 mainly associated with the proximal part of most of the large rivers. Although their restricted spatial extension, an accurate monitoring of the recent evolution of the biogeochemical quality of these water masses is however essential considering their vulnerability to environmental changes of natural and anthropic origin impacting the transfer of matter along the land-sea continuum (Abril et al., 2022). Our results however clearly question the pertinence of considering Chl-a concentration as a relevant indicator for monitoring from satellite ocean color observation such environments where the

phytoplankton signal on the marine reflectance seems to be too low for being detected considering band ratios based on both visible and NIR wavelengths.

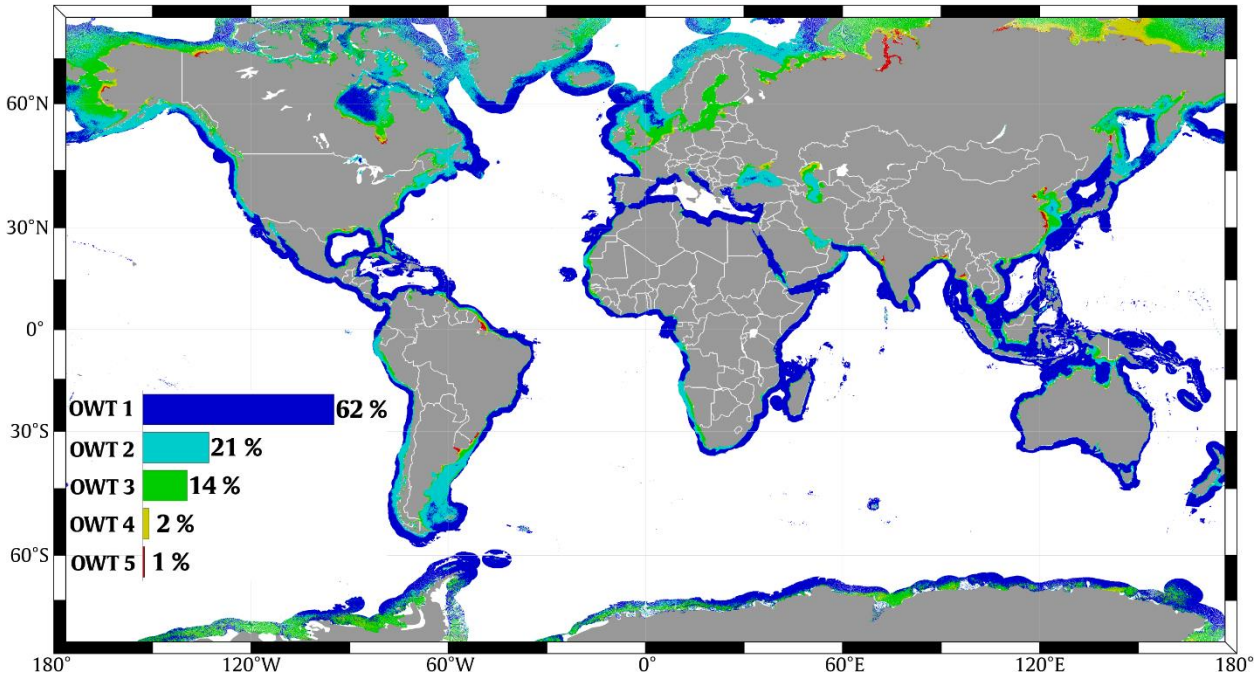

Figure 3.22. *Global distribution of the most frequent optical water type among the 5 optical water types considered in the frame of this study observed from the monthly MERIS 1-km observation between 2002 and 2012. The histogram chart provides an illustration of the relative spatial coverage (in %) associated with each optical water type over the whole domain considered here.*

The present study only allows the pixels for which Chl-a estimates are not reliable considering the evaluated models to be dynamically identified using optical water types information to potentially mask the corresponding areas. A possible way to overcome this issue could consist in adopting alternative methods for instance taking advantage of the new potential offered by upcoming hyperspectral satellite sensors (e.g., NASA PACE mission). Cheng et al., (2013) for instance, documented the interest of a R_{rs} derivative-based approach for estimating Chl-a in turbid inland waters. More specifically, these authors demonstrated that the first R_{rs} derivative at 699 nm was a good proxy for estimating Chl-a in turbid lakes. The pertinence of this approach was evaluated on the OWT 5 dataset testing the best combination considering wavelengths ranging from 412 to 740 nm (Cheng et al., 2013). Our preliminary results show that the highest correlation with Chl-a (R^2 = 0.40, N = 57) is obtained when using the second

derivative at 671 nm ($R_{rs}''(671)$, using R_{rs} measurements at 671 and Y nm, these two parameters follow a linear relationship indicated in **Figure 3.23**.

Derivative-based approach, although its potential interest, will not fully allow to solve the issue represented by the Chl-a inversion in ultra-turbid OWT 5 waters (**Figure 3.23**). Indeed, a clear over-estimation of the Chl-a concentration is observed for the low Chl-a samples in OWT 5 (<1 $mg.m^{-3}$) which data are corresponding to samples showing extremely to fairly low values for the Chl-a/SPM ratio (< 3.9×10^{-5}). However, the performance of this latter model has proven a significant improvement in retrieving Chl-a over such optically complex waters when comparing the R^2 value to that of the traditional approaches (see **Figure 3.14**). It is also important to recognize that additional in-situ observations are required to further confirm the latter statement and deliver more robust information on the current limitations of ocean-color-based observation for depicting Chl-a in such ultra-turbid environments.

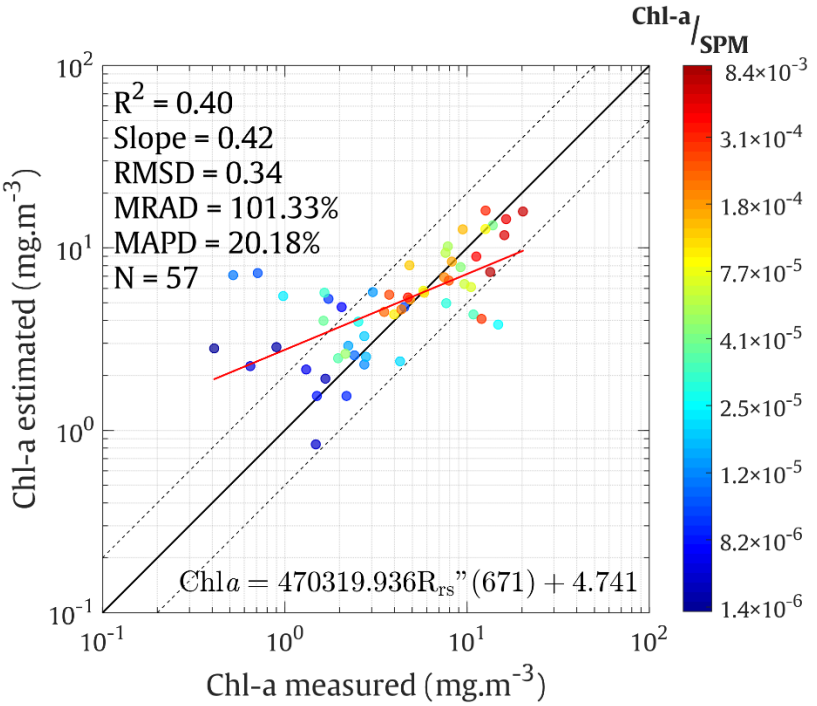

Figure 3.23. *Illustration of the potential of a $R_{rs}(671)$ second derivative-based model for estimating Chl-a concentration in ultra-turbid waters (OWT 5).*

3.8.5. Conclusions

This work aimed at evaluating the performance of band-ratio-based algorithms for estimating Chl-a in coastal waters from Sentinel2-MSI and Sentinel3-OLCI observation from an extensive in-situ dataset covering a large spectrum of coastal environments in terms of optical

characteristics (from clear to ultra-turbid waters) and trophic status (from oligotrophic to ultra-eutrophic environments). The best combination found from our dataset consists in mixing a visible band ratios model (MUBR) for clear to medium turbid waters (OWTs 1, 2, and 3) and an adapted version of the Red-NIR model (NDCI-based) for highly turbid/high Chl-a waters. Such combination can provide relevant Chl-a estimates covering 4 orders of magnitude from oligotrophic to ultra-eutrophic waters covering the vast part of the coastal domain. From our dataset, POLYMER processing was the most adapted to derive Chl-a from the proposed approach although additional matchups should be performed considering more data, especially towards higher turbidity/Chl-a levels. While the methodology proposed in this work can be transposed to other sensors (e.g., MERIS) future works should be performed for other sensors (e.g., MODIS) for which less information is available in the NIR domain, which is however crucial for coastal waters applications. Finally, classical band-ratio-based methods show clear limitations failing, whatever the model considered, for delivering Chl-a in ultra-turbid environments (e.g., proximal part of main river plumes). While optical water types information could allow to dynamically flag the corresponding pixels, this work further emphasizes the necessity to develop specific approaches for these waters (e.g., exploiting the potential offered by future hyperspectral missions).

CHAPTER 3 – PART III

3.9. Match-up validation of bio-optical models

The match-up exercise has been performed using the in-situ dataset measured within French Guiana coastal waters in order to validate the accuracy of the regionally adapted bio-optical models. The inversion algorithm corresponding to each considered parameter was applied to the satellite $R_{rs}(\lambda)$ extracted at different wavelengths of Sentinel-3/OLCI and Sentinel-2/MSI sensors. Loss in optical signals due to sun glint effect has been documented to present permanently over tropical areas including French Guiana (Abascal-Zorrilla et al., 2019) as in response to the combination of high solar incidence angle and the low wind speeds (Harmel & Chami, 2013; Tavares et al., 2021). In this examination, the POLYMER atmospheric correction method proposed by Steinmetz et al., (2011) has been used to to derive the level 2 products as such AC processors have shown its reliability to retrieve the reflectance values for sun-glinted pixels (Steinmetz et al., 2011). Through this match-up analysis, we aim at validating the accuracy of satellite-derived values of the remote sensing reflectance $R_{rs}(\lambda)$ as well as the estimated concentrations of different biogeochemical parameters.

The comparison between measured and Polymer-derived $R_{rs}(\lambda)$, for Sentinel-3/OLCI and Sentinel-2/MSI shown in **Figure 3.24** and **Figure 3.25**, indicates an increase in uncertainties to retrieve optical signals toward the blue part of the spectrum. In particular, a low R^2 value of 0.09 and a poor Slope of 0.26 were observed at the wavelength of 412 nm, while these values were found to be significantly improved at 665 nm (R^2 = 0.91, Slope = 1.02) considering OLCI matchups. A similar tendency was also witnessed for MSI matchups, which confirms the challenge to atmospherically correct the $R_{rs}(\lambda)$ in the blue domain (Liu et al., 2022; Mograne et al., 2019; Pereira-Sandoval et al., 2019). The limited performances in this spectral region might be due to sky glint and backscatter from haze (Pahlevan et al., 2021) or even the low signal-to-noise effect (Xu et al., 2020) as blue bands have lower energy than red and green bands. Another notable feature is that low reflectance values tend to be underestimated and six points were marked as being negative at 709 nm, suggesting a limitation of POLYMER algorithm to estimate $R_{rs}(\lambda)$ in the NIR region. The results of our study also emphasize the significance of utilizing satellite sensors that offer a high spatial resolution to retrieve $R_{rs}(\lambda)$ from space. This is evidenced when comparing the reflectance obtained for the (MSI) sensor to that of (OLCI), the

examination on MSI sensor seems to yield better accuracy as demonstrated in **Figure 3.24** and **Figure 3.25**.

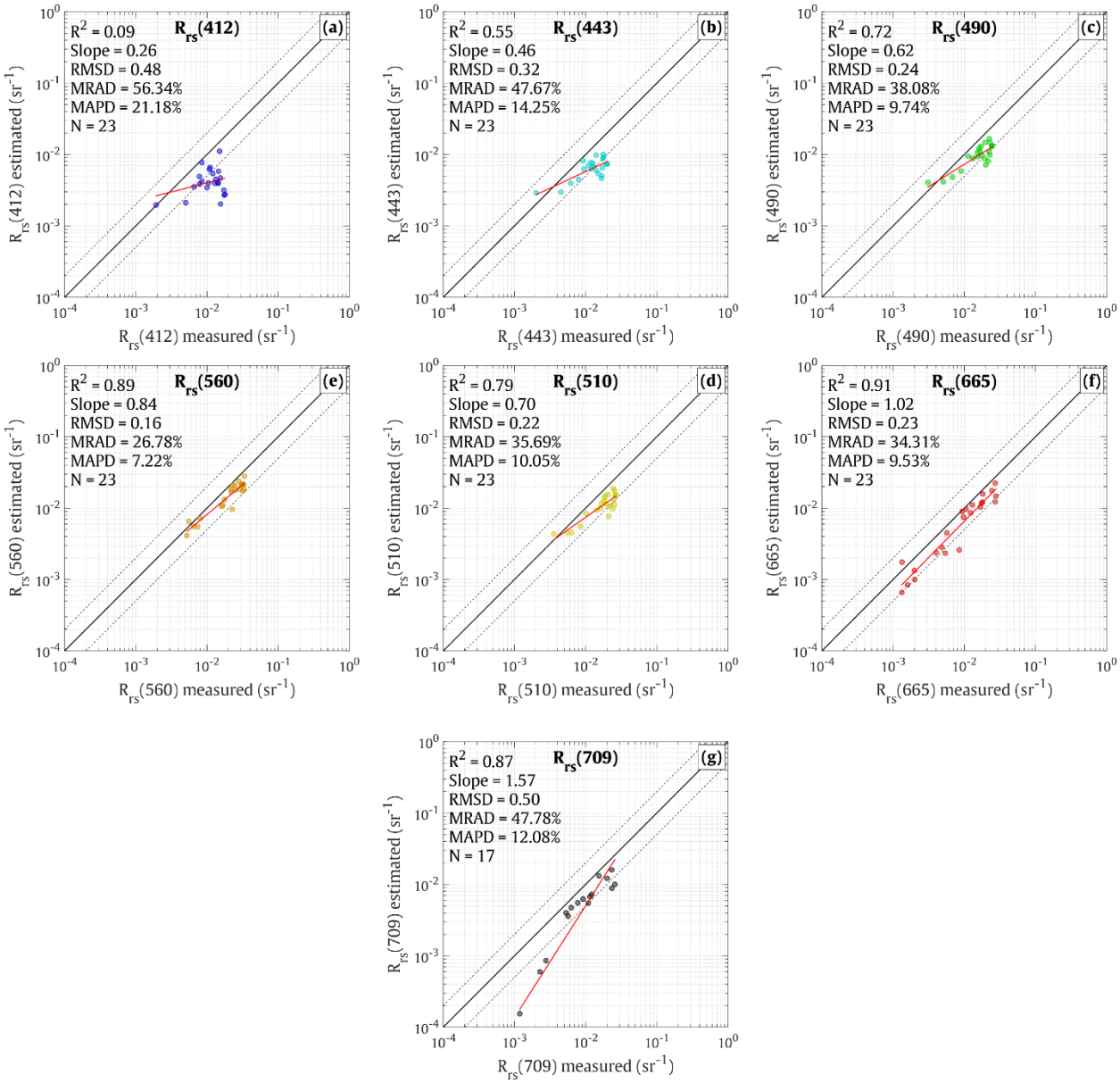

Figure 3.24. *Retrieval of remote sensing reflectance for Sentinel-3/OLCI sensors using POLYMER atmospheric correction processor at* ***a)*** *$R_{rs}(412)$,* ***b)*** *$R_{rs}(443)$,* ***c)*** *$R_{rs}(490)$,* ***d)*** *$R_{rs}(510)$,* ***e)*** *$R_{rs}(560)$,* ***f)*** *$R_{rs}(665)$, and* ***g)*** *$R_{rs}(709)$.*

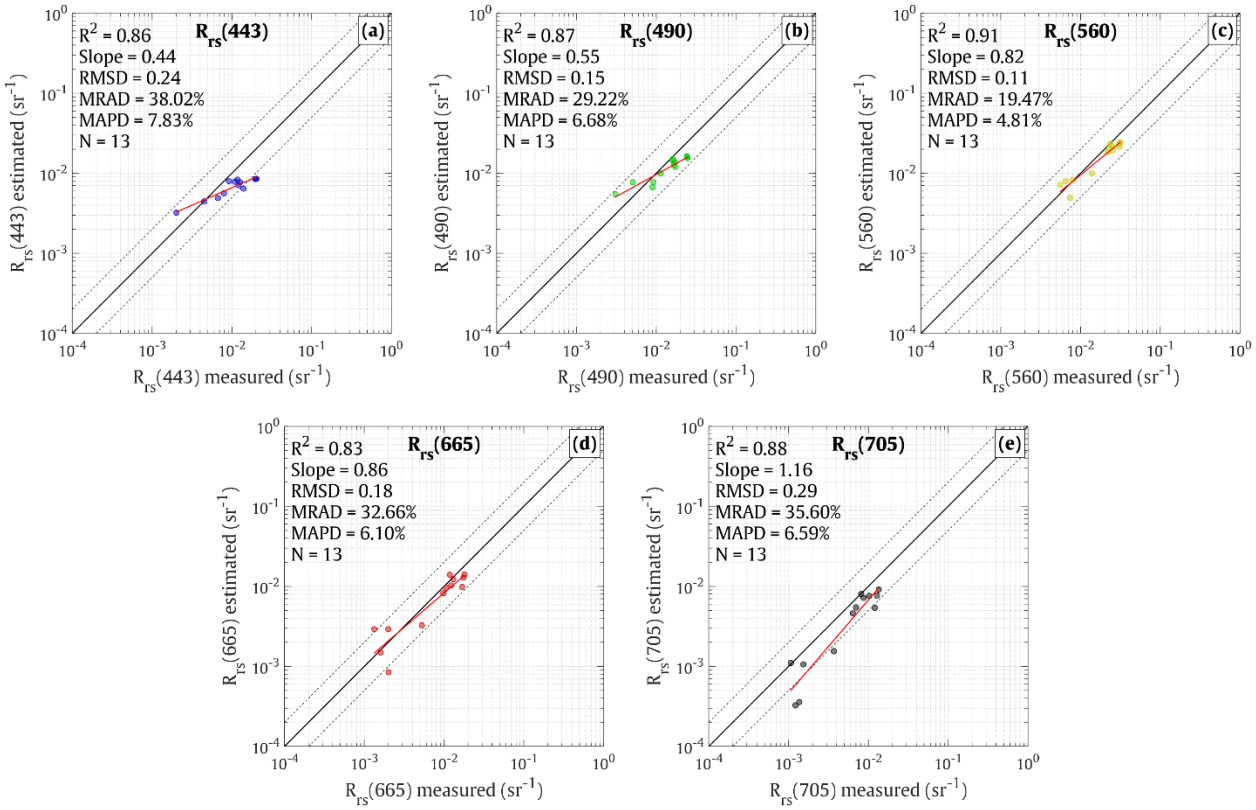

Figure 3.25. *Retrieval of remote sensing reflectance for Sentinel-2/MSI sensors using POLYMER atmospheric correction processor at* ***a)*** *$R_{rs}(443)$,* ***b)*** *$R_{rs}(490)$,* ***c)*** *$R_{rs}(560)$,* ***d)*** *$R_{rs}(665)$, and* ***e)*** *$R_{rs}(705)$.*

As a matter of fact, the uncertainties associated with the retrieval of reflectance might lead to significant bias in bio-optical estimation. These uncertainties can arise from a variety of sources, such as variations in the sensor's calibration, the presence of atmospheric aerosols, and changes in the water's optical properties over time. Therefore, it is important to keep in mind that the results obtained from the match-up analysis of biogeochemical parameters should be interpreted with caution due to the presence of noise originating from the atmospheric correction step. The match-up performances of the selected algorithms for 5 corresponding water quality indicators regarding Sentinel-3/OLCI and Sentinel-2/MSI are shown in **Figure 3.26** and **Figure 3.27**, respectively. We found that the retrievals of SPM provide a satisfactory SPM estimation as confirmed by a relatively good R^2 of 0.67 and excellent Slope of 0.86 considering OLCI matchups. This result is consistent with the $R_{rs}(\lambda)$ match-up exercise shown in the previous section since the POLYMER algorithm performs fairly well for retrieving information in the red band. However, the underestimation in SPM retrieval for OLCI sensor, indeed, reflects biases stemming from atmospherically corrected $R_{rs}(665)$ illustrated in **Figure 3.24.a**. The satellite-

derived concentrations of the remaining variables are observed to be inferior compared to SPM results. This can be explained by the fact that the inversion algorithms corresponding to these parameters usually take into account multiple bands in the visible region, especially the blue bands, which potentially generates more inaccurate predictions. For example, the estimation of POC for both considered sensors exhibits a poor performance, evidenced by a gentler slope of 0.29 and 0.28, respectively. However, the limitation in the number of data points encompassed in our match-up dataset might be inadequate to conclude on the performance of the selected bio-optical models as well as the atmospheric correction algorithms. In addition, the predictions from remotely sensed data did not lead to a strong deviation from the 1:1 line as can be witnessed in both cases of Sentinel-2 and Sentinel-3, suggesting a promising solution to combine the selected models and POLYMER AC processor to extract the information about the water quality over French Guiana coastal domain.

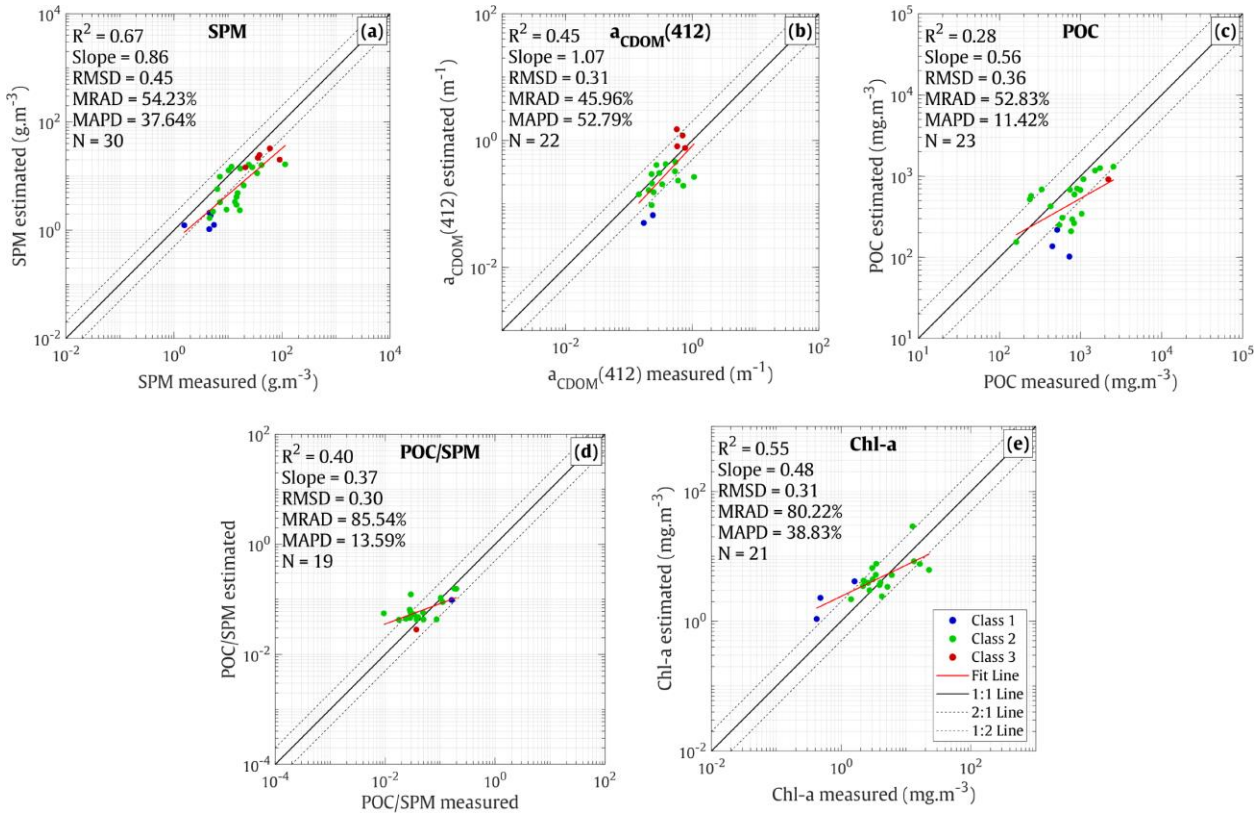

Figure 3.26. *Sensitivity of selected algorithms for* ***a)*** *SPM,* ***b)*** $a_{CDOM}(412)$, ***c)*** *POC,* ***d)*** *POC/SPM, and* ***e)*** *Chl-a to uncertainties in* $R_{rs}(\lambda)$ *retrieved by POLYMER atmospheric correction processor applied to Sentinel-3/OLCI sensor.*

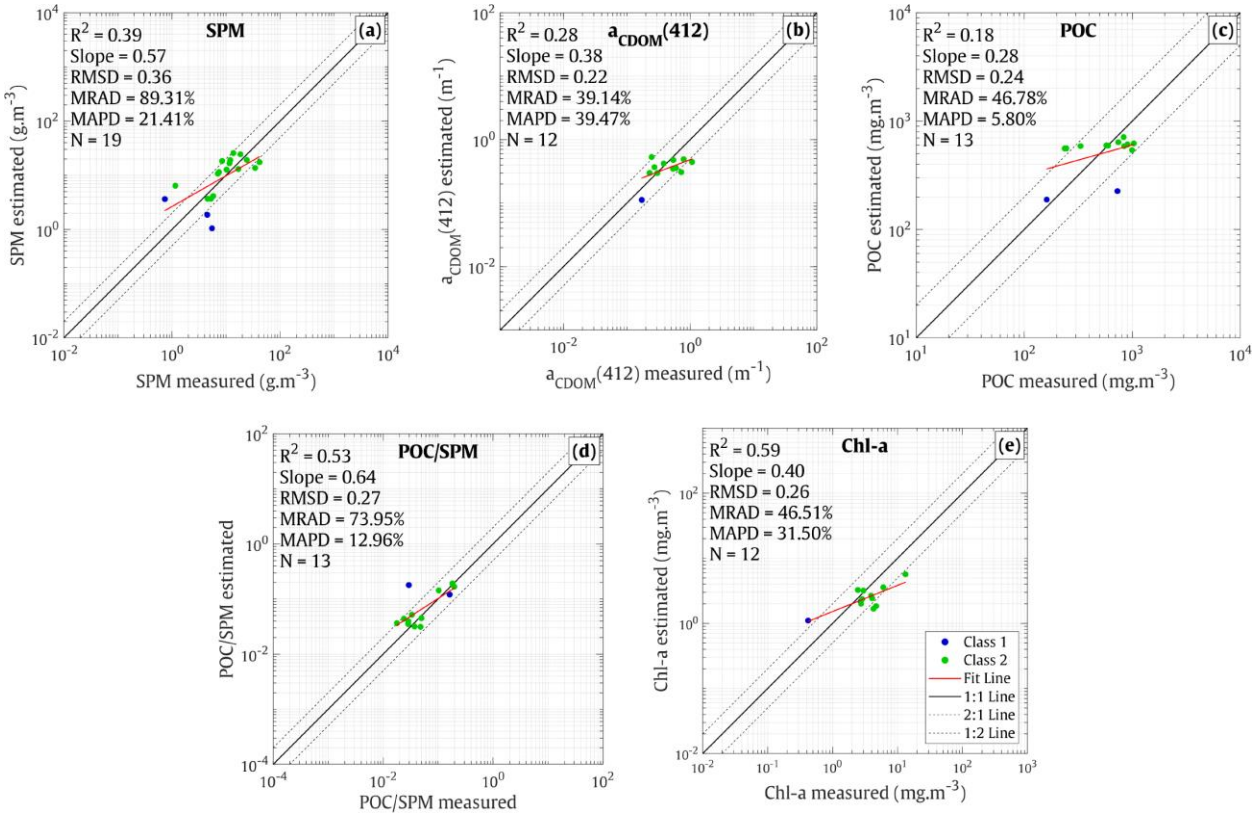

Figure 3.27. *Sensitivity of selected algorithms for* ***a)*** *SPM,* ***b)*** $a_{CDOM}(412)$, ***c)*** *POC,* ***d)*** *POC/SPM, and* ***e)*** *Chl-a to uncertainties in* $R_{rs}(\lambda)$ *retrieved by POLYMER atmospheric correction processor applied to Sentinel-2/MSI.*

3.10. Conclusions and perspectives

A tuning procedure has been applied to historical inversion algorithms in an attempt to determine the most suitable models to estimate the concentration of different water quality parameters from space. The results of the selection process are represented in **Table 3.8**. For SPM, the majority of tested algorithms generally perform quite well. In comparison to the Red-NIR and Green-Red models, the models that were built only through the use of the red channel appear to have a more accurate retrieval of SPM. The BingHan16 algorithm, which is developed based on a weighting approach with the core of Nechad10, was selected as this model exhibits the most accurate SPM estimation globally. The selection of the optimal model for POC was induced from the evaluation of five empirical algorithms which estimate POC concentration directly from $R_{rs}(\lambda)$. Although the model Le17 outperforms the candidate algorithms, this model did not provide a satisfied POC estimation in satellite images over clear water, which implies the inadequacy of in-situ measurements belonging to open ocean waters. The solution to deal with

this issue is to perform a combination of two adapted models Le17 (applied to OWT 3) and KienTran19 (applied to OWTs 1 and 2) by using the probabilities corresponding to each group of classes as the blending coefficients. Different approaches to predict a_{CDOM} over French Guiana waters have been examined. The analysis demonstrates that it is relevant to select the tuned model proposed by Cao et al., (2018) which was constructed based on a multivariate regression method. Considering the difficulties to estimate accurately Chl-a over French Guiana water, a publication focusing on the development of two Chl-a inversion algorithms (MUBR and NDCI-based models) has been submitted. This work is also dedicated to the establishment of an optical classification scheme to combine these two models as well as to identify the distribution of the corresponding OWTs at the global scale. The obtained results further emphasized the challenges of estimating Chl-a over ultra turbid waters and highlighted the interest of using hyperspectral data to retrieve information about phytoplankton biomass in such optically complex environments.

Table 3.8. *Selected inversion algorithms for 5 biogeochemical variables regarding high and medium spatial resolution sensors.*

	High spatial resolution	**Medium spatial resolution**	
	Sentinel-2	**GlobCoast/Sentinel-3**	**GlobColour Data**
SPM	Original BingHan16	Original BingHan16	Original BingHan16
aCDOM(412)	Adapted Cao18	Adapted Cao18	Adapted Cao18
POC	Combined KienTran19 & Le17	Combined KienTran19 & Le17	Combined KienTran19 & Le17
DOC	Vantrepotte15	Vantrepotte15	Vantrepotte15
Chl-a	MuBR & NDCI-based	MuBR & NDCI-based	MuBR & NDCI-based

CHAPTER 4: Description of main spatio-temporal variability patterns of key biogeochemical parameters over French Guiana marine domain

4.1. Introduction

Current knowledge on the spatio-temporal dynamics of key biogeochemical descriptors over French Guiana water is still restricted, in which historical studies have been focusing mostly on sediment dynamics related to the mudbanks system (Abascal-Zorrilla et al., 2020; Gardel & Gratiot, 2005; Gensac et al., 2016; Vantrepotte et al., 2013) and very locally on the carbon exchanges along the land sea continuum (Ray et al., 2018). This lack of information is mainly due to the missing data of consistent long-lasting observations at regional scale.

The first goal of this chapter is to characterize the temporal variability considering biogeochemical variables estimated from space using regionally adapted algorithms (Chapter 3). This work was conducted with an application to different ocean color data including medium and high spatial satellite archives which have been analyzed using adapted statistical tools. In particular, the Census X-11 time series decomposition method has been applied to long lasting time series (Globcoast and Globcolour data) in order to attain a comprehensive understanding of the variation in surface concentration of particulate and dissolved matter while a focus was performed on the French Guiana coast exploiting the information of more recent sensors (Sentinel-2 and Sentinel-3). Second, we aim at identifying the main environmental drivers that govern this variation with a focus on various regions across the French Guiana waters. The information about physical factors such as SST and SSS or river discharges, which was described in section 2.6, was also considered and compared with different parameters in support of this objective. Finally, the selection of the pertinent indicators to follow in terms of biogeochemical representativeness and water quality significance will be proposed as a basis for better partitioning the water masses.

This chapter, therefore, attempts to answer four scientific questions: 1) What is the variability of biogeochemical variables in French Guiana coastal waters at different time scales (i.e., episodic, seasonal, interannual)? 2) What are the main drivers that are responsible for this

variability? 3) What is the co-variation between different parameters and what are the key parameters to follow? 4) How about the long-term changes?

4.2. Description of the biogeochemical dynamics of French Guiana waters

4.2.1. Variability of particulate matter and phytoplankton biomass

4.2.1.1. General distribution patterns

The seasonal distribution of particulate matter and phytoplankton biomass in the study area was investigated using SPM, POC, and Chl-a data with monthly climatology maps generated from the entire Globcoast MERIS archive (1 km^2 of spatial resolution, 04/2002-04/2012). The analysis focused on wet and dry seasons, which typically occur from January to June and from July to December, respectively. Overall, the spatial distribution of particulate materials exhibits a gradual increasing gradient towards from the shore to the open ocean with averaged SPM concentration varying from <1 $g.m^{-3}$ in the off-shore region to > 110 $g.m^{-3}$ in the vicinity of the continental shelf region (**Figure 4.1**). This observation emphasizes the contribution of particulate materials originating from terrestrial inputs on the French Guiana coastal ecosystem. The concentration of SPM in the eastern part (Oiapoque River) was found to be relatively higher compared to that in the western part (Maroni River), indicating the easterly permanent and strong influence of sediment loads from the Amazon River, this area has been identified as the origin area of the Amazonian mudbank system (Gardel & Gratiot, 2005; Gratiot et al., 2007). For example, the averaged SPM concentration observed close to the Oiapoque estuary can reach up to more than 170 $g.m^{-3}$, meanwhile, this value was recorded to be approximately above 80 $g.m^{-3}$ in the Maroni river's outlet, resulting in a lower value for this parameter. Remarkably, the extension of SPM towards off-shore regions reaches its maximum in the eastern areas at longitudes -52°W to -51 °W from July to September with the concentration up to approximately 2 $g.m^{-3}$ **Figure 4.1.b**. This observation agrees with previous studies underlining the presence of retroflected flow of the North Brazil Current (NBC) and North Equatorial Counter Current (NECC) during this period (Carton & Katz, 1990; Garzoli et al., 2004). A similar pattern is also found for POC and Chl-a for which the surface concentration can reach up to approximately 700 $mg.m^{-3}$ and 2 $mg.m^{-3}$ in the retroflection zone, respectively (**Figure 4.1.d,f**). In the inner shelf, regions with high SPM (> 70 $g.m^{-3}$) interspersed with lower SPM regions (≈ 15 $g.m^{-3}$) can be

observed, illustrating the impact of the resuspension processes related to the Amazonian mudbanks (Abascal-Zorrilla et al., 2018; J. M. Froidefond et al., 1988; Gardel & Gratiot, 2005; Vantrepotte et al., 2013; Vantrepotte et al., 2011) along the French Guiana coast (**Figure 4.1.a,b**). Interestingly, the particulate organic carbon pool in the coastal domain (< 20 km away from the coast) tends to be higher in the wet season (> 1000 $mg.m^{-3}$ in April) compared to that recorded during the dry season (800 – 900 $mg.m^{-3}$ in September). It is worth noting that pixels corresponding to ultra-turbid waters (see section 3.8) were masked in this analysis as the Chl-a estimate is not reliable for such optical environments. The remaining pixels present a relatively similar variability to POC observation in off-shore waters where the NBC separates from the Guianese coastline and curves back on itself starting from June to October.

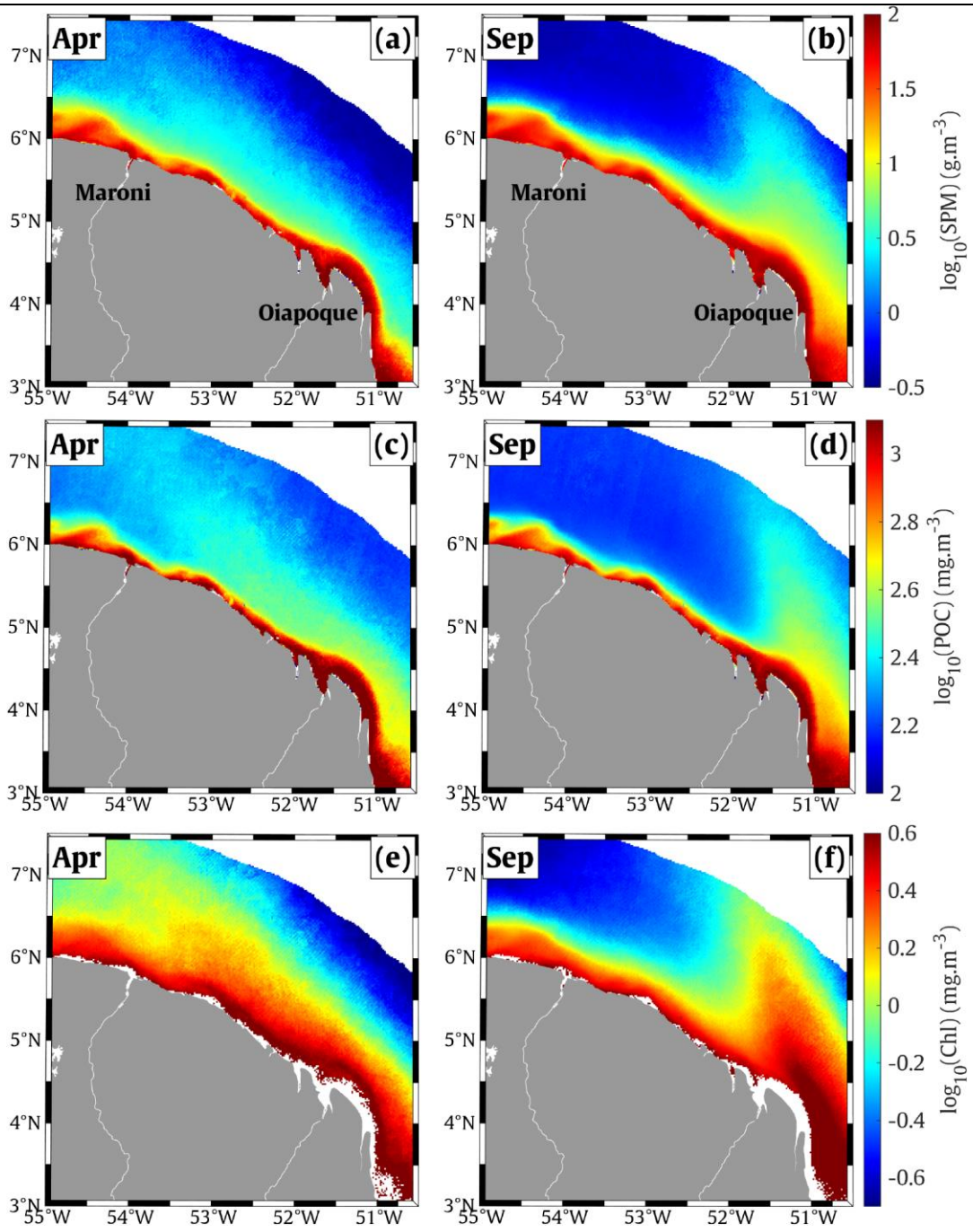

Figure 4.1. *Climatology maps of particulate matter including (a - b) SPM, (c - d) POC, and (e - f) Chl over French Guiana coastal waters during the Wet Season (illustrated here in April) and Dry Season (illustrated here in September).*

4.2.1.2. Main patterns of spatio-temporal variability

The coefficient of variation maps (CV in %, **Figure 4.2**) of particulate materials (SPM, POC) and phytoplankton biomass (Chl-a) derived from the selected bio-optical models over the

MERIS lifetime period. In general, the spatio-temporal variations found for POC and Chl-a tend to follow similar patterns. However, in certain locations, these patterns contrast with that found for SPM. Remarkably, Chla, SPM and POC variables are witnessed to present the highest CV in eastern off-shore waters where the Amazon retroflection occurs. The amplitude of SPM variation is significant around the middle shelf (40 – 50 %) and up to 60% in the retroflection zone (**Figure 4.2.a**). This variation adopted a northwest orientation, aligning with the flow direction of the NBC and the geomorphology of the French Guiana coastline. In contrast, the variation in concentration of Chl-a for open ocean (> 80%) appears to be much higher compared to that reported for SPM and POC and diminishes gradually towards the coast. This emphasizes the substantial degree of variation in phytoplankton productivity in French Guiana off-shore regions and the relative stability thereof close to the shore.

The non-significant alterations in amplitude of Chl-a overtime in the ultra-coastal domain (bathymetry < 30 m, **Figure 1.1**) might be related to different aspects that affect phytoplankton dynamics such as availability of sunlight supporting photosynthesis, the amount of nutrient concentration and/or physical processes (e.g., sediment resuspension, waves, and tidal currents, etc.). In addition, the difference in variability between POC and Chl-a is potentially in response to the amount of non-living organic matter like detritus within the water column or the organic pool exported from local sources (e.g., local rivers, mangroves, mudbanks) as further discussed in the next sections.

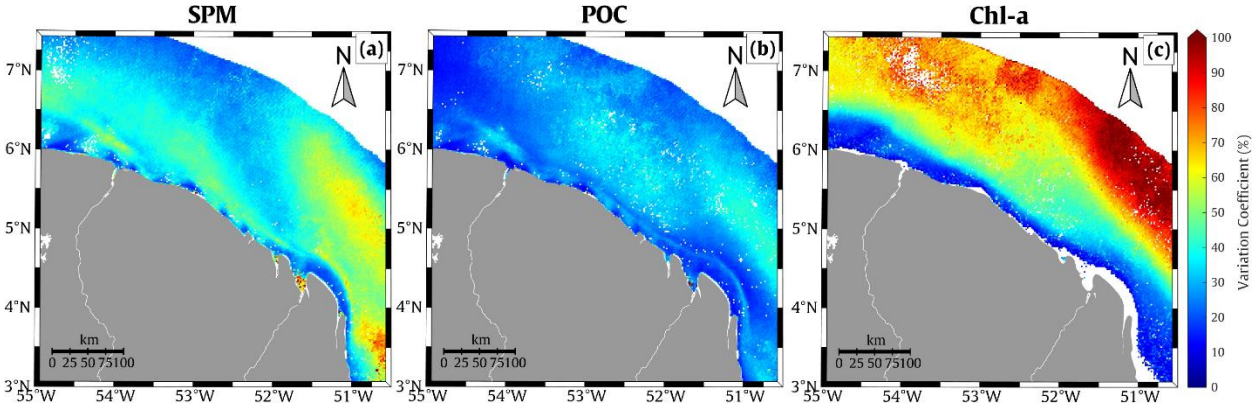

Figure 4.2. *Variation coefficient (CV in %) of* ***a)*** *SPM,* ***b)*** *POC, and* ***c)*** *Chl-a calculated over 10-year period of monthly MERIS GlobCoast data from 2002-2012.*

The analysis of long-term changes in SPM across French Guiana coastal waters has been carried out using the Census X-11 time series decomposition method, which was applied to 121 monthly SPM maps derived from MERIS data (see section 2.5.1) in order to assess the relative

importance of the temporal variation patterns at different scales (seasonal, interannual, irregular/sub-annual) on the variability observed for each parameter.

The relative contributions of seasonal, trend and irregular components to SPM temporal variability are described in **Figure 4.3**. Overall, SPM temporal variability is dominated by seasonal fluctuations which contribution to the variance of the SPM time series (Var-S) ranges from 40 to 90 %. High seasonal variation (60 – 90 %) is observable in the off-shore waters of the eastern part of the study area where the the seasonal retroflection of the NBC current transports Amazon waters to the north and then the east towards the central Atlantic (Johns et al., 1990). Remarkable annual cycle spots are also found in the off-shore areas (Var-S > 70 %) straight from the direction of the Maroni estuary, while a seasonal belt (Var-S ≈ 60 %) parallel to the coast, 20 km off-shore, can also be observed (**Figure 4.3.a**) The increased variability for SPM in these two particular areas is probably due to the influence of oceanic currents that transport the sediment loads supplied from the Amazon River plume as well as to the seasonal export of sediments related to Amazonian mudbanks (Abascal-Zorrilla, 2019).

Importantly, the lowest seasonal contributions appear to the west of the retroflection zone (53ºW – 52 ºW) and are situated about more than 60 km away from the shoreline. This specific region is characterized by relatively high irregular variations (Var-I) which contribute up to > 60% to the total variance **Figure 4.3.c**. The significant contribution of the irregular variation patterns for SPM here is potentially linked to the impact of meso-scale and submeso-scale processes (e.g., NBC rings typically occurring 5 to 6 times per year) (Fratantoni & Glickson, 2002; Goni & Johns, 2001a, 2001; Vantrepotte, Loisel et al., 2011).

Interestingly, SPM changes in the inner shelf domain exhibit a relatively high contribution of trend components (Var-T > 40 %, see **Figure 4.3.b**) throughout 10 years of observation, related to the presence of moving mudbanks along the coast with an annual velocity of 2 km/year (Abascal-Zorrilla et al., 2018; Gardel & Gratiot, 2005; Vantrepotte et al., 2013).

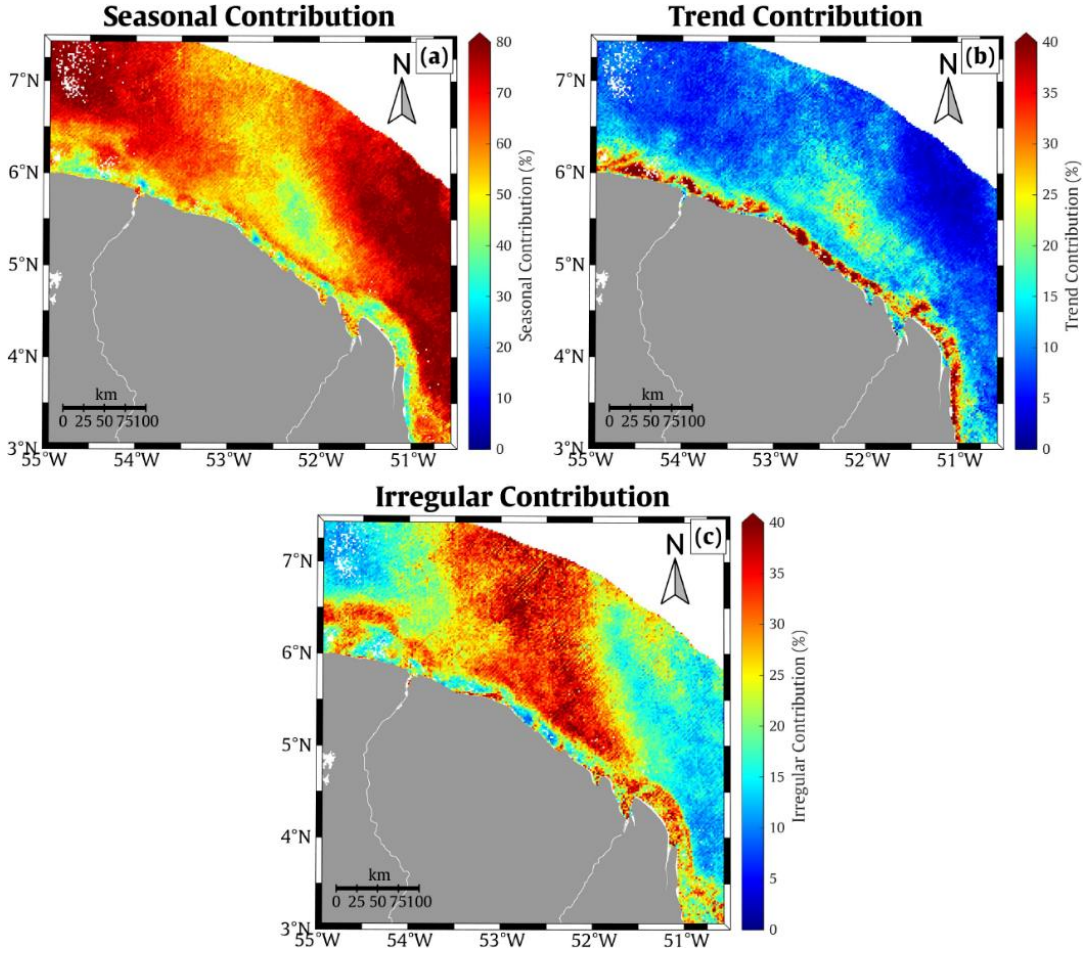

Figure 4.3. *Relative contribution (in %) of the* ***a)*** *seasonal (Var-S),* ***b)*** *trend (Var-T),* ***c)*** *irregular (Var-I) components to the total variance of SPM as calculated using the Census X-11 method over the MERIS time period*

While the analysis on POC shows a substantially higher variability in offshore areas (**Figure 4.4.b**), an overall dominance of the seasonal patterns is globally found for this parameter. Regions exhibiting high seasonal modulations (Var-S > 60 %) are more precisely observed beyond 30 km from the coast (**Figure 4.4.a**), suggesting strong annual-cycle oscillations of particulate organic matter pool occurring in French Guiana's outer shelf ecosystem. These oscillations are characterized by relatively high POC concentration, which can reach up to 500 $mg.m^{-3}$. In addition, the map corresponding to the X-11 trend component for POC reveals a remarkable correspondence with that found for SPM (**Figure 4.3.b**). This similar pattern between SPM and POC might indicate that the mudbank migration processes as a crucial impact not only on the sediment dynamics but more largely the whole biogeochemical dynamics of the coastal band. As a matter of fact, a strong correlation between POC and SPM is also found in-

situ ($p < 0.001$, $N = 85$). This finding agrees with previous studies as the organic matter present could be attributed to elements originating from the mangrove forests that were destroyed and buried during the mudbank migration processes (Berlamont et al., 1993; Gardel & Gratiot, 2005). Further, a significant contribution of the irregular variations is found within a coastal belt located at about 20 km away from French Guiana's coastline with an irregular contribution to the total variance of the POC signal higher than 40 %.

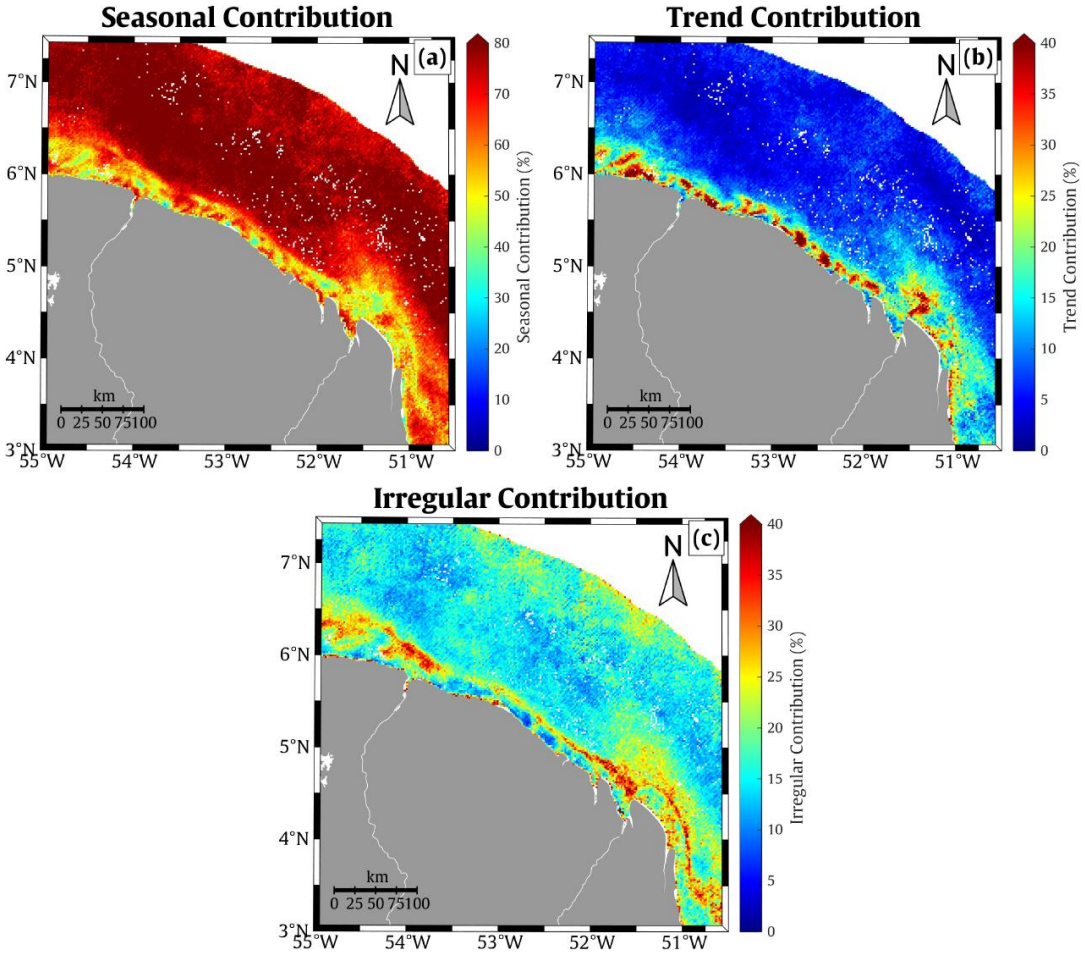

Figure 4.4. *Relative contribution (in %) of the* ***a)*** *seasonal (Var-S),* ***b)*** *trend (Var-T), c) irregular (Var-I) components to the total variance of POC as calculated using the Census X-11 method over the MERIS time period.*

The X-11 outputs exhibit a relatively similar pattern in variability between POC and Chl-a over French Guiana marine waters. The seasonal patterns globally dominate the Chl-a temporal variability (> 80%) with maxima mainly recorded in open ocean as well as a Chl-a seasonal belt along the shoreline (**Figure 4.5.a**). This latter feature might be related to the occurrence of phytoplankton bloom caused by the nutrients transported from freshwater input originating from

local rivers. A relatively high irregular area of 25 % - 40 % is observed at about 20 km from the mouth of the Oiapoque River where the NBC is split into two current flows. Except this area, the trend and irregular variation patterns seem to slightly govern the Chl-a variability over the French Guiana coastal domain with median contributions of Var-T and Var-I of 7.1 % and 16.5 %, respectively.

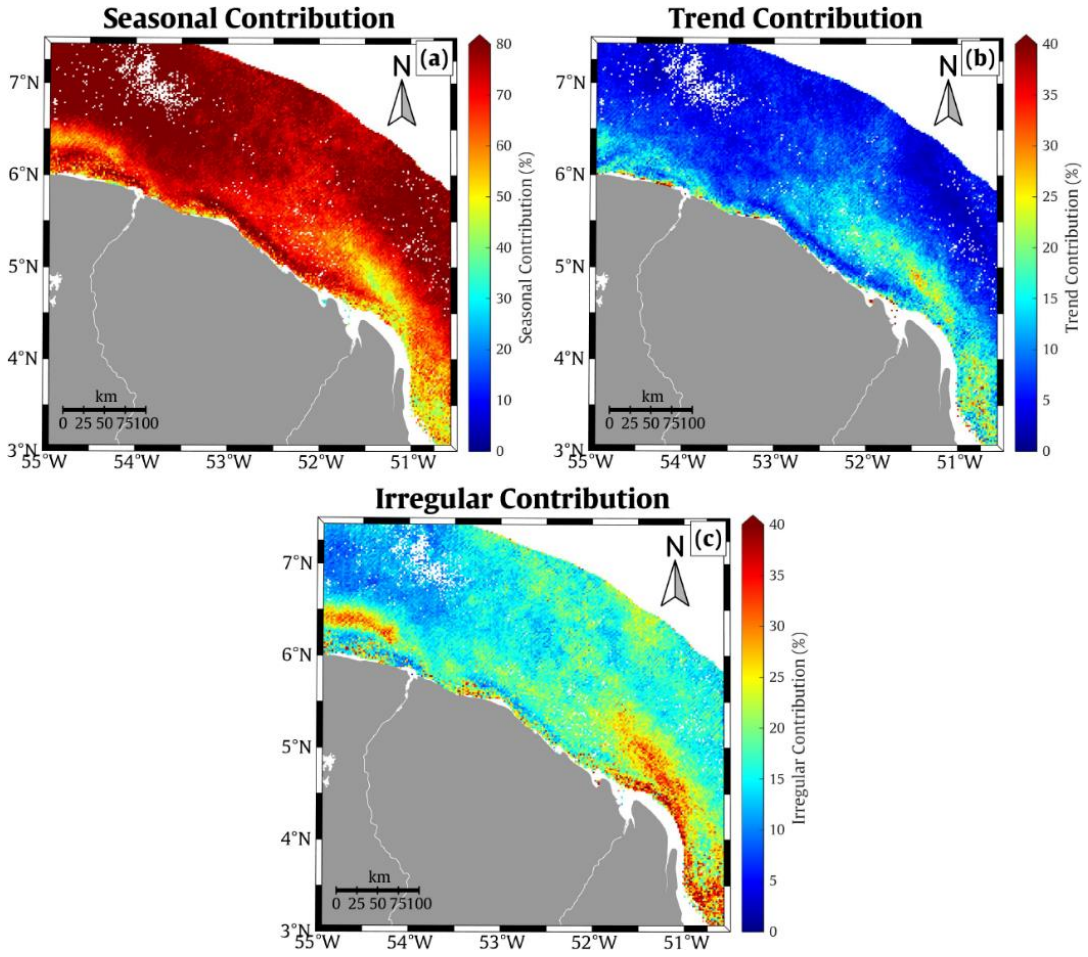

Figure 4.5. *Relative contribution (in %) of the* ***a)*** *seasonal,* ***b)*** *trend,* ***c)*** *irregular components to the total variance of Chl-a as calculated using the Census X-11 method over the MERIS time period.*

4.2.2. Variability of dissolved organic matter

4.2.2.1. General distribution patterns

The satellite-derived maps generated for $a_{CDOM}(412)$ and DOC present a very similar pattern during the two seasons in French Guiana coastal waters. This is due to the fact that $a_{CDOM}(412)$ is the proxy for DOC, which has been estimated through $a^{*}_{CDOM}(412)$ (Del Vecchio & Blough,

2004; Ferrari, 2000; Fichot et al., 2014; Kowalczuk et al., 2010; Mannino et al., 2008; Vantrepotte et al., 2015). The extension in the distribution of $a_{CDOM}(412)$ and DOC to the west in the rainy season and to the east in the dry season towards the off-shore domain, again confirms the seasonal signature of terrestrial inputs driven by physical processes such as river discharge and oceanic currents. A notable feature that can be witnessed from this analysis is that the DOC and $a_{CDOM}(412)$ values are generally higher in the wet season compared to the dry season. This seasonal increase in $a_{CDOM}(412)$ and DOC concentration in the inner shelf of the Cayenne coastal region is found to be approximately 17 % and 5.3%, respectively. This different pattern reflects the impact of the hydrodynamics and the biological processes occurring in French Guiana ecosystems, which can be referred to as significant terrestrial organic pools flushed out through river runoff during the rainy season. The Amazon retroflection tends to spread the organic substances off-shore as observed in **Figure 4.6.a-d** especially between June and October.

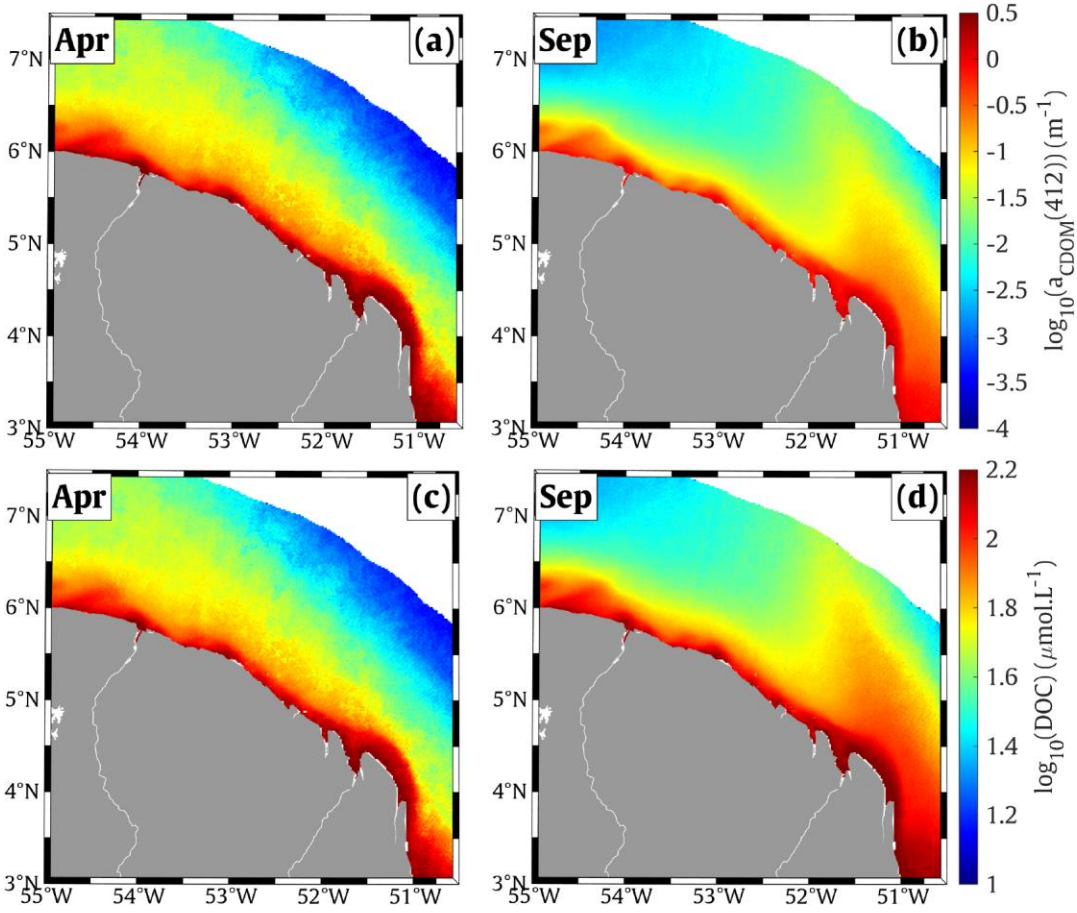

Figure 4.6. *Distribution maps of dissolved matter including* ***a-b)*** $a_{CDOM}(412)$ *and* ***c-d)*** *DOC over French Guiana coastal waters during the Wet Season (in April) and Dry Season (in September).*

4.2.2.2. Main patterns of spatio-temporal variability

Interestingly, the amplitude of the temporal variation of the dissolved organic carbon within the retroflected flow is found relatively higher in the off-shore domain (bathymetry > 40 m) when compared to the coastal one for both $a_{CDOM}(412)$ and DOC, with the corresponding averaged CV values of approximately 210% and 60% (**Figure 4.7.a,b**). The seasonal alteration in dissolved organic content is globally consistent to that observed in particulate organic materials where the concentration of these components is more pronounced in very coastal waters during the wet period (**Figure 4.1**).

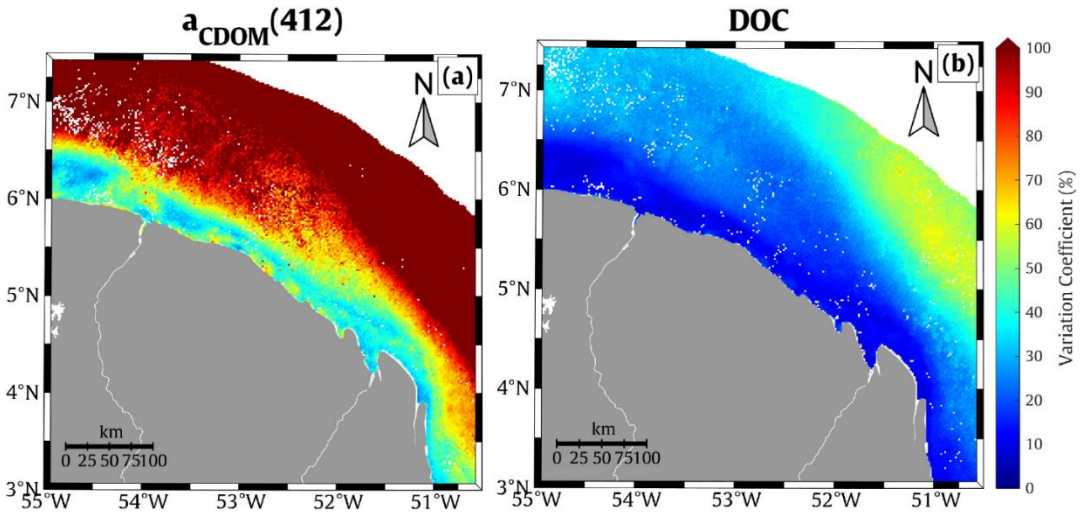

Figure 4.7. *Variation coefficient (CV in %) of* ***a)*** $a_{CDOM}(412)$ *and* ***b)*** *DOC calculated over 10-year period of MERIS data from 2002-2012.*

The X-11 outputs for $a_{CDOM}(412)$ (**Figure 4.8**) emphasize that the temporal variability of the dissolved organic matter pool in French Guiana is primarily governed by seasonal oscillations, which is evidenced by the averaged seasonal contribution over the whole study area of 68% for $a_{CDOM}(412)$. The temporal analysis also emphasizes the consistency in variation between particulate and dissolved organic carbon especially in off-shore waters. High trend contribution is constantly visible along the coast suggesting a similar pattern between dissolved and particulate organic content associated with mudbank drift. An irregular belt of dissolved matter appears at a distance of 20 km from the shore and irregular contributions of more than 35%. The width of this belt (≈ 6 km), is however found to be significantly thinner than that recorded for POC (≈ 11 km). These temporal patterns of dissolved and particulate organic carbon should be interpreted with caution considering the bias potentially generated from the bio-optical models selected in the Chapter 3. However, as aforementioned, such irregular variation in this particular

area (approximately 20 km away from the French Guiana continent) could be related to the modulated export of organic matter from local origins (i.e., mangroves) and small-scale processes tidal impact French Guiana (Ray et al., 2020).

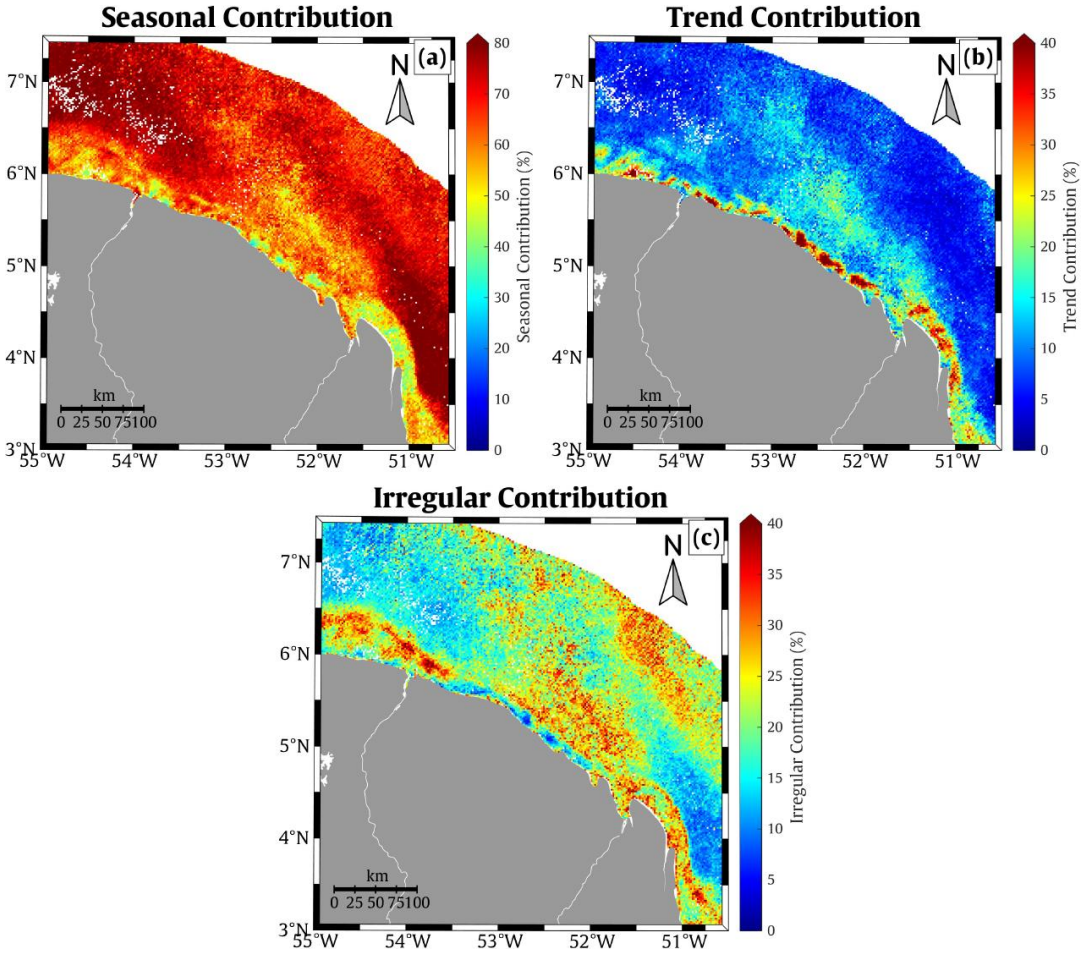

Figure 4.8. *Relative contribution (in %) of the* ***a)*** *seasonal,* ***b)*** *trend,* ***c)*** *irregular components to the total variance of* $a_{CDOM}(412)$ *as calculated using the Census X-11 method over the MERIS time period.*

4.3. Main drivers of French Guiana waters biogeochemical variability

4.3.1. Off-shore processes

4.3.1.1. North Brazil Current Retroflection and western extension of biogeochemical variables

The observed consistency in seasonal variation of the five optical water quality indicators in the eastern areas of the French Guiana off-shore domain (Var-S > 60 %) underlines the strong

impact of the NBC retroflected flow on the biogeochemical dynamics over French Guiana marine waters, transporting not only dissolved but also particulate matter originating from the Amazon plume (**Figure 4.9.a-d**, **Figure 4.10.a-d**, and **Figure 4.11.a-d**). The presence of NBC retroflection is further highlighted by the concentration peaks observed during dry season between July and October at point A (6°03'25.2"N, 51°33'39.6"W, see **Figure 4.9**), which coincides with the timing and the maximum northerly extent of the NBC retroflection as documented in various studies (Baklouti et al., 2007; Hu et al., 2004, Salisbury et al., 2011, Medeiros et al., 2015, Fonseca et al., 2004; Garzoli et al., 2004; Johns et al., 1990).

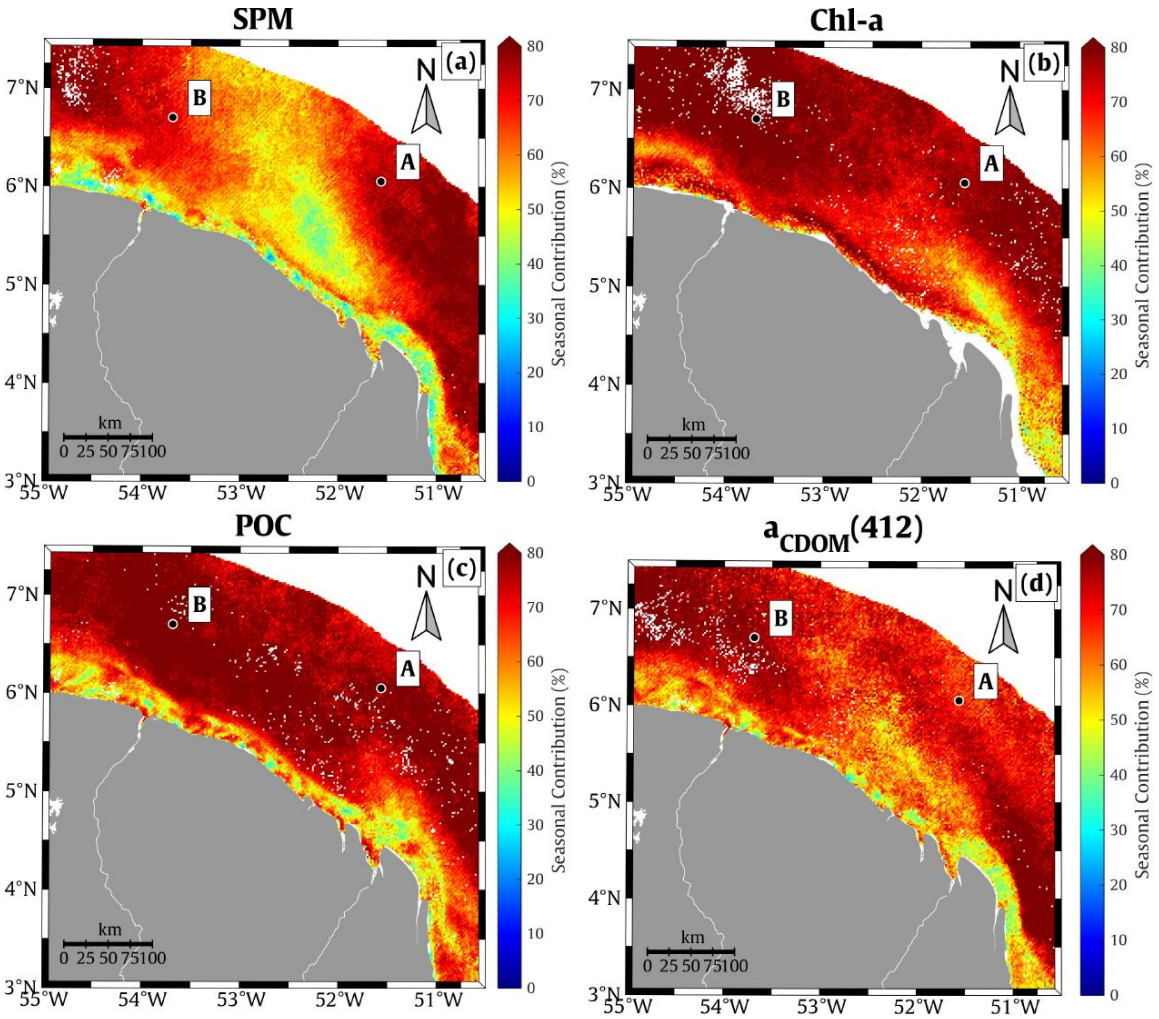

Figure 4.9. *Location of the two extracted points A and B in the eastern and western areas characterized by strong seasonal fluctuation of* ***a)*** *SPM,* ***b)*** *Chlorophyll-a,* ***c)*** *POC, and* ***d)*** $a_{CDOM}(412)$.

More specifically, a remarkable feature at this particular location is that the early and lower peaks of particulate and dissolved organic concentration seem to appear one to two months

before the main ones in August (**Figure 4.11.a,c**). This pattern is also observable in the fluctuation of Chl-a concentration, suggesting that the particulate organic pool here is rigidly related to the development of phytoplankton biomass (**Figure 4.10.c**). This might be in response to the maximum precipitation during the high flow period in May, which leads to a significant proportion of the riverine nutrients exported to the ocean. Although the variability of biogeochemical parameters at the point A exhibits a prominent seasonal pattern, the amplitude of variation for considered biogeochemical parameters here is generally substantial as described in sections 4.2.1.2 and 4.2.2.2. This characteristic illustrates a strong biogeochemical dynamic in the fluctuations of particulate and dissolved substances within the retroflected flow. In addition, the analysis in organic content (POC and CDOM, see **Figure 4.11**) indicates nutrient-rich waters have been conveyed and spread towards the Caribbean Sea by ocean currents, thus impacts on French Guiana waters. Some studies further underlined, that a significant portion of nutrients carried by rivers to the ocean are used up before the plume reaches the continental margin (as noted by Goes et al., 2014). However, some nutrients corresponding to the remaining part are further transported off-shore in addition with nutrients produced by nitrogen-fixing symbionts can support substantial phytoplankton blooms within the Amazon plume (Foster et al., 2007; Subramaniam et al., 2008; Yeung et al., 2012). The fate of the organic matter and the processes governing organic matter dynamics within the Amazon plume however still remain unclear (Medeiros et al., 2015).

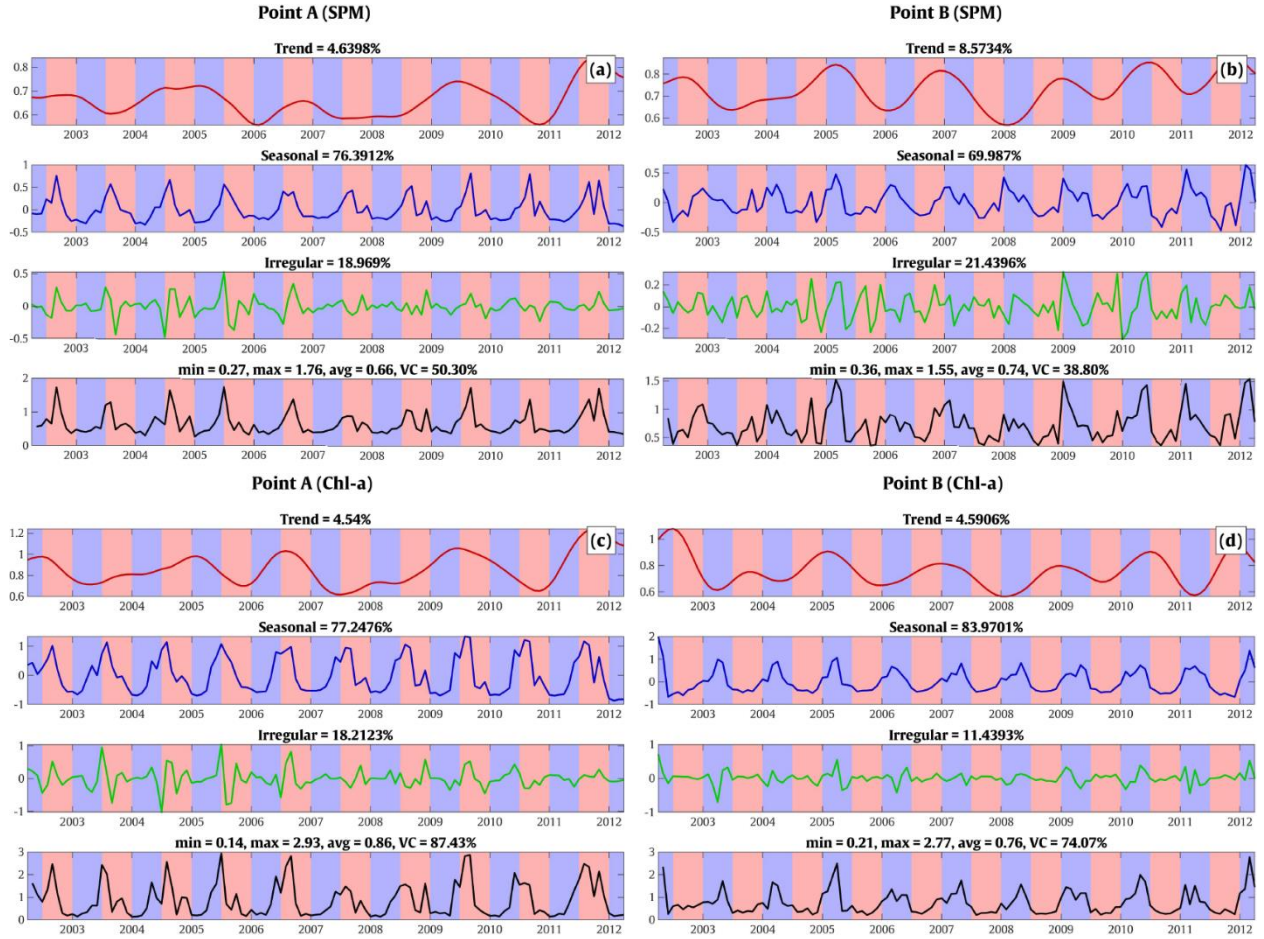

Figure 4.10. *X-11 term statistics calculated for* ***a-b)*** *SPM,* ***c-d)*** *Chlorophyll-a for the points A and B shown in* ***Figure 4.9****. The red, blue, and green solid lines correspond to Trend, Seasonal, and Irregular terms, respectively. The black solid line presents the original time series. Pink and Blue areas indicate wet and dry seasons, respectively.*

During windy and wet season especially, between March and April, a considerable seasonal contribution in the variability of all considered biogeochemical parameters is observed in the western areas of the French Guiana off-shore domain (point B (6°42'18.0"N, 53°41'06.0"W), see **Figure 4.9.a,c** and **Figure 4.10.a,c**). This observation is consistent with the results attained from 11-year MODIS data (2003-2014) conducted by the work of Lampert et al., (2016) where an expansion of Chl-a was identified during the same period. This unique feature is hereby referred as an “off-shore extension” of dissolved and particulate materials in the western regions of the study area. The lower variation coefficient values considering both particulate and dissolved substances (as depicted in **Figure 4.10** and **Figure 4.11**) in this off-shore extension area indicate a more stable condition compared to that observed in the retroflection zone in terms of

amplitudes. In addition to this, the amount of sediment loads delivered to this region seem to be related to cooler water with higher salinity when comparing to the observations in the eastern area (**Figure 4.12**). This might be attributed to of the combined effect of bathymetry (off-shore extension of the continental Shelf, **Figure 1.1**) and seasonal shifts in the wind and current directions. Indeed, the interpretation from the present analysis should be performed in consideration of the difference in spatial resolution of the data as well as the uncertainties from SST and SSS models that need to be validated regionally. Further analysis and in-situ monitoring programs dedicated to seasonal alterations of the water body and current regime are necessary to better understand the impact of this feature.

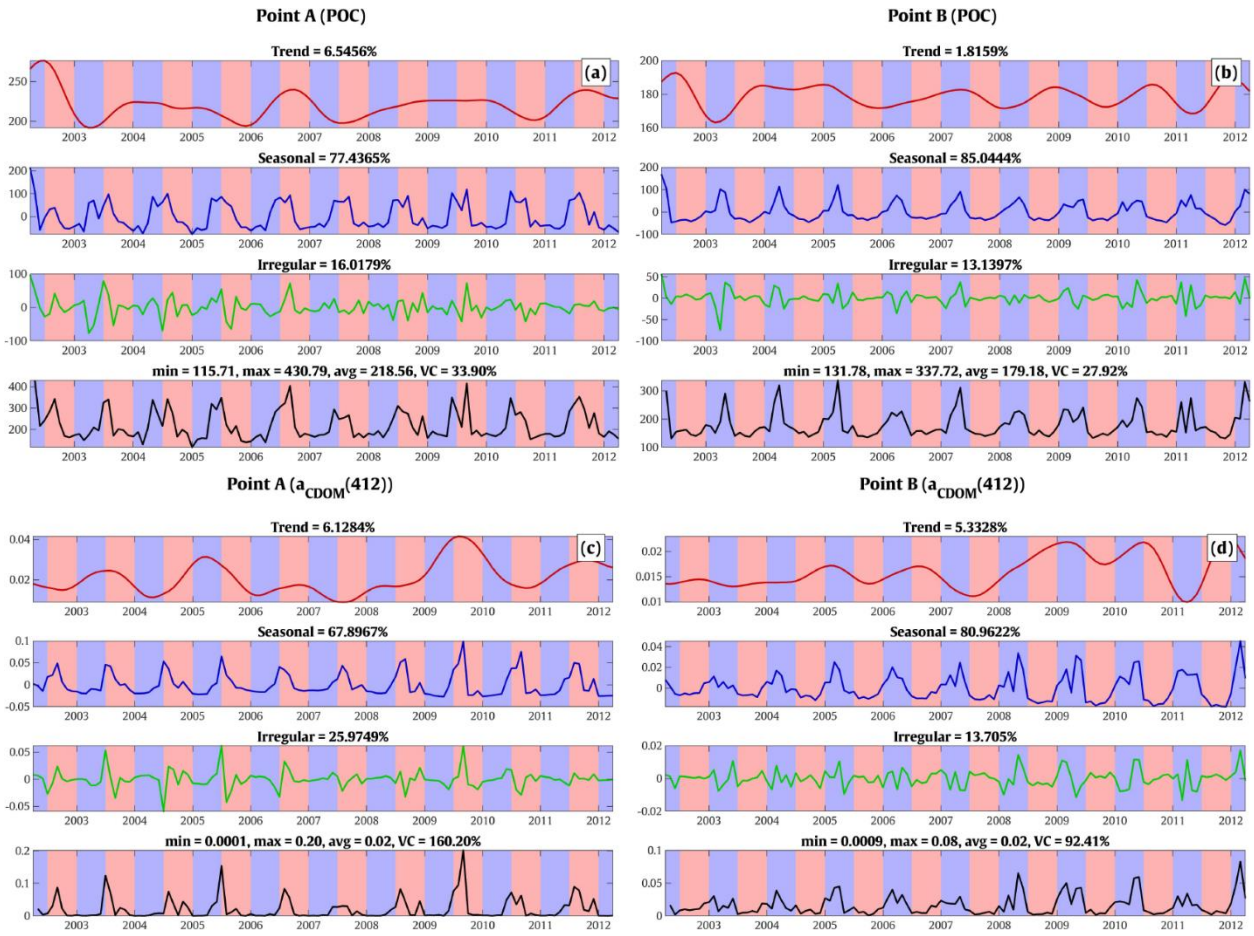

Figure 4.11. *X-11 term statistics calculated for* ***a-b)*** *POC,* ***c-d)*** $a_{CDOM}(412)$ *for the points A and B shown in* ***Figure 4.9****. The red, blue, and green solid lines correspond to Trend, Seasonal, and Irregular terms, respectively. The black solid line presents the original time series. Pink and Blue areas indicate wet and dry seasons, respectively.*

The correlation maps (**Figure 4.12**) depicting the co-variation between the considered biogeochemical parameters and other oceanic variables including SST and SSS, shows a deeper understanding about the origin of the NBC retroflected flow. In particular, the significant positive correlation between SPM and SST and the negative correlation between SPM and SSS in the eastern regions (latitudes 5°N - 7°N and longitudes 52.5°W - 51°W), implies that the NBC retroflection is related to fresh water origin characterized by a warm and less salty flow. This latter feature aligns well with the results obtained from the mooring stations conducted by Baklouti et al., (2007).

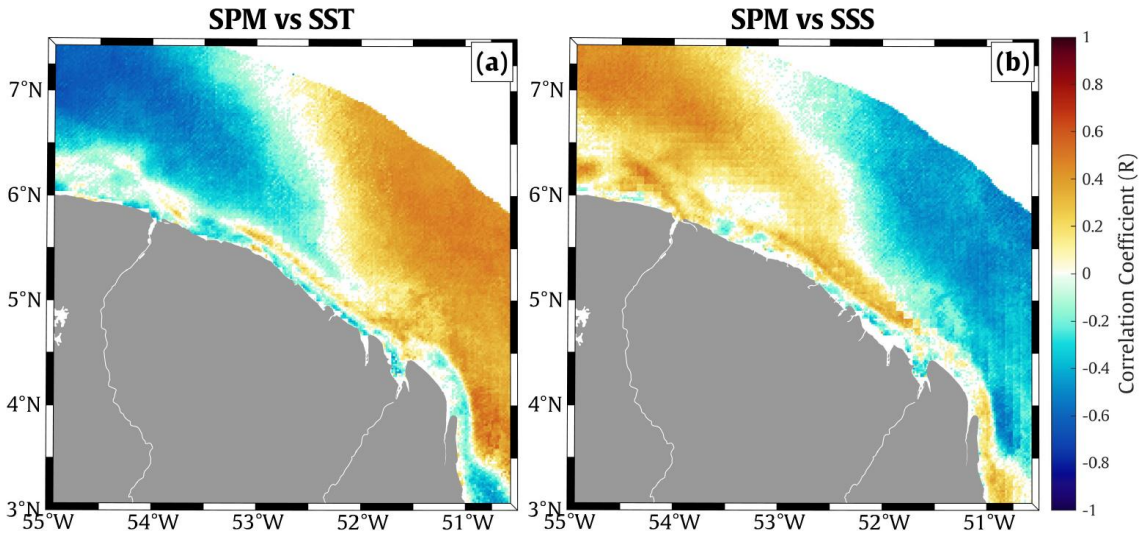

Figure 4.12. *Temporal correlation between SPM and* ***a)*** *SST and* ***b)*** *SSS*

4.3.1.2. North Brazil Current Rings

The influence of the NBC Rings on the biogeochemical variability over French Guiana marine waters can be illustrated by an irregular pattern observed for SPM as previously discussed in the section 4.2.1.2. This assumption is mainly due to the frequency of occurrence (time interval between the formulations) of these anti-cyclonic rings that detach from the retroflection (i.e., 5 to 6 times per year). According to the obtained results from the X-11 method, the irregular area implying the manifestation of NBC rings are typically located off-shore in between the retroflection zone and the western extension (see section 4.3.1.1). To have a comprehensive and more specific view about the NBC rings with respect to biological processes and organic dynamics, the location of the point C (5°41'49.2"N, 52°17'56.4"W) and the corresponding temporal variations considering SPM, Chl-a, and $a_{CDOM}(412)$ are displayed in **Figure 4.13** and **Figure 4.14**, respectively. The presence of NBC rings seems to be more visible

with the variability of SPM, and less pronounced with that of Chl-a, POC, and $a_{CDOM}(412)$. This latter feature suggests the organic pool in this region tends to be modulated by additional biological factors leading to the dominance of seasonal patterns (i.e., phytoplankton bloom) as higher organic content and Chl-a were found in the rainy season (**Figure 4.14.a-c**).

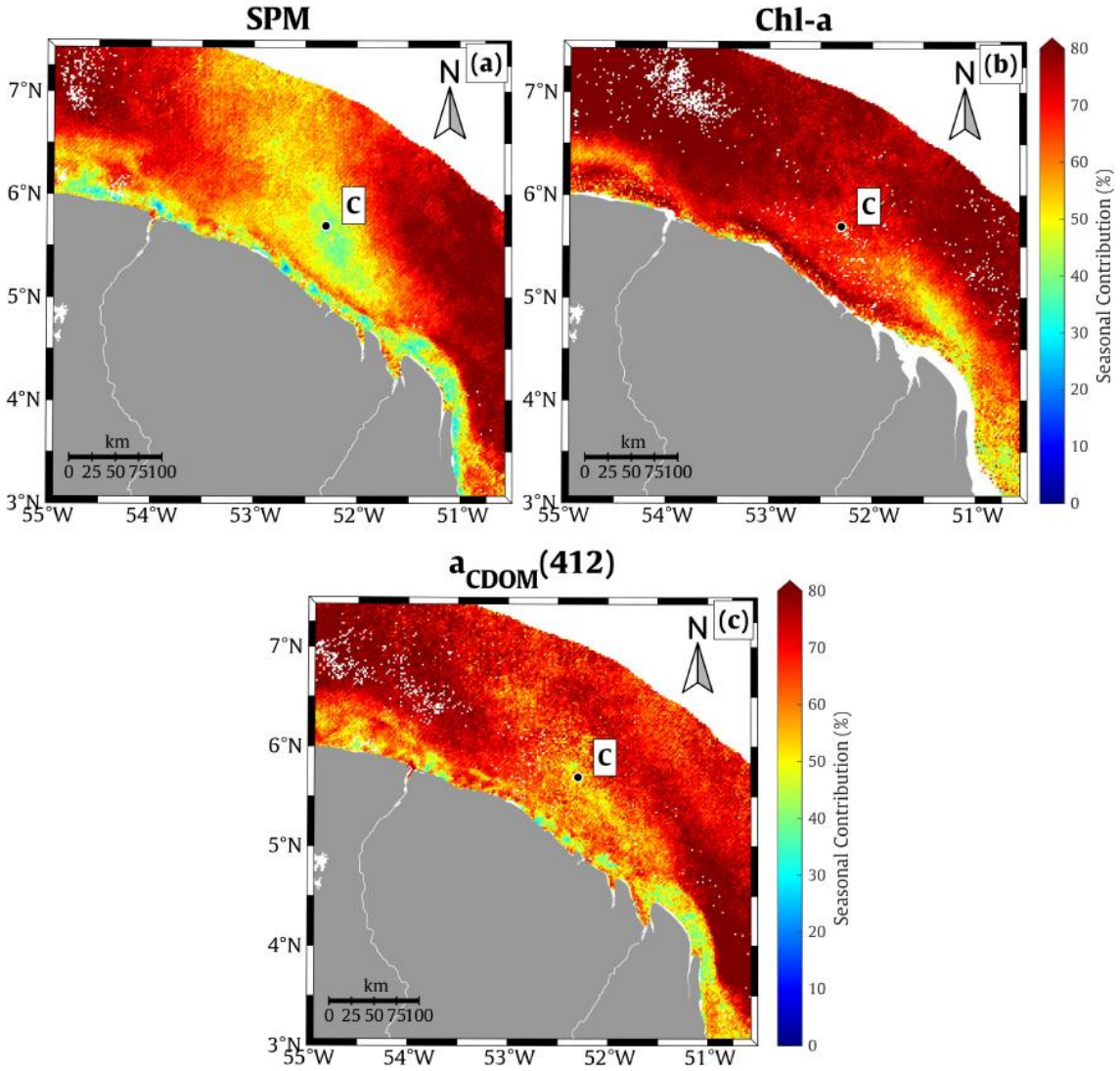

Figure 4.13. *Location of the extracted point C for the seasonal term of* ***a)*** *SPM,* ***b)*** *Chlorophyll-a, and* ***c)*** $a_{CDOM}(412)$.

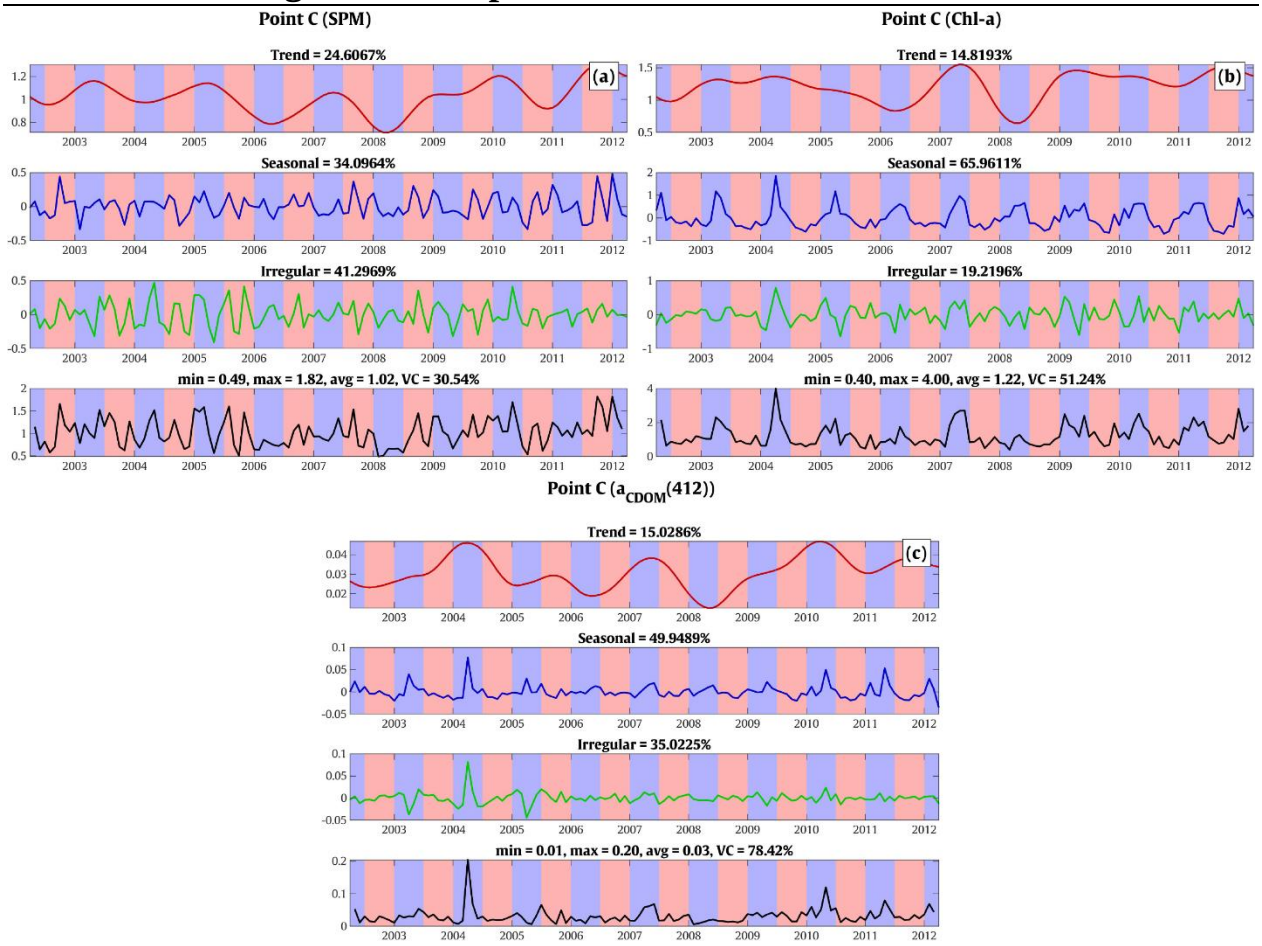

Figure 4.14. *X-11 term statistics calculated for* ***a)*** *SPM,* ***b)*** *Chlorophyll-a, and* ***c)*** $a_{CDOM}(412)$ *for the point C shown in* ***Figure 4.13****. The red, blue, and green solid lines correspond to Trend, Seasonal, and Irregular terms, respectively. The black solid line presents the original time series. Pink and Blue areas indicate wet and dry seasons, respectively.*

4.3.2. Nearshore processes

4.3.2.1. Mudbank influence

As denoted in section 4.2.1, The migration of mudbanks from Cassiporé Cape to the Orinoco River prevails the coastal domain and attaches to the coastline of French Guiana. To discover the biogeochemical dynamics associated with mudbanks, the time series extracted for the point D, (5°16'58.8"N, 52°41'42.0"W) where the variability of SPM, POC, and $a_{CDOM}(412)$ is predominantly characterized by the contribution of interannual (trend-cycle) variation, are shown in **Figure 4.16**. This area exhibits a pronounced mineral-dominated environment, as evidenced by the consistently low POC/SPM values, which remain below 0.08 throughout the study period. The seasonal fluctuations of both particulate and dissolved matter here typically present an

increase from January to May, emphasizing the significant contribution to the biogeochemical dynamics of resuspension process as in response to energetic wind-induced waves during the windy period (Eisma et al., 1991; Gratiot et al., 2007; Vantrepotte et al., 2013).

POC and SPM exhibit a strong correlation in the mudbank areas, which can be seen in both in-situ and satellite data as mentioned in section 4.2.1.2. This latter feature further highlights that these mudbanks can hold a "stock" of organic matter in addition to the inorganic fraction. This can be explained by the presence of organic matter that could be related to exports from the mangrove forests that were destroyed and buried during the mudbank migration processes (Aller & Blair, 2006; Berlamont et al., 1993; Gardel & Gratiot, 2005).

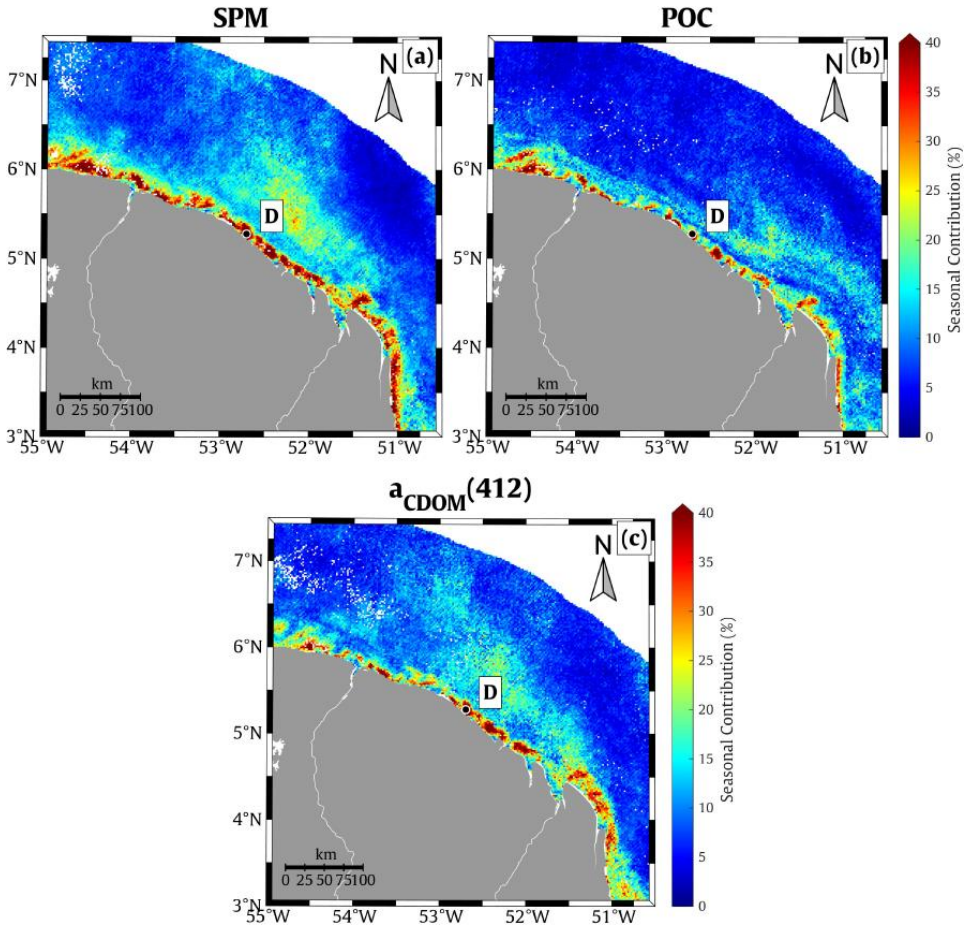

Figure 4.15. *Location of the extracted point D for the trend term of* ***a)*** *SPM,* ***b)*** *Chlorophyll-a, and* ***c)*** $a_{CDOM}(412)$.

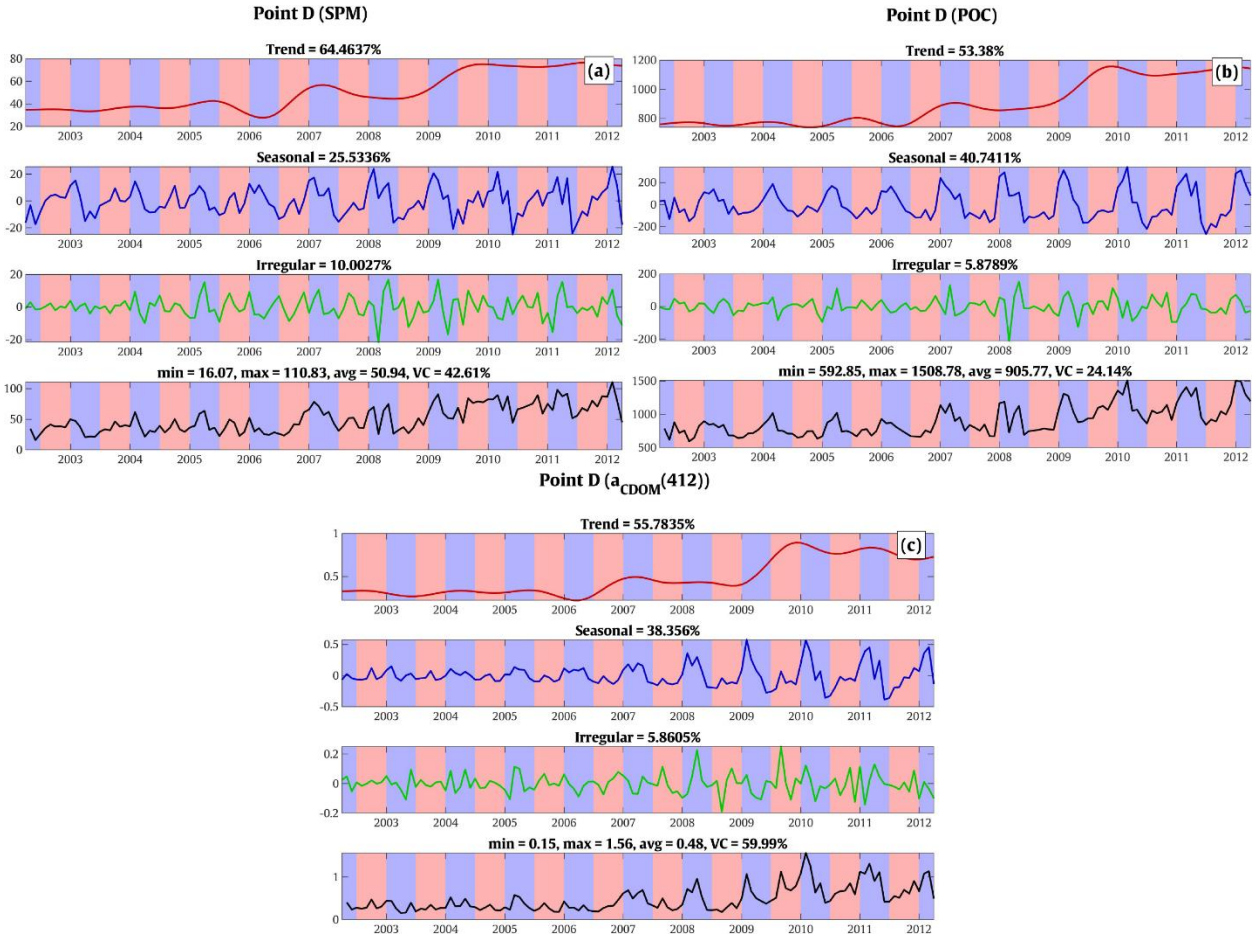

Figure 4.16. *X-11 term statistics calculated for* ***a)*** *SPM,* ***b)*** *POC, and* ***c)*** $a_{CDOM}(412)$ *for the point D shown in* ***Figure 4.15****. The red, blue, and green solid lines correspond to Trend, Seasonal, and Irregular terms, respectively. The black solid line presents the original time series. Pink and Blue areas indicate wet and dry seasons, respectively.*

In order to evaluate the impact of French Guiana rivers on the longshore-distributed mudbanks during high flow conditions, the discharge data collected from the station located in the Maroni River (see section 2.4) was used to perform the correlation with the satellite-derived variation of different considered parameters with a focus on the inner shelf area (**Figure 4.17**). The results show that the organic concentration within the mudbanks seems to be more regulated by river discharge when comparing with SPM, which exhibits a higher correlation in the Maroni River outlet than that of the Oiapoque River. This finding is in agreement with earlier research (Lambs et al., 2007; Prost, 1989) as the amount of suspended sediment originating from local sources is relatively minor in comparison with the sediment transported along the shore (see section 1.2.1.1). Besides, contribution of dissolved organic substances stemming from local

rivers to the coastal domain might be more pronounced during dry season due to the dilution effect occurring under high flow condition, which leads to a factor of 1.3 increase in DOC in dry period (Ray et al., 2018). This latter feature was further confirmed by the CDOM plume captured by Sentinel-2 satellite over the Counamama's estuarine areas in the end of the wet season (**Figure 4.18**).

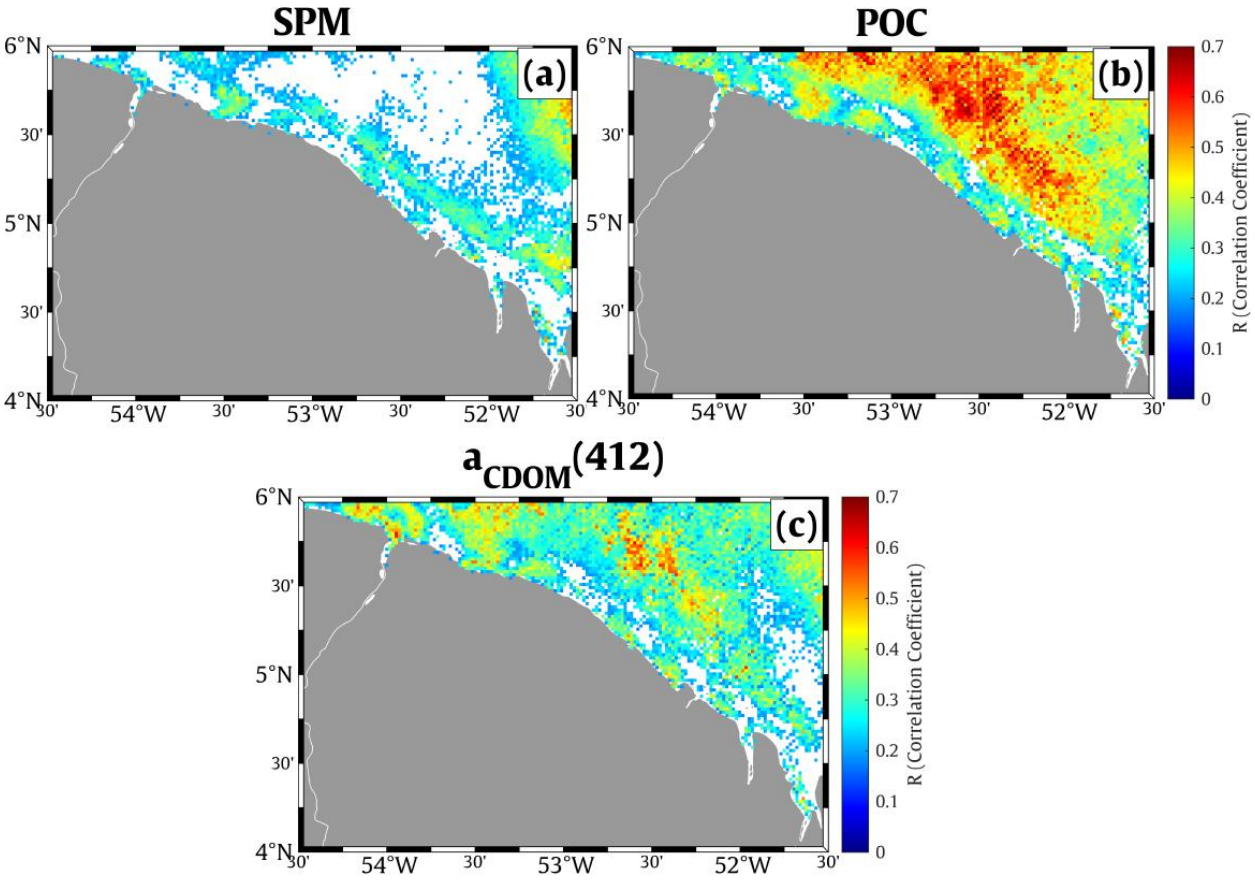

Figure 4.17. *Correlation between Oiapoque River's discharge and* ***a)*** *SPM,* ***b)*** *POC, and* ***c)*** *$a_{CDOM}(412)$ over 10-year period of MERIS data.*

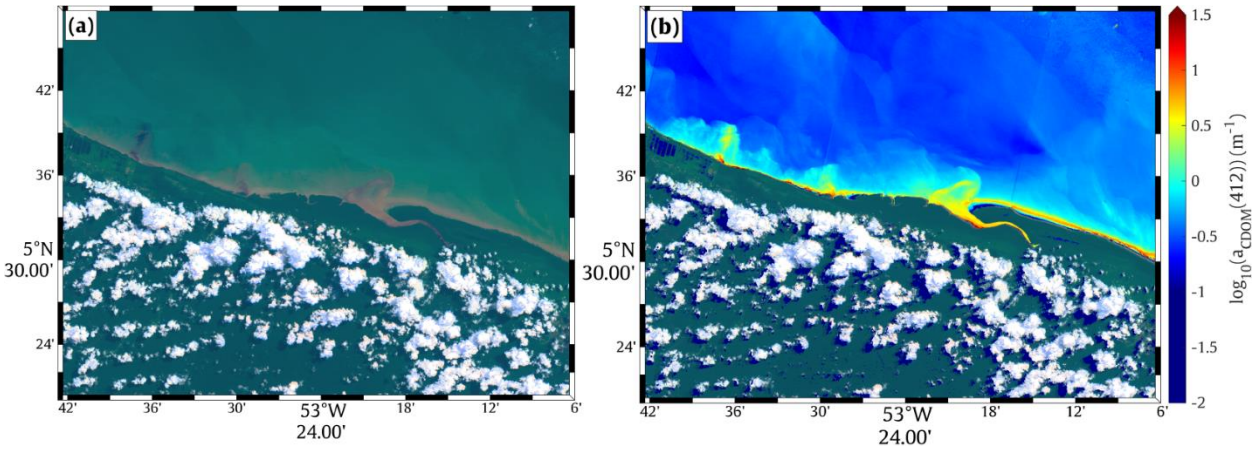

Figure 4.18. *Illustration of the river plume captured from Sentinel-2 image in Counamama's estuary in 19/06/2018;* ***a)*** *True color image and* ***b)*** $a_{CDOM}(412)$

4.3.2.2. Seasonal modulation of Guiana excursion

A seasonal modulation of NBC excursion can be observed beyond the mudbank areas in the seaward direction by a seasonal SPM belt passing through the point E (5°10'30.0"N, 52°23'20.4"W). This seasonal pattern showed higher sediment loads transported to this area between August and October, which appears about 1 – 2 months of delay after the period of retroflection (Baklouti et al., 1998; Johns et al., 1998) . The lowest SPM concentration observed here is about 1.5 $g.m^{-3}$ during the rainy season (in March) and can reach up to 8 times higher with an SPM value of 12.5 $g.m^{-3}$ in the dry season **Figure 4.20**. The factor leading to this annual-cycle variation in SPM can be related to two possible processes. During the retroflection with a maximum intensity of NBC, it bifurcated into two flows with different directions. A part of NBC deviated to the North to join the retroflected flow between latitudes 5°N - 7°N. The remaining portion of NBC continues flowing over the inner shelf, which delivers a significant amount of Amazon sediment loads and also implies an excursion of NBC along the French Guiana's coast with a buffer of about one month (Baklouti et al., 2007; Didden & Schott, 1992; Fonseca et al., 2004).

Unlike the observations obtained in the retroflection zone, the temporal variability of phytoplankton biomass within the aforementioned seasonal belt displayed an opposite pattern to the fluctuation of SPM. A significant contribution of the seasonal component for Chl-a (≈ 80 %) presents remarkable peaks during the rainy season between February and March. The annual rainfall and local river runoffs might be responsible for the growth of phytoplankton in this area (Cloern, 1996; Harding et al., 2016). On the other hand, another possible process can be related

to the sediment transports from the Amazon river's mouth, which is potentially induced by shifts in wind direction during the dry period. This might increase light attenuation which directly hampers the development of phytoplankton productivity (Cloern, 1987; Dokulil, 1994). Such result is consistent with POC observations in local estuarine waters (the Sinnamary River, See **Figure 1.10**) conducted by Ray et al., (2018) as the source of POC is potentially related to freshwater phytoplankton and could be attributed to monsoonal run-off.

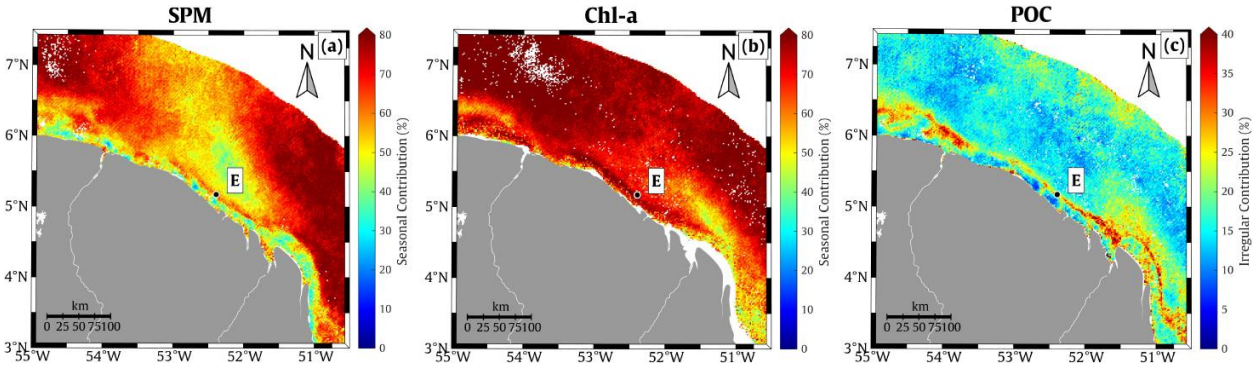

Figure 4.19. *Location of the extracted points E located about 18 km away from the shore for* ***a)*** *seasonal contribution of SPM,* ***b)*** *seasonal contribution of Chl-a, and* ***c)*** *irregular contribution of POC.*

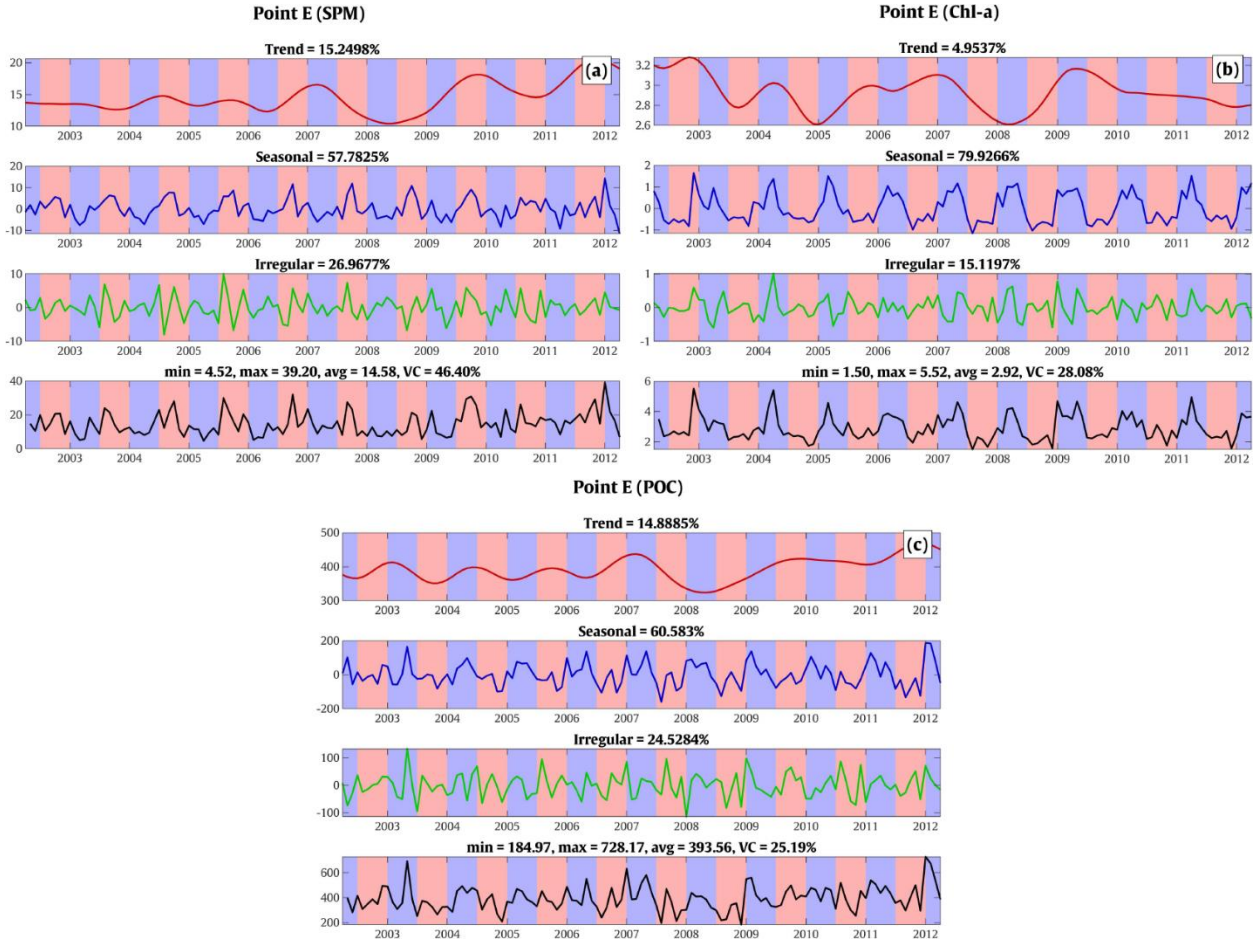

Figure 4.20. *X-11 term statistics calculated for* ***a)*** *SPM,* ***b)*** *Chl-a, and* ***c)*** *POC for the point E shown in* ***Figure 4.19****. The red, blue, and green solid lines correspond to Trend, Seasonal, and Irregular terms, respectively. The black solid line presents the original time series. Pink and Blue areas indicate wet and dry seasons, respectively.*

The temporal dynamics of the POC within the irregular belt (**Figure 4.19.c** and **Figure 4.20.c**) are associated with Var-I reaching up to 24 %. Since the seasonal development of phytoplankton mainly appears during the wet season, the persist presence of the POC here is potentially linked to the contribution of non-living sources such as detritus that could be transported from the Amazon river's plume between August and October (Salisbury et al., 2011). In addition, the higher organic concentration generally appears during the high flow period, emphasizing the importance of river discharge and surface runoff that potentially introduces more mangrove-derived organic matter (Ray et al., 2018). The obtained results also suggest a comparable POC pool originating from the Amazon River and local origins, which might lead to the unstable variation of organic matter. Further, this might also be due to fine scale processes

(tidal pumping) shown as an important driver of organic carbon exchanges in the mangrove-dominated Sinnamary estuary (Ray et al., 2020) as well as modulations in POC exports towards the open ocean in terms of freshwaters inputs or current regimes.

4.3.2.3. Organic fraction in local estuaries

Sentinel-3/OLCI archives have been used to illustrate the impact of the local rivers of French Guiana (including Oiapoque and Maroni) as the higher spatial resolution of these satellite sensors allows for a more in-depth view into the estuarine regions. Here, we considered the averaged maps of POC/SPM presented in **Figure 4.21** since this ratio explains the fraction of organic pool to the total suspended materials. In off-shore regions, the properties of the waters are mainly dominated by organic components with POC/SPM values > 0.06 (Gardner et al., 2006; Loisel & Morel, 1998; Stramski et al., 2008; Woźniak et al., 2010). An extension of POC/SPM content into the mouth of these two rivers and the coastal domain observed during dry season clearly indicates an intrusion of organic materials related to the Amazon plume **Figure 4.21.b,d**. This aligns well with previous work of Gardel et al., (2021) as a periodic external supply of saline waters and mud was recorded from August to December. In contrast, this "inorganic boundary" tends to be pushed down stream in wet season as a consequence of increased river discharge. Interestingly, the POC/SPM value seems to be more significant during high flow period in the upstream areas of the Maroni and Oiapoque rivers, which suggests an increased concentration of organic materials flushed out from the local rivers (**Figure 4.21.a,c**). In addition, the persistent presence of mineral-dominated waters along the shoreline can explain the discontinuity of the POC/SPM gradients.

The medium spatial resolution of Sentinel-3/OLCI archives has enabled a comprehensive analysis of the impact of local rivers in French Guiana on estuarine regions, highlighting the fluctuations of organic and inorganic materials in these areas. Seasonal variations in POC/SPM values further underscore the complex interplay between river discharge, Amazon plume intrusion, and biogeochemical dynamics in estuarine regions.

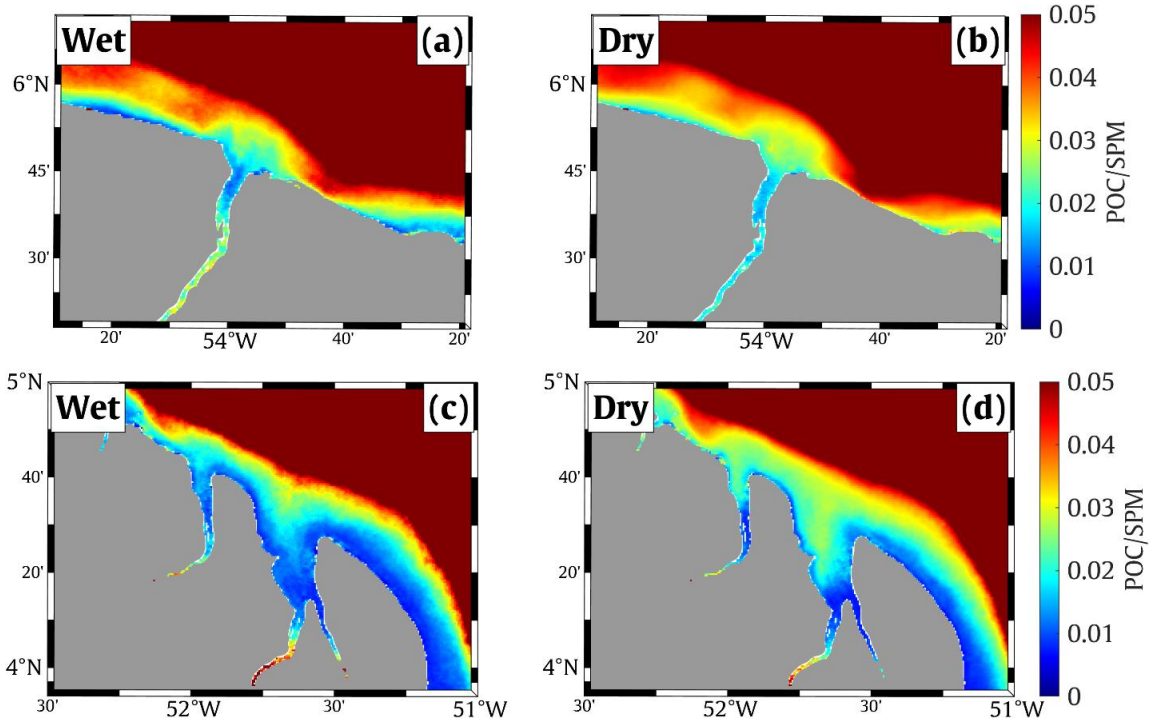

Figure 4.21. *POC/SPM ratio calculated from Sentinel-3/OLCI data in Wet and Dry seasons for* ***a, b)*** *the Maroni estuary and for* ***c, d)*** *the Oiapoque estuary.*

The contribution of dissolved and particulate organic carbon from local rivers is described in **Figure 4.22**, where the monthly fluctuations of different biogeochemical variables in the river outlet and the Maroni River discharge are presented as a function of time. The temporal variation of POC and $a_{CDOM}(412)$ exhibits a fine covariation with the river flow, while this pattern seems to be less pronounced for SPM concentration. In addition, the increasing trend found for all parameters from January to April can also be attributed to the influence of strong Trade winds through resuspension process (Eisma et al., 1991; Gratiot et al., 2007; Vantrepotte et al., 2013).

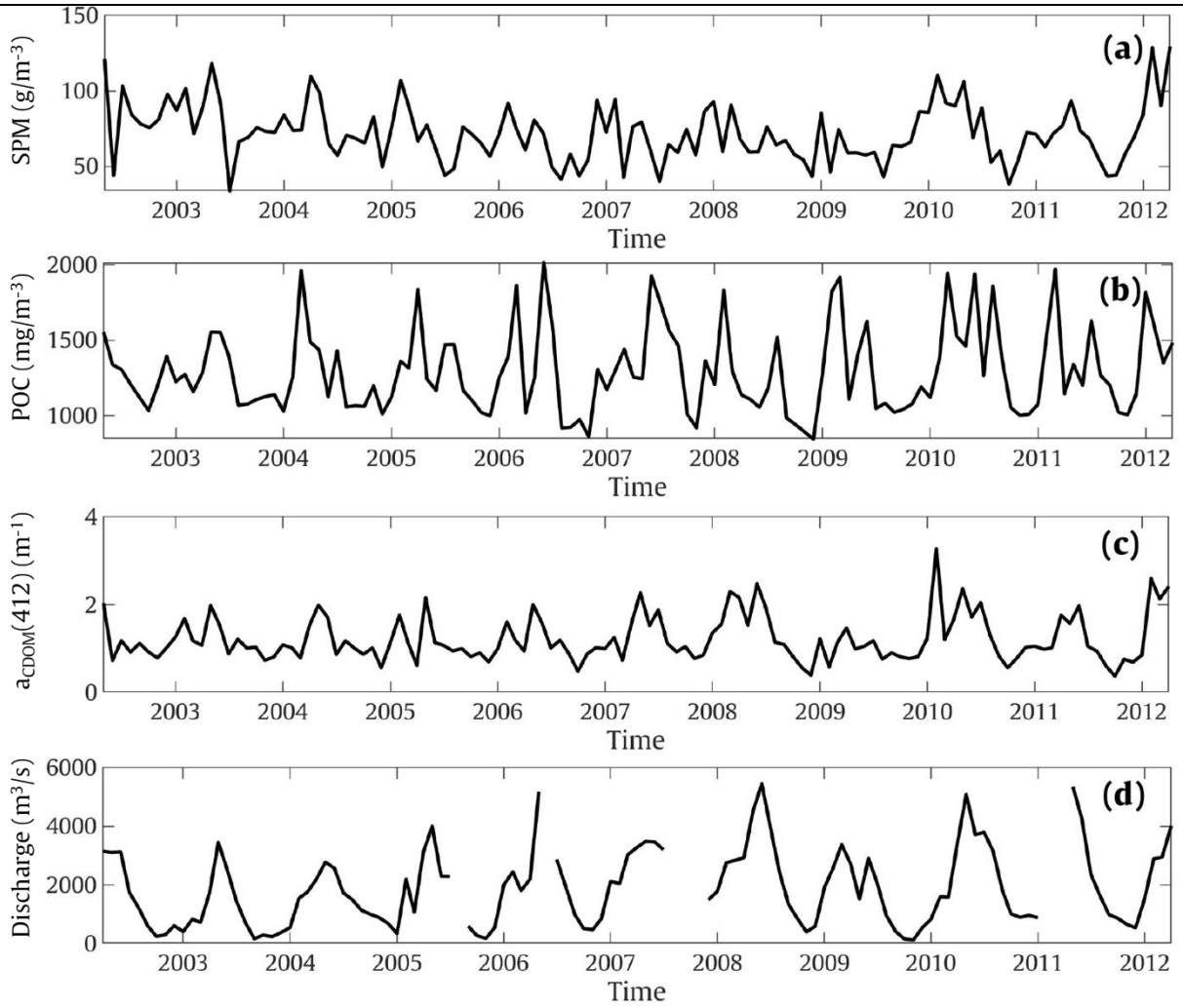

Figure 4.22. *Temporal evolution of monthly* ***a)*** *SPM,* ***b)*** *POC,* ***c)*** $a_{CDOM}(412)$ *extracted in the Maroni River outflow, and* ***d)*** *river discharge measured at the station located in the Maroni River over GlobCoast time period.*

4.4. Long-term changes

In addition to the examination of the spatio-temporal variability patterns of biogeochemical parameters, specific analyses were performed to detect the presence of significant long-term changes (seasonal Mann Kendall test and Sen's slope estimator) in the biogeochemical quality of the French Guiana marine waters. This was in practice performed over the GlobCoast MERIS (2002-2012) and GlobColour (1997-2021) archives (**Figure 4.23** and **Figure 4.24**, respectively).

The alteration of increasing-decreasing patterns found for all the parameters considered in the ultra-coastal domain up to about 20 km from the shore. This feature, as underlined in previous works (Vantrepotte et al., 2011, 2013; Gensac et al., 2016) is associated with the migration of

mudbanks along the coast of French Guiana, affecting the biogeochemical properties of the whole coastal domain (see section 4.3.2.1). The number of these adjacent accretion-erosion areas implies the presence of seven mudbanks stretching over the French Guiana shelf during the 10-year MERIS time period. Mudbank drift is depicted through the accumulation of both dissolved and particulate matter over time as denoted in section 4.3.2.1, for instance at the point D where the contribution of trend term (Var-T) was found to be significantly high up to 64.5% for SPM (**Figure 4.15**). The highest rate of change is found in the mudbank located between Sinnamary river and Kourou river (52°41'42.0"W, 5°16'58.8"N) with a highly increasing rate of mud accumulation up to 17.97 %/year. The highest trends (> 5%/year in absolute value) are clearly found for SPM but are also found for CDOM. These trends are less pronounced for both Chl-a and POC (< 3%/year in absolute value). Besides these mudbanks, which are related interannual changes, indicates no clear pattern can be evidenced over the whole period investigated. This result confirms the impact of mudbanks as a main driver in the coastal domain as well as the pristine status of the study area as well as the trivial impacts of anthropogenic forcings on the French Guiana coastal waters, which is consistent with the MODIS observations conducted by Gallay et al., (2018).

The analysis over 21 years of GlobColour data (**Figure 4.24**) offers a limited understanding of finer details (4-km spatial resolution) and is more likely designed to assess the changes occurring in medium to low turbid waters. When focusing on the most off-shore waters some a small but significant decreasing pattern appears for Chl-a (1%/year; **Figure 4.24.a**) in the area significantly impacted by the NBC current retroflection. Conversely, a restricted increase in CDOM is also visible in a patchy area corresponding to the transition zone between coastal and off-shore waters (**Figure 4.24.b**)

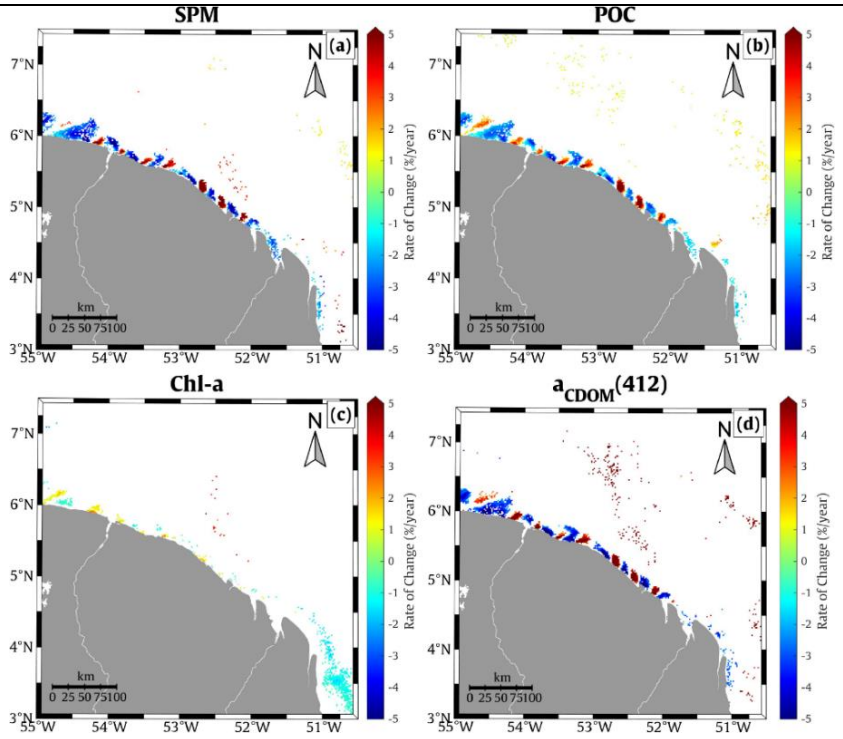

Figure 4.23. *Significant monotonic trend in % per year (seasonal Kendall test, $p < 0.05$) for* ***a)*** *SPM,* ***b)*** *POC,* ***c)*** *Chlorophyll-a, and* ***d)*** *$a_{CDOM}(412)$ calculated over the MERIS time period (2002 - 2012). Non-significant areas are presented in white.*

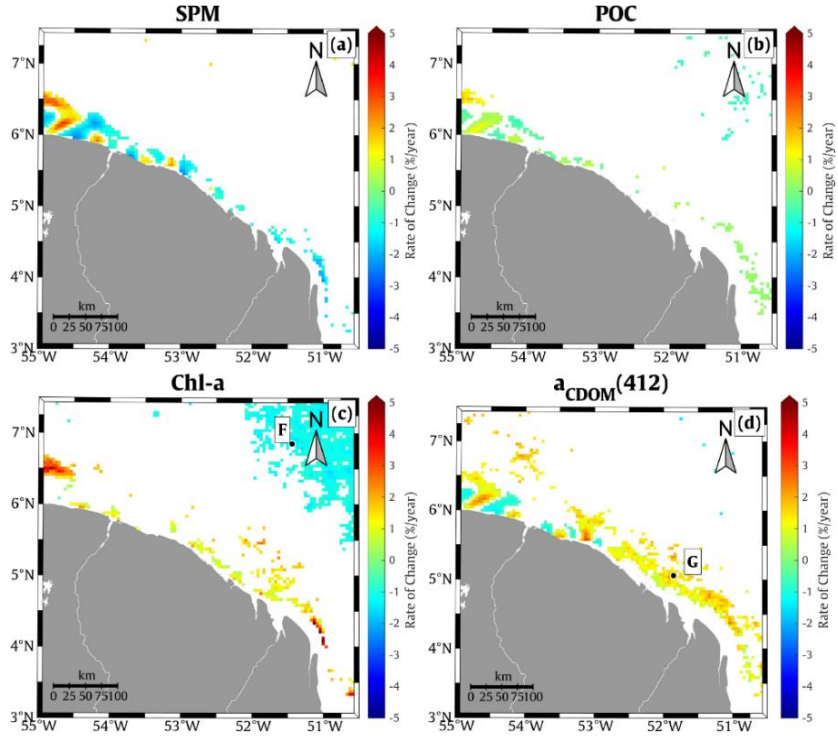

Figure 4.24. *Same as* ***Figure 4.24*** *but for GlobColour dataset (1997 - 2021)*

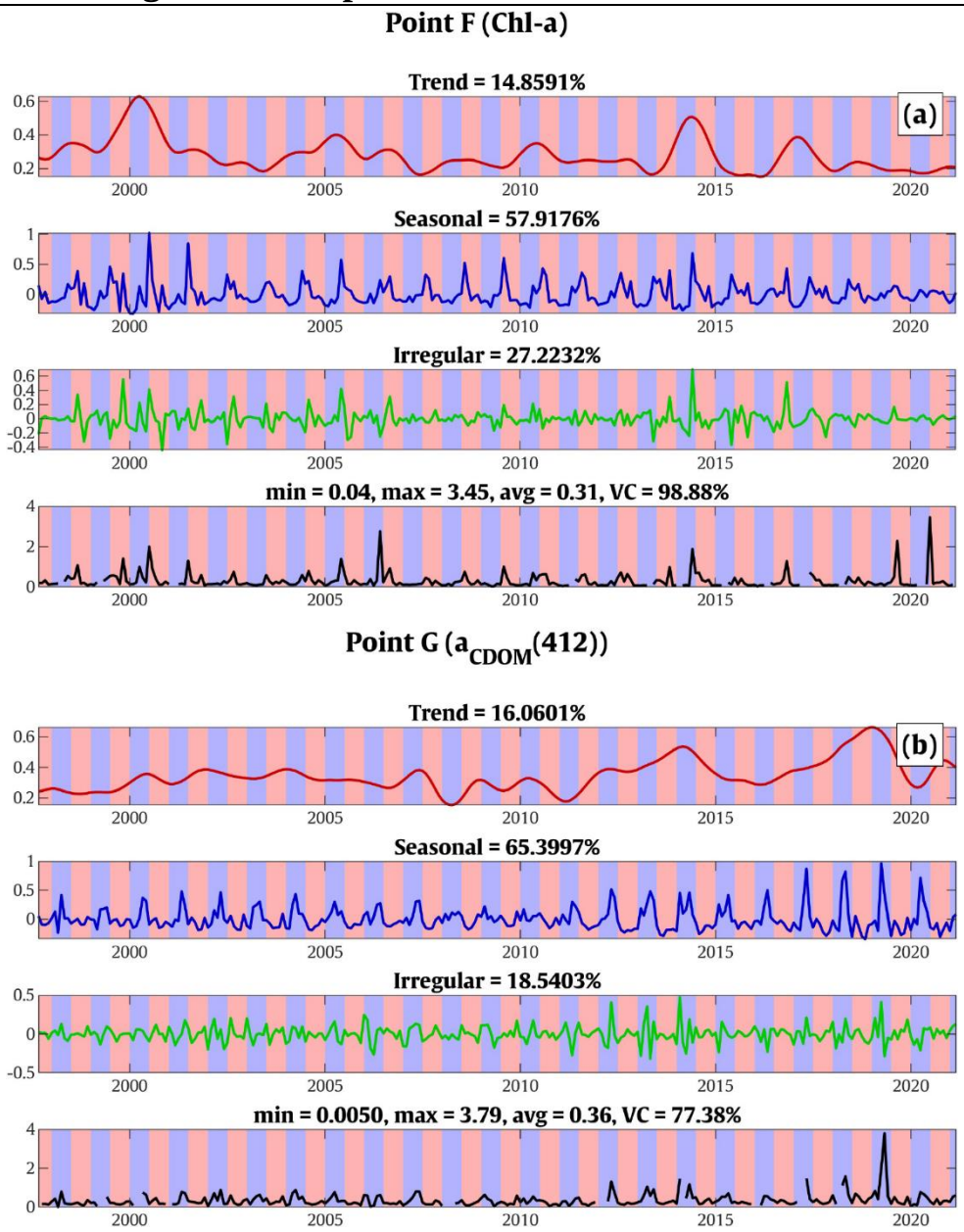

Figure 4.25. *X-11 term statistics calculated for* ***a)*** *Chl-a and* ***b)*** $a_{CDOM}(412)$ *for the points F and G shown in* ***Figure 4.24*** *using GlobColour data (1997 - 2021). The red, blue, and green solid lines correspond to Trend, Seasonal, and Irregular terms, respectively. The black solid line presents the original time series. Pink and Blue areas indicate wet and dry seasons, respectively.*

4.5. Proxies for monitoring French Guiana marine waters

To investigate redundancy between various biogeochemical variables, co-variation analyses were conducted using the GlobCoast ocean color archive. Indeed, the SPM which represents both organic and inorganic content in the water mass, which confirms the importance of this

parameter in terms of coastal water quality context. Further, the correlations in the variation between SPM and other parameters were fairly different over 12 years of MERIS's lifetime **Figure 4.28.a,c**. As aforementioned, even though being a crucial parameter for monitoring water quality, the estimation of Chl-a over the study area has been found to be not reliable as the optical signal of Chl-a is typically influenced by co-occurring constituents such as SPM and CDOM within ultra-turbid environments (OWT 5, see section 3.8). **Figure 4.26** and **Figure 4.27** clearly illustrate the limitation of Chl-a retrieval in optically complex environments where pixels corresponding to ultra-turbid waters (i.e., mudbanks regions) have been masked. While POC/SPM values can provide useful information in these particular regions.

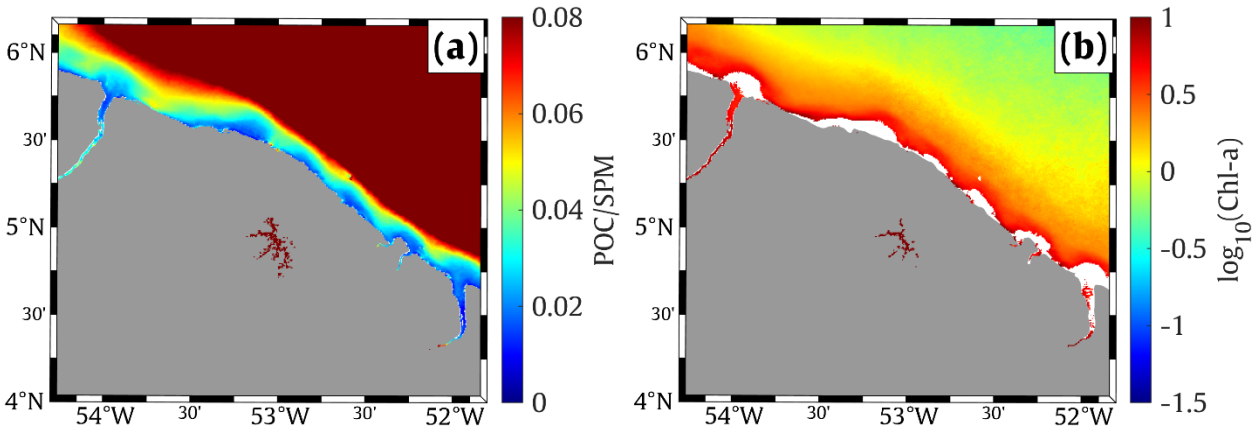

Figure 4.26. *Sentinel-3/OLCI averaged* ***a)*** *POC/SPM and* ***b)*** *Chlorophyll-a computed over French Guiana coastal domain from 04/2016 until 11/2022. The ultra-turbid waters (OWT 5) were masked in white (see section 3.8).*

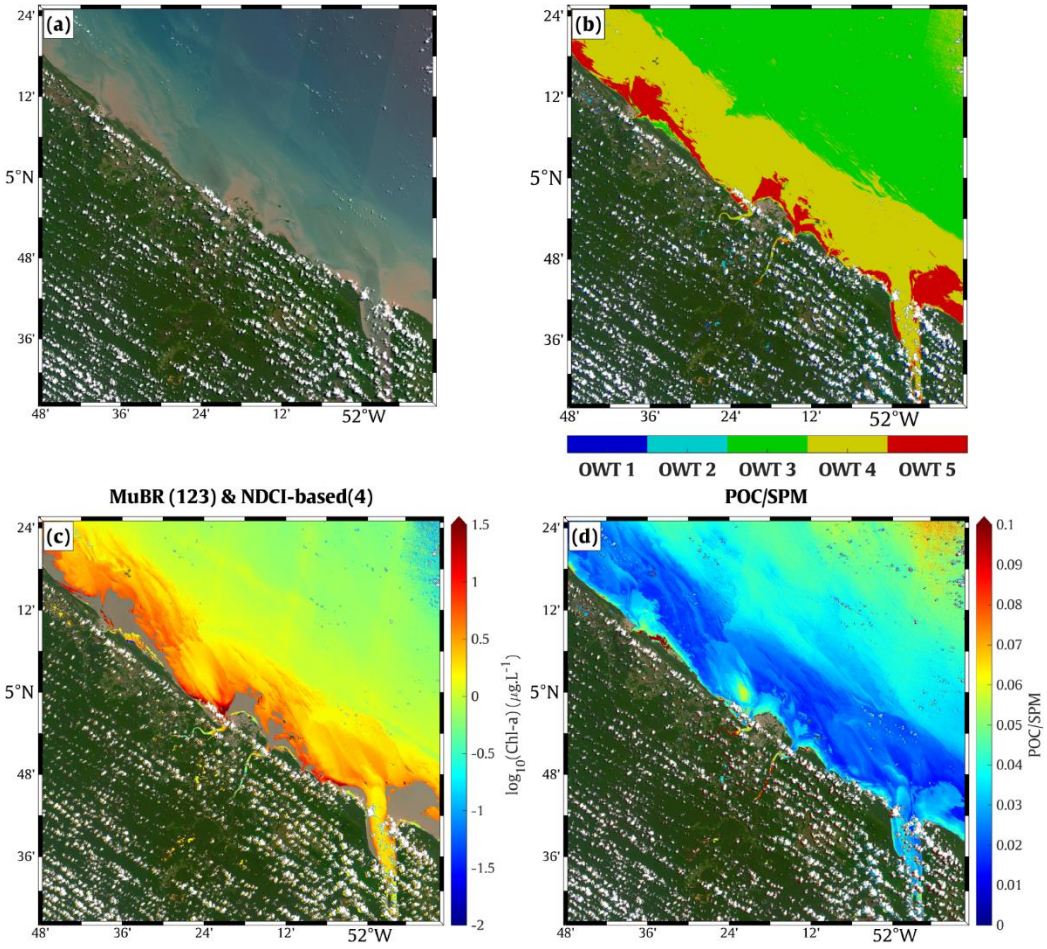

Figure 4.27. *Illustration for the potential of POC/SPM ratio as an indicator to monitor coastal water quality in French Guiana.* ***a)*** *True color image of a Sentinel-2 scene capturing Cayenne's coastal zone on 14th August of 2020,* ***b)*** *spatial distribution of the 5 OWTs (see section 3.8) in which ultra-turbid waters (OWT 5) were masked,* ***c)*** *Chlorophyll-a and d) POC/SPM ratio estimated by the selected model indicated in section 3.7.*

Moreover, the variation of phytoplankton biomass primarily follows a similar pattern to that observed for POC presenting a high Pearson correlation coefficient value (R) of > 0.8 in the off-shore domain **Figure 4.28.b**. This can be explained by the fact that phytoplankton biomass contributes significantly to the POC pool through their production of organic matter via photosynthesis over open ocean (Legendre & Rassoulzadegan, 2012; Stramski et al., 2008). Therefore, considering both Chl-a and POC simultaneously might lead to a redundancy which potentially elevates the complexity of subsequent analyses. The covariation between SPM and POC exhibits a non-significant correlation in the off-shore domain especially where the formulation of NBC rings present, signifying the importance of these two parameters in terms of

biogeochemical dynamics over the department. Such results also reflect appropriately the variability of POC and SPM obtained from the X-11 analysis (**Figure 4.28.a,d**). In addition, the covariation examination deployed on $a_{CDOM}(412)$ demonstrates a strong connection between dissolved organic content and sediment loads transported from the Amazon river mouth. This is marked by the positive correlation of SPM and $a_{CDOM}(412)$ variations found in different regions. In addition, the Proxy of Particulate Composition (PPC) has been identified to serve as a suitable indicator for characterizing the nature of the bulk suspended particulate matter (Loisel et al., 2023). With this in mind, the ratios POC/SPM have been further inspected to identify the pertinent variable to follow.

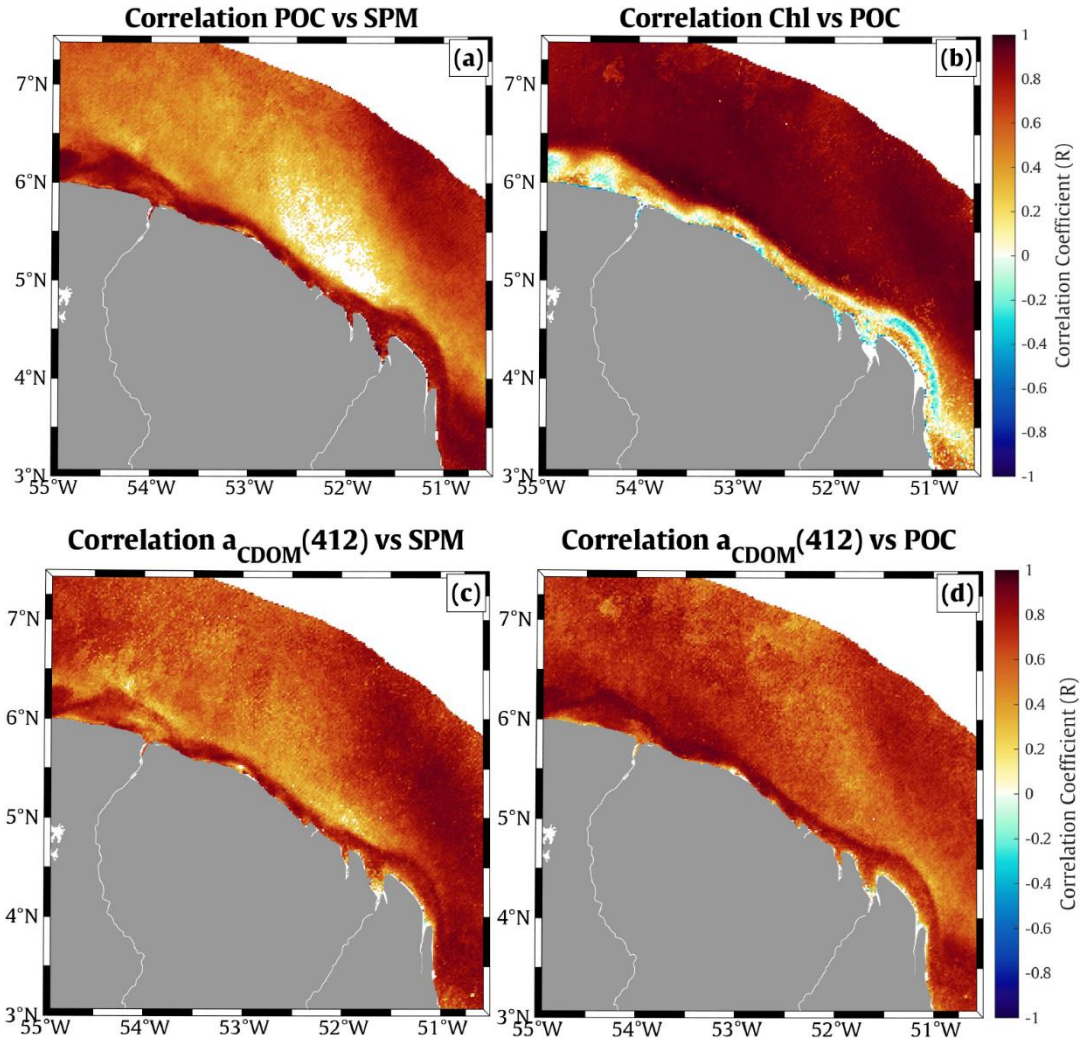

Figure 4.28. *Pearson correlation calculated between* ***a)*** *POC and SPM,* ***b)*** *Chl-a and POC,* ***c)*** *$a_{CDOM}(412)$ and SPM, and d) $a_{CDOM}(412)$ and POC with $p < 0.05$ over the period of MERIS's lifetime.*

Although the POC concentration at the retroflection zone (the point A) shows the highest values from August to October **Figure 4.10.e**, the proportion of organic pool to the total suspended particulate reaches its annual maximum 1-2 months earlier between May and June **Figure 4.30.a**. The variation in POC/SPM ratio in combination with the temporal analysis performed on each individual parameter indicates the presence of organic-dominated water associated with high seasonal contribution (83 %) at the end of the rainy season in the eastern part of the study area. When the retroflection occurs due to southeast winds blowing to a northwest direction, POC/SPM value diminishes gradually and remains stable throughout the rest of the year, presenting a dominance of mineral composition in this region. This result suggests that the Amazon plume transported by the retroflected flow might encompass a significant portion of inorganic matter. In contrast, the coastal domain (the point C) of French Guiana is likely to be driven by physical factors manifesting during the wet season which is potentially related to local sources such as surface run-off from Guianese rivers or/and dilution effects caused by higher rainfall. While the irregular pattern has shifted to the west compared to that observed for SPM. In addition, the tidal currents are possibly responsible for the irregular fluctuation of the POC/SPM ratio in the inner shelf areas **Figure 4.29.c**.

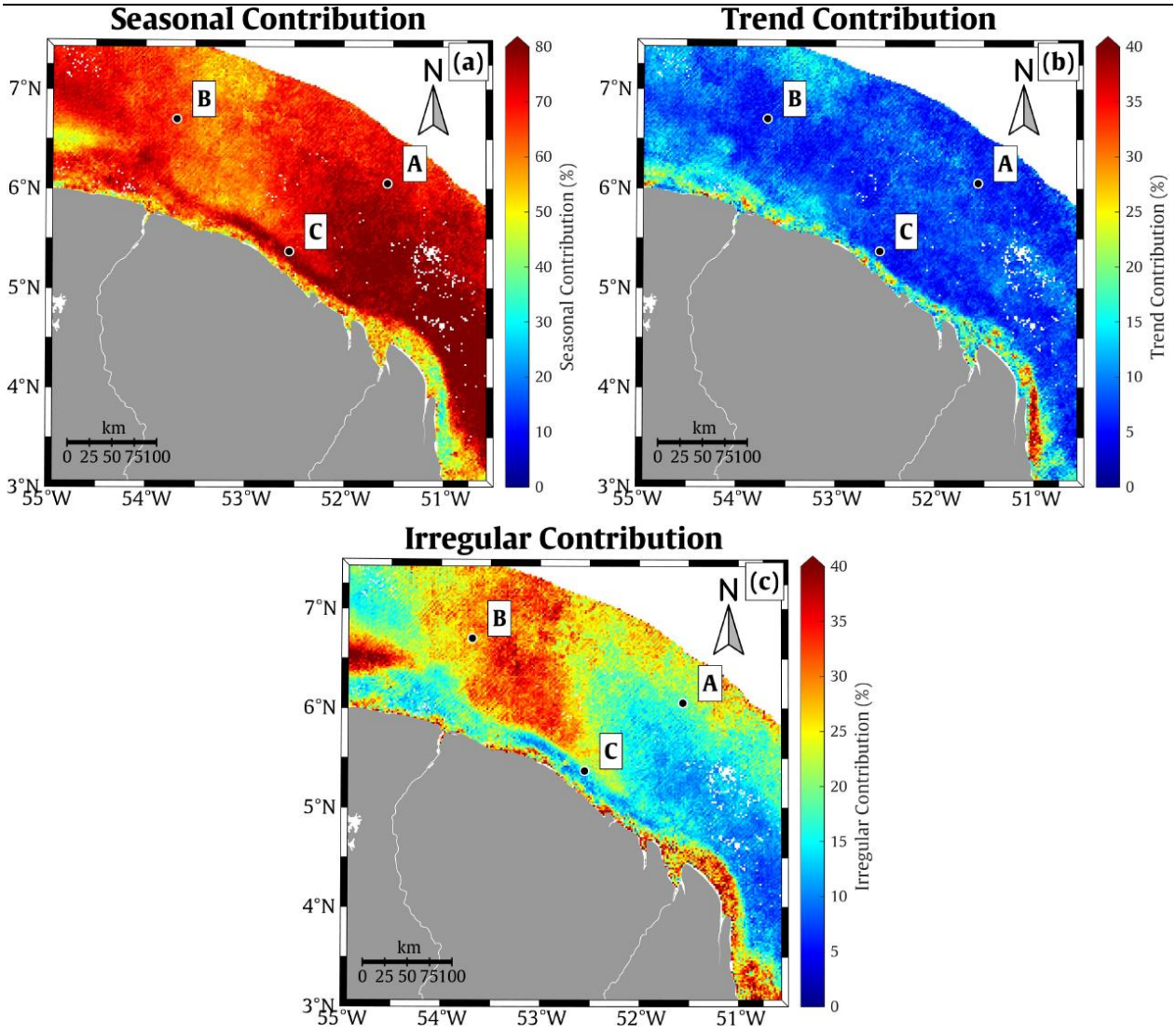

Figure 4.29. *Relative contribution (in %) of the* ***a)*** *seasonal,* ***b)*** *trend,* ***c)*** *irregular components to the total variance of POC/SPM ratio as calculated using the Census X-11 method over the MERIS time period associated with the locations of the extracted points A, B, and C.*

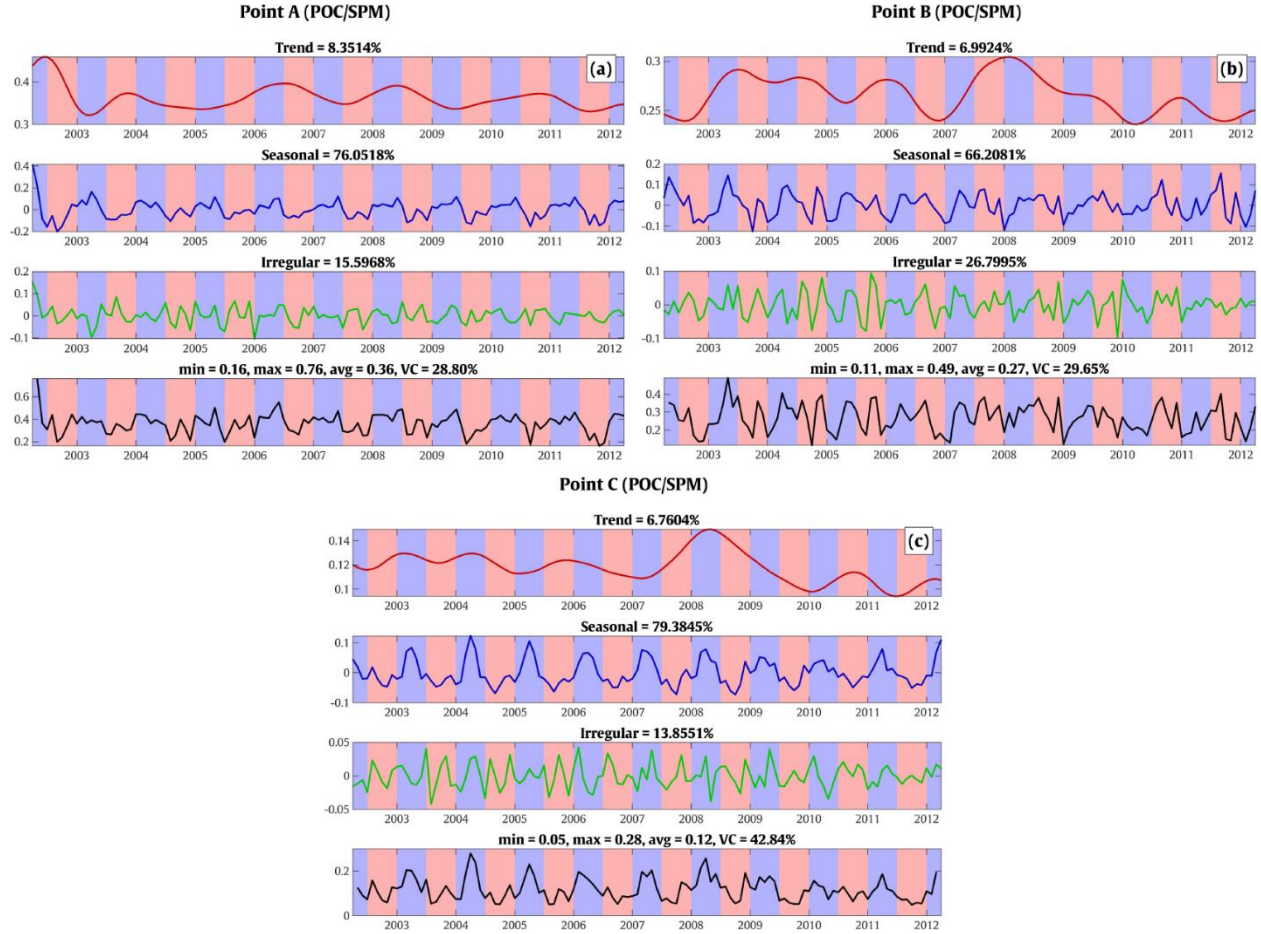

Figure 4.30. *X-11 term statistics calculated for the ratio POC/SPM at the point* ***a)*** *A,* ***b)*** *B, and* ***c)*** *C shown in* ***Figure 4.29****. The red, blue, and green solid lines correspond to Trend, Seasonal, and Irregular terms, respectively. The black solid line presents the original time series. Pink and Blue areas indicate wet and dry seasons, respectively.*

4.6. Conclusions and perspectives

The biogeochemical variability in French Guiana coastal waters has been inspected using spatio-temporal analysis performed on diverse ocean color data sets (monthly MERIS and Globcolour, Sentinel-2 and 3 individual images and temporal composites). The amount of sediment loads in the estuarine vicinity of the Oiapoque river tends to be higher compared to that observed in the Maroni river's outlet with a difference in SPM of 5 to 10 $g.m^{-3}$. Such feature suggests that the Amazon influence seems to be more significantly pronounced in the eastern areas of the Guianese coast.

In off-shore domain, high seasonal contribution found at latitudes 5°N - 7°N and longitudes 52.5°W - 51°W with a distance of beyond 50 km from Oiapoque estuary, confirms the annual-

cycle variation of retroflected flow occurring in the dry season (July - October) due to the manifestation of Trade winds blowing from the southeast direction. An extension of biogeochemical content towards the off-shore regions to the west of French Guiana marine environment during the wet season could be due to the influence of bathymetry and shifts in wind direction. Although these processes were evidenced in the variability of all biogeochemical variables considered, the amplitude of variations of dissolved and particulate substances in the western off-shore extension were found to be relatively lower with respect to that observed in the retroflected flow, indicating a more stable condition. An irregular region of SPM observed in the off-shore domain to the west of the retroflection zone is possibly related to the formulation of the anti-cyclonic NBC rings generated 5 to 6 times per year. The impacts of these NBC rings seem to be more pronounced for SPM compared to other parameters.

In the coastal domain, remarkable values of trend component associated with an increase-decrease pattern have been found in the continental shelf, clearly illustrating the northwestward migration of mudbanks originating from the Amazon plume with an average speed of 1-2 km/year. The seasonal alteration in SPM concentration associated with the mud drifts emphasizes the importance of the wind stress caused by northeasterly trade winds (January - March) in modulating the accretion and erosion of the mudbanks (Gardel & Gratiot, 2005; Vantrepotte et al., 2013). The organic content contributed from local rivers are deemed to be more significant compared to the amount of total suspended solids, which is evidenced by a higher correlation between POC and the Maroni River's discharge.

The periodic modulation of the NBC excursion (Guiana current) over the inner shelf might be related to a seasonal belt of SPM witnessed with a distance of 18 km to the coast, which appears 1 to 2 months delay after the retroflection reaches its maximum northerly location. However, the opposite variation found for Chl-a in this specific belt is possibly caused by the availability of light required for phytoplankton growth in the dry season. Further, the fluctuation of POC and $a_{CDOM}(412)$ here exhibits strong irregular variations, which might be explained by the organic carbon contents exported from the mangroves in combination with the sediment transported from the Amazon river's mouth which is potentially in response to the seasonal alteration of wind direction. Another reason is that the impacts at lower time scales such as tidal factors are also potentially responsible for the unstable variability of the organic carbon pool in this particular region.

The monotonic trends depicted from MERIS data covering the 10-year period from 2002 to 2012 shows that there are no significant long-term changes detected except the fingerprint of the mudbank migration along the coastline, which confirms the trivial disturbance caused by anthropogenic forcings acting on the study area. The tight relationship between biogeochemical variability and wind-driven factors over the inner shelf implies that trade winds play a crucial role in governing the biogeochemical dynamics especially particulate materials in coastal domain.

The co-variation test between each pair of biogeochemical parameters highlights the importance of the two parameters POC and SPM in explaining the hydrodynamic and environmental forcings impacting coastal water quality. Further, the PPC also allows to retrieve information over ultra-turbid waters such as those observed in mudbanks regions. This suggests that the POC/SPM ratio could serve as a potential representative parameter for discovering the biogeochemical variability as well as monitoring water quality over the French Guiana coastal ecosystem.

Considering the uncertain factors driving changes in biogeochemical dynamics (i.e., NBC rings, off-shore western extension, Guiana current), the need for additional and periodic in-situ measurements, along with the incorporation of other factors such as wind/current direction and intensity, appears to be of paramount importance to enhance our understanding of these complex processes and their interactions within the marine ecosystem. Questions remain unanswered, for instance, what is the proportion of organic components from local origins compared to that transported from the Amazon River? What is the main reason resulting in an off-shore extension of all biogeochemical parameters to the west? And why the NBC rings are more visible with the variation of SPM compared to other parameters? Therefore, it is crucial to develop an efficient framework (i.e., a relevant classification scheme) to facilitate the implementation of regional monitoring programs, which allows focus on specific areas or water types to effectively establish sampling work.

CHAPTER 5: Partition of the water masses and insights into monitoring water quality in French Guiana

5.1. Introduction

The delimitation of the French Guiana marine waters and their "standard" status are crucial for stakeholders to conduct biogeochemical monitoring campaigns as well as to support the regional policies. In this chapter, we aim at examining different classification methodologies to partition the water masses of the French Guiana marine domain. These classification schemes were developed based on different frames (e.g., optical, temporal, and POC/SPM based) and applied to both medium and high spatial resolution satellite archives, allowing for a comprehensive analysis of the biogeochemical properties associated with each water type. The concept of optical classification involves grouping reflectance spectra and analyzing the associated biogeochemical characteristics to comprehend the properties of the water body. By examining the variations in spectral shapes, we can identify patterns that correspond to specific water properties, such as suspended particulate matter, dissolved organic matter, and phytoplankton communities (Lubac & Loisel, 2007; Mélin & Vantrepotte, 2015; Vantrepotte et al., 2012). The goal of the POC/SPM classification is to partition the water masses into different categories including organic-dominated, mixed, and mineral-dominated, based on the organic fraction to the total suspended particulate assemblages (POC/SPM) present in the water body. This classification approach allows to better understand the composition and distribution of organic and inorganic materials within various water masses, which can provide valuable insights into the biogeochemical dynamics of the marine ecosystem (Loisel et al., 2023; Woźniak et al., 2010). Whereas, the temporal classification using Self-Organizing Maps (SOM) will be used to cluster pixels that exhibit similar variability patterns over time, providing useful information about the spatial distribution of biogeochemical variables in different regions. The identification of marine waters with comparable temporal variations can facilitate the analysis of the biogeochemical dynamics more effectively, which also explains the environmental processes driving the changes in the marine ecosystem (El Hourany et al., 2021). The integration of these classification schemes for partitioning the water masses from satellite data will be described particularly in this chapter, which facilitates the establishment of field cruises for monitoring coastal water quality in the study area.

An addition key objective of this chapter is to propose a sampling strategy based on different classification schemes that can be used as a framework for conducting regional monitoring programs to keep track of the status of the water properties as well as to assess the potential impacts of variations in the environmental conditions. Given the fact that no apparent long-term disturbance was found as denoted in Chapter 4, this chapter also aims at defining a reference state of French Guiana coastal waters for generating a baseline condition that can be used to detect exceptional events. These reference values will be generated from satellite-derived climatological statistics, allowing the identification of deviations from this state as well as the potential disturbances in biogeochemical properties over the marine ecosystems. Such information is essential for stakeholders to develop effective conservation and management of coastal waters, ensuring that policies and actions are well-informed and responsive to the unique characteristics of this marine environment.

5.2. Optical Classification

5.2.1. In-situ $R_{rs}(\lambda)$ Classification

Even though the implementation of in-situ measurements typically is labor-intensive and time-consuming, these data offer accurate and direct information about various water quality parameters. Therefore, the field data collected over the French Guiana coastal waters serve as a valuable ground truth for validating and calibrating the attained outcomes from the assimilation of remotely sensed archives, helping to improve the reliability and accuracy of satellite-based observations and understand the complex dynamics of coastal water quality.

It is crucial to note that French Guiana coastal waters are strongly characterized by the influence of the Amazon plume with annual transportation of 1.5×10^8 tons of suspended sediments along the Guianese coast (Wells & Coleman, 1977), which leads to a highly turbid environment observed in the coastal regions. The statistics for SPM extracted from the present dataset confirm this feature as the highest SPM concentration can reach up to 1945.34 $g.m^{-3}$ (**Table 5.1**). As specified in the previous chapter, the highly concentrated SPM and its variability are typically linked to different physical factors such as the migration of mud banks, resuspension processes, the direction as well as the intensity of winds, and ocean currents (J.-M. Froidefond et al., 2002; Gratiot et al., 2007; Vantrepotte et al., 2013). The Chlorophyll-a concentration measured over the study area varies from 0.08 to 48.32 $mg.m^{-3}$ with an average of 6.27 $mg.m^{-3}$. The maximal phytoplankton biomass was recorded on the 25^{th} of August, 2015 at a

distance of approximately 10 km away from the Mahury estuary. As the majority of the water samples were collected within 20 m isobath toward the estuarine vicinity, the summary of the in-situ data exhibits a strong influence of terrestrial inputs. For example, the average concentrations of organic indicators, such as POC, DOC, and $a_{CDOM}(412)$, remain at a remarkable level, with values of 1150.45 $mg.m^{-3}$, 136.65 $\mu mol.L^{-1}$, and 0.94 m^{-1}, respectively. Although the number of sampling points is not always available for all considered parameters, the statistics calculated from our in-situ dataset thoroughly reflect the status of French Guiana coastal waters.

Considering the unique biogeochemical conditions of the study area, the unsupervised classification has been performed on 200 measurements of hyperspectral $R_{rs}(\lambda)$ that were normalized in order to partition the water masses into four distinct Optical Water Types (OWTs). Indeed, the results obtained from this clustering approach rely on the performance of the hierarchical classification proposed by Ward, (1963) as mentioned in section 2.2.1. Conceptually, each optical OWT is associated with a number of measurements that are relatively similar in terms of spectral reflectance shape. It is worth noting that, the measurements belonging to a specific OWT do not necessarily elucidate a similarity in the magnitude of the remote sensing reflectance values due to the normalization.

Different numbers of OWTs were examined using the in-situ $R_{rs}(\lambda)$ data with the aim of selecting the optimal number of water types that adequately capture the biogeochemical variability in the region. The shape of the most contrasted OWT remains similar across all three cases, implying robustness in the classification method (**Figure 5.1**). However, 3 OWTs might not be adequate to represent sufficiently the input data as the clear waters, typically peaking in the blue domain, are not apparent in this case. This can be resolved in the case of 4 OWTs allowing offshore waters to be more distinguishable. The case of 5 OWTs seems to complicate the situation by splitting the OWT 3 of the 4-OWT case into two OWTs, which does not bring more useful information. In addition to this, the increase in the number of OWTs in the unsupervised classification step also elevates the similarity between OWTs in terms of spectral shape, which might be susceptible to uncertainties in satellite image application due to various factors (i.e., biases from atmospheric noises, number of samples for each OWT, etc.). Thus, the in-situ dataset has been classified into 4 OWTs for further analysis in this chapter. It is worth noting that depending on the objectives and how large the dataset is, the number of OWTs might

vary accordingly (e.g., 3 OWTs were selected for regional adaptation of inversion algorithms in Chapter 3).

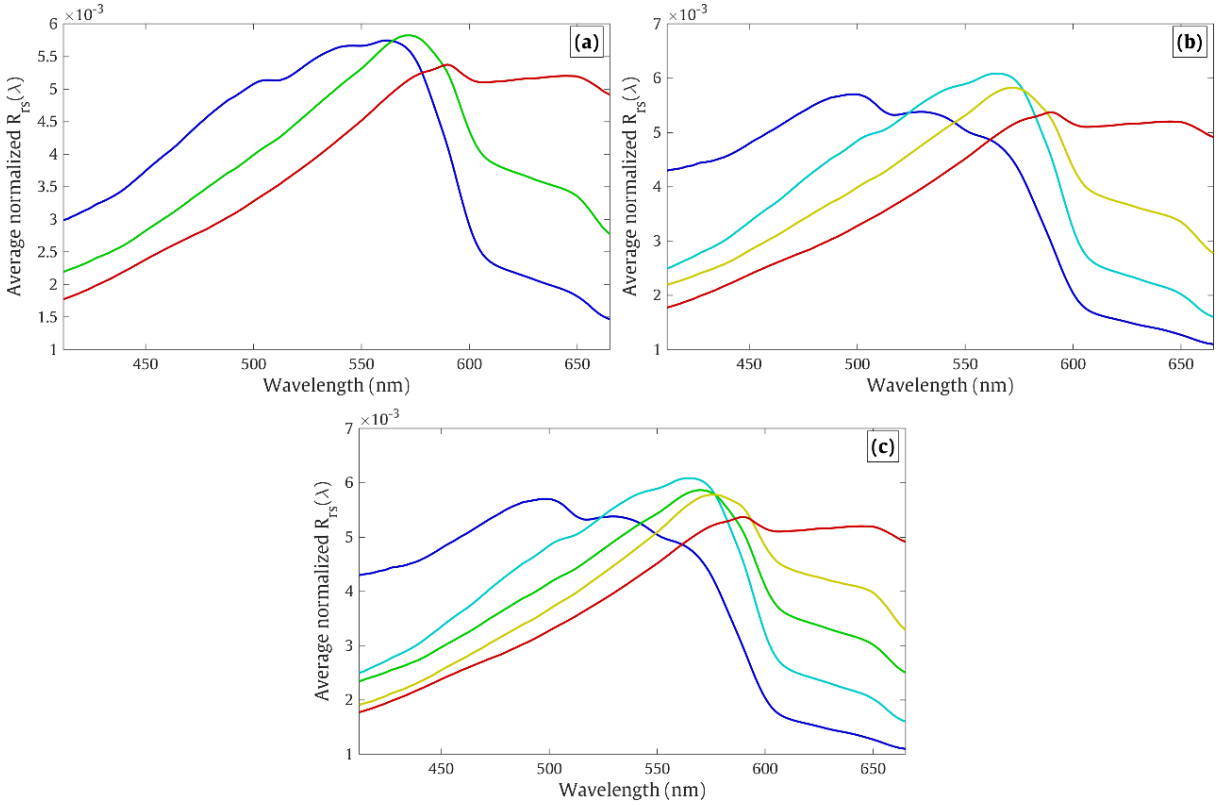

Figure 5.1. *Unsupervised classification performed on 200 $R_{rs}(\lambda)$ spectra collected over French Guiana marine waters using Ward's linkage (see Section 2.2.1) considering the case of* ***a)*** *3 OWTs,* ***b)*** *4 OWTs, and* ***c)*** *5 OWTs.*

Overall, our dataset shows that the highest number of samples was found in OWT 3 with 72 data points, while OWT 1 occupies the smallest proportion with only 16 measurements. The tendency in the appearance of the reflectance shapes from OWT 1 to 4 is illustrated by a gradual increase in the red domain and a diminishment in the blue part of the spectra (**Figure 5.2.a-g**). These shifts in terms of reflectance values can be attributed to the varying types of particles and materials such as sediment or phytoplankton present in the water body (Lubac & Loisel, 2007; Vantrepotte et al., 2012). It is essential to understand the defined OWTs in order to interpret remote sensing data accurately and to identify different environmental conditions of the water masses. Further, the difference in the magnitude of the raw reflectance, as can be seen in **Figure 5.2.b-h**, confirms a wide range of variability associated with each OWT.

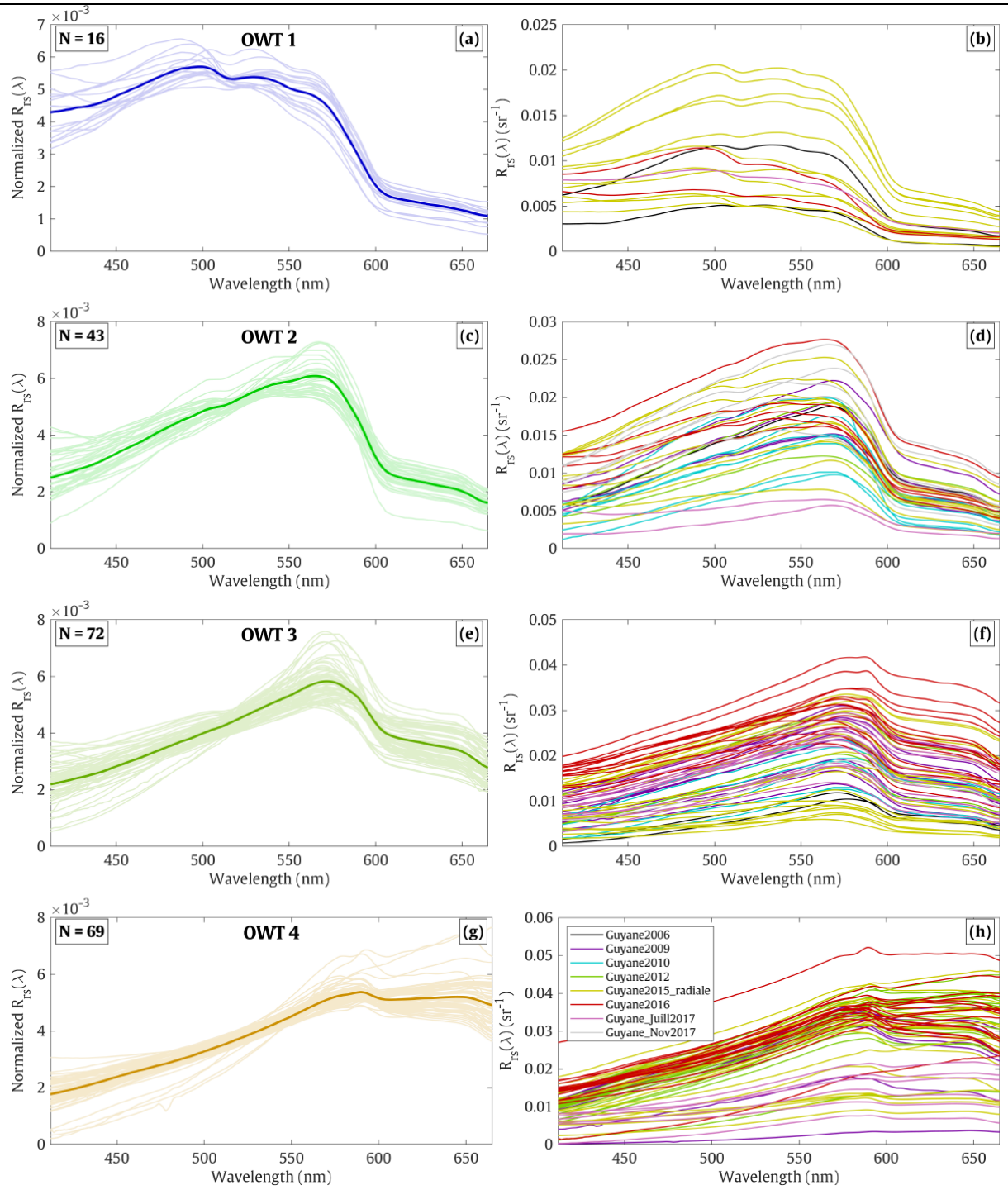

Figure 5.2. *The left panels* ***a-g)*** *show the normalized reflectance associated with the 4 optical OWTs defined from the in-situ dataset. The solid bold lines present the mean of the normalized $R_{rs}(\lambda)$. The right panels* ***b-h)*** *show the raw reflectance for the corresponding OWTs with the colors indicating the names of conducted missions.*

As a matter of fact, the biogeochemical components within a water body can have direct effects on its optical properties, thereby impacting the way remote-sensing reflectance behaves in terms of shape and magnitude. Therefore, the defined optical clusters are related to a range of biogeochemical conditions covered by the current dataset. The significant parameters of each optical OWT are highlighted in bold in **Table 5.1**. These biogeochemical features associated with the corresponding OWT can be elaborated particularly as below:

OWT 1: The analysis performed on the present dataset shows that the average normalized remote sensing reflectance, $R_{rs}(\lambda)$, belonging to OWT 1 is primarily characterized by a strong peak in the blue-green region, specifically around 490 nm. This peak is followed by a steady decline towards 560 nm, before a sharp decrease in the red region around 600 nm. Additionally, the statistics extracted from 16 data points of this OWT indicate that OWT 1 exhibits a relatively lower concentration of suspended particulate matter (SPM) compared to OWT 2 and significant lower than that of OWT 3 and 4. More specifically, the mean and median values of SPM concentration of the collected in-situ dataset are 6.22 $g.m^{-3}$ and 4.39 $g.m^{-3}$, respectively (**Table 5.1**), present an indication of a clear-water environment. Further, the highest value of the POC/SPM ratio (up to 0.1) recorded for OWT 1 indicates a substantial contribution of particulate organic content. The combination of these features associated with OWT-1 waters (i.e., the spectral shape, lower SPM concentration) confirms that this OWT is representative of open ocean water.

OWT 2: OWT 2, which accounts for 43 data points out of a total of 200 samples in our dataset, presents a unique characteristic in its reflectance shape. In particular, the average normalized reflectance of this OWT shows a strong peak in the green part of the spectrum around the wavelength of 560 nm, with the normalized $R_{rs}(560)$ value of approximately 6×10^{-3}, as can be seen in **Figure 5.2**. Unlike OWT-1 waters, which are characterized by a remarkable peak in the blue-green region, OWT-2 waters reflect less blue light and display slightly higher reflectance in the red **(Figure 5.4.a**). Such differences in the reflectance values can be attributed to variations in the biogeochemical composition of the water, such as the presence of dissolved/particulate matter and phytoplankton. This is evidenced by a higher concentration in both particulate and dissolved materials compared to OWT 1. In addition to this, the average value of the POC/SPM ratio observed for this OWT (0.09) falling between 0.08 and 0.2 (Loisel et al., 2023), indicating a mixed situation.

OWT 3: Similar to OWT 2, the reflectance value of OWT 3 also exposes a significant amplitude in the green part of the visible spectrum. However, we find that OWT-3 water also shows higher reflectance values in the red part of the spectrum, which is typically related to the spectral absorption signature of Chl-a in blue and red wavebands (Gons et al., 2008). The highest Chl-a concentration, with a maximum of 48.32 $mg.m^{-3}$ and a mean of 8.16 $mg.m^{-3}$, is recorded in OWT 3, further emphasizing the specific pattern related to the contribution of relatively high phytoplankton biomass to this OWT. This can also be indicated by the highest values observed in Chl-a/POC and a_{ph}/a_p ratios (**Figure 5.3**). Moreover, the higher values in SPM concentration, and lower POC/SPM ratio value (0.05) compared to OWT 1 and OWT 2, imply a relatively high contribution of inorganic materials within the water body. Therefore, OWT-3 water serves as an illustrative example of the involvement of different biogeochemical components, corresponding to mineral-dominated waters with a dominance of phytoplankton population.

OWT 4: With 49 samples, the average reflectance shape belonging to OWT-4 water appears to have strong peaks in the red domain particularly from 590 nm to 665 nm. In contrast, the amplitude of normalized $R_{rs}(\lambda)$ is significantly less pronounced in the blue region of the spectrum. This feature implies that OWT 4 is a good example of Case-2 highly turbid waters, which is representative of an optically complex environment. Indeed, the high turbidity level within this water type is confirmed by the highest in-situ SPM concentration measured among the 4 OWTs within a range of 155.88 ± 278.42 $g.m^{-3}$. The low value of averaged POC/SPM (0.03) presents a significant proportion of mineral particles compared to organic fraction for this OWT.

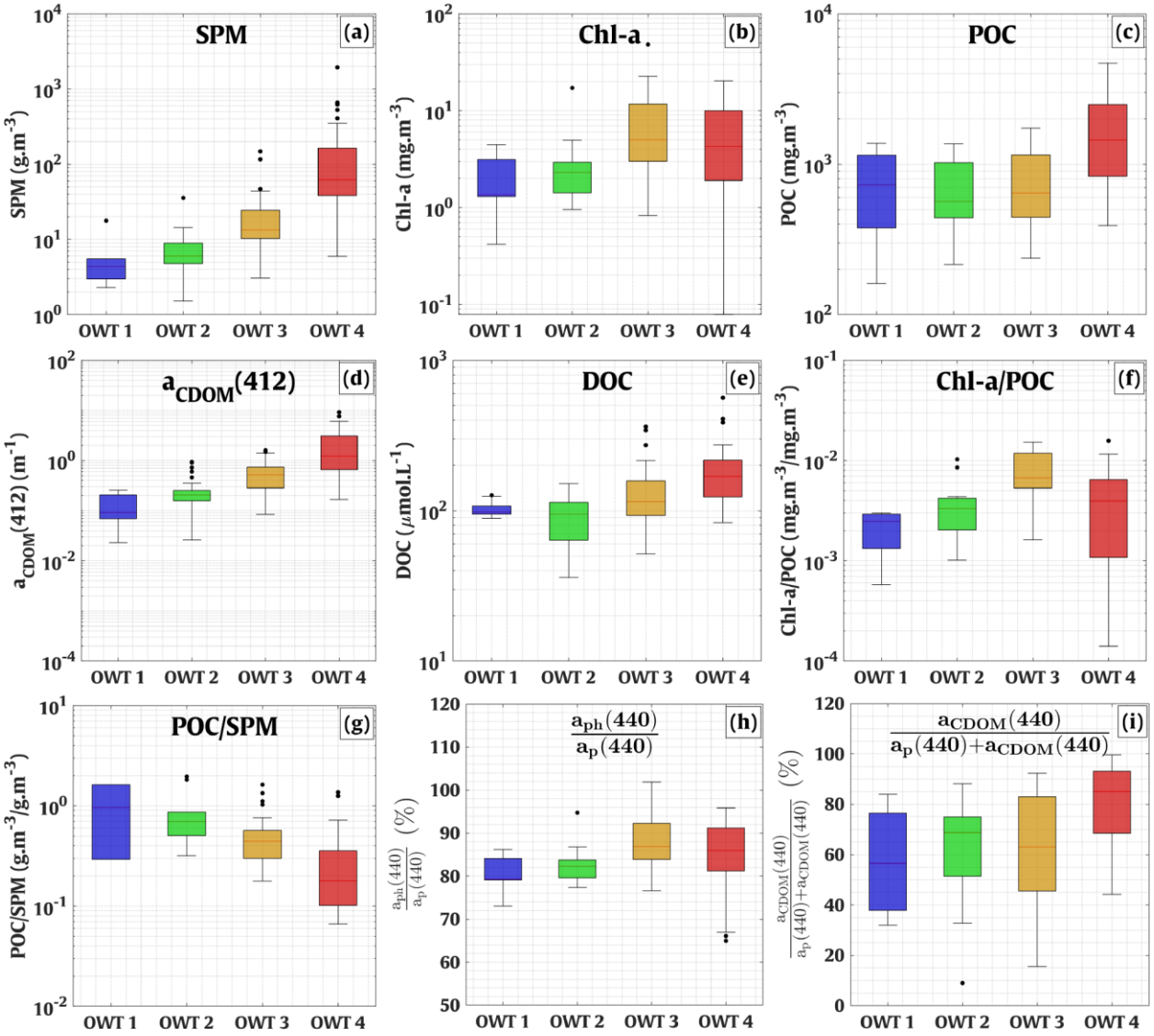

Figure 5.3. *Box plots of* ***a)*** *SPM,* ***b)*** *Chl-a,* ***c)*** *POC,* ***d)*** $a_{CDOM}(412)$, ***e)*** *DOC,* ***f)*** *Chl-a/POC,* ***g)*** *POC/SPM,* ***h)*** $a_{ph}(440)/a_p(440)$, *and* ***i)*** $a_{CDOM}(440)/(a_p(440)+a_{CDOM}(440))$

Table 5.1. *Statistic of the biogeochemical parameters associated with four optical OWTs extracted from the in-situ dataset deployed in French Guiana coastal waters. The parameters with highest mean values among all OWTs are highlighted in bold.*

	Parameters	N	min	max	mean	median	stdv
OWT 1	SPM ($g.m^{-3}$)	6	2.30	17.75	6.22	4.39	5.76
	Chl-a ($mg.m^{-3}$)	7	0.42	4.47	2.14	1.36	1.42
	POC ($mg.m^{-3}$)	5	161.47	1381.09	758.18	729.65	484.02
	a_{CDOM} (412) (m^{-1})	12	0.004	0.26	0.11	0.09	0.09
	DOC ($\mu mol.L^{-1}$)	11	88.92	126.80	102.48	98.27	12.76
	POC/SPM	**2**	**0.03**	**0.16**	**0.10**	**0.10**	**0.09**

	Chl-a/POC	4	0.001	0.003	0.002	0.002	0.001
	$a_{ph}(400)/a_p(400)$	7	0.73	0.86	0.81	0.79	0.04
	$a_{CDOM}(400)/(a_{CDOM}(400)+a_p(400))$	5	0.32	0.84	0.57	0.57	0.22
OWT 2	SPM ($g.m^{-3}$)	31	1.52	35.55	7.55	6.00	5.98
	Chl-a ($mg.m^{-3}$)	18	0.96	17.22	3.22	2.31	3.69
	POC ($mg.m^{-3}$)	20	215.97	1368.54	707.99	566.96	351.52
	a_{CDOM} (412) (m^{-1})	42	0.03	0.94	0.26	0.21	0.20
	DOC ($\mu mol.L^{-1}$)	32	35.99	151.11	90.53	94.83	29.03
	POC/SPM	10	0.03	0.20	0.09	0.07	0.06
	Chl-a/POC	12	0.001	0.010	0.004	0.003	0.003
	$a_{ph}(400)/a_p(400)$	18	0.77	0.95	0.83	0.82	0.04
	$a_{CDOM}(400)/(a_{CDOM}(400)+a_p(400))$	16	0.09	0.88	0.63	0.69	0.20
OWT 3	SPM ($g.m^{-3}$)	56	3.06	148.13	21.38	13.41	24.40
	Chl-a ($mg.m^{-3}$**)**	**41**	**0.83**	**48.32**	**8.16**	**5.01**	**8.60**
	POC ($mg.m^{-3}$)	27	236.90	1739.14	754.82	643.93	410.02
	a_{CDOM} (412) (m^{-1})	70	0.08	1.61	0.56	0.53	0.35
	DOC ($\mu mol.L^{-1}$)	38	51.60	361.82	136.66	115.03	69.66
	POC/SPM	25	0.02	0.16	0.05	0.04	0.04
	Chl-a/POC	**16**	**0.002**	**0.015**	**0.008**	**0.007**	**0.004**
	$a_{ph}(400)/a_p(400)$	**41**	**0.77**	**1.02**	**0.87**	**0.87**	**0.06**
	$a_{CDOM}(400)/(a_{CDOM}(400)+a_p(400))$	40	0.16	0.92	0.62	0.63	0.22
OWT 4	**SPM (**$g.m^{-3}$**)**	**59**	**5.93**	**1945.34**	**155.88**	**62.07**	**278.42**
	Chl-a ($mg.m^{-3}$)	53	0.08	20.24	6.38	4.29	5.60
	POC ($mg.m^{-3}$**)**	**40**	**391.73**	**4705.48**	**1687.82**	**1447.39**	**1106.28**
	$a_{CDOM}(412)$ (m^{-1})	**69**	**0.17**	**9.24**	**1.88**	**1.17**	**1.77**
	DOC ($\mu mol.L^{-1}$**)**	**37**	**83.18**	**564.08**	**189.89**	**169.32**	**96.89**
	POC/SPM	38	0.01	0.14	0.03	0.02	0.03
	Chl-a/POC	34	0.000	0.016	0.005	0.004	0.004
	$a_{ph}(400)/a_p(400)$	53	0.65	0.96	0.85	0.86	0.08
	$a_{CDOM}(400)/(a_{CDOM}(400)+a_p(400))$	**53**	**0.44**	**1.00**	**0.82**	**0.85**	**0.14**
Overall	SPM ($g.m^{-3}$)	121	2.30	1945.34	86.21	29.10	205.93
	Chl-a ($mg.m^{-3}$)	101	0.08	48.32	6.81	4.29	6.96
	POC ($mg.m^{-3}$)	72	161.47	4705.48	1273.39	995.77	982.21
	a_{CDOM} (412) (m^{-1})	151	0.00	9.24	1.13	0.65	1.40
	DOC ($\mu mol.L^{-1}$)	86	51.60	564.08	155.19	127.91	84.53
	POC/SPM	65	0.01	0.16	0.04	0.03	0.04
	Chl-a/POC	54	0.0001	0.016	0.005	0.005	0.004
	$a_{ph}(400)/a_p(400)$	101	0.65	1.02	0.86	0.86	0.07
	$a_{CDOM}(400)/(a_{CDOM}(400)+a_p(400))$	98	0.16	1.00	0.73	0.78	0.21

5.2.2. Satellite image application

It should be noted that the hyperspectral $R_{rs}(\lambda)$ considered in this application were resampled to multispectral bands of common ocean color satellite sensors (i.e., SeaWiFS, OLCI, MERIS; see **Figure 5.4**) before being used to compute the mean (μ) and the covariance (∑) matrices as the input for the $R_{rs}(\lambda)$ labelling procedure. This supervised classification technique has been implemented according to the process explained in Section 2.2.1.

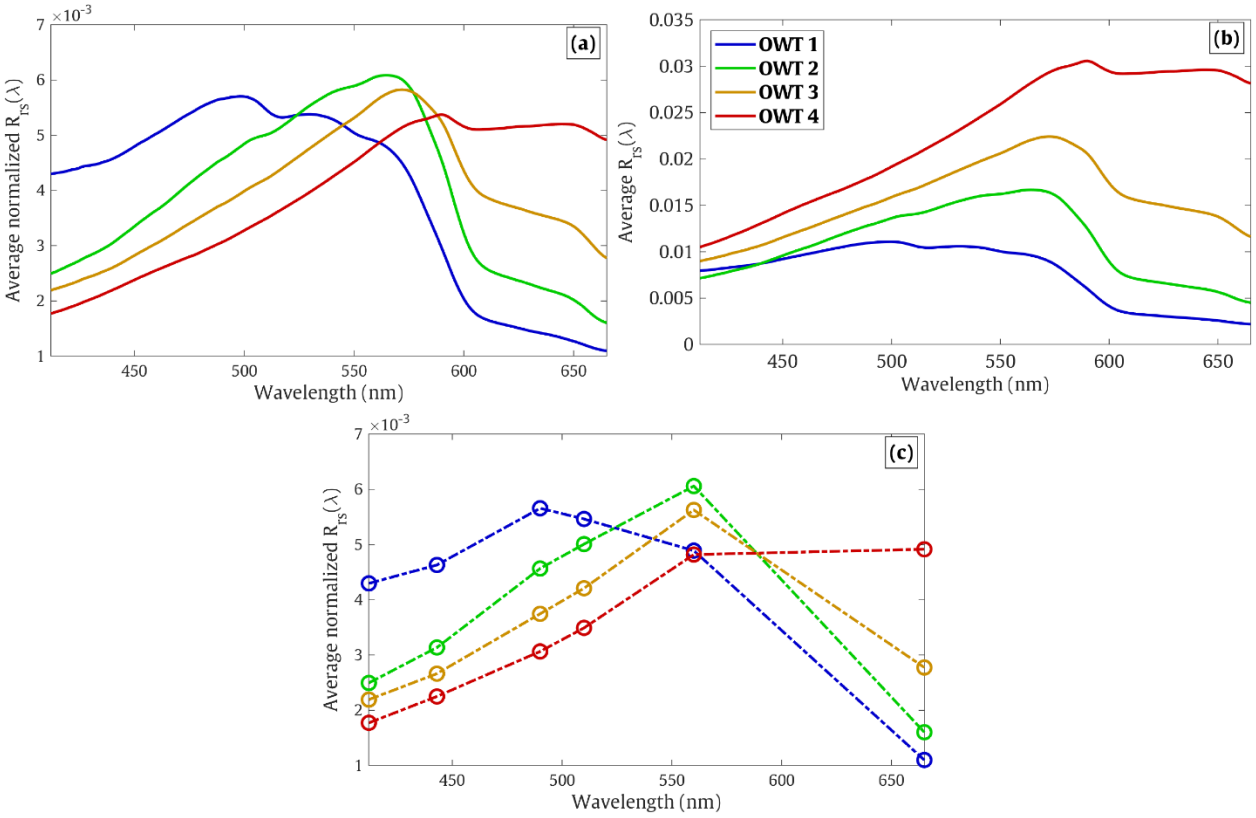

Figure 5.4. *Average reflectance spectra derived from Ward's hierarchical classification applied on* ***a)*** *normalized (OWTs 1, 2, 3, and 4) and* ***b)*** *raw reflectance $R_{rs}(\lambda)$.* ***c)*** *Average normalized reflectance spectra resampled to MERIS bands.*

5.2.2.1. Medium-spatial-resolution classification

The OWT membership labeling for satellite images has been performed on the monthly Level 4 products of Sentinel-3/OLCI sensor with 300 m spatial resolution provided by CMEMS (see section 2.3.1) between 04/2016 and 11/2022. **Figure 5.5.a-d** depict the similarity between the averaged normalized $R_{rs}(\lambda)$ of in-situ measurements and satellite products. The 6-year mean spectral reflectance of Sentinel-3 data are globally consistent with those of in-situ samples considering four defined OWTs. This latter feature confirms the reliability of using optical

classification as a framework to label the corresponding OWTs in remotely sensed data (Mélin & Vantrepotte, 2015; Vantrepotte et al., 2012). However, a slight difference can be observed in the red band for OWT 4 with a remarkable corresponding standard deviation value of 0.0092 of the satellite normalized $R_{rs}(665)$. Indeed, the interpretation from satellite images should be deployed with caution as noises originating from the substantial atmospheric contribution influencing the water leaving optical signals (Pahlevan et al., 2021; Vantrepotte et al., 2012). Moreover, the lack of in-situ measurements in riverine waters for defining OWT sample distributions might also be responsible for this (see Section 2.8.1.2).

Figure 5.5.e describes the spatial distribution of the most-frequent OWT computed for each pixel. As denoted in the previous section, the turbidity level encompassed in a water body increases from OWT 1 to OWT 4, which explains different levels of terrestrial influence on the water masses. For instance, the most turbid waters (OWT 4) were frequently detected over the inner shelf where the biogeochemical dynamics are dominated by mudbank migration (see section 4.3.2.1). Meanwhile, OWT 1, which was identified as a standard illustration of clear water, logically appeared further in offshore regions. These observations present a well-distinguishable delimitation of the water masses and are in good agreement with the optical classification results performed by Mélin & Vantrepotte, (2015); Vantrepotte et al., (2012). Interestingly, the environments holding a high degree of phytoplankton biomass (OWT 3) with Chl-a can reach up to 48.3 $mg.m^{-3}$ were found adjacent to the areas of mudbank manifestation towards the offshore direction. OWT 2, which presents organic-dominated waters according to the threshold of POC/SPM values (> 0.02) recently proposed by Loisel et al., (2023), was observed to be situated between OWT 1 and OWT 3. The spatial dispersion of OWT over French Guiana coastal waters provides valuable insights into the biogeochemical characteristics of the water masses that introduce a better understanding of different aquatic environments co-existing in the region.

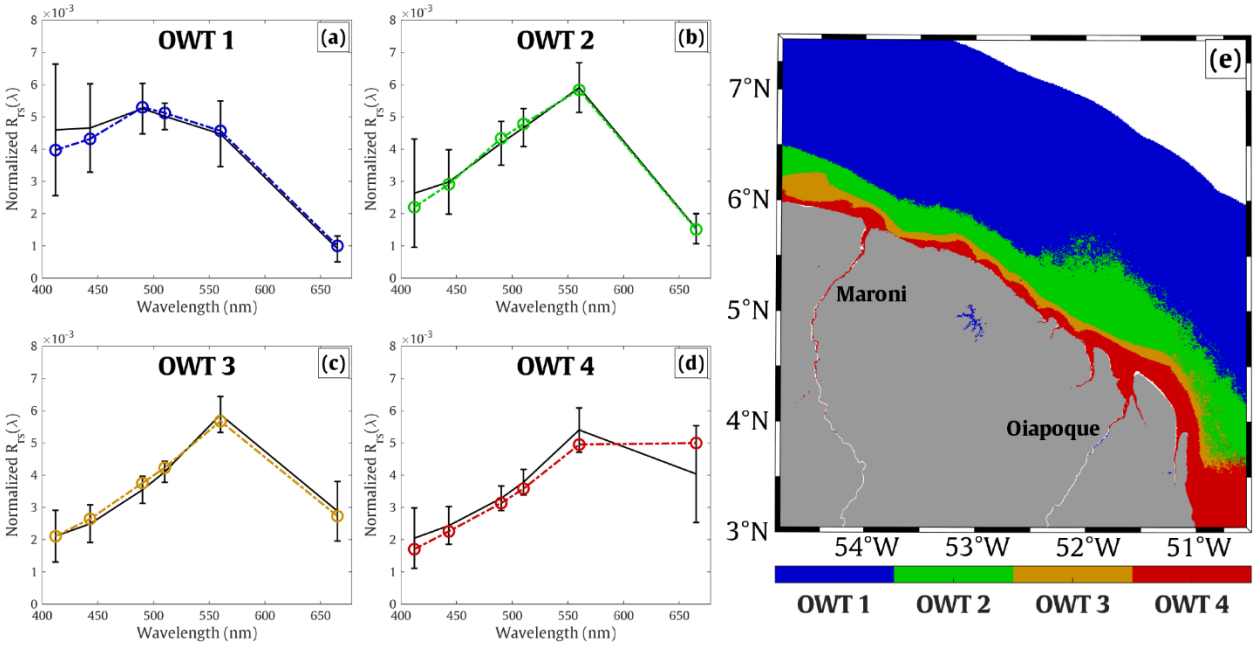

Figure 5.5. *The averaged normalized $R_{rs}(\lambda)$ for* ***a)*** *OWT 1,* ***b)*** *OWT 2,* ***c)*** *OWT 3, and* ***d)*** *OWT 4 where the solid line represents the mean spectra during the Sentinel-3 period (04/2016-11/2022) and the dashed line corresponds to the degraded in-situ spectra (see* ***Figure 5.4.d****); e) most-frequent distribution of OWTs (dominant OWT) over French Guiana coastal waters.*

In order to further exploit the information offered by the optical classification, the number of occurrences for each OWT has been summarized in **Figure 5.6**. A high frequency of OWT 1 has been recorded in the offshore domain, especially on the western side of the study area. This observation indicates less turbid waters are significantly concentrated (about 70 % of the considered period) in this particular region. The results obtained from the analysis of MERIS data in section 4.3.2, particularly presented in **Figure 4.12** and **Figure 5.6.a**, further confirm this feature as the concentrations of both particulate and dissolved matter are relatively lower in the eastern part (point B) compared to those in the western part (point A). In addition, the distribution of OWT 2 was found to be more frequent beyond 15 km from the shore and extended further offshore in the retroflection zone at around 52°W to 51°W. The lower dispersion of occurrence for OWT 3 and 4 in this region implies that higher contrasted waters tend to appear more frequently in the eastern offshore domain due to NBC retroflection.

In general, OWT-1 pixels were spatially distributed in the off-shore domain of French Guiana marine ecosystem. Whereas, OWT-2 waters were mainly found in the transition zone between coastal and clear-water regions with a relative dispersion in the eastern part. OWT 3

appeared as a thin belt connecting the shallow coastal waters and the mixed waters of OWT 3. The location of the most turbid waters can be identified from the distribution of OWT-4 pixels which exclusively dominate the very coastal areas.

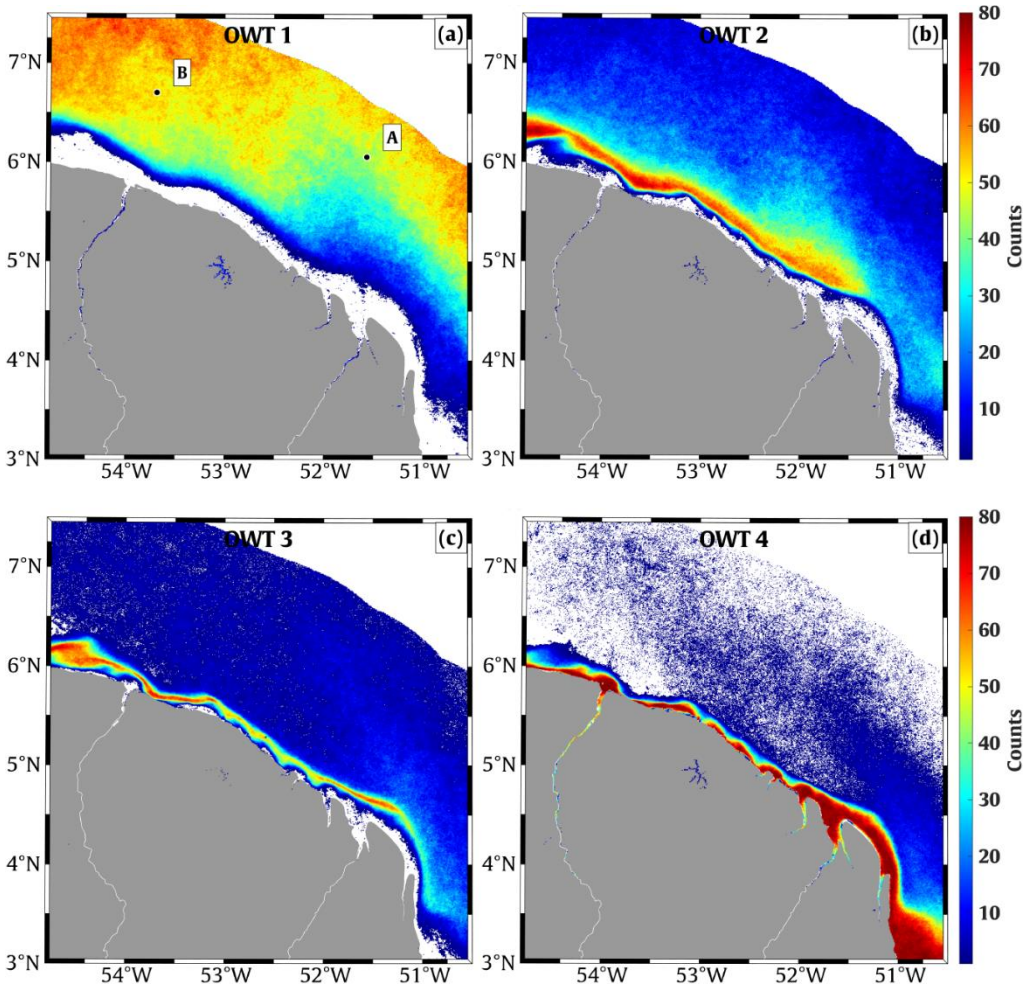

Figure 5.6. *The frequency of occurrence extracted for* ***a)*** *OWT 1,* ***b)*** *OWT 2,* ***c)*** *OWT 3, and* ***d)*** *OWT 4 over Sentinel3/OLCI time period.*

5.2.2.2. High-spatial-resolution classification

The adoption of high-spatial-resolution sensors for classification purposes offers advantages considering the level of spatial detail. In this thesis, the Sentinel-2/MSI satellite archives with a spatial resolution resampled to 60 m have been used to optically classify the water masses in the coastal zone of French Guiana. Such ocean-color products have been atmospherically processed using POLYMER processor to obtain the $R_{rs}(\lambda)$ on the water surface (see section 2.3.1). Indeed, the enhancement of spatial resolution allows for deeper insights regarding biogeochemical processes as well as the local distribution of OWTs which might be attributed to local

environmental factors. In this analysis, the investigation was conducted with a focus on two main rivers of French Guiana (i.e., the Maroni and Oiapoque rivers) to discover fine-scale features and patterns related to hydro-sedimentary such as Amazon river inputs and the contribution of local rivers.

The frequency of occurrence and the spatial distribution of the four defined OWTs for wet (from January to June) and dry (from July to December) seasons in the Maroni estuary are presented in **Figure 5.7**. The map illustrating the most frequent OWTs during 4 years from 2016 to 2020 shows that the vicinity of Maroni river's outlet is mainly characterized by OWT 2, 3, and 4, while OWT-1 pixels are absent most of the time in this particular area. The extension as well as the positions of different OWTs are consistent with that recorded in the analysis of the medium-spatial-resolution sensor. The influences of the Maroni River on the coastal ecosystem could partly be described through the interpretation from this analysis as an extension of OWTs 3 and 4 was observed in the rainy season, thus inducing more terrestrial inputs downstream during this period (Abascal-Zorrilla et al., 2020). In addition, this augmentation of contrasted waters (**Figure 5.7.a,b**) around the estuarine vicinity might also be attributed to the dominance of Trade winds leading to the transportation of Amazon sediment supply through currents and local resuspension from January to April (Eisma et al., 1991). It should be noted, however, that the lack of available data presented over the Maroni River in the high flow condition is majorly due to the presence of cloud pixels that were masked in the statistics.

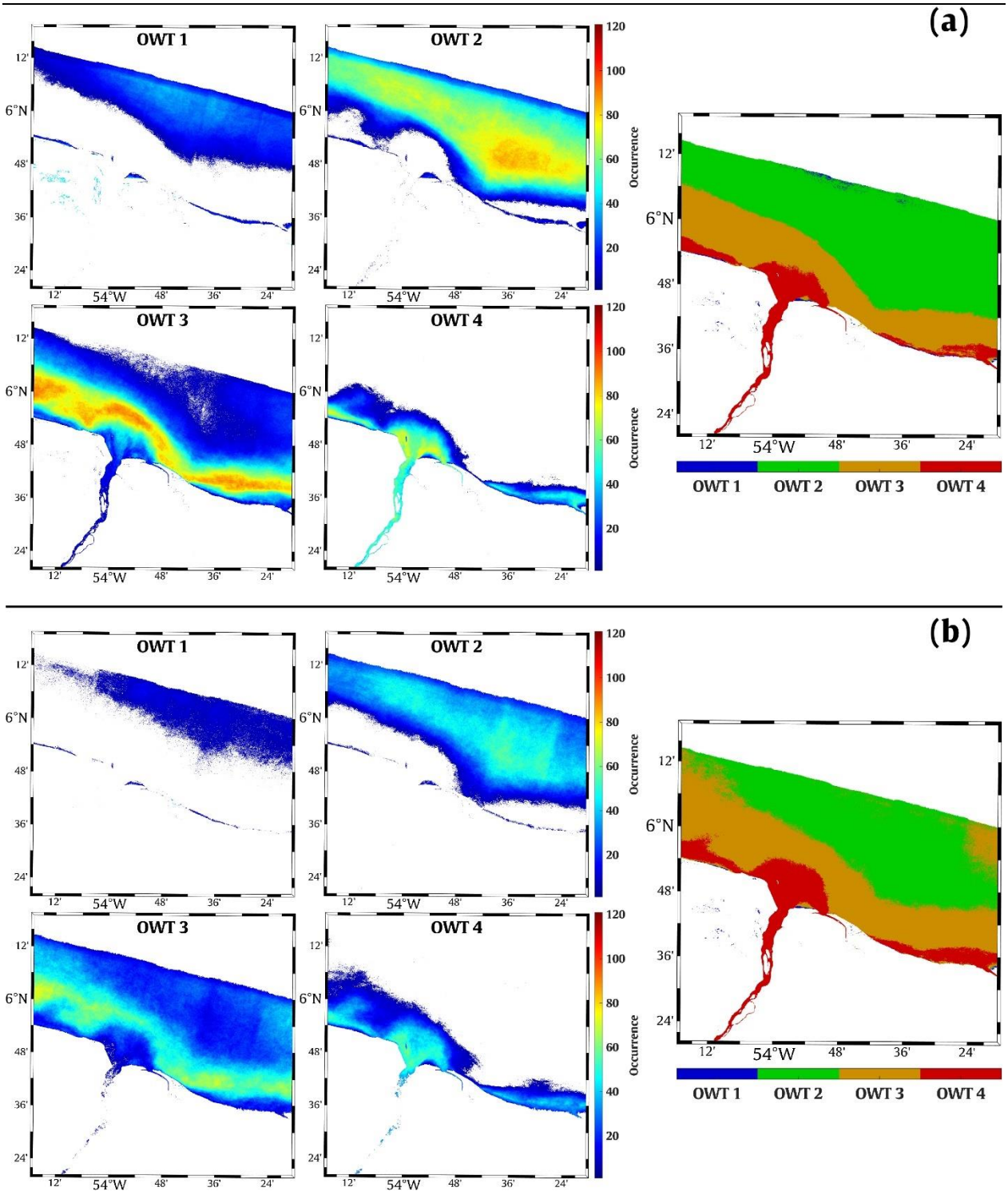

Figure 5.7. *The Sentinel-2 summary of frequency and spatial distribution of the four Optical Water Types for* ***a)*** *Dry and* ***b)*** *Wet seasons in the Maroni estuary during the period of 2016-2020.*

The analysis for the Oiapoque river outlet is shown in **Figure 5.8.a,b** in which the coastal waters are mainly characterized by OWTs 3 and 4. The spatial distributions of these OWTs are relatively stable considering both wet and dry seasons. This result confirms the significance of land-based impacts on the coastal domain of French Guiana. In the inner shelf and Oiapoque River's mouth, the water body is primarily controlled by OWT 4 which indicates a high contribution of mineral constituents originating from the Amazon River plume. It is worth mentioning that even though the suspended sediment supply from local rivers is low (C. J. M. de Oliveira & Clavier, 2000), the highly contrasted properties of the water masses observed in the riverine areas might be in response to the contribution of Chlorophyll-a or dissolved organic matter (Vantrepotte et al., 2012, 2015) that are released through leaf litter from the surrounding tropical rainforest upstream or from mangrove fringe (Ray et al., 2018; Tamooh et al., 2012). This could partly explain the presence of OWT-3 pixels found in the upstream part of the Oiapoque river (**Figure 5.8.b**). Indeed, the availability of organic and nutrient content, which potentially leads to the development of phytoplankton biomass, could also be related to seasonal river. No huge seasonal difference in the spatial distribution of OWTs was detected in the Oiapoque estuary from our analysis, as evidenced by steady patterns of the considered OWTs observed in this particular area **Figure 5.8.a,b**. However, the seasonal variation might be more apparent with further investigations performed for each individual OWT with the integration of in-situ measurements considering different physical factors such as wind, wave, river discharge, and tidal data as for instance as shown in the study of (Abascal-Zorrilla et al., 2020).

The analysis of OWTs performed on the high-resolution satellite images (Sentinel-2) with a focus on the two main rivers in French Guiana (i.e., the Maroni and Oiapoque Rivers) shows a consistency with that obtained for medium resolution images. No huge seasonal modulation regarding the spatial distribution of OWTs was identified in this examination. Although the river plume areas are observable however they can be categorized as the same OWT as those belonging to mudbanks. This finding suggests that further classification methods allowing finer detailed information, such as optical index, Apparent Visible Wavelength (AVW) proposed by Vandermeulen et al., (2020), or a more robust in-situ dataset might provide a better performance in differentiating riverine and coastal waters at high resolutions.

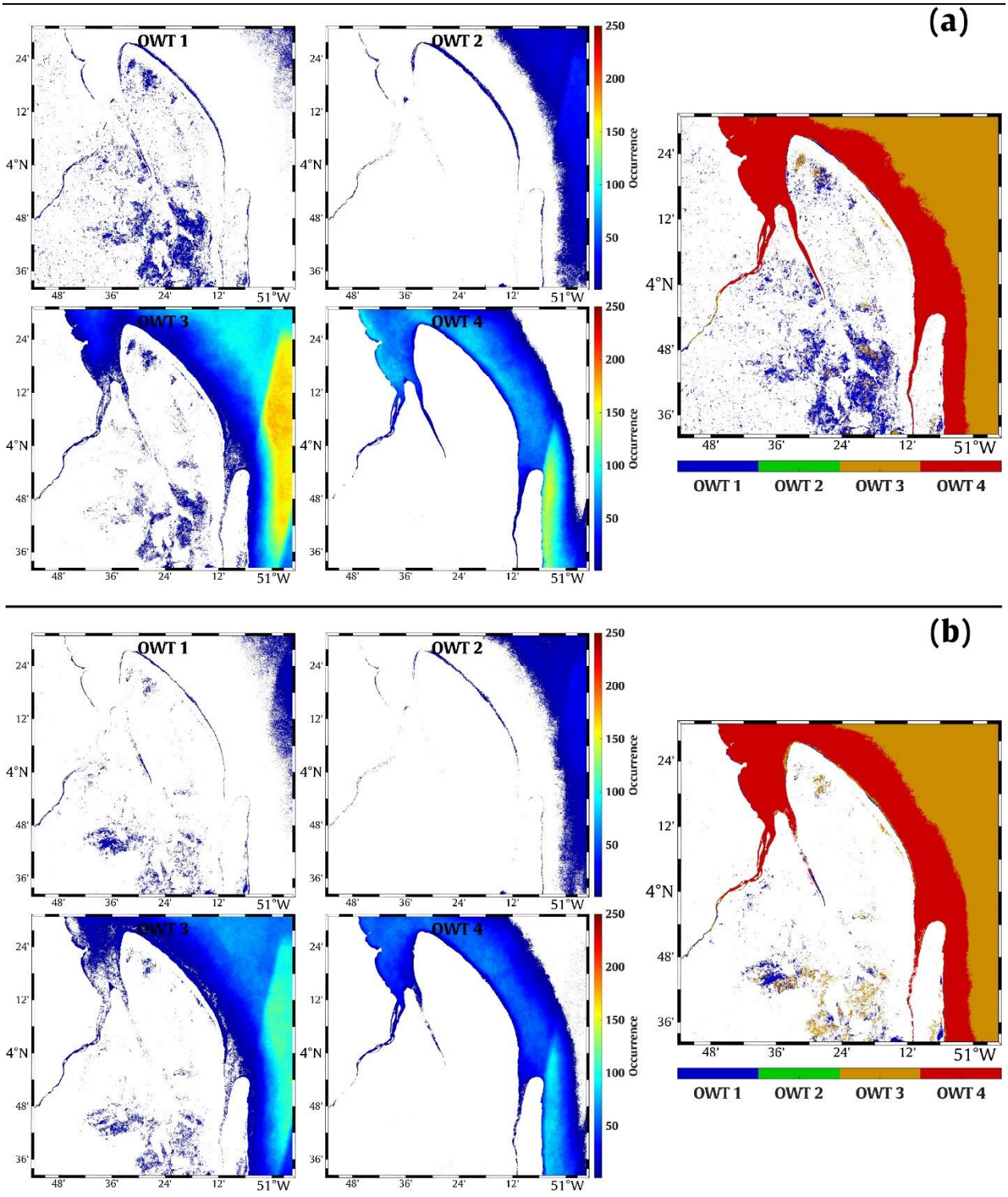

Figure 5.8. *The Sentinel-2 summary of frequency and spatial distribution of the four Optical Water Types for* ***a)*** *Dry and* ***b)*** *Wet seasons in the Oiapoque estuary during the period of 2016-2020.*

5.3. POC/SPM Classification

Considering the importance of the POC/SPM ratio in assessing biogeochemical variability in Section 4.5, this thesis employs the thresholds proposed by LOG (Loisel et al., 2023) for coastal waters. These thresholds were established based on the relationship between POC/SPM and b_{bp}/b_p ratios, aiming to better define the delimitation suggested by Woźniak et al., (2010) using a larger in-situ dataset. Thus, the POC/SPM ratio serves as an indicator to categorize water masses into organic-dominated, mixed, and mineral-dominated waters. Accordingly, the new threshold values of 0.08 and 0.2 were applied to the monthly averaged Level 4 products of the Sentinel-3/OLCI sensor, which covered a time period spanning from 2016 to 2022 and featured a 300-meter spatial resolution. These data were processed by the Copernicus Marine Environment Monitoring Service (CMEMS) as outlined in Section 2.3.1.

The monthly variation of POC/SPM values focusing on the 4 defined OWTs is presented in **Figure 5.9**. Most offshore waters, OWT 1, exhibit a low amplitude in POC/SPM fluctuations, which varies in a range of above 0.2, indicating an organic-dominated environment. In addition, the alteration of suspended organic fractions for OWT 2 implies a mixed situation as the POC/SPM variation frequently appears between 0.08 and 0.2. This finding aligns with the biogeochemical features associated with the OWT 2 as aforementioned in Section 5.2. A high contribution of mineral materials to the particulate assemblage was found for OWT-3 and OWT-4 waters, which are representative of nearshore waters. Overall, the changes in the particulate components from the dominance of mineral particles to the dominance of organic particles within the water masses over the French Guiana marine ecosystem are described relatively well by the optical classification.

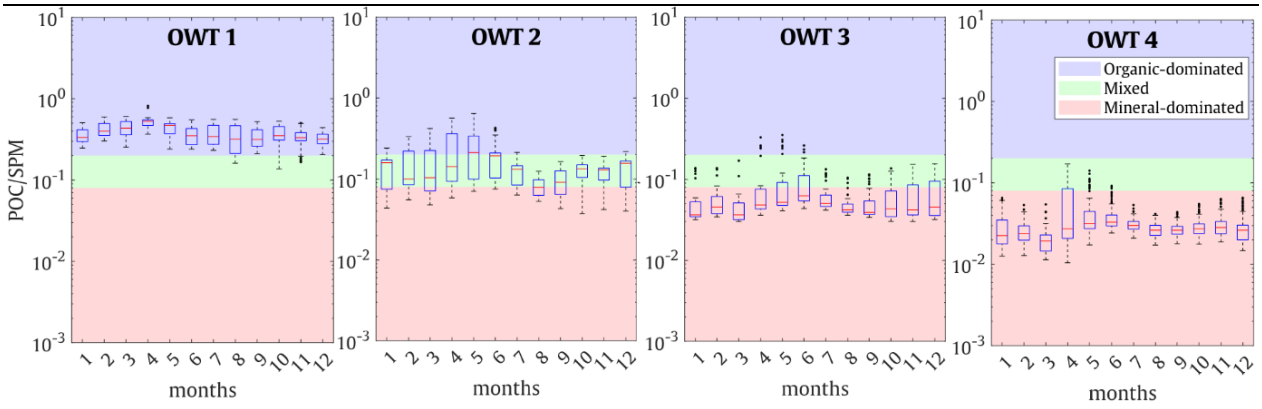

Figure 5.9. *Climatological variation of POC/SPM ratio considering different Optical Water Types.*

Figure 5.10 illustrates the most frequent appearance of the three water types defined by POC/SPM classification approach. The dominance of organic fractions mainly appears in offshore domain, whereas the mineral-dominated waters is predominantly located over the continental shelf in which the manifestation of mudbanks present. Interestingly, the mixed waters tend to be more pronounced to west of the French Guiana coastal domain, particularly in a coastal area located at a distance of approximately 40 km away from the Maroni river mouth. A similar pattern however less pronounced was found about 20 km away from Cayenne. This suggest that environmental forcings related to both local and regional origins (i.e., the Amazon River and local rivers plume) in these areas induce a strong variation in the composition of the particulate matter with varying proportions of organic and mineral particles. However, additional in-situ measurements with the integration of physical factors (i.e., winds and currents) monitoring conducted are requited to fully understand the biogeochemical dynamics at these spots.

The subsequent analysis produced a monthly climatology of POC/SPM values, as illustrated in **Figure 5.11**. During the rainy period between March and May, there is a noticeable shift in the distribution of minerals and mixed waters along the coast. This is likely due to the increased precipitation, which dilutes the inorganic fractions and allows for more organic material to be transported to the estuary. It is however worth noting that even though the mineral-dominated and mixed water regions appear to be compressed and attach to the coast, the concentration of suspended particulate matter might still increase over the inner shelf in the mudbank area. This can be explained by the resuspension process caused by stronger trade winds manifesting from January to April as mentioned in Section 1.1.2.1. In contrast, these areas expanded further

offshore during the dry season when winds blow from the southeast, emphasizing the important role of environmental factors in regulating biogeochemical dynamics in the French Guiana coastal ecosystem.

The partition of the water masses based on the POC/SPM ratio provides a better understanding of the distribution of the organic and mineral proportions encompassed in the particulate assemblages. The outcomes also show a consistency with the optical classification, further enhancing the reliability of this approach to gain valuable insights into the biogeochemical processes occurring within the marine ecosystems.

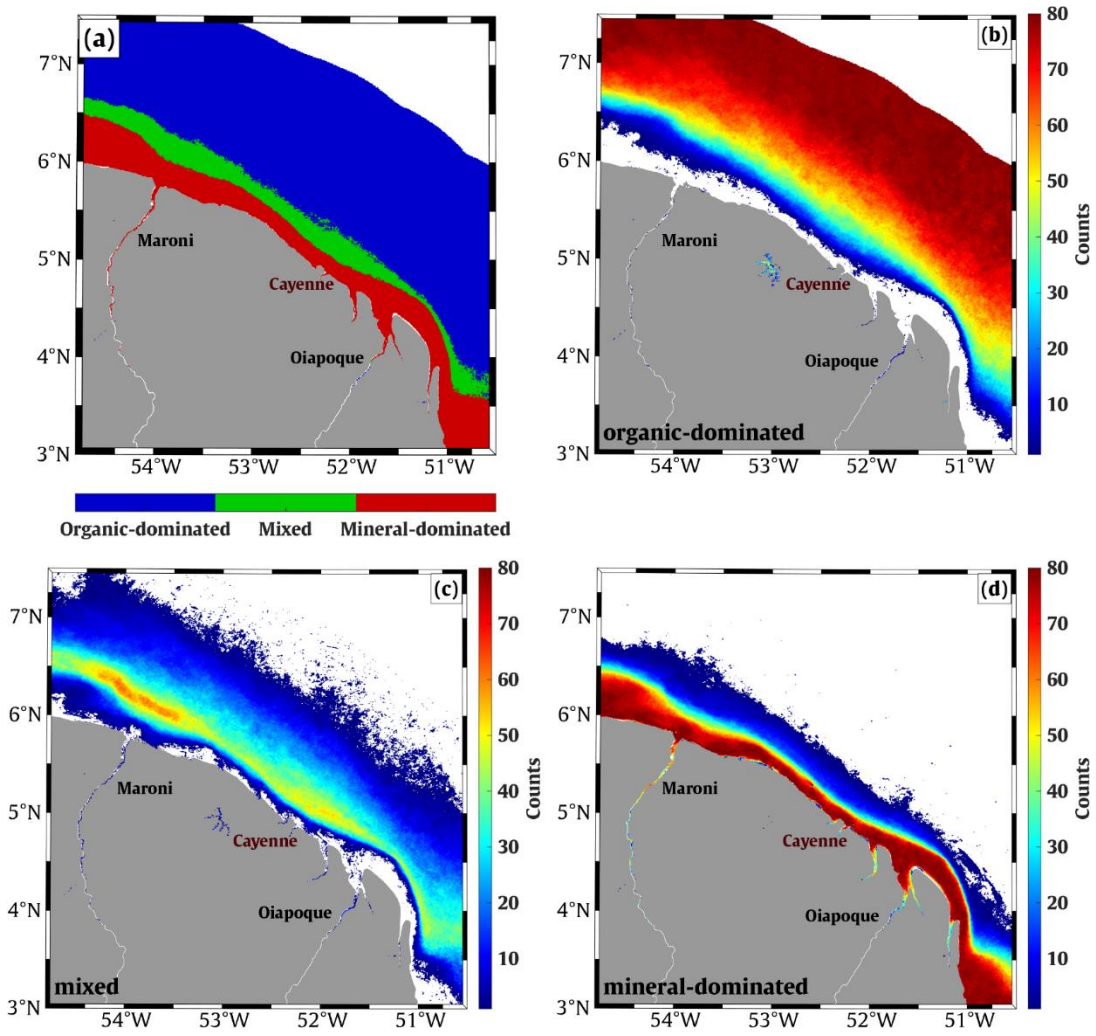

Figure 5.10. a) *The most frequent occurrence of three water types defined from POC/SPM values calculated from Sentinel-3 data and the corresponding frequency for* ***b)*** *organic-dominated,* ***b)*** *mixed, and* ***c)*** *mineral-dominated waters.*

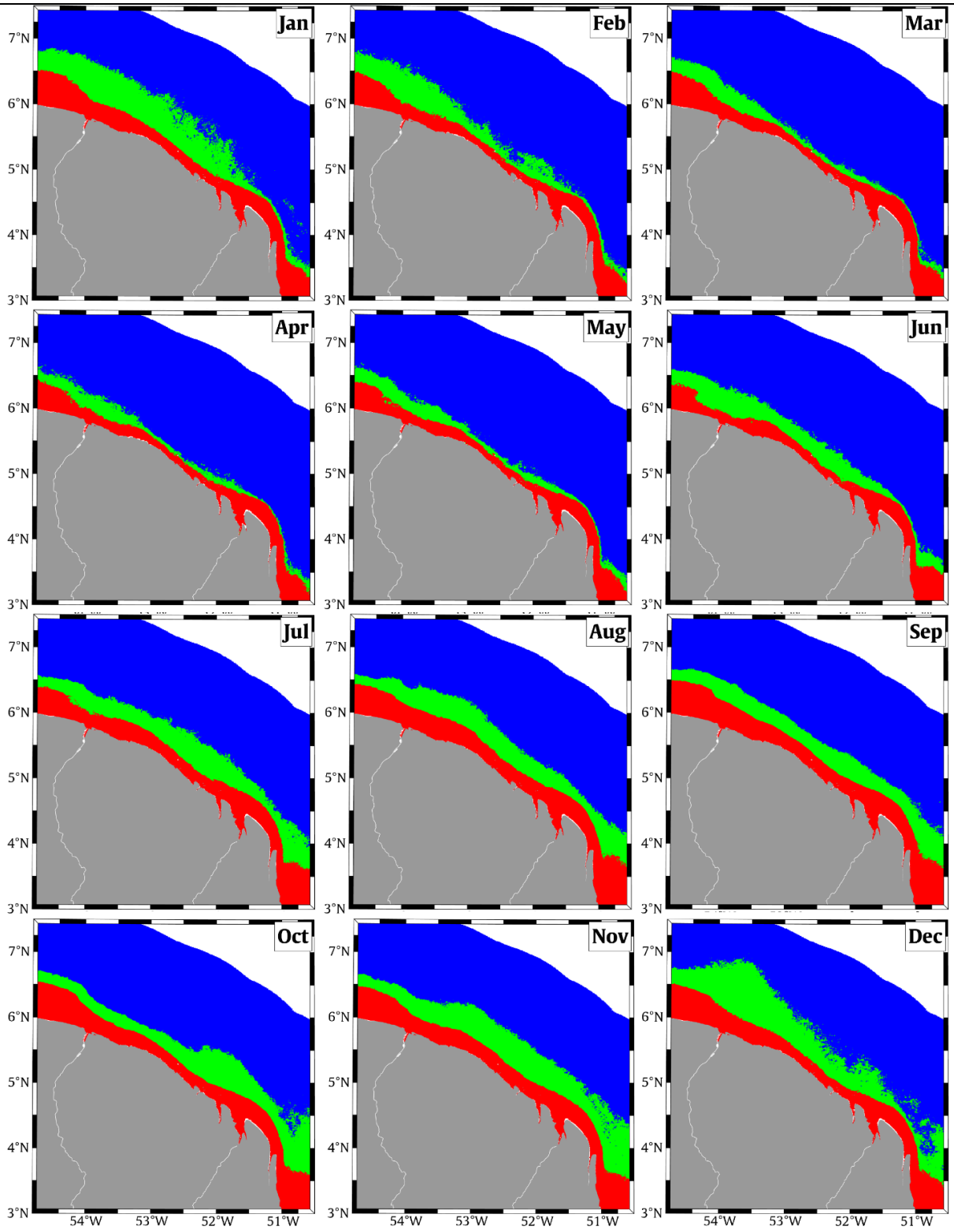

Figure 5.11. *Temporal mean of POC/SPM classification over the study area extracted from Sentinel-3 data. Red, green, and blue areas correspond to mineral-dominated, mixed, and organic dominated waters, respectively.*

5.4. Temporal Classification

As denoted in the section 4.5, the POC/SPM ratio has shown to be a relevant parameter to monitor the coastal water quality in French Guiana since its variability captured relatively well the hydrodynamic processes acting on the coastal ecosystem of the study area. The importance of this parameter is also emphasized by the fact that the variations in POC and SPM exhibit lesser spatial redundancies (**Figure 4.26**). Hence, to obtain a comprehensive temporal partition of water masses, the series of POC/SPM maps derived from MERIS sensor were classified using the SOM neural network approach previously explained in Section 2.2.3. Such satellite data were considered as the input for this temporal clustering method because these data offer a wider time coverage compared to that of Sentinel-2 and Sentinel-3 data. In practice, each POC/SPM time series of the corresponding pixel was initially treated with gap filling and then standardized according to the procedure described in Suominen, (2018) as in the following equation:

$$S_{POC/SPM}=\frac{TS_{POC/SPM}-\mu_{POC/SPM}}{\sigma_{POC/SPM}} \quad 5.1$$

where the terms are defined as follows:

- $S_{POC/SPM}$ indicates the standardized time series.
- $TS_{POC/SPM}$ corresponds to the initial POC/SPM sequence.
- $\mu_{POC/SPM}$ is the mean of the initial POC/SPM sequence.
- $\sigma_{POC/SPM}$ is the standard deviation of the initial POC/SPM sequence.

The input matrix for SOM was defined by n rows × m columns, where n corresponds to the number of image pixels (number of observations) and m indicates the number of each time step (number of features). The parameterization for the SOM implementation also consists of a network of 7 × 4 neurons which has been trained iteratively with a radius (the standard deviation of the Gaussian function that constraint the movement of surrounding neurons) of 0.1 in 80 epochs to represent effectively the defined input matrix. The yielded weights for the corresponding neurons with respect to the features were then clustered into 4 classes using a hierarchical tree with the linkage (distance between clusters) that was defined by Ward's method (Ward, 1963). The illustrations of the dendrogram and the final classified network in this process are presented in **Figure 5.12.a,b**. The distinct groups determined for the neural network map

imply a good performance of the SOM to delimit the data, in which no neuron of the belonging class was found to be positioned in between those of other classes.

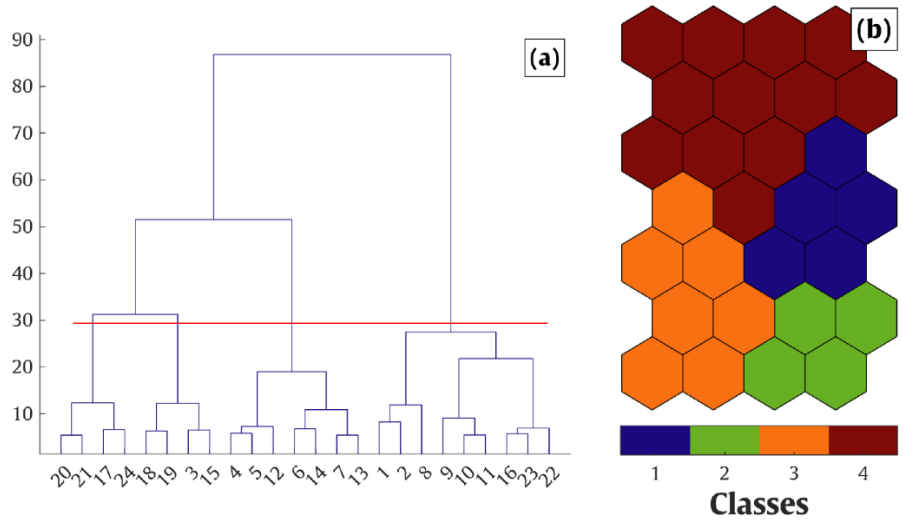

Figure 5.12. a) *Dendrogram representing the hierarchical tree attained from Ward's linkage.* ***b)*** *Representation of the SOM network plane, each individual color indicates neurons that were clustered in the same class.*

The results of this classification scheme are depicted in **Figure 5.13**, where each time series of a given pixel has been assigned to a cluster representing a specific temporal pattern of POC/SPM values over the MERIS time period. The POC/SPM variation for these 4 clusters is further described in **Figure 5.14** in the consideration of the thresholds for mineral-dominated, mixed, and organic-dominated waters as defined in Loisel et al., (2023). The temporal characteristics of each class and its associated biogeochemical processes are particularly described as follows:

Class 1: Situating in proximity to the shore **Figure 5.13**, Class-1 waters appear to be a crucial region that primarily is subjected to terrestrial influences. As discussed in section 4.3.2.1, this area was found to be tightly related to the migration of mudbanks. This interface between oceanic and local impacts exhibits a strong domination of mineral particles as demonstrated by the low POC/SPM values consistently remaining below 0.08. The variability of POC/SPM for this class seems to be more pronounced from April to June which potentially suggests an enhanced contribution of organic origins during the Wet season. However, the prevalence of inorganic substances presented within the water body confirms the significant role of mudbank manifestation for this water type.

Class 2: The Class-2 pixels are mainly located in the western part of the French Guiana offshore domain. The temporal variability of this water type displays strong seasonal fluctuations in which the organic proportion usually reaches its peaks between April and July (**Figure 5.14**). Even though the spatial distribution of Class-2 waters is plausibly connected to an extension of both dissolved and particulate matter from January to June as mentioned in section 4.3.1.1. The variation of POC/SPM over the Class-2 regions tend to be more stable compared to other areas with a CV of 26.23%.

Class 3: The majority of Class-1 pixels are located in the offshore domain with a relatively high irregular variation of 28.54 % to the total variance, as shown by anomalous increases in POC/SPM values. This might be related to the presence of NBC rings established in this area, which is in good agreement with the results obtained in section 4.3.1.2 as the NBC ring cycle is related to variations at a shorter time period (i.e., 5-6 times/year). The POC/SPM variability corresponding to this class exhibits a fairly high averaged variation coefficient (31.21%), implying a substantial amplitude in the fluctuation throughout the examined period.

Class 4: Unlike Class-2 waters in which the POC/SPM ratio normally presents the highest values from April to July, Class-4 pixels display consistently higher suspended organic fractions during the wet season then gradually diminish until November. This temporal shift indicates the Amazons' influence in transporting freshwaters to this particular region through the NBC retroflection. The seasonal modulation of the Guiana current during this period is also visible and described by an extension of the Class-4 pixels parallel to the coast. Further, the averaged VC value obtained for this class is higher than the other classes, underlining a substantial difference in minimum and maximum values of POC/SPM.

The SOM classification performed on the MERIS archives has proven as a relevant partitioning method for characterizing the temporal variability of four regions associated with different variations in POC/SPM values. The attained results are consistent with the analysis deployed in Section 4.3 where areas related to NBC retroflection, NBC rings, western extension of biogeochemical dynamics, seasonal modulation of the Guiana current, and mudbank are identified clearly from the satellite data. In addition, the SOM classification is also capable to provide the information on the weights of the input features (in this case, each time step). The application of such approach considering multiple biogeochemical variables, therefore, might give an idea about most significant parameters for each class.

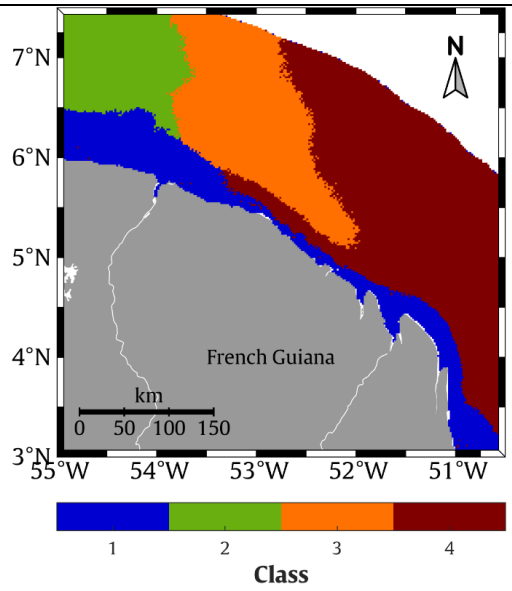

Figure 5.13. *Spatial distribution of 4 classes defined using SOM classification scheme applied to POC/SPM MERIS data (2016-2022)*

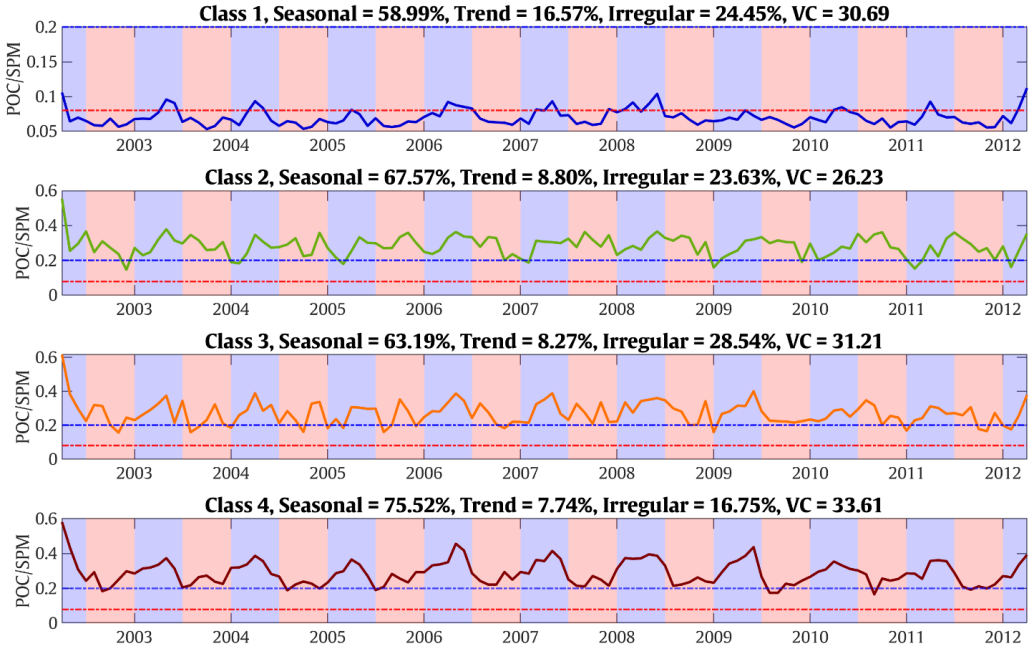

Figure 5.14. *Temporal variability of POC/SPM ratio considering 4 Classes defined from the SOM classification performed on the MERIS data. Red and blue dashed lines represent the two thresholds of 0.08 and 0.2 as suggested in Loisel et al., (2023). Values of the relative contribution of Census X-11 terms are provided corresponding to the 4 classes.*

5.5. Climatological analysis and reference state

5.5.1. Monthly Climatological interpretation

The monthly Sentinel-3 archives have been used to perform the climatological analysis based on the mask extracted from the most frequent OWT map (**Figure 5.5**). The results from this analysis are shown in **Figure 5.15** where the monthly median values corresponding to each parameter have been presented in the box plots considering different OWTs. The biogeochemical variables generally exhibit a gradual increase in concentration towards very coastal waters (from OWT 1 to OWT 4). In the offshore domain, phytoplankton biomass and organic materials seem to be governed by rainfall intensity, as demonstrated by higher concentrations found during high flow conditions for OWTs 1 and 2 (**Figure 5.15.b-d**). This latter feature suggests that nutrient-rich freshwater from local river runoff potentially plays an important role in marine productivity in the study area. However, the monthly variation of SPM over this region, especially for OWT 2, shows an increased amount during the dry season, describing relatively well the influence of NBC retroflection occurring from July to October. In coastal regions, the majority of considered parameters tend to be significantly modulated by the manifestation of Trade winds blowing from NE between January to April (Augustinus, 2004; Chevalier et al., 2004; Gratiot et al., 2007), which can be seen from the fluctuations of SPM, POC, and Chl-a for OWTs 3 and 4. This result confirms the impact of wind-induced waves in the biogeochemical dynamics in the French Guiana coastal domain through for instance resuspension process as aforementioned in Section 4.3.2. Nevertheless, the variability of dissolved organic materials in near-shore waters presents a different pattern peaking between the months of April and May, which implies a considerable contribution of CDOM stemming from local rivers during the high discharge period.

The climatological analysis from satellite data describes effectively the biogeochemical characteristics associated with the four OWTs considering offshore and coastal waters in French Guiana. This provides deeper insights into the seasonal variability of the investigated parameters and is in good agreement with the observations indicated in Chapter 4.

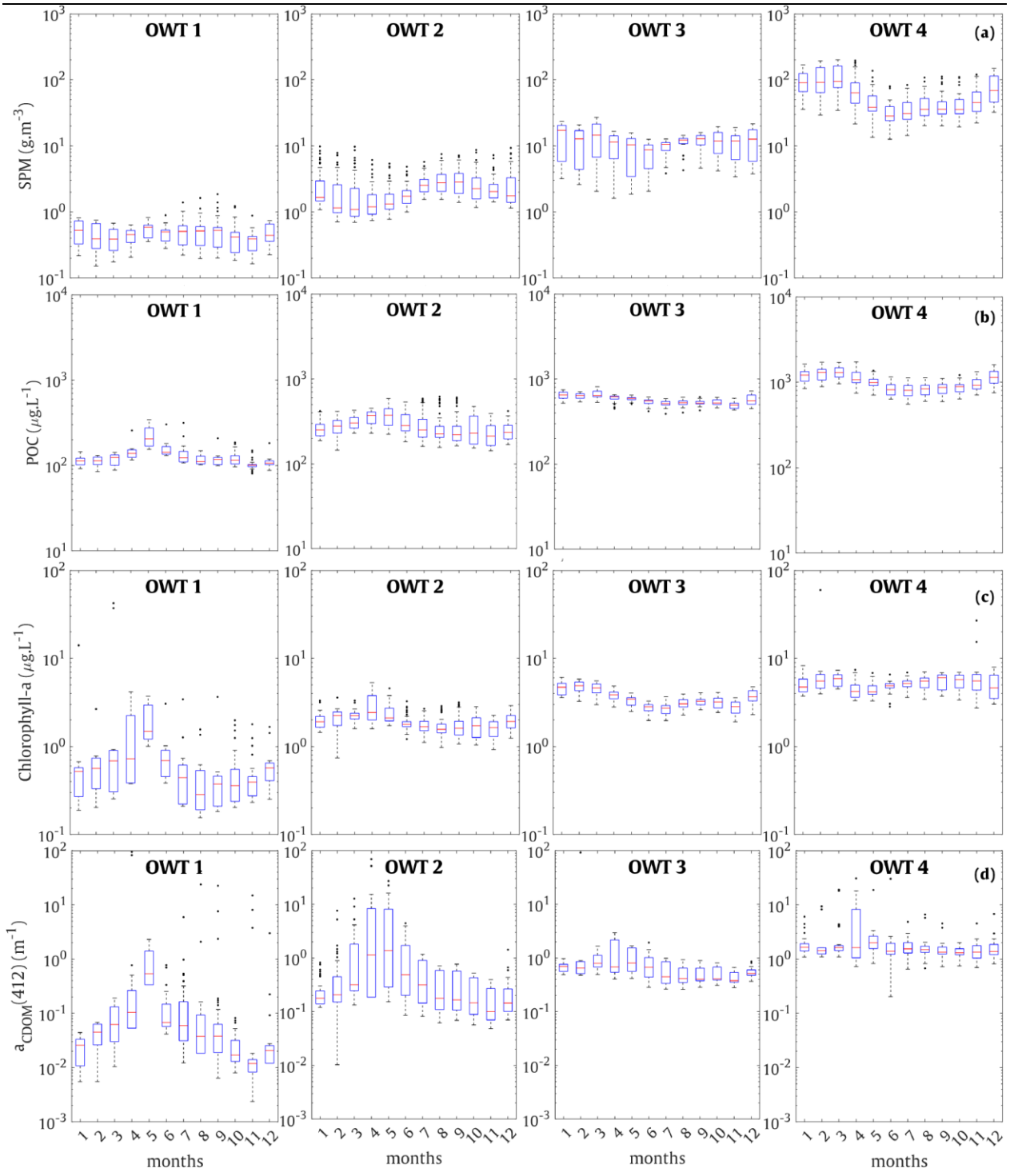

Figure 5.15. *Monthly climatological cycles of the 4 Optical Water Types considering* ***a)*** *SPM,* ***b)*** *POC,* ***c)*** *Chlorophyll-a,* ***d)*** $a_{CDOM}(412)$ *using Sentinel-3/OLCI archives (04/2016 - 11/2022).*

5.5.2. Reference state definition and exceptional event detection

To establish a reference state that can be used to support local monitoring programs as well as to detect exceptional events, the yearly percentile 90 (P90) values have been statistically extracted over 7 years (2016-2022) of the Sentinel-3 archives focusing on different OWTs. The concentration ranges of biogeochemical parameters defined for the reference state are presented in **Table 5.2**. To better understand the potential deviations from the normal conditions, the information of an unusual occurrence where an exceptional rainfall was recorded in September of 2021 was used to compare with the baseline defined from the P90 of Sentinel-3 data. As mentioned in Section 1.1.1, September is usually the driest month in French Guiana. However, 148% excess rainfall was observed in the department and the temperature was higher than the normal level of the dry season (+0.6°C) during this period. The activity of the ITCZ might be responsible for this phenomenon when the southern margin of the ITCZ remained close to French Guiana (Bulletin climatique mensuel de Guyane Septembre 2021 Par Météo-France). It is however important to note that the ranges of the referenced values defined from satellite data in this examination might be higher than that observed with in-situ data especially OWT-1 waters. This can be explained due to the fact that our in-situ measurements are very restricted to the coast leading to a small number of data points belonging to clear waters (OWT 1). Another reason is that the reference state has been established based on the P90 values which are relatively close to the upper limit of the satellite-derived concentration of each biogeochemical variable.

Table 5.2. *The reference values for each OWT considering different parameters defined by the P90 values extracted from Sentinel-3 satellite archives over 7 years (2016-2022).*

	Parameters	min	max	mean	median	stdv
OWT 1	SPM ($g.m^{-3}$)	0.683	0.945	0.811	0.826	0.091
	POC ($mg.m^{-3}$)	134.860	170.051	153.673	151.903	12.165
	Chl-a ($mg.m^{-3}$)	0.709	1.269	1.030	1.061	0.209
	$a_{CDOM}(412)$ (m^{-1})	0.078	0.179	0.117	0.109	0.034
	POC/SPM	0.474	0.558	0.522	0.523	0.025
OWT 2	SPM ($g.m^{-3}$)	4.232	5.114	4.716	4.678	0.321
	POC ($mg.m^{-3}$)	383.663	441.134	409.671	411.100	25.535
	Chl-a ($mg.m^{-3}$)	2.285	3.064	2.609	2.646	0.275
	$a_{CDOM}(412)$ (m^{-1})	0.635	1.702	1.068	0.942	0.389
	POC/SPM	0.143	0.275	0.216	0.231	0.042
OWT 3	SPM ($g.m^{-3}$)	17.633	20.441	19.385	19.694	1.152
	POC ($mg.m^{-3}$)	647.551	693.339	673.498	672.933	19.797
	Chl-a ($mg.m^{-3}$)	4.580	5.362	4.944	4.914	0.297
	$a_{CDOM}(412)$ (m^{-1})	0.841	1.210	0.998	0.940	0.144
	POC/SPM	0.056	0.135	0.095	0.090	0.025
OWT 4	SPM ($g.m^{-3}$)	90.299	207.992	144.327	138.717	48.663
	POC ($mg.m^{-3}$)	1267.050	1515.118	1388.479	1367.800	89.401
	Chl-a ($mg.m^{-3}$)	6.758	7.415	7.074	7.087	0.200
	$a_{CDOM}(412)$ (m^{-1})	1.799	2.095	1.937	1.919	0.105
	POC/SPM	0.034	0.067	0.046	0.047	0.011

The SPM concentration in September of 2021 in very coastal waters (OWT 4) was found to be significantly lower than the median value typically observed (138.7 $g.m^{-3}$), registering at 41.4 $g.m^{-3}$, whereas the standard range is from 90.3 to 208 $g.m^{-3}$. This might be attributed to the dilution caused by excessive precipitation associated with low sediment loads contributed by the French Guiana rivers. The lower particulate materials (POC and SPM) compared to the standard can also be explained by the fact that the resuspension process driven by Trade winds is less pronounced in September (see Section 1.1.2.1). The higher rainfall might also lead to an increase in the phytoplankton biomass flushed toward the estuarine vicinity, as evidenced by a higher concentration of Chl-a within OWT-4 waters compared to the reference values (Ray et al., 2018). However, dissolved organic materials exhibit a minor deviation from the P90 ranges, indicating that their response to the event was relatively trivial. Interestingly, the POC/SPM values over the continental shelf were recorded to be higher than the normal state regarding all OWTs.

Figure 5.16 depicts the comparison between the distribution of the 4 OWTs during the exceptional event in consideration of their reference states (i.e., the most frequent occurrence). More specifically, there was a spatial contraction of OWTs 2, 3, and 4 toward the coastline, whereas areas corresponding to OWT-1 waters presented an extension, implying that substantial suspended inorganic fractions were diluted, and more organic materials were introduced into the coastal domain under the high rainfall and discharge condition.

The changes in concentration of the biogeochemical variables during the presence of exceptional events remained unclear except a dilution of SPM can be witnessed for OWT-4 waters. Meanwhile, POC/SPM values demonstrate a substantial response to the extreme precipitation in September of 2021. This result confirms the reliability of the POC/SPM ratio as a metric in detecting abnormal events (i.e., environmental, or anthropogenic forcings) as well as monitoring coastal waters quality in French Guiana.

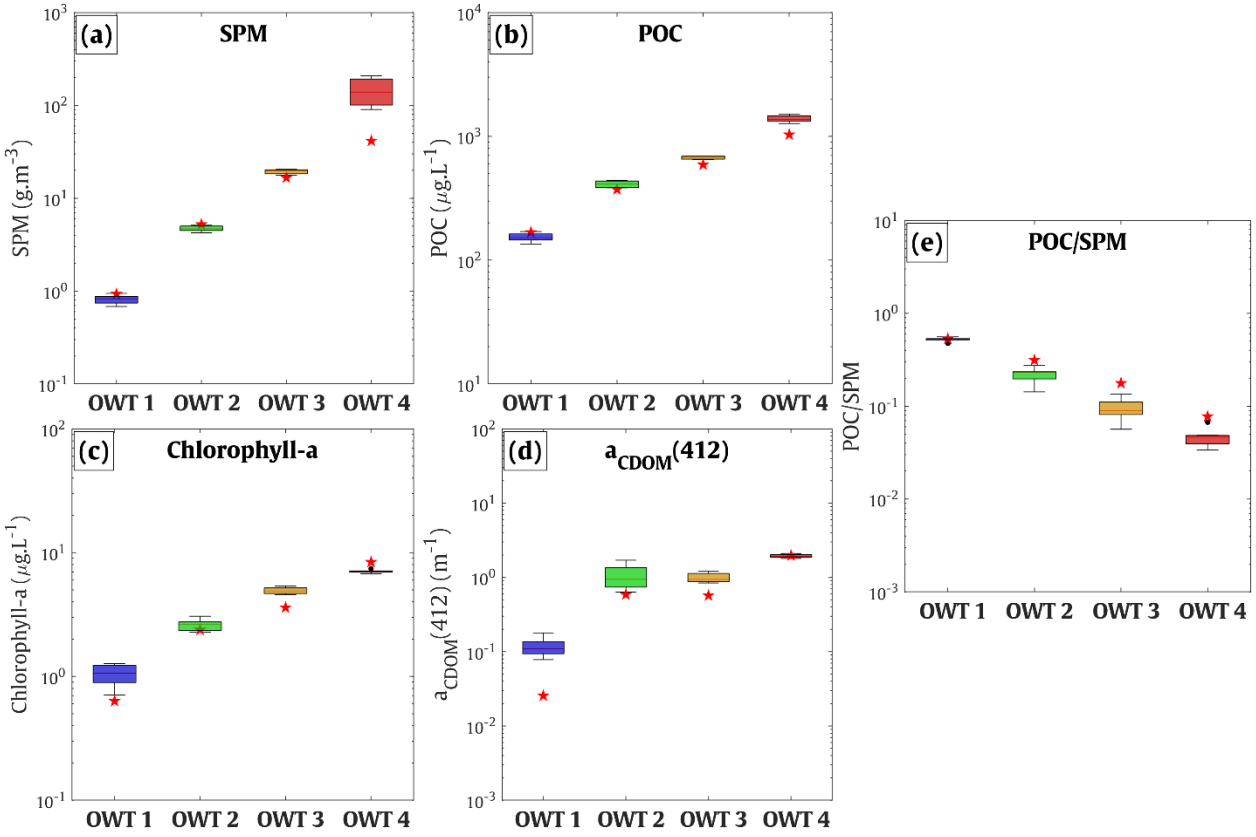

Figure 5.18. *Reference ranges of* ***a)*** *SPM,* ***b)*** *POC,* ***c)*** *Chlorophyll-a,* ***d)*** $a_{CDOM}(412)$*, and* ***e)*** *POC/SPM considering 4 OWTs defined in Section 5.2. Red stars correspond to the P90 concentrations of different parameters extracted for the monthly Sentinel-3 scene in September of 2021.*

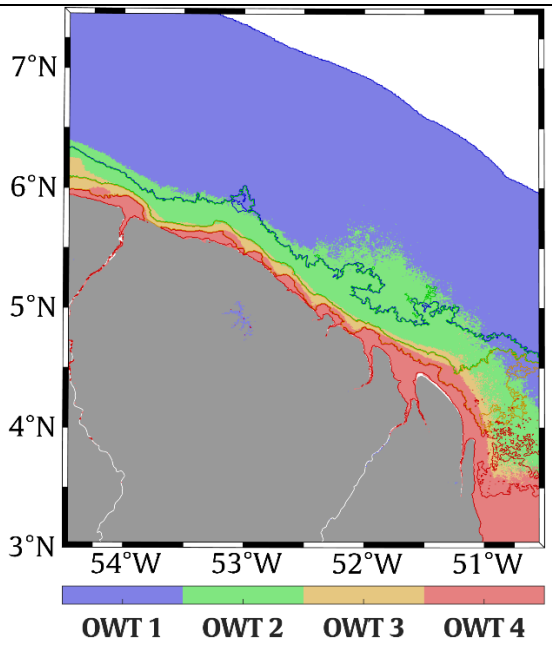

Figure 5.16. *The distribution of the 4 OWTs in September of 2021 (solid lines) concerning their most frequent occurrence over the Sentinel-3 time period.*

5.6. Classification summary and interest for refining regional monitoring strategy.

The relationship between the water types defined by Optical, Temporal, and POC/SPM classification approaches reveals a consistency regarding spatio-temporal patterns of biogeochemical variability in French Guiana marine waters. In particular, the climatological variation range of POC/SPM values for each OWT suggests that OWT 3 and 4 characterized as mineral-dominated, OWT 2 as mixed, and OWT 1 as organic-dominated environments (**Figure 5.9**). At the same time, Classes 2, 3, and 4 yielded from the temporal classification are predominantly represent organic-dominated waters, since their POC/SPM variations were typically observed to reach above 0.2 during the MERIS time period. In contrast, Class 1 signifies mineral-dominated environments, with its POC/SPM variation generally falling below 0.08 (**Figure 5.14**). Moreover, the classification schemes explored in this study demonstrate greater robustness and provide a more detailed information about the biogeochemical attributes of the water masses compared to traditional classification techniques. This is due to the fact that the new technique is developed based on actual satellite data capturing the French Guiana coastal zone, encompassing detailed biogeochemical features in both coastal and offshore domains (see Sections 5.2, 5.3, and 5,4). Moreover, the conventional methods often result in delimitations that

closely attached to the coast presenting a spatial limitation as illustrated in **Figure 5.17.a,b** where the extension of the 4 zones is relatively restricted to the coast. Such disadvantage might lead to insignificant difference found in the seasonal variability patterns between the defined zones **Figure 5.17.c** in which the variations of Chl-a over these zones present higher values typically in wet period.

Therefore, considering POC/SPM classification as a frame, a summary of the outcomes from the optical and temporal classification schemes was proposed aiming at developing a monitoring strategy. More specifically, Classes 2, 3, and 4 obtained from the temporal classification were selected as the main descriptor in offshore waters (organic-dominated waters), whereas OWTs 2, 3, and 4 defined from the optical classification were considered as the primary delimitation in coastal domain (mixed and mineral-dominated waters). This classification combination is presented in **Figure 5.18** where the French Guiana marine waters have been partitioned into six domains. Accordingly, 12 stations located over different aquatic environments of French Guiana marine waters have been suggested with three field campaigns that can be conducted from Cayenne, Sinnamary, and Maroni rivers (**Figure 5.18**, **Table 5.3**). This sampling strategy was established with a consideration of the biogeochemical dynamics denoted in Chapter 4. For instance, stations 4, 8, and 12 are strategically placed to monitor the Amazon's influence on offshore regions, including the NBC retroflection, NBC rings, and the westward extension of biogeochemical variables. In coastal waters, stations 3, 7, and 11, located within OWT-2 regions, are designed to observe changes in marine waters characterized by both mineral and organic compositions. This is particularly relevant at station 11, where the presence of mixed waters is significantly pronounced (**Figure 5.10**). Stations 2, 6, and 10, corresponding to OWT-3 waters, offer valuable insights into the development of phytoplankton biomass in the coastal region of French Guiana. Moreover, stations within OWT-2 and OWT-3 pixels can be utilized to monitor biogeochemical alterations induced by the Guiana current and/or freshwater discharge from local rivers. Lastly, stations 1, 5, and 9 can be beneficial for investigating mudbank phenomena and their associated hydro-sedimentary processes. Indeed, the implementation of the in-situ monitoring at these locations should take into account the seasonality of multiple forcings acting on the study area such as strong wind period, dry, and wet seasons. Simultaneous measurements of different parameters (i.e., SPM, Chl-a, POC, DOC, $a_{CDOM}(412)$, SSS, and SST) will deliver a better understanding about the biogeochemical dynamics occurring in the region. The synergistic application of the mentioned classification schemes and the sampling plan serve as a

recommendation to effectively support coastal management strategies and policies considering the unique characteristic and complexity of French Guiana marine ecosystem.

Regarding practical deployment, it is suggested that the Cayenne cruise (**Table 5.3**) including stations 1, 2, and 3 should be prioritized to conduct in-situ measurements due to the availability of accessible shipping facility and infrastructure required for the implementation of sampling work. Moreover, the biogeochemical alterations at the location of these stations can provide valuable information on the manifestation of significant coastal processes such as mudbank migration, local river influence (Mahury river), tide/wind modulation, phytoplankton biomass oscillation, presence of mixed water, and Guiana current.

Table 5.3. *Information on the proposed sampling strategy considering offshore and coastal waters with the spatial location of stations shown in* ***Figure 5.18****.*

Cruise	Station	Location (longitude, latitude)	Description	Water Properties	Domain
Cayenne	1	-52.2425, 4.9307	Mudbanks and local river interface, tide/wind modulation	Mineral-dominated	Coastal
	2	-52.2091, 4.9974	Phytoplankton contribution, Guiana current	Mineral-dominated	Coastal
	3	-52.0869, 5.2696	Mixed water, Guiana current	Mineral-dominated	Coastal
	4	-51.9369, 5.6530	NBC Retroflection	Organic-dominated	Offshore
Sinnamary	5	-53.0147, 5.4807	Mudbanks and local river interface, tide/wind modulation	Mineral-dominated	Coastal
	6	-52.9647, 5.5252	Phytoplankton contribution, Guiana current	Mineral-dominated	Coastal
	7	-52.9091, 5.6585	Mixed water, Guiana current	Mixed	Coastal
	8	-52.8091, 5.9141	NBC Rings	Organic-dominated	Offshore
Maroni	9	-53.9592, 5.8030	Mudbanks and local river interface, tide/wind modulation	Mineral-dominated	Coastal
	10	-53.9869, 5.9530	Phytoplankton contribution	Mineral-dominated	Coastal
	11	-54.0147, 6.0919	Concentrated mixed water	Mixed	Coastal
	12	-54.0703, 6.3919	Western extension of biogeochemical variables during wet season	Organic-dominated	Offshore

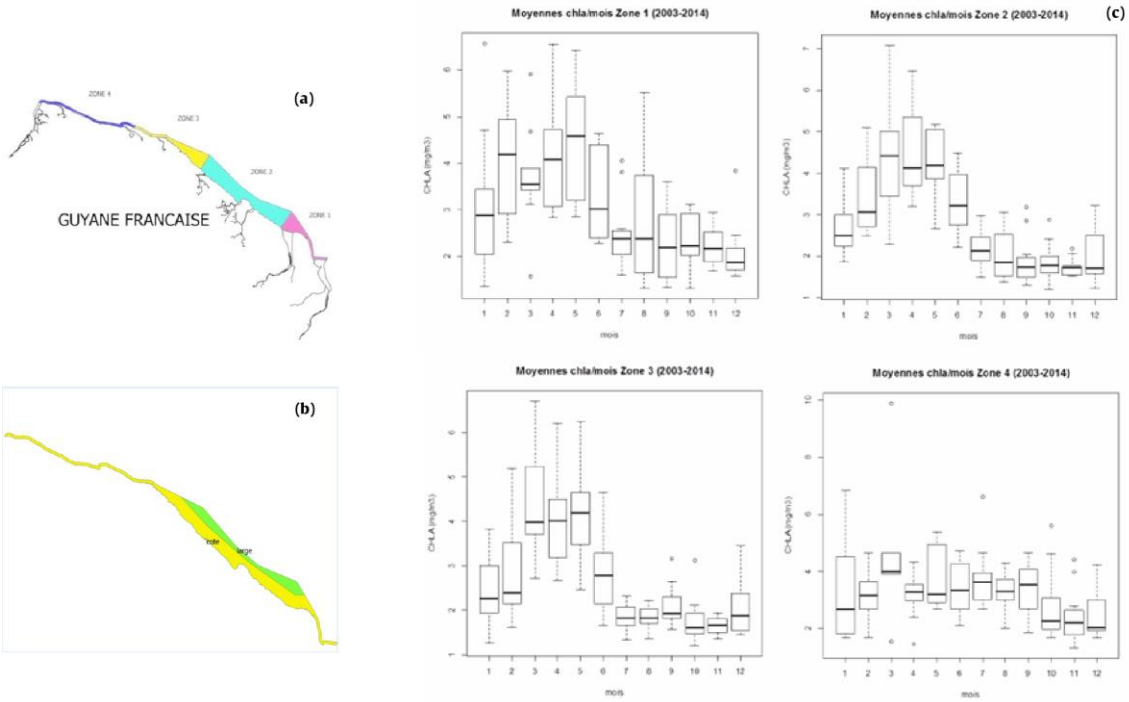

Figure 5.17. *The historical classification schemes in French Guiana considering* ***a)*** *fishing areas and* ***b)*** *coastal and offshore waters.* ***c)*** *seasonal variability of Chl-a extracted for four zones (Lampert et al., 2015).*

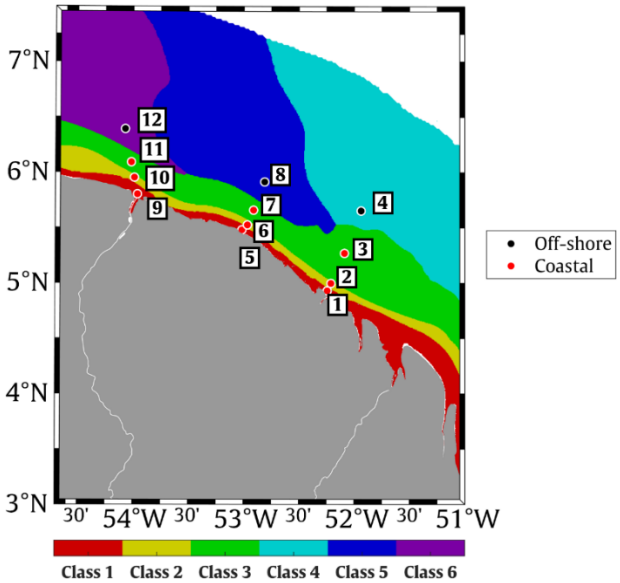

Figure 5.18. *Summary of Optical and Temporal Classification schemes, with sampling station locations proposed in the present study.*

To better understand the biogeochemical dynamics in the location of the autonomous station established near Saint-Joseph Island (Iles du Salut archipelago) since 09/01/2020 (see Section

2.2), the POC/SPM timeseries of the pixel at this location has been extracted over the time period of Sentinel-3 data. However, due to the spatial resolution limitation which leads to a masked pixel, the considered location here was shifted 2 km to the west of the autonomous station at 5°16'46.6"N 52°36'00.0"W and is presented in **Figure 5.19.a**. The water properties in this region primarily vary from mineral-dominated to mixed conditions and present a strong seasonal oscillation in which the organic proportions appear to be more pronounced in the beginning of high flow period. This is consistent to the previous analysis denoted in Section 5.3 as the most frequent OWT presented here is OWT 3. Therefore, the establishment of this station can provide useful information about the significance of phytoplankton biomass as well as the associated environmental forcings such as the Guiana current, organic exchanges from mangroves. The results from this analysis confirms the relevance of establishing the autonomous station even though its collapse was due to practical issues.

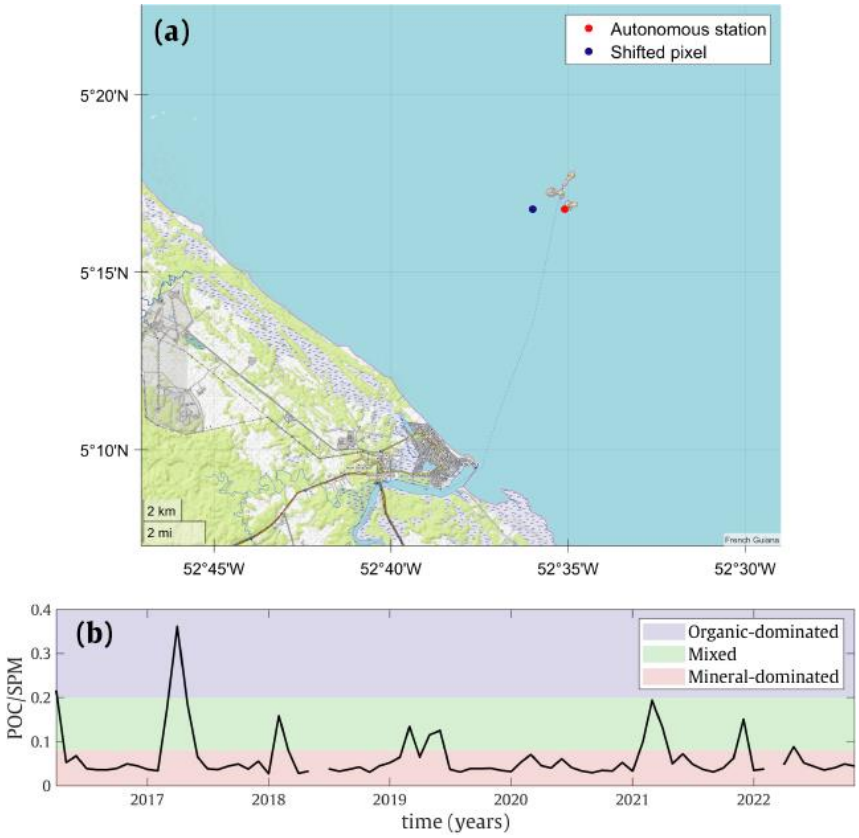

Figure 5.19. a) *Locations of the autonomous station and the shifted pixel and* ***b)*** *Variability of POC/SPM extracted for the shifted pixel over Sentinel-3 period.*

5.7. Conclusions and perspectives

The optical classification was used to partition the water masses into 4 different OWTs ranging from clear to highly contrasted waters. The consistency between the in-situ and satellite $R_{rs}(\lambda)$ spectra shapes have proven the reliability of adopting ocean color data in delimiting the marine waters in French Guiana. The analysis performed on high-spatial-resolution data (Sentinel-2) showed that the Maroni River exhibits a spatial extension in OWTs during the wet season, meanwhile, no significant seasonal difference was found in the estuarine vicinity of the Oiapoque River, suggesting alternative approaches (e.g., Apparent Visible Wavelength) and/or the deployment of additional in-situ measurements could potentially enhance the identification of boundaries between riverine and coastal waters when utilizing high-resolution satellite archives.

The Temporal Classification using the Self-Organizing Map (SOM) technique, which was performed on POC/SPM values, aligns well with the findings discussed in Chapter 4. This classification approach provides a comprehensive description of the Amazon influence on off-shore waters, taking into account factors such as NBC rings, NBC retroflection, and westward extensions of biogeochemical parameters. However, it is important to note that this approach requires a long time series of data to generate robust and reliable results.

The POC/SPM partitioning outcomes including the identification of mineral-dominated, mixed, and organic-dominated environments offer a better understanding about the seasonal alteration in suspended organic fractions in coastal regions which typically presents a spatial contraction during high flow conditions, which is probably due to the dilution caused by high rainfall. Variability range of POC/SPM values regarding different OWTs aligns well with the field measurements.

The information on PPC (i.e., POC/SPM-based classification) has been used as a frame to select and combine the optimal partitioning methods over French Guiana marine waters considering both coastal and off-shore domains. Such combination approach serves as a general summary for the delimitation of the water masses that provides more in-depth information about the biogeochemical characteristics of French Guiana marine waters regarding both temporal and spatial patterns (i.e., classification of the time series, optical water types) with a more robust statistical computation which might be a limitation of the historical classification technique. Accordingly, a field measurement strategy was proposed through the combined classification

scheme with 12 stations located over a variety of water types in order to provide to stakeholders a generic framework for deploying regional monitoring programs and policies.

The biogeochemical properties associated with each OWT, which exhibits unique patterns in seasonal variation throughout the year, offering valuable insights into the seasonality of the investigated parameters. The reference values were defined for considered parameters regarding four OWTs with the aim of establishing a baseline to identify exceptional events. The presence of an unusual extreme precipitation event in September of 2021 was clearly detected by the higher POC/SPM values compared to the reference ranges, which might be attributed to the dilution caused by high rainfall intensity. This result highlights the appropriateness of using POC/SPM parameter as an indicator to identify unusual deviations for French Guiana marine waters.

It is worth mentioning that the involvement of multiple biogeochemical variables (i.e., POC, SPM, Chl-a, a_{CDOM}) and physical variables (i.e., SST, SSS, Mixed Layer Depth (MLD), Winds, and Waves) can be considered as the parameterization for the SOM classification method. Since such approach has the capability to provide the weights for the input parameters, the importance of each variable regarding each water type thus can be revealed. This information could be valuable to attain more profound knowledge of the water body that could be closely related to ecological niches as the relationship between biogeochemical dynamics and ecological distribution is a fundamental aspect of ecosystem functioning and structure.

GENERAL CONCLUSION

Main findings

This dissertation contributes to the efforts to better characterize the French Guiana's coastal water quality using remote sensing technique through the examination performed on regional variability of various biogeochemical parameters, and the analysis of different classification schemes.

The adaptation of bio-optical inversion algorithms in Chapter 3 reveals that the tuned version of existing models is sufficient to estimate the concentration of most considered water quality descriptors except Chl-a. In particular, the model proposed by Han et al., (2016) is the most accurate model for estimating SPM over the French Guiana coastal waters. Whereas, a combination of two adapted models suggested by T. K. Tran et al., (2019) and Le et al., (2017) has proven its reliability to predict POC. The tuned model of Cao et al., (2018) was selected to derive $a_{CDOM}(412)$ which can be used as a proxy to compute the DOC through an approach documented in Vantrepotte et al., (2015). However, the performance of existing Chl-a models on the in-situ dataset did not yield a satisfying result primarily due to the signature characteristics of the water body. Such unique characteristics are typically related to highly turbid environment caused by excessive sediment loads transported from the Amazon River's mouth. The retrieval of information on phytoplankton biomass over the entire marine domain of the study area, therefore, requires a combination of multiple inversion algorithms (i.e., MuBR, and NDCI-based) with a consideration of different OWTs as a frame. The challenges of estimating Chl-a over ultra-turbid waters are also addressed, highlighting the potential of using hyperspectral data in optically complex environments (M. D. Tran et al., 2023).

The temporal analysis on biogeochemical variability of French Guiana marine waters in Chapter 4 indicates the influence of the Amazon River through different hydro-dynamic processes. The NBC retroflection were identified to exhibit a seasonal pattern through all considered parameters that typically occurs between July and October in the eastern regions. Whereas, NBC rings were found to be more sensitive to irregular variations of SPM. An offshore extension of both dissolved and particulate materials in the western regions might be in response to the effect of bathymetry and wind modulation. These processes were detected to primarily present significant influence on French Guiana off-shore domain. The variations of different

biogeochemical parameters over coastal waters are attributed to the manifestation of mudbank migration which is typically regulated by the wind-induced waves from January to April. The impact of Guiana current during dry season and/or dilution effects caused by high rainfall intensity might be responsible for a seasonal belt in SPM found with a distance of 20 km from the coast. The irregular variation of POC and $a_{CDOM}(412)$ here is also potentially related to the organic exchange from the local mangroves. Results show that no evidence of significant long-term changes has been detected except the fingerprint of mudbank migration along the coast. The study also suggests POC/SPM value as one of the most important parameters in describing the biogeochemical variability and monitoring coastal water quality over French Guiana marine ecosystem.

Optical classification applied on Sentinel-2 data showed a spatial extension of OWT over Maroni River in the wet season, while no significant change occurred near Oiapoque River, indicating alternative approaches (e.g., AVW) or additional in-situ measurements could improve the delimitation between riverine and coastal waters. The PPC partitioning results illustrate a spatial contraction of suspended organic fractions from February to May which might be in response to the dilution effect caused by high discharge condition. Results attained from temporal classification using the SOM technique performed on POC/SPM values aligns well with the findings discussed in Chapter 4 in which the NBC rings, NBC retroflection, and off-shore extensions to the west were detected.

The PPC-based classification method has been employed as a frame to select and combine the optimal partitioning schemes for French Guiana's marine waters, including coastal and offshore areas. This approach offers a comprehensive overview of the water masses and presents spatial and temporal advancements compared to traditional approach performed in French Guiana by using more reliable statistical calculations. A field measurement plan with 12 stations across various water types has been suggested, which can be a helpful foundation for regional monitoring programs and policies. Reference values were established for these OWTs to identify unusual events. For example, an exceptional rainfall event in September 2021 led to higher POC/SPM values recorded for all OWTs, which could be attributed to dilution caused by high precipitation. This demonstrates the effectiveness of using POC/SPM as one of important indicators for detecting anomalies in French Guiana's marine waters.

Perspectives

Besides the attained results, the main drivers responsible for different processes acting on the study area are left to be discovered. This involves the factors leading to the presence of Guiana current through a seasonal belt of SPM and an extension of all biogeochemical variables to the western part in the off-shore domain during the wet and windy seasons. Further research should be conducted with the aim of seeking explanations for the irregular variations of SPM that is potentially related to NBC rings. It is also necessary to develop advanced and appropriate methodologies to quantify or at least differentiate the contribution of local (i.e., river inputs, organic exchanges from mangroves, human forcings) and regional (i.e., the Amazon River's influence) origins to the biogeochemical dynamics over the French Guiana marine ecosystem. To gain a better understanding about these remaining questionable issues, future efforts are suggested to focus on obtaining more robust and adequate in-situ measurements, which can be conducted according to the proposed sampling strategy with the integration of other physical factors related to winds and currents. Longer and more recent time series of high and medium spatial resolution satellite products are required for the temporal analysis with the focus on coastal domain to obtain more up-to-date observations.

The proposed partitioning schemes, such as optical classification (through different OWTs), temporal classification (through an application of SOM), and PPC classification (through POC/SPM values) accompanied with the summarized classification can be applied to other aquatic environments in different geographic locations (e.g., regions that are also influenced by the Amazon's mudbank system including North Brazil, Suriname, Guyana, and Venezuela coastal waters). In this thesis, these methods have proven to be a promising tool to support the deployment of in-situ monitoring programs over French Guiana's marine waters. Further, such approaches are also useful to extract a comprehensive insight into the biogeochemical dynamics considering both spatial and temporal patterns such as the detection of anomalies and understanding about the fate of Amazon's input in the context of climate impacts or modulation of the seasonal patterns.

Moreover, the potential to gain more in-depth knowledge about the water properties can be accomplished through the application of SOM classification on multiple biogeochemical variables (i.e., POC, SPM, Chl-a, a_{CDOM}) and physical variables (i.e., SST, SSS, Mixed Layer Depth (MLD), Winds, and Waves) for identifying the importance of each parameter regarding

different water types. For instance, the MLD alteration can be related to vertical mixing and availability of nutrient/light, which contribute to changes of biogeochemical properties in coastal waters. Further, such information might also be useful to better understand the regional marine ecosystem's structure and functioning (e.g., ecological niches definition) and the dynamics of the higher trophic levels.

REFERENCES

Abascal-Zorrilla, N. (2019). Dynamics of the Amazonian mud bank system through spatial observation and hydro-sedimentary modeling: Application to the coastal domain of French Guiana. https://www.theses.fr/2019YANE0002

Abascal-Zorrilla, N., Vantrepotte, V., Gensac, E., Huybrechts, N., & Gardel, A. (2018). The advantages of Landsat 8-OLI-derived suspended particulate matter maps for monitoring the subtidal extension of Amazonian coastal mud banks (French Guiana). Remote Sensing, 10(11), 0–17. https://doi.org/10.3390/rs10111733

Abascal-Zorrilla, N., Vantrepotte, V., Huybrechts, N., Ngoc, D. D., Anthony, E. J., & Gardel, A. (2020). Dynamics of the estuarine turbidity maximum zone from landsat-8 data: The case of the maroni river Estuary, French Guiana. Remote Sensing, 12(13). https://doi.org/10.3390/rs12132173

Abascal-Zorrilla, N., Vantrepotte, V., Ngoc, D. D., Huybrechts, N., & Gardel, A. (2019). Automated SWIR based empirical sun glint correction of Landsat 8-OLI data over coastal turbid water. Optics Express, 27(8), A294. https://doi.org/10.1364/oe.27.00a294

Abril, G., Jr., L. C. C., Nepomuceno, A., Erbas, T., Costa, S., Ramos, V. v., Moser, G., Fernandes, A., Negri, E., Knoppers, B. A., Brandini, N., Machado, W., Bernardes, M., & Vantrepotte, V. (2022). Spreading eutrophication and changing CO_2 fluxes in the tropical coastal ocean: A few lessons from Rio De Janeiro. *ACMAR*, *55*(Especial), 461–476. https://doi.org/10.32360/ACMAR.V55IESPECIAL.78518

Adame, M. F., & Lovelock, C. E. (2011). Carbon and nutrient exchange of mangrove forests with the coastal ocean. Hydrobiologia, 663(1), 23–50. https://doi.org/10.1007/S10750-010-0554-7

Adyel, T. M., & Macreadie, P. I. (2022). Plastics in blue carbon ecosystems: A call for global cooperation on climate change goals. The Lancet Planetary Health, 6(1), e2–e3. https://doi.org/10.1016/S2542-5196(21)00327-2

Akopian, M., & Lampert, L. (2018). Analysis of the relevance of the current delimitation of the coastal water body of Guyana.

Aller, R. C., & Blair, N. E. (2006). Carbon remineralization in the Amazon-Guianas tropical mobile mudbelt: A sedimentary incinerator. Continental Shelf Research, 26(17–18), 2241–2259. https://doi.org/10.1016/j.csr.2006.07.016

Allison, M. A., & Lee, M. T. (2004). Sediment exchange between Amazon mudbanks and shore-fringing mangroves in French Guiana. Marine Geology, 208(2–4). https://doi.org/10.1016/j.margeo.2004.04.026

Alongi, D. M. (2002). Present state and future of the world's mangrove forests. Environmental Conservation, 29(3), 331–349. https://doi.org/10.1017/S0376892902000231

REFERENCES

Alparslan, E., Aydöner, C., Tufekci, V., & Tüfekci, H. (2007). Water quality assessment at Ömerli Dam using remote sensing techniques. Environmental Monitoring and Assessment, 135(1–3). https://doi.org/10.1007/s10661-007-9658-6

Anthony, E. J., Gardel, A., Gratiot, N., Proisy, C., Allison, M. A., Dolique, F., & Fromard, F. (2010). The Amazon-influenced muddy coast of South America: A review of mud-bank-shoreline interactions. In Earth-Science Reviews (Vol. 103, Issues 3–4, pp. 99–121). https://doi.org/10.1016/j.earscirev.2010.09.008

Arnault, S., Bourlès, B., Gouriou, Y., & Chuchla, R. (1999). Intercomparison of the upper layer circulation of the western equatorial Atlantic Ocean: In situ and satellite data. In Journal of Geophysical Research: Oceans (Vol. 104, Issue C9, pp. 21171–21194). Blackwell Publishing Ltd. https://doi.org/10.1029/1999jc900124

Augustinus, P. G. E. F. (2004). The influence of the trade winds on the coastal development of the Guianas at various scale levels: A synthesis. Marine Geology, 208(2–4), 145–151. https://doi.org/10.1016/j.margeo.2004.04.007

Augustinus, P. G. E. F., Hazelhoff, L., & Kroon, A. (1989). The chenier coast of Suriname: Modern and geological development. In Marine Geology (Vol. 90).

Babin, M., Morel, A., Fournier-Sicre, V., Fell, F., & Stramski, D. (2003). Light scattering properties of marine particles in coastal and open ocean waters as related to the particle mass concentration. Limnology and Oceanography, 48(2). https://doi.org/10.4319/lo.2003.48.2.0843

Babin, M., Stramski, D., Ferrari, G. M., Claustre, H., Bricaud, A., Obolensky, G., & Hoepffner, N. (2003). Variations in the light absorption coefficients of phytoplankton, nonalgal particles, and dissolved organic matter in coastal waters around Europe. Journal of Geophysical Research: Oceans, 108(7). https://doi.org/10.1029/2001jc000882

Baklouti, M., Devenon, J. L., Bourret, A., Froidefond, J. M., Ternon, J. F., & Fuda, J. L. (1998). Annual cycle and variability of the North Brazil current. Journal of Physical Oceanography, 28(1), 103–128. https://doi.org/10.1175/1520-0485(1998)028<0103:ACAVOT>2.0.CO;2

Baklouti, M., Devenon, J. L., Bourret, A., Froidefond, J. M., Ternon, J. F., & Fuda, J. L. (2007). New insights in the French Guiana continental shelf circulation and its relation to the North Brazil Current retroflection. Journal of Geophysical Research: Oceans, 112(2), 1–18. https://doi.org/10.1029/2006JC003520

Be, S., Babin, M., Larouche, P., & Seas, N. (2008). An empirical ocean color algorithm for estimating the contribution of chromophoric dissolved organic matter to total light absorption in optically complex waters. 113, 1–14. https://doi.org/10.1029/2007JC004436

Bélanger, S., Babin, M., & Larouche, P. (2008). An empirical ocean color algorithm for estimating the contribution of chromophoric dissolved organic matter to total light absorption in optically complex waters. Journal of Geophysical Research: Oceans, 113(4). https://doi.org/10.1029/2007JC004436

Berlamont, J., Ockenden, M., Toorman, E., & Winterwerp, J. (1993). The characterisation of cohesive sediment properties. Coastal Engineering, 21(1–3). https://doi.org/10.1016/0378-3839(93)90047-C

Betoulle, J. L., Fromard, F., Fabre, A., & Puig, H. (2001). Caractérisation des chutes de litière et des apports au sol en nutriments dans une mangrove de Guyane française. Https://Doi.Org/10.1139/B00-154, 79(2), 238–249. https://doi.org/10.1139/B00-154

Bi, S., Li, Y., Liu, G., Song, K., Xu, J., Dong, X., Cai, X., Mu, M., Miao, S., & Lyu, H. (2022). Assessment of algorithms for estimating Chlorophyll-a concentration in inland waters: a round-robin scoring method based on the optically fuzzy clustering. IEEE Transactions on Geoscience and Remote Sensing, 60. https://doi.org/10.1109/TGRS.2021.3058556

Bonelli, A. G., Vantrepotte, V., Jorge, D. S. F., Demaria, J., Jamet, C., Dessailly, D., Mangin, A., Fanton d'Andon, O., Kwiatkowska, E., & Loisel, H. (2021). Colored dissolved organic matter absorption at global scale from ocean color radiometry observation: Spatio-temporal variability and contribution to the absorption budget. Remote Sensing of Environment, 265. https://doi.org/10.1016/J.RSE.2021.112637

Bourret, A., Devenon, J. L., & Chevalier, C. (2008). Tidal influence on the hydrodynamics of the French Guiana continental shelf. Continental Shelf Research, 28(7), 951–961. https://doi.org/10.1016/j.csr.2008.01.008

Brando, V. E., & Dekker, A. G. (2003). Satellite hyperspectral remote sensing for estimating estuarine and coastal water quality. IEEE Transactions on Geoscience and Remote Sensing, 41(6 PART I). https://doi.org/10.1109/TGRS.2003.812907

Brockmann, C., Doerffer, R., Peters, M., Stelzer, K., Embacher, S., & Ruescas, A. (2016). Evolution of the C2RCC neural network for Sentinel 2 and 3 for the retrieval of ocean colour products in normal and extreme optically complex waters. European Space Agency, (Special Publication) ESA SP, SP-740.

Bui, Q. T., Jamet, C., Vantrepotte, V., Mériaux, X., Cauvin, A., & Mograne, M. A. (2022). Evaluation of Sentinel-2/MSI Atmospheric Correction Algorithms over Two Contrasted French Coastal Waters. Remote Sensing, 14(5). https://doi.org/10.3390/rs14051099

Bulletin climatique mensuel de Guyane Septembre 2021 par Météo-France. Retrieved April 1, 2023, from https://meteofrance.gf/fr/climat/bulletin-climatique-mensuel-de-guyane-septembre-2021

Campbell, J. W. (1995). The lognormal distribution as a model for bio-optical variability in the sea. Journal of Geophysical Research, 100(C7), 13237. https://doi.org/10.1029/95JC00458

Cao, F., Tzortziou, M., Hu, C., Mannino, A., Fichot, C. G., Del Vecchio, R., Najjar, R. G., & Novak, M. (2018). Remote sensing retrievals of colored dissolved organic matter and dissolved organic carbon dynamics in North American estuaries and their margins. Remote Sensing of Environment, 205(October 2017), 151–165. https://doi.org/10.1016/j.rse.2017.11.014

REFERENCES

Carton, J. A., & Katz, E. J. (1990). Estimates of the zonal slope and seasonal transport of the Atlantic North Equatorial Countercurrent. Journal of Geophysical Research, 95(C3). https://doi.org/10.1029/JC095iC03p03091

Cheng, C., Wei, Y., Sun, X., & Zhou, Y. (2013). Estimation of chlorophyll-a concentration in Turbid Lake using spectral smoothing and derivative analysis. International Journal of Environmental Research and Public Health, 10(7), 2979–2994. https://doi.org/10.3390/ijerph10072979

Chevalier, C., Baklouti, M., & Ramamonjiarisoa, A. (2004). Modeling the influence of wind and rivers on current, salinity and temperature over the French Guiana continental shelf during the rainy season. Journal of Coastal Research, 20(4), 1183–1197. https://doi.org/10.2112/03-0059r.1

Chevalier, C., Froidefond, J. M., & Devenon, J. L. (2008). Numerical analysis of the combined action of littoral current, tide and waves on the suspended mud transport and on turbid plumes around French Guiana mudbanks. Continental Shelf Research, 28(4–5), 545–560. https://doi.org/10.1016/j.csr.2007.09.011

Cloern, J. E. (1987). Turbidity as a control on phytoplankton biomass and productivity in estuaries. Continental Shelf Research, 7(11–12). https://doi.org/10.1016/0278-4343(87)90042-2

Cloern, J. E. (1996). Phytoplankton bloom dynamics in coastal ecosystems: A review with some general lessons from sustained investigation of San Francisco Bay, California. In Reviews of Geophysics (Vol. 34, Issue 2). https://doi.org/10.1029/96RG00986

Cloern, J. E. (2001). Our evolving conceptual model of the coastal eutrophication problem. In Marine Ecology Progress Series (Vol. 210). https://doi.org/10.3354/meps210223

Conley, D. J., Carstensen, J., Vaquer-Sunyer, R., & Duarte, C. M. (2009). Ecosystem thresholds with hypoxia. Hydrobiologia, 629(1). https://doi.org/10.1007/s10750-009-9764-2

Coynel, A., Etcheber, H., Abril, G., Maneux, E., Dumas, J., & Hurtrez, J. E. (2005). Contribution of small mountainous rivers to particulate organic carbon input in the Bay of Biscay. Biogeochemistry, 74(2), 151–171. https://doi.org/10.1007/S10533-004-3362-1/METRICS

Cummings, J. A., & Smedstad, O. M. (2013). Variational data assimilation for the global ocean. In Data Assimilation for Atmospheric, Oceanic and Hydrologic Applications (Vol. II). https://doi.org/10.1007/978-3-642-35088-7_13

D'Alimonte, D., Mélin, F., Zibordi, G., & Berthon, J. F. (2003). Use of the novelty detection technique to identify the range of applicability of empirical ocean color algorithms. IEEE Transactions on Geoscience and Remote Sensing, 41(12 PART I), 2833–2843. https://doi.org/10.1109/TGRS.2003.818020

Del Vecchio, R., & Blough, N. V. (2004). Spatial and seasonal distribution of chromophoric dissolved organic matter and dissolved organic carbon in the Middle Atlantic Bight. Marine Chemistry, 89(1–4). https://doi.org/10.1016/j.marchem.2004.02.027

Didden, N., & Schott, F. (1992). Seasonal variations in the western tropical Atlantic: Surface circulation from Geosat altimetry and WOCE model results. Journal of Geophysical Research, 97(C3), 3529–3541. https://doi.org/10.1029/91JC02860

Dierssen, H. M., & Karl, D. M. (2010). Perspectives on empirical approaches for ocean color remote sensing of chlorophyll in a changing climate. Proceedings of the National Academy of Sciences, 107(40), 17073–17078. https://doi.org/10.1073/PNAS.0913800107

Dokulil, M. T. (1994). Environmental control of phytoplankton productivity in turbulent turbid systems. Hydrobiologia, 289(1–3). https://doi.org/10.1007/BF00007409

Douillet, P., Ouillon, S., & Cordier, E. (2001). A numerical model for fine suspended sediment transport in the southwest lagoon of New Caledonia. Coral Reefs, 20(4), 361–372. https://doi.org/10.1007/S00338-001-0193-6/METRICS

Doxaran, D., Devred, E., & Babin, M. (2015). A 50 % increase in the mass of terrestrial particles delivered by the Mackenzie River into the Beaufort Sea (Canadian Arctic Ocean) over the last 10 years. Biogeosciences, 12(11), 3551–3565. https://doi.org/10.5194/BG-12-3551-2015

Doxaran, D., Ehn, J., Bélanger, S., Matsuoka, A., Hooker, S., & Babin, M. (2012). Optical characterisation of suspended particles in the Mackenzie River plume (Canadian Arctic Ocean) and implications for ocean colour remote sensing. Biogeosciences, 9(8), 3213–3229. https://doi.org/10.5194/BG-9-3213-2012

Doxaran, D., Froidefond, J. M., Lavender, S., & Castaing, P. (2002). Spectral signature of highly turbid waters: Application with SPOT data to quantify suspended particulate matter concentrations. Remote Sensing of Environment, 81(1). https://doi.org/10.1016/S0034-4257(01)00341-8

D'sa, E. J., Miller, R. L., & Castillo, C. Del. (2006). Bio-optical properties and ocean color algorithms for coastal waters influenced by the Mississippi River during a cold front.

Duarte, C. M., Losada, I. J., Hendriks, I. E., Mazarrasa, I., & Marbà, N. (2013). The role of coastal plant communities for climate change mitigation and adaptation. *Nature Climate Change 2013 3:11*, *3*(11), 961–968. https://doi.org/10.1038/nclimate1970

Ehn, J. K., Reynolds, R. A., Stramski, D., Doxaran, D., Lansard, B., & Babin, M. (2019). Patterns of suspended particulate matter across the continental margin in the Canadian Beaufort Sea during summer. Biogeosciences, 16(7), 1583–1605. https://doi.org/10.5194/BG-16-1583-2019

Eisma, D., Augustinus, P. G. E. F., & Alexander, C. (1991). Recent and subrecent changes in the dispersal of Amazon mud. In Netherlands Journal of Sea Research (Vol. 28, Issue 3).

El Hourany, R., Mejia, C., Faour, G., Crépon, M., & Thiria, S. (2021). Evidencing the Impact of Climate Change on the Phytoplankton Community of the Mediterranean Sea Through a Bioregionalization Approach. Journal of Geophysical Research: Oceans, 126(4). https://doi.org/10.1029/2020JC016808

REFERENCES

Emmerton, C. A., Lesack, L. F. W., & Vincent, W. F. (2008). Nutrient and organic matter patterns across the Mackenzie River, estuary and shelf during the seasonal recession of sea-ice. Journal of Marine Systems, 74(3–4), 741–755. https://doi.org/10.1016/J.JMARSYS.2007.10.001

European Commission. (2018). Annual activity reports 2018. https://commission.europa.eu/publications/annual-activity-reports-2018_en#description

Faatau, J.-T. (2019, March 30). Démographie en Guyane : Vers un doublement de la population d'ici 2050 ? https://outremers360.com/societe/demographie-en-guyane-vers-un-doublement-de-la-population-dici-2050

Ferrari, G. M. (2000). The relationship between chromophoric dissolved organic matter and dissolved organic carbon in the European atlantic coastal area and in the West Mediterranean Sea (Gulf of Lions). Marine Chemistry, 70(4). https://doi.org/10.1016/S0304-4203(00)00036-0

Ferreira, L., & Hitchcock, D. B. (2009). A comparison of hierarchical methods for clustering functional data. Communications in Statistics: Simulation and Computation, 38(9), 1925–1949. https://doi.org/10.1080/03610910903168603

Fichot, C., Lohrenz, S., Geophysical, R. B.-J. of, & 2014, undefined. (2014). Pulsed, cross-shelf export of terrigenous dissolved organic carbon to the Gulf of Mexico. Wiley Online Library, 119(2), 1176–1194. https://doi.org/10.1002/2013JC009424

Fonseca, C. A., Goni, G. J., Johns, W. E., & Campos, E. J. D. (2004). Investigation of the North Brazil Current retroflection and North Equatorial Countercurrent variability. Geophysical Research Letters, 31(21). https://doi.org/10.1029/2004GL020054

Ford, D., & Barciela, R. (2017). Global marine biogeochemical reanalyses assimilating two different sets of merged ocean colour products. Remote Sensing of Environment, 203. https://doi.org/10.1016/j.rse.2017.03.040

Foster, R. A., Subramaniam, A., Mahaffey, C., Carpenter, E. J., Capone, D. G., & Zehr, J. P. (2007). Influence of the Amazon River plume on distributions of free-living and symbiotic cyanobacteria in the western tropical north Atlantic Ocean. Limnology and Oceanography, 52(2), 517–532. https://doi.org/10.4319/LO.2007.52.2.0517

Fratantoni, D. M., & Glickson, D. A. (2002). North Brazil Current ring generation and evolution observed with sea WiFS. Journal of Physical Oceanography, 32(3), 1058–1074. https://doi.org/10.1175/1520-0485(2002)032<1058:NBCRGA>2.0.CO;2

French Guiana climate: Average weather, temperature, precipitation. (n.d.). Retrieved March 26, 2023, from https://www.climatestotravel.com/climate/french-guiana

Froidefond, J. M., Pujos, M., & Andre, X. (1988). Migration of mud banks and changing coastline in French Guiana. Marine Geology, 84(1–2), 19–30. https://doi.org/10.1016/0025-3227(88)90122-3

Froidefond, J.M., Gardel, L., & Guiral, D. (2002). Spectral remote sensing reflectances of coastal waters in French Guiana under the Amazon influence. Remote Sensing of Environment, 80(2), 225–232.

Fromard, F., Puig, H., Mougin, E., Marty, G., Betoulle, J. L., & Cadamuro, L. (1998). Structure, above-ground biomass and dynamics of mangrove ecosystems: New data from French Guiana. Oecologia, 115(1–2), 39–53. https://doi.org/10.1007/S004420050489/METRICS

Gallay, M., Martinez, J. M., Allo, S., Mora, A., Cochonneau, G., Gardel, A., Doudou, J. C., Sarrazin, M., Chow-Toun, F., & Laraque, A. (2018). Impact of land degradation from mining activities on the sediment fluxes in two large rivers of French Guiana. Land Degradation and Development, 29(12), 4323–4336. https://doi.org/10.1002/ldr.3150

Gallay, M., Martinez, J. M., Mora, A., Castellano, B., Yépez, S., Cochonneau, G., Alfonso, J. A., Carrera, J. M., López, J. L., & Laraque, A. (2019). Assessing Orinoco river sediment discharge trend using MODIS satellite images. Journal of South American Earth Sciences, 91. https://doi.org/10.1016/j.jsames.2019.01.010

Gallay, M., Mora, A., Martinez, J. M., Gardel, A., Laraque, A., Sarrazin, M., Beaucher, E., Doudou, J. C., & Lagane, C. (2018). Dynamics and fluxes of organic carbon and nitrogen in two Guiana Shield river basins impacted by deforestation and mining activities. Hydrological Processes, 32(1), 17–29. https://doi.org/10.1002/hyp.11394

Gardel, A., Anthony, E. J., F. dos Santos, V., Huybrechts, N., Lesourd, S., Sottolichio, A., Maury, T., & Jolivet, M. (2021). Fluvial sand, Amazon mud, and sediment accommodation in the tropical Maroni River estuary: Controls on the transition from estuary to delta and chenier plain. Regional Studies in Marine Science, 41(December 2020), 101548. https://doi.org/10.1016/j.rsma.2020.101548

Gardel, A., Gensac, E., Anthony, E. J., Lesourd, S., Loisel, H., & Marin, D. (2011). Wave-formed mud bars: Their morphodynamics and role in opportunistic mangrove colonization. Journal of Coastal Research, SPEC. ISSUE 64, 384–387.

Gardel, A., & Gratiot, N. (2005). A satellite image-based method for estimating rates of mud bank migration, French Guiana, South America. Journal of Coastal Research, 21(4), 720–728. https://doi.org/10.2112/03-0100.1

Garnesson, P., Mangin, A., Fanton d'Andon, O., Demaria, J., & Bretagnon, M. (2019). The CMEMS GlobColour chlorophyll-a product based on satellite observation: Multi-sensor merging and flagging strategies. Ocean Science, 15(3), 819–830. https://doi.org/10.5194/os-15-819-2019

Garzoli, S. L., Ffield, A., Johns, W. E., & Yao, Q. (2004). North Brazil Current retroflection and transports. Journal of Geophysical Research: Oceans, 109(1). https://doi.org/10.1029/2003jc001775

Garzoli, S. L., Ffield, A., & Yao, Q. (2003). North Brazil Current rings and the variability in the latitude of retroflection. Elsevier Oceanography Series, 68(C), 357–373. https://doi.org/10.1016/S0422-9894(03)80154-X

REFERENCES

Gensac, E., Martinez, J. M., Vantrepotte, V., & Anthony, E. J. (2016). Seasonal and inter-annual dynamics of suspended sediment at the mouth of the Amazon river: The role of continental and oceanic forcing, and implications for coastal geomorphology and mud bank formation. Continental Shelf Research, 118, 49–62. https://doi.org/10.1016/j.csr.2016.02.009

Gholizadeh, M. H., Melesse, A. M., & Reddi, L. (2016). A comprehensive review on water quality parameters estimation using remote sensing techniques. Sensors (Switzerland), 16(8). https://doi.org/10.3390/s16081298

Gilbert, R. O. (1988). Statistical Methods for Environmental Pollution Monitoring. Biometrics, 44(1). https://doi.org/10.2307/2531935

Gilerson, A. A., Gitelson, A. A., Zhou, J., Gurlin, D., Moses, W., Ioannou, I., & Ahmed, S. A. (2010). Algorithms for remote estimation of chlorophyll-a in coastal and inland waters using red and near infrared bands. Optics Express, 18(23), 24109. https://doi.org/10.1364/OE.18.024109

Gjelstrup, C. V. B., Sejr, M. K., de Steur, L., Christiansen, J. S., Granskog, M. A., Koch, B. P., Møller, E. F., Winding, M. H. S., & Stedmon, C. A. (2022). Vertical redistribution of principle water masses on the Northeast Greenland Shelf. Nature Communications 2022 13:1, 13(1), 1–12. https://doi.org/10.1038/s41467-022-35413-z

Gohin, F., Bryère, P., Lefebvre, A., Sauriau, P. G., Savoye, N., Vantrepotte, V., Bozec, Y., Cariou, T., Conan, P., Coudray, S., Courtay, G., Françoise, S., Goffart, A., Fariñas, T. H., Lemoine, M., Piraud, A., Raimbault, P., & Rétho, M. (2020). Satellite and in situ monitoring of chl-a, turbidity, and total suspended matter in coastal waters: Experience of the year 2017 along the french coasts. Journal of Marine Science and Engineering, 8(9), 1–25. https://doi.org/10.3390/jmse8090665

Gohin, F., Druon, J. N., & Lampert, L. (2002). A five-channel Chlorophyll concentration algorithm applied to Sea WiFS data processed by SeaDAS in coastal waters. International Journal of Remote Sensing, 23(8), 1639–1661. https://doi.org/10.1080/01431160110071879

Gohin, F., Saulquin, B., Oger-Jeanneret, H., Lozac'h, L., Lampert, L., Lefebvre, A., Riou, P., & Bruchon, F. (2008). Towards a better assessment of the ecological status of coastal waters using satellite-derived chlorophyll-a concentrations. Remote Sensing of Environment, 112(8), 3329–3340. https://doi.org/10.1016/j.rse.2008.02.014

Gohin, F., Van der Zande, D., Tilstone, G., Eleveld, M. A., Lefebvre, A., Andrieux-Loyer, F., Blauw, A. N., Bryère, P., Devreker, D., Garnesson, P., Hernández Fariñas, T., Lamaury, Y., Lampert, L., Lavigne, H., Menet-Nedelec, F., Pardo, S., & Saulquin, B. (2019). Twenty years of satellite and in situ observations of surface chlorophyll-a from the northern Bay of Biscay to the eastern English Channel. Is the water quality improving? Remote Sensing of Environment, 233, 111343. https://doi.org/10.1016/j.rse.2019.111343

Goni, G. J., & Johns, W. E. (2001). A census of North Brazil current rings observed from TOPEX/POSEIDON altimetry: 1992-1998. Geophysical Research Letters, 28(1), 1–4. https://doi.org/10.1029/2000GL011717

Gons, H. J., Auer, M. T., & Effler, S. W. (2008). MERIS satellite chlorophyll mapping of oligotrophic and eutrophic waters in the Laurentian Great Lakes. Remote Sensing of Environment, 112(11), 4098–4106. https://doi.org/10.1016/j.rse.2007.06.029

Gons, H. J., Rijkeboer, M., & Ruddick, K. G. (2002). A chlorophyll-retrieval algorithm for satellite imagery (Medium Resolution Imaging Spectrometer) of inland and coastal waters. Journal of Plankton Research, 24(9), 947–951. https://doi.org/10.1093/plankt/24.9.947

Gordon, H. R. (1997). Atmospheric correction of ocean color imagery in the Earth observing system era. Journal of Geophysical Research Atmospheres, 102(14), 17081–17106. https://doi.org/10.1029/96JD02443

Gordon, H. R., & Morel, A. Y. (1983). Remote Assessment of Ocean Color for Interpretation of Satellite Visible Imagery: A Review. In Lect. Notes Coastal Estuarine Stud. (Vol. 4).

Gower, J., King, S., Borstad, G., & Brown, L. (2005). Detection of intense plankton blooms using the 709 nm band of the MERIS imaging spectrometer. International Journal of Remote Sensing, 26(9), 2005–2012. https://doi.org/10.1080/01431160500075857

Gower, S. T., Kucharik, C. J., & Norman, J. M. (1999). Direct and indirect estimation of leaf area index, f(APAR), and net primary production of terrestrial ecosystems. Remote Sensing of Environment, 70(1). https://doi.org/10.1016/S0034-4257(99)00056-5

Gratiot, N., Gardel, A., & Anthony, E. J. (2007). Trade-wind waves and mud dynamics on the French Guiana coast, South America: Input from ERA-40 wave data and field investigations. Marine Geology, 236(1–2), 15–26. https://doi.org/10.1016/j.margeo.2006.09.013

Groom, S. B., Sathyendranath, S., Ban, Y., Bernard, S., Brewin, B., Brotas, V., Brockmann, C., Chauhan, P., Choi, J. K., Chuprin, A., Ciavatta, S., Cipollini, P., Donlon, C., Franz, B. A., He, X., Hirata, T., Jackson, T., Kampel, M., Krasemann, H., … Wang, M. (2019). Satellite ocean colour: Current status and future perspective. In Frontiers in Marine Science (Vol. 6, Issue JUL). https://doi.org/10.3389/fmars.2019.00485

Gupta, A. K., Gupta, S. K., & Patil, R. S. (2003). A comparison of water quality indices for coastal water. Journal of Environmental Science and Health - Part A Toxic/Hazardous Substances and Environmental Engineering, 38(11), 2711–2725. https://doi.org/10.1081/ESE-120024458

Gurlin, D., Gitelson, A. A., & Moses, W. J. (2011). Remote estimation of chl-a concentration in turbid productive waters - Return to a simple two-band NIR-red model? Remote Sensing of Environment, 115(12), 3479–3490. https://doi.org/10.1016/j.rse.2011.08.011

Han, B., Loisel, H., Vantrepotte, V., Mériaux, X., Bryère, P., Ouillon, S., Dessailly, D., Xing, Q., & Zhu, J. (2016). Development of a semi-analytical algorithm for the retrieval of suspended particulate matter from remote sensing over clear to very turbid waters. Remote Sensing, 8(3). https://doi.org/10.3390/rs8030211

Harding, L. W., Gallegos, C. L., Perry, E. S., Miller, W. D., Adolf, J. E., Mallonee, M. E., & Paerl, H. W. (2016). Long-Term Trends of Nutrients and Phytoplankton in Chesapeake Bay. Estuaries and Coasts, 39(3). https://doi.org/10.1007/s12237-015-0023-7

REFERENCES

Harley, C. D. G., Hughes, A. R., Hultgren, K. M., Miner, B. G., Sorte, C. J. B., Thornber, C. S., Rodriguez, L. F., Tomanek, L., & Williams, S. L. (2006). The impacts of climate change in coastal marine systems. Ecology Letters, 9(2), 228–241. https://doi.org/10.1111/J.1461-0248.2005.00871.X

Harmel, T., & Chami, M. (2013). Estimation of the sunglint radiance field from optical satellite imagery over open ocean: Multidirectional approach and polarization aspects. Journal of Geophysical Research: Oceans, 118(1). https://doi.org/10.1029/2012JC008221

Helms, J. R., Stubbins, A., Ritchie, J. D., Minor, E. C., Kieber, D. J., & Mopper, K. (2008). Absorption spectral slopes and slope ratios as indicators of molecular weight, source, and photobleaching of chromophoric dissolved organic matter. Limnology and Oceanography, 53(3). https://doi.org/10.4319/lo.2008.53.3.0955

Henderikx Freitas, F., & Dierssen, H. M. (2019). Evaluating the seasonal and decadal performance of red band difference algorithms for Chlorophyll in an optically complex estuary with winter and summer blooms. Remote Sensing of Environment, 231. https://doi.org/10.1016/j.rse.2019.111228

Hieronymi, M., Müller, D., & Doerffer, R. (2017). The OLCI neural network swarm (ONNS): A bio-geo-optical algorithm for open ocean and coastal waters. Frontiers in Marine Science, 4(MAY). https://doi.org/10.3389/fmars.2017.00140

Hirsch, R. M., Slack, J. R., & Smith, R. A. (1982). Techniques of trend analysis for monthly water quality data. Water Resources Research, 18(1). https://doi.org/10.1029/WR018i001p00107

Holm-Hansen, O., Lorenzen, C. J., Holmes, R. W., & Strickland, J. D. H. (1965). Fluorometric determination of chlorophyll. ICES Journal of Marine Science, 30(1), 3–15. https://doi.org/10.1093/icesjms/30.1.3

Ibanez, F., & Conversi, A. (2002). Prediction of missing values and detection of “exceptional events” in a chronological planktonic series: A single algorithm. Ecological Modelling, 154(1–2). https://doi.org/10.1016/S0304-3800(02)00033-9

IOCCG. (2000). Reports of the International Ocean-Colour Coordinating Group Remote Sensing of Ocean Colour in Coastal, and Other Optically-Complex, Waters. In Reports and Monographs of the International OceanColour Coordinating Group (Vol. 3). http://www.vliz.be/imis/imis.php?module=ref&refid=134621&request=147862

IOCCG. (2006). Remote Sensing of Inherent Optical Properties: Fundamentals, Tests of Algorithms, and Applications. (Z. Lee, Ed.).

Jackson, J. B. C., Kirby, M. X., Berger, W. H., Bjorndal, K. A., Botsford, L. W., Bourque, B. J., Bradbury, R. H., Cooke, R., Erlandson, J., Estes, J. A., Hughes, T. P., Kidwell, S., Lange, C. B., Lenihan, H. S., Pandolfi, J. M., Peterson, C. H., Steneck, R. S., Tegner, M. J., & Warner, R. R. (2001). Historical overfishing and the recent collapse of coastal ecosystems. Science, 293(5530), 629–637. https://doi.org/10.1126/SCIENCE.1059199

Jamet, C., Loisel, H., & Dessailly, D. (2012). Retrieval of the spectral diffuse attenuation coefficient $K_d(\lambda)$ in open and coastal ocean waters using a neural network inversion .

Journal of Geophysical Research: Oceans, 117(C10), n/a-n/a. https://doi.org/10.1029/2012jc008076

Jänes, H., Macreadie, P. I., Zu Ermgassen, P. S. E., Gair, J. R., Treby, S., Reeves, S., Nicholson, E., Ierodiaconou, D., & Carnell, P. (2020). Quantifying fisheries enhancement from coastal vegetated ecosystems. Ecosystem Services, 43, 101105. https://doi.org/10.1016/J.ECOSER.2020.101105

Jha, D. K., Devi, M. P., Vidyalakshmi, R., Brindha, B., Vinithkumar, N. V., & Kirubagaran, R. (2015). Water quality assessment using water quality index and geographical information system methods in the coastal waters of Andaman Sea, India. Marine Pollution Bulletin, 100(1), 555–561. https://doi.org/10.1016/j.marpolbul.2015.08.032

Johns, W. E., Lee, T. N., Schott, F. A., Zantopp, R. J., & Evans, R. H. (1990). The North Brazil Current retroflection: Seasonal structure and eddy variability. Journal of Geophysical Research, 95(C12), 22103. https://doi.org/10.1029/jc095ic12p22103

Joshi, I. D., D'Sa, E. J., Osburn, C. L., Bianchi, T. S., Ko, D. S., Oviedo-Vargas, D., Arellano, A. R., & Ward, N. D. (2017). Assessing chromophoric dissolved organic matter (CDOM) distribution, stocks, and fluxes in Apalachicola Bay using combined field, VIIRS ocean color, and model observations. Remote Sensing of Environment, 191, 359–372. https://doi.org/10.1016/j.rse.2017.01.039

Julius Shiskin, Allan H. Young, & John C.Musgrave. (1967). The X-11 Variant of the Census Method II Seasonal Adjustment Program. Technical Paper No.15.

Kay, S., Hedley, J. D., & Lavender, S. (2009). Sun glint correction of high and low spatial resolution images of aquatic scenes: A review of methods for visible and near-infrared wavelengths. Remote Sensing, 1(4), 697–730. https://doi.org/10.3390/RS1040697

Kohonen, T. (1998). The self-organizing map. Neurocomputing, 21(1–3), 1–6. https://doi.org/10.1016/S0925-2312(98)00030-7

Kowalczuk, P., Zabłocka, M., Sagan, S., Kuliński, K., Kowalczuk, P., Zabłocka, M., Sagan, S., & Kuliński, K. (2010). Fluorescence measured in situ as a proxy of CDOM absorption and DOC concentration in the Baltic Sea*. In OCEANOLOGIA (Vol. 52, Issue 3). http://www.iopan.gda.pl/oceanologia/432

Kristensen, E., Bouillon, S., Dittmar, T., & Marchand, C. (2008). Organic carbon dynamics in mangrove ecosystems: A review. Aquatic Botany, 89(2), 201–219. https://doi.org/10.1016/J.AQUABOT.2007.12.005

Kutser, T., Pierson, D. C., Kallio, K. Y., Reinart, A., & Sobek, S. (2005). Mapping lake CDOM by satellite remote sensing. Remote Sensing of Environment, 94(4), 535–540. https://doi.org/10.1016/j.rse.2004.11.009

Lambs, L., Muller, E., & Fromard, F. (2007). The Guianese paradox: How can the freshwater outflow from the Amazon increase the salinity of the Guianan shore? Journal of Hydrology, 342(1–2), 88–96. https://doi.org/10.1016/j.jhydrol.2007.05.022

REFERENCES

Lampert, L., Bryere, P., & Gohin, F. (2015, November). Etude de la variation des paramètres température, biomasse et turbidité sur plus de 10 années dans les eaux marines guyanaises par imagerie satellite.

Lampert, L., Bryere, P., & Gohin, F. (2016). Etude de la variation des paramètres biomasse (Chla) et turbidité sur plus de 10 années dans les eaux marines guyanaises par imagerie satellite. - Phase 2 : utilisation de la résolution à 300 m.

Lampert, L., Bryere, P., & Gohin, F. (2017). Mesures de turbidité satellitaire des eaux fortement chargées en MES – Utilisation de l'algorithme OC5-HT en Guyane française.

Laperche, V., Hellal, J., Maury-Brachet, R., Joseph, B., Laporte, P., Breeze, D., & Blanchard, F. (2014). Regional distribution of mercury in sediments of the main rivers of French Guiana (Amazonian basin). SpringerPlus, 3(1). https://doi.org/10.1186/2193-1801-3-322

Lavigne, H., Van der Zande, D., Ruddick, K., Cardoso Dos Santos, J. F., Gohin, F., Brotas, V., & Kratzer, S. (2021). Quality-control tests for OC4, OC5 and NIR-red satellite chlorophyll-a algorithms applied to coastal waters. Remote Sensing of Environment, 255, 112237. https://doi.org/10.1016/j.rse.2020.112237

Le, C., Hu, C., English, D., Cannizzaro, J., Chen, Z., Kovach, C., Anastasiou, C. J., Zhao, J., & Carder, K. L. (2013). Inherent and apparent optical properties of the complex estuarine waters of Tampa Bay: What controls light? Estuarine, Coastal and Shelf Science, 117, 54–69. https://doi.org/10.1016/j.ecss.2012.09.017

Le, C., Lehrter, J. C., Hu, C., MacIntyre, H., & Beck, M. W. (2017). Satellite observation of particulate organic carbon dynamics on the Louisiana continental shelf. Journal of Geophysical Research: Oceans, 122(1), 555–569. https://doi.org/10.1002/2016JC012275

Le, C., Zhou, X., Hu, C., Lee, Z., Li, L., & Stramski, D. (2018). A Color-Index-Based Empirical Algorithm for Determining Particulate Organic Carbon Concentration in the Ocean From Satellite Observations. Journal of Geophysical Research: Oceans, 123(10), 7407–7419. https://doi.org/10.1029/2018JC014014

Leathers, R. A., Downes, T. V., & Mobley, C. D. (2004). Self-shading correction for oceanographic upwelling radiometers. Optics Express, 12(20), 4709. https://doi.org/10.1364/opex.12.004709

Legendre, L., & Rassoulzadegan, F. (2012). Plankton and nutrient dynamics in marine waters. Http://Dx.Doi.Org/10.1080/00785236.1995.10422042, 41(1), 153–172. https://doi.org/10.1080/00785236.1995.10422042

Li, P., Ke, Y., Wang, D., Ji, H., Chen, S., Chen, M., Lyu, M., & Zhou, D. (2021). Human impact on suspended particulate matter in the Yellow River Estuary, China: Evidence from remote sensing data fusion using an improved spatiotemporal fusion method. Science of The Total Environment, 750, 141612. https://doi.org/10.1016/J.SCITOTENV.2020.141612

Liu, H., He, X., Li, Q., Hu, X., Ishizaka, J., Kratzer, S., Yang, C., Shi, T., Hu, S., Zhou, Q., & Wu, G. (2022). Evaluation of Ocean Color Atmospheric Correction Methods for Sentinel-3 OLCI Using Global Automatic In Situ Observations. IEEE Transactions on Geoscience and Remote Sensing, 60. https://doi.org/10.1109/TGRS.2021.3136243

Loisel, H., Duforêt-Gaurier, L., Tran, T. K., Jorge, D., Steinmetz, F., Mangin, A., Bretagnon, M., & Fanton d'Andon, O. (2023). Characterization of the organic vs. inorganic fraction of suspended particulate matter in coastal waters based on ocean color radiometry remote sensing. 7th Edition of the Copernicus Marine Service Ocean State Report (OSR 7).

Loisel, H., Mangin, A., Vantrepotte, V., Dessailly, D., Ngoc Dinh, D., Garnesson, P., Ouillon, S., Lefebvre, J. P., Mériaux, X., & Minh Phan, T. (2014). Variability of suspended particulate matter concentration in coastal waters under the Mekong's influence from ocean color (MERIS) remote sensing over the last decade. Remote Sensing of Environment, 150. https://doi.org/10.1016/j.rse.2014.05.006

Loisel, H., Mériaux, X., Berthon, J. F., & Poteau, A. (2007). Investigation of the optical backscattering to scattering ratio of marine particles in relation to their biogeochemical composition in the eastern English Channel and southern North Sea. Limnology and Oceanography, 52(2), 739–752. https://doi.org/10.4319/LO.2007.52.2.0739

Loisel, H., Stramski, D., Dessailly, D., Jamet, C., Li, L., & Reynolds, R. A. (2018). An Inverse Model for Estimating the Optical Absorption and Backscattering Coefficients of Seawater From Remote-Sensing Reflectance Over a Broad Range of Oceanic and Coastal Marine Environments. Journal of Geophysical Research: Oceans, 123(3), 2141–2171. https://doi.org/10.1002/2017JC013632

Loisel, H., Vantrepotte, V., Dessailly, D., & Mériaux, X. (2014). Assessment of the colored dissolved organic matter in coastal waters from ocean color remote sensing Assessment of the colored dissolved organic matter in coastal waters from ocean color remote sensing. May. https://doi.org/10.1364/OE.22.013109

Loisel, H., Vantrepotte, V., Jamet, C., & Ngoc Dat, D. (2013). Challenges and New Advances in Ocean Color Remote Sensing of Coastal Waters. In Topics in Oceanography. https://doi.org/10.5772/56414

Loisel, H., Vantrepotte, V., Ouillon, S., Ngoc, D. D., Herrmann, M., Tran, V., Mériaux, X., Dessailly, D., Jamet, C., Duhaut, T., Nguyen, H. H., & Van Nguyen, T. (2017). Assessment and analysis of the chlorophyll-a concentration variability over the Vietnamese coastal waters from the MERIS ocean color sensor (2002–2012). Remote Sensing of Environment, 190(March), 217–232. https://doi.org/10.1016/j.rse.2016.12.016

Lubac, B., & Loisel, H. (2007). Variability and classification of remote sensing reflectance spectra in the eastern English Channel and southern North Sea. Remote Sensing of Environment, 110(1), 45–58. https://doi.org/10.1016/j.rse.2007.02.012

Lubac, B., Loisel, H., Guiselin, N., Astoreca, R., Artigas, L. F., & Mériaux, X. (2008). Hyperspectral and multispectral ocean color inversions to detect Phaeocystis globosa blooms in coastal waters. Journal of Geophysical Research: Oceans, 113(6). https://doi.org/10.1029/2007JC004451

Ma, Z., Li, H., Ye, Z., Wen, J., Hu, Y., & Liu, Y. (2020). Application of modified water quality index (WQI) in the assessment of coastal water quality in main aquaculture areas of Dalian, China. Marine Pollution Bulletin, 157. https://doi.org/10.1016/j.marpolbul.2020.111285

REFERENCES

Mannino, A., Russ, M. E., & Hooker, S. B. (2008). Algorithm development and validation for satellite-derived distributions of DOC and CDOM in the U.S. Middle Atlantic Bight. Journal of Geophysical Research: Oceans, 113(C7), 7051. https://doi.org/10.1029/2007JC004493

Medeiros, P. M., Seidel, M., Ward, N. D., Carpenter, E. J., Gomes, H. R., Niggemann, J., Krusche, A. V., Richey, J. E., Yager, P. L., & Dittmar, T. (2015). Fate of the Amazon River dissolved organic matter in the tropical Atlantic Ocean. Global Biogeochemical Cycles, 29(5), 677–690. https://doi.org/10.1002/2015GB005115

Mélin, F., & Vantrepotte, V. (2015). How optically diverse is the coastal ocean? Remote Sensing of Environment, 160, 235–251. https://doi.org/10.1016/j.rse.2015.01.023

Mélin, F., Vantrepotte, V., Clerici, M., D'Alimonte, D., Zibordi, G., Berthon, J. F., & Canuti, E. (2011). Multi-sensor satellite time series of optical properties and chlorophyll-a concentration in the Adriatic Sea. Progress in Oceanography, 91(3), 229–244. https://doi.org/10.1016/j.pocean.2010.12.001

Milliman, J. D., & Kao, S. J. (2005). Hyperpycnal discharge of fluvial sediment to the ocean: Impact of super-typhoon herb (1996) on Taiwanese rivers. Journal of Geology, 113(5), 503–516. https://doi.org/10.1086/431906

Mishra, S., & Mishra, D. R. (2012). Normalized difference chlorophyll index: A novel model for remote estimation of chlorophyll-a concentration in turbid productive waters. Remote Sensing of Environment, 117, 394–406. https://doi.org/10.1016/j.rse.2011.10.016

Mitchell, B. G., Mati, K., John, W., & Malgorzata, S. (2003). Determination of spectral absorption coefficients of particles, dissolved material and phytoplankton for discrete. In Ocean Optics Protocols for Satellite Ocean Color Sensor Validation: Vol. IV (pp. 39–64).

MNT bathymétrique de façade de la Guyane. (n.d.). Retrieved March 29, 2023, from https://diffusion.shom.fr/donnees/mnt-facade-guyane-homonim.html

Mobley, C. D. (2015). Polarized reflectance and transmittance properties of windblown sea surfaces. Applied Optics, 54(15), 4828. https://doi.org/10.1364/AO.54.004828

Mograne, M. A., Jamet, C., Loisel, H., Vantrepotte, V., Mériaux, X., & Cauvin, A. (2019). Evaluation of five atmospheric correction algorithms over french optically-complex waters for the sentinel-3a olci ocean color sensor. Remote Sensing, 11(6). https://doi.org/10.3390/RS11060668

Moura, R. L., Amado-Filho, G. M., Moraes, F. C., Brasileiro, P. S., Salomon, P. S., Mahiques, M. M., Bastos, A. C., Almeida, M. G., Silva, J. M., Araujo, B. F., Brito, F. P., Rangel, T. P., Oliveira, B. C. V., Bahia, R. G., Paranhos, R. P., Dias, R. J. S., Siegle, E., Figueiredo, A. G., Pereira, R. C., … Thompson, F. L. (2016). An extensive reef system at the Amazon River mouth. Science Advances, 2(4). https://doi.org/10.1126/sciadv.1501252

Mouw, C. B., Greb, S., Aurin, D., DiGiacomo, P. M., Lee, Z., Twardowski, M., Binding, C., Hu, C., Ma, R., Moore, T., Moses, W., & Craig, S. E. (2015). Aquatic color radiometry remote sensing of coastal and inland waters: Challenges and recommendations for future satellite

missions. In Remote Sensing of Environment (Vol. 160). https://doi.org/10.1016/j.rse.2015.02.001

Nagelkerken, I., Blaber, S. J. M., Bouillon, S., Green, P., Haywood, M., Kirton, L. G., Meynecke, J. O., Pawlik, J., Penrose, H. M., Sasekumar, A., & Somerfield, P. J. (2008). The habitat function of mangroves for terrestrial and marine fauna: A review. Aquatic Botany, 89(2), 155–185. https://doi.org/10.1016/J.AQUABOT.2007.12.007

Nechad, B., Ruddick, K. G., & Park, Y. (2010). Calibration and validation of a generic multisensor algorithm for mapping of total suspended matter in turbid waters. Remote Sensing of Environment, 114(4), 854–866. https://doi.org/10.1016/j.rse.2009.11.022

Neil, C., Spyrakos, E., Hunter, P. D., & Tyler, A. N. (2019). A global approach for chlorophyll-a retrieval across optically complex inland waters based on optical water types. Remote Sensing of Environment, 229(November 2017), 159–178. https://doi.org/10.1016/j.rse.2019.04.027

Nellemann, C., & Corcoran, E. (2009). Blue carbon: the role of healthy oceans in binding carbon: a rapid response assessment (Nairobi: UNEP, GRID-Arendal)

Neukermans, G., Ruddick, K., Loisel, H., & Roose, P. (2012). Optimization and quality control of suspended particulate matter concentration measurement using turbidity measurements. Limnology and Oceanography: Methods, 10(DECEMBER), 1011–1023. https://doi.org/10.4319/lom.2012.10.1011

Ngoc, D. D., Loisel, H., Vantrepotte, V., Xuan, H. C., Minh, N. N., Verpoorter, C., Meriaux, X., Minh, H. P. T., Thi, H. Le, Hong, H. L. V., & Van, T. N. (2020). A simple empirical band-ratio algorithm to assess suspended particulate matter from remote sensing over coastal and inland waters of vietnam: Application to the VNREDSat-1/NAOMI sensor. Water (Switzerland), 12(9). https://doi.org/10.3390/w12092636

Odermatt, D., Gitelson, A., Brando, V. E., & Schaepman, M. (2012). Review of constituent retrieval in optically deep and complex waters from satellite imagery. Remote Sensing of Environment, 118, 116–126. https://doi.org/10.1016/j.rse.2011.11.013

Oliveira, C. J. M. de, & Clavier, J. (2000). Variations spatio-temporelles des matieres en suspension dans I'estuaire du Sinnamary, Guyane Française: Influence du barrage hydroélectrique de Petit Saut. Revista Brasileira de Oceanografia, 48(1). https://doi.org/10.1590/s1413-77392000000100003

Oliveira, E. N., Fernandes, A. M., Kampel, M., Cordeiro, R. C., Brandini, N., Vinzon, S. B., Grassi, R. M., Pinto, F. N., Fillipo, A. M., & Paranhos, R. (2016). Assessment of remotely sensed chlorophyll- a concentration in Guanabara Bay, Brazil. Journal of Applied Remote Sensing, 10(2), 026003. https://doi.org/10.1117/1.jrs.10.026003

O'Reilly, J. E., Maritorena, S., Mitchell, B. G., Siegel, D. A., Carder, K. L., Garver, S. A., Kahru, M., & McClain, C. (1998). Ocean color chlorophyll algorithms for SeaWiFS. Journal of Geophysical Research: Oceans, 103(C11), 24937–24953. https://doi.org/10.1029/98JC02160

REFERENCES

O'Reilly, J. E., & Werdell, P. J. (2019). Chlorophyll algorithms for ocean color sensors - OC4, OC5 & OC6. Remote Sensing of Environment, 229(October 2018), 32–47. https://doi.org/10.1016/j.rse.2019.04.021

Pahlevan, N., Mangin, A., Balasubramanian, S. V., Smith, B., Alikas, K., Arai, K., Barbosa, C., Bélanger, S., Binding, C., Bresciani, M., Giardino, C., Gurlin, D., Fan, Y., Harmel, T., Hunter, P., Ishikaza, J., Kratzer, S., Lehmann, M. K., Ligi, M., … Warren, M. (2021). ACIX-Aqua: A global assessment of atmospheric correction methods for Landsat-8 and Sentinel-2 over lakes, rivers, and coastal waters. Remote Sensing of Environment, 258. https://doi.org/10.1016/j.rse.2021.112366

Pahlevan, N., Smith, B., Schalles, J., Binding, C., Cao, Z., Ma, R., Alikas, K., Kangro, K., Gurlin, D., Hà, N., Matsushita, B., Moses, W., Greb, S., Lehmann, M. K., Ondrusek, M., Oppelt, N., & Stumpf, R. (2020). Seamless retrievals of chlorophyll-a from Sentinel-2 (MSI) and Sentinel-3 (OLCI) in inland and coastal waters: A machine-learning approach. Remote Sensing of Environment, 240. https://doi.org/10.1016/j.rse.2019.111604

Pauly, D., Christensen, V., Guénette, S., Pitcher, T. J., Sumaila, U. R., Walters, C. J., Watson, R., & Zeller, D. (2002). Towards sustainability in world fisheries. Nature 2002 418:6898, 418(6898), 689–695. https://doi.org/10.1038/nature01017

Pereira-Sandoval, M., Ruescas, A., Urrego, P., Ruiz-Verdú, A., Delegido, J., Tenjo, C., Soria-Perpinyà, X., Vicente, E., Soria, J., & Moreno, J. (2019). Evaluation of atmospheric correction algorithms over spanish inland waters for sentinel-2 multi spectral imagery data. Remote Sensing, 11(12). https://doi.org/10.3390/rs11121469

Pezzulli, S., Stephenson, D. B., & Hannachi, A. (2005). The Variability of Seasonality.

Platt, T., & Sathyendranath, S. (2008). Ecological indicators for the pelagic zone of the ocean from remote sensing. Remote Sensing of Environment, 112(8), 3426–3436. https://doi.org/10.1016/J.RSE.2007.10.016

Fry, E. S., & Pope, R. M. (1997). Absorption spectrum (380–700 nm) of pure water. II. Integrating cavity measurements. *Applied Optics, Vol. 36, Issue 33, Pp. 8710-8723*, *36*(33), 8710–8723. https://doi.org/10.1364/AO.36.008710

Prost, M. T. (1989). Coastal dynamics and chenier sands in French Guiana. In Marine Geology (Vol. 90).

Ray, R., Michaud, E., Aller, R. C., Vantrepotte, V., Gleixner, G., Walcker, R., Devesa, J., Le Goff, M., Morvan, S., & Thouzeau, G. (2018). The sources and distribution of carbon (DOC, POC, DIC) in a mangrove dominated estuary (French Guiana, South America). Biogeochemistry, 138(3). https://doi.org/10.1007/s10533-018-0447-9

Ray, R., Thouzeau, G., Walcker, R., Vantrepotte, V., Gleixner, G., Morvan, S., Devesa, J., & Michaud, E. (2020). Mangrove-Derived Organic and Inorganic Carbon Exchanges Between the Sinnamary Estuarine System (French Guiana, South America) and Atlantic Ocean. Journal of Geophysical Research: Biogeosciences, 125(8). https://doi.org/10.1029/2020JG005739

Reflectances : Ocean Optics Web Book. Retrieved April 23, 2023, from https://www.oceanopticsbook.info/view/inherent-and-apparent-optical-properties/reflectances

Rodriguez, H. N., Mehta, A. J., Beach, W. P., Rodriguezt, H. N., & Mehta, A. J. (2001). Modeling Muddy Coast Response to Waves. Journal of Coastal Research, 27(27).

Saad El-Din, M., Gaber, hmed, Koch, M., Ahmed, R. S., & Bahgat, I. (2013). Remote Sensing Application for Water Quality Assessment in Lake Timsah, Suez Canal, Egypt. Journal of Remote Sensing Technology. https://doi.org/10.18005/jrst0103002

Salisbury, J., Vandemark, D., Campbell, J., Hunt, C., Wisser, D., Reul, N., & Chapron, B. (2011). Spatial and temporal coherence between Amazon River discharge, salinity, and light absorption by colored organic carbon in western tropical Atlantic surface waters. Journal of Geophysical Research: Oceans, 116(7). https://doi.org/10.1029/2011JC006989

Salter, I., Garcia, N., Rigaut-Jalabert, F., Gregori, G., Marie, D., & Pineau, P. (2021). *Procédure : Protocole national Prélèvement, fixation, stockage et envoi des échantillons pour la cytométrie en flux*. https://www.somlit.fr/parametres-et-protocoles/

Santos, J. I., Vidal, T., Gonçalves, F. J. M., Castro, B. B., & Pereira, J. L. (2021). Challenges to water quality assessment in Europe – Is there scope for improvement of the current Water Framework Directive bioassessment scheme in rivers? In Ecological Indicators (Vol. 121). https://doi.org/10.1016/j.ecolind.2020.107030

Sanz, N., Diop, B., Blanchard, F., & Lampert, L. (2017). On the influence of environmental factors on harvest: the French Guiana shrimp fishery paradox. Environmental Economics and Policy Studies, 19(2), 233–247. https://doi.org/10.1007/S10018-016-0153-6/TABLES/4

Schott, F. A., Stramma, L., & Fischer, J. (1995). The warm water inflow into the western tropical Atlantic boundary regime, spring 1994. Journal of Geophysical Research, 100(C12). https://doi.org/10.1029/95jc02803

Sen, P. K. (1968). Estimates of the Regression Coefficient Based on Kendall's Tau. Journal of the American Statistical Association, 63(324). https://doi.org/10.1080/01621459.1968.10480934

Siswanto, E., Tang, J., Yamaguchi, H., Ahn, Y. H., Ishizaka, J., Yoo, S., Kim, S. W., Kiyomoto, Y., Yamada, K., Chiang, C., & Kawamura, H. (2011). Empirical ocean-color algorithms to retrieve chlorophyll-a, total suspended matter, and colored dissolved organic matter absorption coefficient in the Yellow and East China Seas. Journal of Oceanography, 67(5), 627–650. https://doi.org/10.1007/s10872-011-0062-z

Smith, M. E., Robertson Lain, L., & Bernard, S. (2018). An optimized Chlorophyll a switching algorithm for MERIS and OLCI in phytoplankton-dominated waters. Remote Sensing of Environment, 215(June), 217–227. https://doi.org/10.1016/j.rse.2018.06.002

Sondag, F., Guyot, J. L., Moquet, J. S., Laraque, A., Adele, G., Cochonneau, G., Doudou, J. C., Lagane, C., & Vauchel, P. (2010). Suspended sediment and dissolved load budgets of two Amazonian rivers from the Guiana Shield: Maroni River at Langa Tabiki and Oyapock

River at Saut Maripa (French Guiana). Hydrological Processes, 24(11), 1433–1445. https://doi.org/10.1002/HYP.7603

Soppa, M. A., Silva, B., Steinmetz, F., Keith, D., Scheffler, D., Bohn, N., & Bracher, A. (2021). Assessment of polymer atmospheric correction algorithm for hyperspectral remote sensing imagery over coastal waters. Sensors, 21(12). https://doi.org/10.3390/s21124125

Steinmetz, F., Deschamps, P.-Y., & Ramon, D. (2011). Atmospheric correction in presence of sun glint: application to MERIS. Optics Express, 19(10), 9783. https://doi.org/10.1364/oe.19.009783

Stramski, D., Boss, E., Bogucki, D., & Voss, K. J. (2004). The role of seawater constituents in light backscattering in the ocean. In Progress in Oceanography (Vol. 61, Issue 1, pp. 27–56). Elsevier Ltd. https://doi.org/10.1016/j.pocean.2004.07.001

Stramski, D., Reynolds, R. A., Babin, M., Kaczmarek, S., Lewis, M. R., Röttgers, R., Sciandra, A., Stramska, M., Twardowski, M. S., Franz, B. A., & Claustre, H. (2008). Relationships between the surface concentration of particulate organic carbon and optical properties in the eastern South Pacific and eastern Atlantic Oceans. Biogeosciences, 5(1), 171–201. https://doi.org/10.5194/bg-5-171-2008

Subramaniam, A., Yager, P. L., Carpenter, E. J., Mahaffey, C., Björkman, K., Cooley, S., Kustka, A. B., Montoya, J. P., Sañudo-Wilhelmy, S. A., Shipe, R., & Capone, D. G. (2008). Amazon River enhances diazotrophy and carbon sequestration in the tropical North Atlantic Ocean. Proceedings of the National Academy of Sciences of the United States of America, 105(30), 10460–10465. https://doi.org/10.1073/PNAS.0710279105/SUPPL_FILE/SD1.XLS

Suominen, T. (2018). Applying MERIS time series and dynamic time warping for delineating areas with similar temporal behaviour in the northern Baltic Sea. Ecological Indicators, 95(August), 794–804. https://doi.org/10.1016/j.ecolind.2018.08.023

Syvitski, J. P. M., Vörösmarty, C. J., Kettner, A. J., & Green, P. (2005). Impact of humans on the flux of terrestrial sediment to the global coastal ocean. Science, 308(5720), 376–380. https://doi.org/10.1126/SCIENCE.1109454

Taillardat, P., Friess, D. A., & Lupascu, M. (2018). Mangrove blue carbon strategies for climate change mitigation are most effective at the national scale. Biology Letters, 14(10). https://doi.org/10.1098/RSBL.2018.0251

Tamooh, F., Van Den Meersche, K., Meysman, F., Marwick, T. R., Borges, A. V., Merckx, R., Dehairs, F., Schmidt, S., Nyunja, J., & Bouillon, S. (2012). Distribution and origin of suspended matter and organic carbon pools in the Tana River Basin, Kenya. Biogeosciences, 9(8). https://doi.org/10.5194/bg-9-2905-2012

Tassan, S. (1994). Local algorithms using SeaWiFS data for the retrieval of phytoplankton, pigments, suspended sediment, and yellow substance in coastal waters.

Tavares, M. H., Lins, R. C., Harmel, T., Fragoso, C. R., Martínez, J. M., & Motta-Marques, D. (2021). Atmospheric and sunglint correction for retrieving chlorophyll-a in a productive

tropical estuarine-lagoon system using Sentinel-2 MSI imagery. ISPRS Journal of Photogrammetry and Remote Sensing, 174. https://doi.org/10.1016/j.isprsjprs.2021.01.021

Th, N., Nguyên, T., Loan, K., & Hi, N. C. (2013). Development of Water Quality Index for Coastal Zone and Application in the H Long Bay. In VNU Journal of Earth and Environmental Sciences (Vol. 29, Issue 4).

Theuerkauf, S. J., Barrett, L. T., Alleway, H. K., Costa-Pierce, B. A., St Gelais, A., Jones, R. C., & Seth Theuerkauf, C. J. (2021). Habitat value of bivalve shellfish and seaweed aquaculture for fish and invertebrates: Pathways, synthesis and next steps. Wiley Online Library, 14(1), 54–72. https://doi.org/10.1111/raq.12584

Tran, M. D., Vantrepotte, V., Loisel, H., Oliveira, E. N., Tran, K. T., Jorge, D., Mériaux, X., & Paranhos, R. (2023). Band Ratios Combination for Estimating Chlorophyll-a from Sentinel-2 and Sentinel-3 in Coastal Waters. Remote Sensing 2023, Vol. 15, Page 1653, 15(6), 1653. https://doi.org/10.3390/RS15061653

Tran, T. K., Duforêt-Gaurier, L., Vantrepotte, V., Ferreira Jorge, D. S., Mériaux, X., Cauvin, A., d'Andon, F., & Loisel, H. (2019). Deriving particulate organic carbon in coastal waters from remote sensing: Inter-comparison exercise and development of a maximum band-ratio approach. Remote Sensing, 11(23). https://doi.org/10.3390/rs11232849

Vandermeulen, R. A., Mannino, A., Craig, S. E., & Werdell, P. J. (2020). 150 shades of green: Using the full spectrum of remote sensing reflectance to elucidate color shifts in the ocean. Remote Sensing of Environment, 247. https://doi.org/10.1016/j.rse.2020.111900

Vanhellemont, Q. (2019). Adaptation of the dark spectrum fitting atmospheric correction for aquatic applications of the Landsat and Sentinel-2 archives. Remote Sensing of Environment, 225. https://doi.org/10.1016/j.rse.2019.03.010

Vanhellemont, Q., & Ruddick, K. (2014). Turbid wakes associated with offshore wind turbines observed with Landsat 8. Remote Sensing of Environment, 145, 105–115. https://doi.org/10.1016/J.RSE.2014.01.009

Vantrepotte, V., Danhiez, F.-P., Loisel, H., Ouillon, S., Mériaux, X., Cauvin, A., & Dessailly, D. (2015). CDOM-DOC relationship in contrasted coastal waters: Implication for DOC retrieval from ocean color remote sensing observation. Optics Express, 23(1), 33. https://doi.org/10.1364/oe.23.000033

Vantrepotte, V., Gensac, E., Loisel, H., Gardel, A., Dessailly, D., & Mériaux, X. (2013). Satellite assessment of the coupling between in water suspended particulate matter and mud banks dynamics over the French Guiana coastal domain. Journal of South American Earth Sciences, 44(April 2020), 25–34. https://doi.org/10.1016/j.jsames.2012.11.008

Vantrepotte, V., Loisel, H., Dessailly, D., & Mériaux, X. (2012). Optical classification of contrasted coastal waters. Remote Sensing of Environment, 123. https://doi.org/10.1016/j.rse.2012.03.004

Vantrepotte, V., Loisel, H., Mériaux, X., Neukermans, G., Dessailly, D., Jamet, C., Gensac, E., & Gardel, A. (2011). Seasonal and inter-annual (2002-2010) variability of the suspended

particulate matter as retrieved from satellite ocean color sensor over the French Guiana coastal waters. Journal of Coastal Research, SPEC. ISSUE 64, 1750–1754.

Vantrepotte, V., Loisel, H., Mlin, F., Desailly, D., & Duforêt-Gaurier, L. (2011). Global particulate matter pool temporal variability over the SeaWiFS period (1997-2007). Geophysical Research Letters, 38(2). https://doi.org/10.1029/2010GL046167

Vantrepotte, V., & Mélin, F. (2011). Inter-annual variations in the SeaWiFS global chlorophyll a concentration (1997-2007). Deep-Sea Research Part I: Oceanographic Research Papers, 58(4), 429–441. https://doi.org/10.1016/j.dsr.2011.02.003

Walcker, R., Gandois, L., Proisy, C., Corenblit, D., Mougin, É., Laplanche, C., Ray, R., & Fromard, F. (2018). Control of "blue carbon" storage by mangrove ageing: Evidence from a 66-year chronosequence in French Guiana. Global Change Biology, 24(6), 2325–2338. https://doi.org/10.1111/GCB.14100

Waliser, D. E., & Gautier, C. (1993). A satellite-derived climatology of the ITCZ. Journal of Climate, 6(11). https://doi.org/10.1175/1520-0442(1993)006<2162:ASDCOT>2.0.CO;2

Ward, J. H. (1963). Hierarchical Grouping to Optimize an Objective Function. Journal of the American Statistical Association, 58(301), 236. https://doi.org/10.2307/2282967

Warren, M. A., Simis, S. G. H., Martinez-Vicente, V., Poser, K., Bresciani, M., Alikas, K., Spyrakos, E., Giardino, C., & Ansper, A. (2019). Assessment of atmospheric correction algorithms for the Sentinel-2A MultiSpectral Imager over coastal and inland waters. Remote Sensing of Environment, 225, 267–289. https://doi.org/10.1016/j.rse.2019.03.018

Wells, J. T., & Coleman, J. M. (1977). Longshore transport of mud by waves: Northeastern Coast Of South America. Geologie En Mijnbouw, 57(2).

Werdell, P. J., & Bailey, S. W. (2005). An improved in-situ bio-optical data set for ocean color algorithm development and satellite data product validation. Remote Sensing of Environment, 98(1). https://doi.org/10.1016/j.rse.2005.07.001

Werdell, P. J., Bailey, S. W., Franz, B. A., Harding, L. W., Feldman, G. C., & McClain, C. R. (2009). Regional and seasonal variability of chlorophyll-a in Chesapeake Bay as observed by SeaWiFS and MODIS-Aqua. Remote Sensing of Environment, 113(6), 1319–1330. https://doi.org/10.1016/J.RSE.2009.02.012

Werdell, P. J., McKinna, L. I. W., Boss, E., Ackleson, S. G., Craig, S. E., Gregg, W. W., Lee, Z., Maritorena, S., Roesler, C. S., Rousseaux, C. S., Stramski, D., Sullivan, J. M., Twardowski, M. S., Tzortziou, M., & Zhang, X. (2018). An overview of approaches and challenges for retrieving marine inherent optical properties from ocean color remote sensing. In Progress in Oceanography (Vol. 160). https://doi.org/10.1016/j.pocean.2018.01.001

Woźniak, S. B., Darecki, M., Zabłocka, M., Burska, D., & Dera, J. (2016). New simple statistical formulas for estimating surface concentrations of suspended particulate matter (SPM) and particulate organic carbon (POC) from remote-sensing reflectance in the southern Baltic Sea. Oceanologia, 58(3), 161–175. https://doi.org/10.1016/j.oceano.2016.03.002

Woźniak, S. B., Meler, J., Lednicka, B., Zdun, A., & Stoń-Egiert, J. (2011). Inherent optical properties of suspended particulate matter in the southern Baltic Sea. Oceanologia, 53(3), 691–729. https://doi.org/10.5697/OC.53-3.691

Woźniak, S. B., Stramski, D., Stramska, M., Reynolds, R. A., Wright, V. M., Miksic, E. Y., Cichocka, M., & Cieplak, A. M. (2010). Optical variability of seawater in relation to particle concentration, composition, and size distribution in the nearshore marine environment at Imperial Beach, California. Journal of Geophysical Research: Oceans, 115(8). https://doi.org/10.1029/2009JC005554

Xi, H., Losa, S. N., Mangin, A., Soppa, M. A., Garnesson, P., Demaria, J., Liu, Y., d'Andon, O. H. F., & Bracher, A. (2020). Global retrieval of phytoplankton functional types based on empirical orthogonal functions using CMEMS GlobColour merged products and further extension to OLCI data. Remote Sensing of Environment, 240, 111704. https://doi.org/10.1016/j.rse.2020.111704

Xu, Y., Feng, L., Zhao, D., & Lu, J. (2020). Assessment of Landsat atmospheric correction methods for water color applications using global AERONET-OC data. International Journal of Applied Earth Observation and Geoinformation, 93. https://doi.org/10.1016/j.jag.2020.102192

Yang, M. M., Ishizaka, J., Goes, J. I., Gomes, H. do R., Maúre, E. de R., Hayashi, M., Katano, T., Fujii, N., Saitoh, K., Mine, T., Yamashita, H., Fujii, N., & Mizuno, A. (2018). Improved MODIS-Aqua chlorophyll-a retrievals in the turbid semi-enclosed Ariake Bay, Japan. Remote Sensing, 10(9), 1–20. https://doi.org/10.3390/rs10091335

Yeung, L. Y., Berelson, W. M., Young, E. D., Prokopenko, M. G., Rollins, N., Coles, V. J., Montoya, J. P., Carpenter, E. J., Steinberg, D. K., Foster, R. A., Capone, D. G., & Yager, P. L. (2012). Impact of diatom-diazotroph associations on carbon export in the Amazon River plume. Geophysical Research Letters, 39(18), 18609. https://doi.org/10.1029/2012GL053356

ANNEX

Table A.1. *Adaptation of inversion models to derive biogeochemical concentration considering MERIS, OLCI, and MSI sensors*

Sensors	Spectral bands	Algorithm formulation	Coefficients				Plot
SPM							
MERIS/ OLCI/ MSI		**Original BingHan16**	A^{ρ}_{L}	C^{ρ}_{L}	A^{ρ}_{H}	C^{ρ}_{H}	
	665	$SPM_L = \frac{A^{\rho}_{L}.\rho_w(\lambda_0)}{1 - \frac{\rho_w(\lambda_0)}{C^{\rho}_{L}}}$ $SPM_H = \frac{A^{\rho}_{H}.\rho_w(\lambda_0)}{1 - \frac{\rho_w(\lambda_0)}{C^{\rho}_{H}}}$ $W_L = \begin{cases} 1, \text{ if } R_{rs}(\lambda_0) \leq 0.03\ sr^{-1} \\ 0, \text{ if } R_{rs}(\lambda_0) \geq 0.04\ sr^{-1} \\ \log_{10}(0.04) - \log_{10}[R_{rs}(\lambda_0)], \text{ otherwise} \end{cases}$ $W_H = \begin{cases} 0, \text{ if } R_{rs}(\lambda_0) \leq 0.03\ sr^{-1} \\ 1, \text{ if } R_{rs}(\lambda_0) \geq 0.04\ sr^{-1} \\ \log_{10}[R_{rs}(\lambda_0)] - \log_{10}(0.03), \text{ otherwise} \end{cases}$ $SPM = \frac{W_L.SPM_L + W_H.SPM_H}{W_L + W_H}$	396.01	0.5	1208.48	0.34	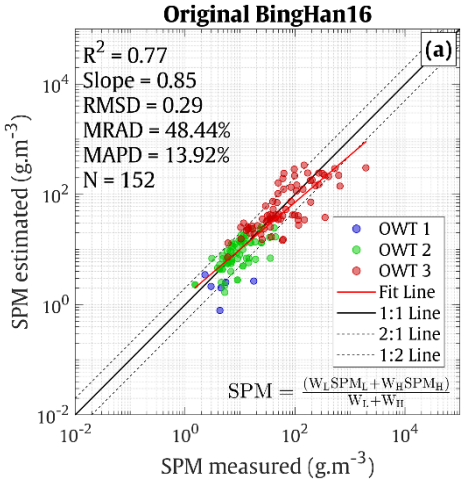

<table>
<tr><th colspan="8">POC</th></tr>
<tr><td rowspan="5">MERIS/
OLCI</td><td rowspan="5">412
443
490
510
560
665</td><td>Tuned Le17 (OWT 3)</td><td>a</td><td>b</td><td>c</td><td>d</td><td>e</td><td rowspan="5"> 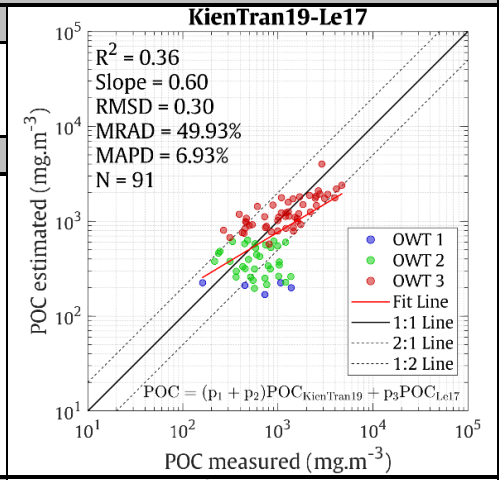 </td></tr>
<tr><td>$POC=1000\times\exp[a\times R_{rs}(490)+b\times R_{rs}(510)+c\times R_{rs}(560)+d\times R_{rs}(665)+e]$</td><td>738.57</td><td>-836.3</td><td>110.71</td><td>52.52</td><td>-0.49</td></tr>
<tr><td>KienTran19 (OWTs 1 & 2)</td><td colspan="2">a</td><td colspan="2">b</td></tr>
<tr><td>$POC=10^{aX+b}$
$X=\log_{10}\left\{\max\left[\frac{R_{rs}(665)}{R_{rs}(490)},\frac{R_{rs}(665)}{R_{rs}(510)},\frac{R_{rs}(665)}{R_{rs}(555)}\right]\right\}$</td><td colspan="2">0.928</td><td colspan="2">2.875</td></tr>
<tr><td rowspan="5">MSI</td><td rowspan="5">443
490
560
665</td><td>Tuned Le17 (OWT 3)</td><td>a</td><td>b</td><td>c</td><td>d</td><td rowspan="5"> 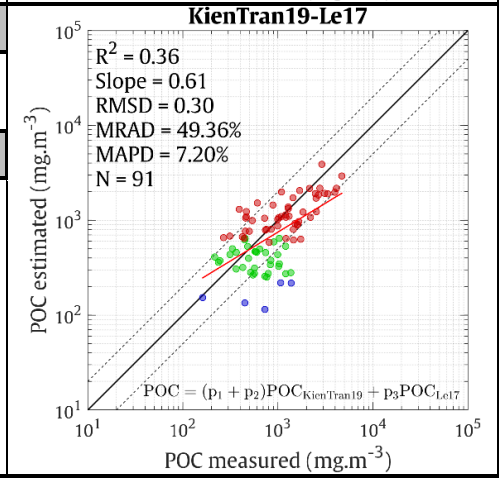 </td></tr>
<tr><td>$POC=1000\times\exp[a\times R_{rs}(490)+b\times R_{rs}(560)+c\times R_{rs}(665)+d]$</td><td>99.25</td><td>-103.67</td><td>64.39</td><td>-0.46</td></tr>
<tr><td>KienTran19 (OWTs 1 & 2)</td><td colspan="2">a</td><td colspan="2">b</td></tr>
<tr><td>$POC=10^{aX+b}$
$X=\log_{10}\left[\frac{R_{rs}(490)}{R_{rs}(560)}\right]$</td><td colspan="2">-1.824</td><td colspan="2">2.34</td></tr>
</table>

<table>
<tr><th colspan="9">$a_{CDOM}(412)$</th></tr>
<tr><td rowspan="2">MERIS/
OLCI</td><td rowspan="2">443
490
510
560
665</td><td>Tuned Cao18</td><td>a</td><td>b</td><td>c</td><td>d</td><td>e</td><td>f</td><td rowspan="2"> 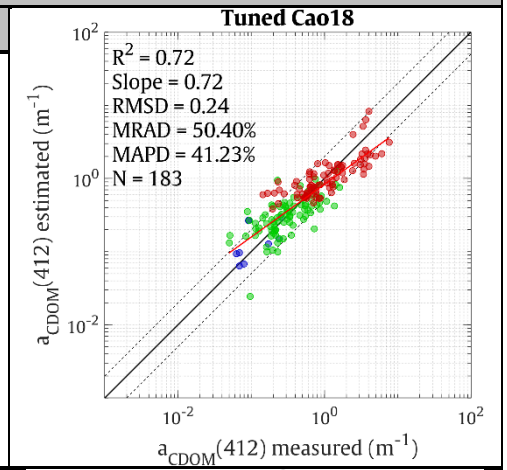
</td></tr>
<tr><td>$\ln(a_{CDOM}(412)) = a\times\ln(R_{rs}(443)) + b\times\ln(R_{rs}(490)) + c\times\ln(R_{rs}(560)) + d\times\ln(R_{rs}(665)) + e$</td><td>3.03</td><td>-20.51</td><td>20.22</td><td>-4.76</td><td>1.3</td><td>-2.89</td></tr>
<tr><td rowspan="2">MSI</td><td rowspan="2">443
490
560
665</td><td>Tuned Cao18</td><td>a</td><td>b</td><td>c</td><td>d</td><td>e</td><td rowspan="2"> 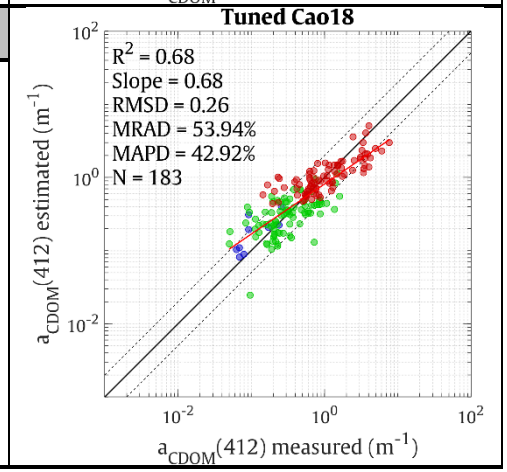
</td></tr>
<tr><td>$\ln(a_{CDOM}(412)) = a\times\ln(R_{rs}(443)) + b\times\ln(R_{rs}(490)) + c\times\ln(R_{rs}(560)) + d\times\ln(R_{rs}(665)) + e$</td><td>0.77</td><td>-2.08</td><td>-0.92</td><td>1.52</td><td>-2.7</td></tr>
</table>

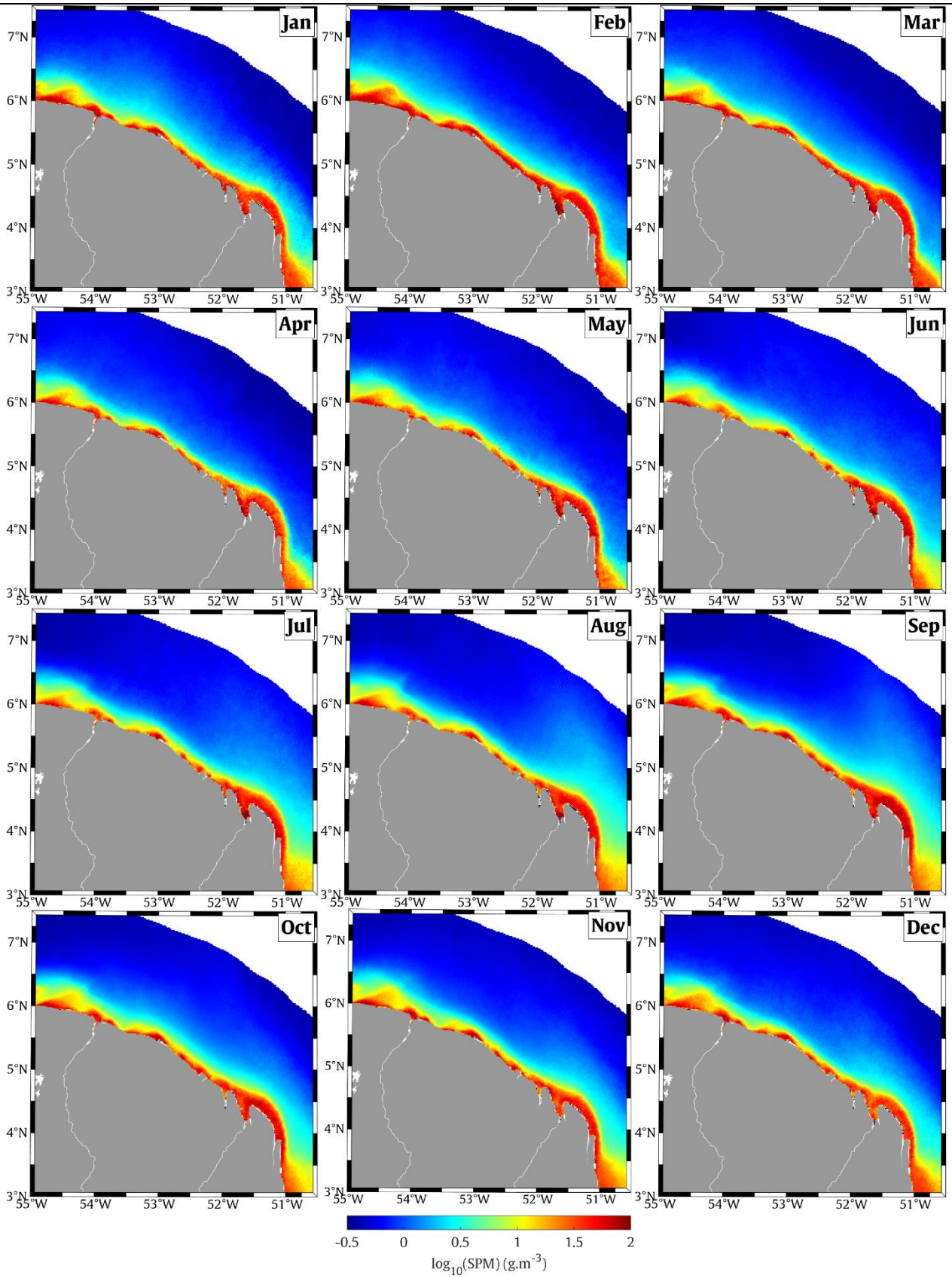

Figure A.1. *Monthly SPM climatology based on the entire MERIS archive.*

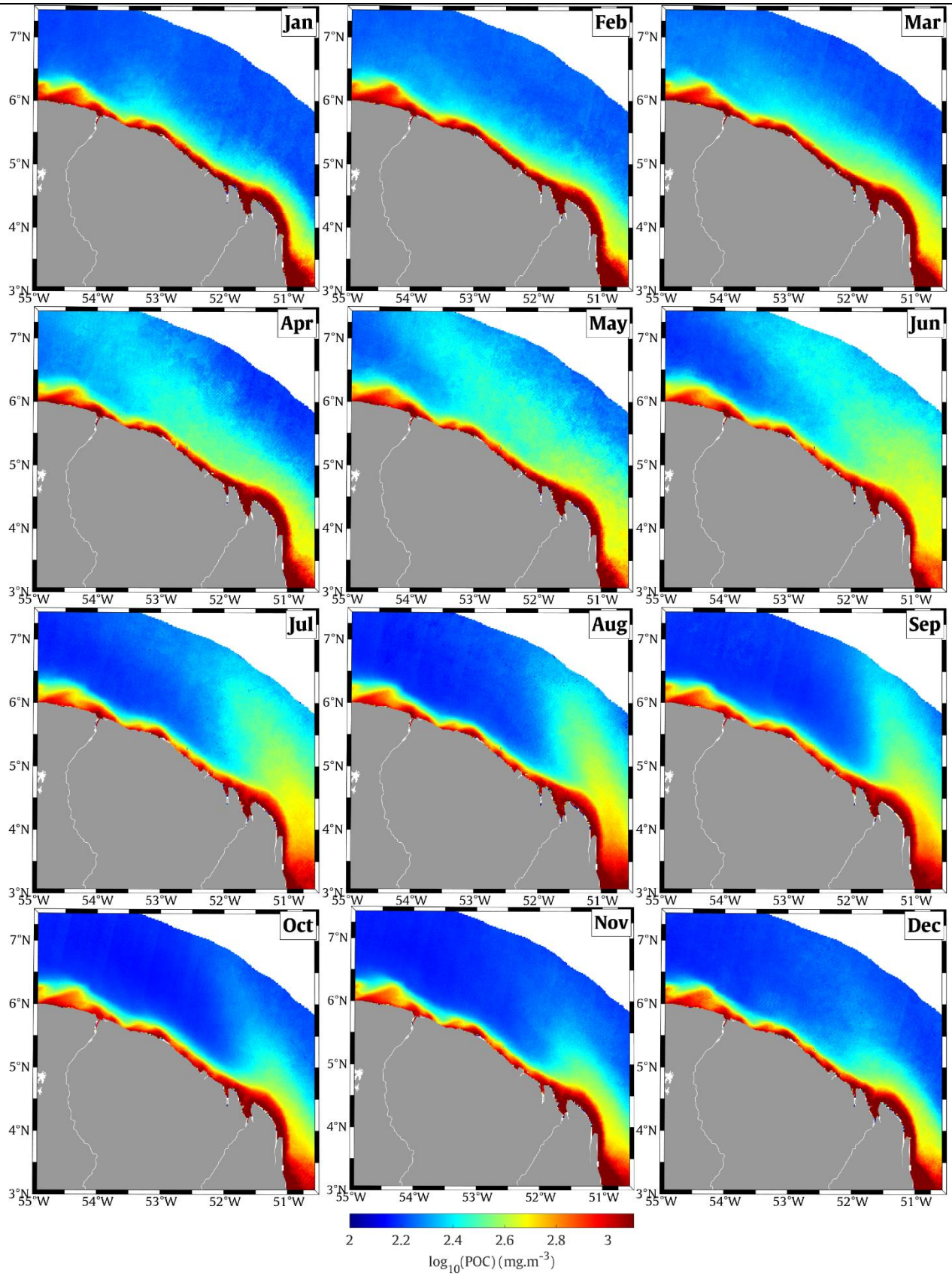

Figure A.2. *Monthly POC climatology based on the entire MERIS archive.*

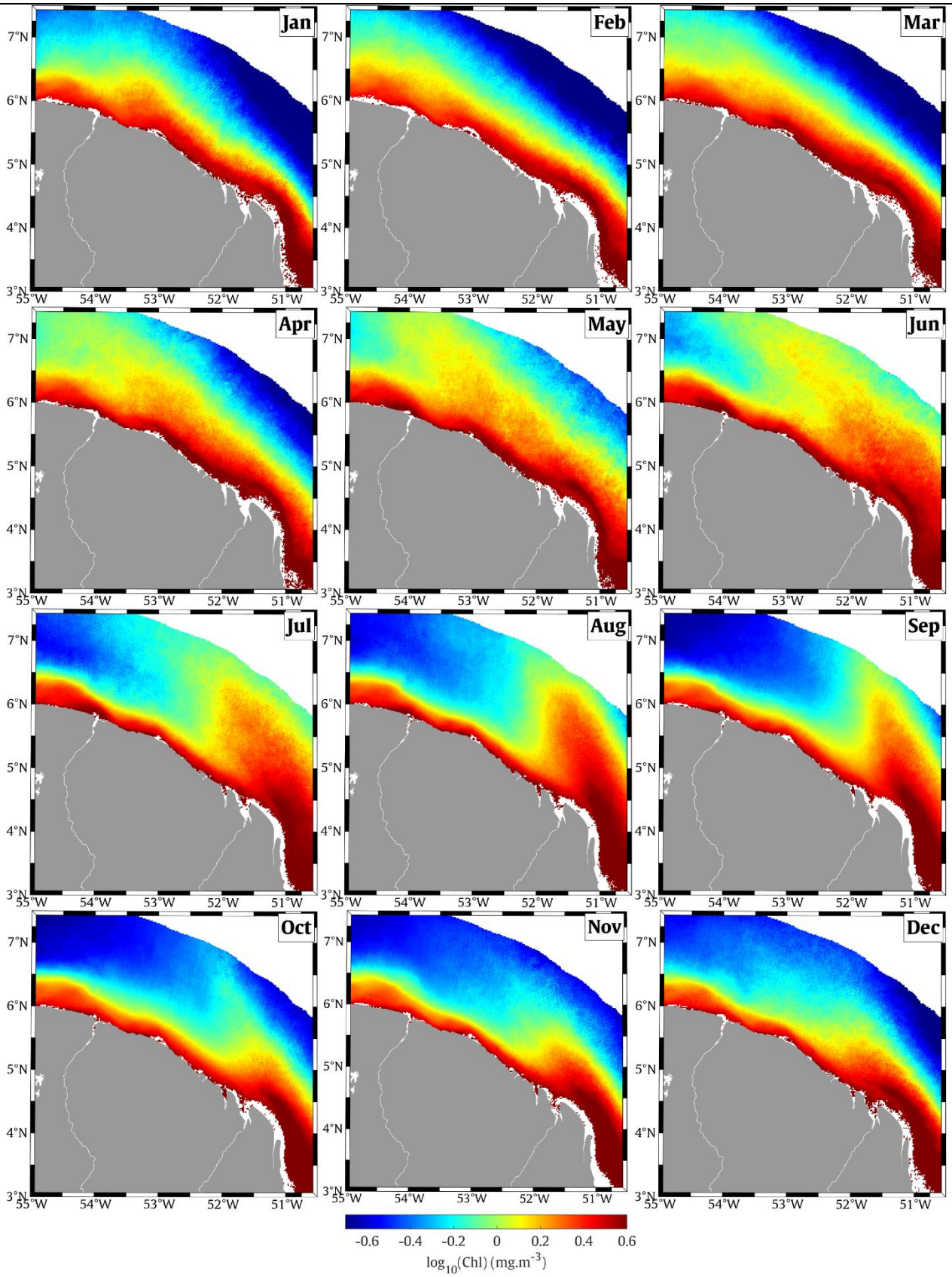

Figure A.3. *Monthly Chl-a climatology based on the entire MERIS archive.*

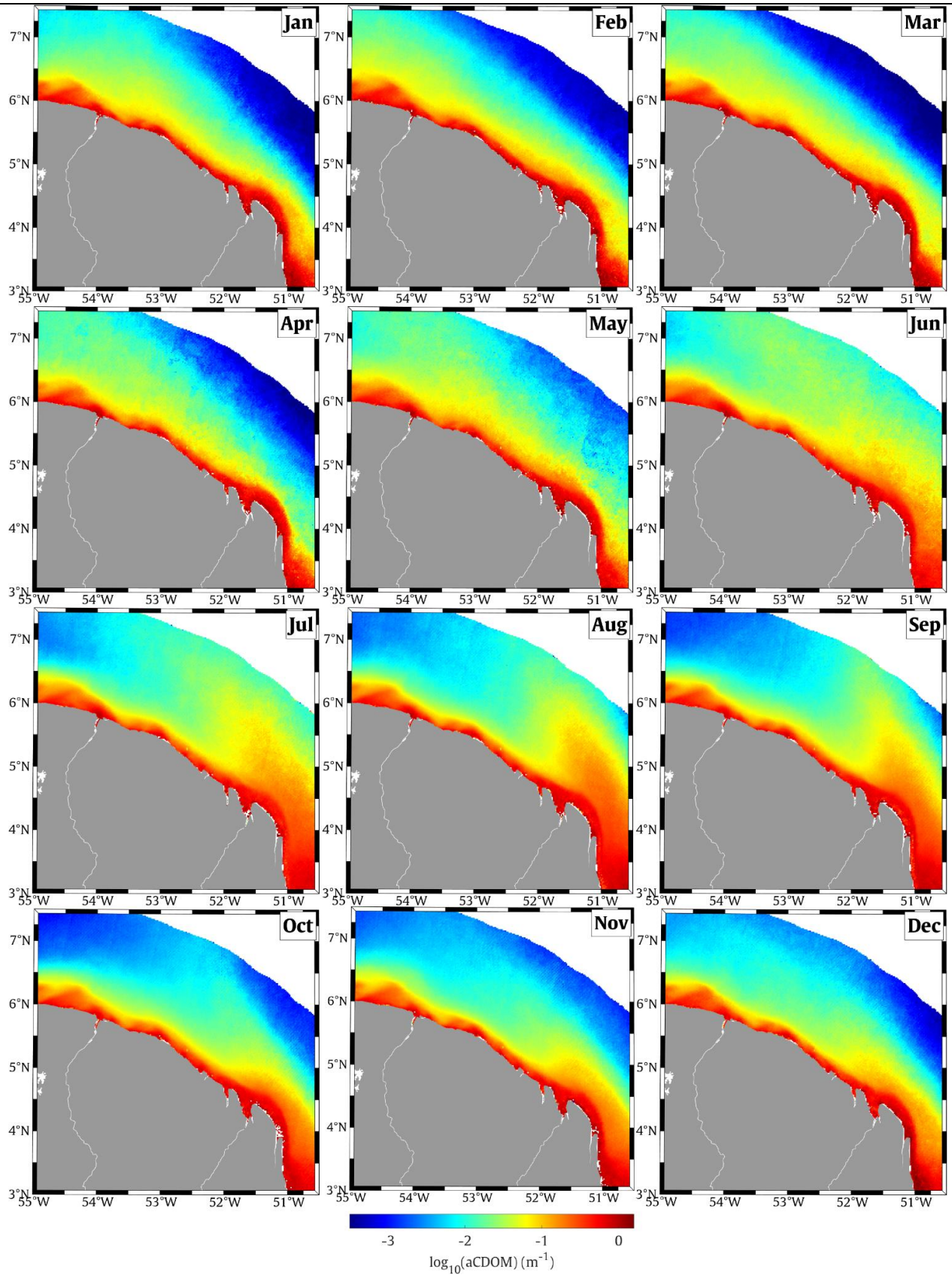

Figure A.4. Monthly $a_{CDOM}(412)$ climatology based on the entire MERIS archive.

Abstract (short version)

French Guiana marine waters hold unique marine environments and habitats representing areas of high ecological, societal, and economical importance. These interface regions (land/Amazon-ocean) are vulnerable to changes in environmental conditions of natural or anthropogenic origins acting on both land and ocean geosystems. Monitoring these coastal waters appears therefore as a priority for supporting the development of sustainable, ecosystem-based environmental policies. Up to now, the lack of in-situ observation in the area represents a limitation to assess the variability of these marine ecosystems. In that context, satellite observation can represent a valuable and cost-effective tool to synoptically depict the biogeochemical spatio-temporal variability of these ecosystems at sufficient spatial and temporal resolutions to also describe local and episodic features. However, ocean color remote sensing application in optically complex waters such as the ones of French Guiana requires the use of 1) adapted inversion methods to deliver valuable information on key biogeochemical descriptors and 2) adapted statistical approaches for extracting insights into the spatiotemporal dynamics of the water masses.

This PhD has been built in this context and divided into 5 Chapters with the principal aims of 1) developing a set of ocean color products (Chlorophyll-a, Chl-a, Suspended Particulate Matter, SPM, Colored Dissolved Organic Matter, CDOM, Particulate And Dissolved Organic Carbon, POC and DOC, respectively) to monitor water quality in French Guiana, 2) describing the biogeochemical dynamics at the regional scale to assess the main factors driving this variability as well as the key biogeochemical descriptors to monitor at the regional scale, and 3) proposing a partition of the water masses in order to support the development of regional monitoring policies.

Chapter 1 provides background information introducing the rationale of this work. Chapter 2 introduces the datasets and statistical approaches used in the frame of this PhD. Chapter 3 presents the methodological developments performed to improve a set of inversion algorithms at the regional scale for diverse high (e.g., Sentinel-2 with 10 m) and medium (e.g., MERIS and Sentinel-3 with 1 km and 300 m, respectively) spatial resolution sensors. The most adapted inversion models for delivering information on phytoplankton, particulate, and dissolved matter were defined from regional optimization/validation exercises. Our results further emphasized the challenges in estimating Chl-a over optically complex waters and a general framework based on optical classification was established to combine different Chl-a models for global applications. Chapter 4 describes the spatio-temporal variability of the considered biogeochemical parameters using time series analysis performed on the generated ocean color archives. Regions under the influence of the Amazon River’s plume have been

well identified from multispectral satellite data (i.e., mudbank migration, North Brazil Current (NBC) retroflection). Our results show no evidence of significant long-term changes has been detected except the fingerprint of mudbank migration along the coast. It is also suggested that POC/SPM ratio might be an appropriate descriptor to monitor French Guiana's coastal water quality. Chapter 5 focuses on the partition of the French Guiana water masses considering different approaches (i.e., optical and temporal classification). In particular, an optical classification scheme can provide a comprehensive and dynamic view of the water masses characteristics in the French Guiana coastal domain. An illustration of the potential offered by temporal variation-based classifications for delimiting French Guiana waters is further illustrated. Such partition of the French Guiana waters can represent a valuable frame to assess reference status, develop in-situ monitoring programs and evaluate potential impact of changes in the environmental conditions on these ecosystems.

Keywords: Ocean Color, biogeochemical dynamics, coastal water quality, Chlorophyll-a, optical classification.

Résumé (version courte)

Les eaux marines de la Guyane française abritent des environnements et des habitats marins uniques représentant des zones de grande importance écologique, sociétale et économique. Ces régions d'interface (terre/Amazone/océan) sont vulnérables aux changements des conditions environnementales d'origine naturelle ou anthropique. La surveillance de ces eaux côtières apparaît donc comme une priorité pour soutenir le développement de politiques environnementales durables. Le manque d'observations in situ dans la zone représente cependant une limitation forte. Dans ce contexte, l'observation spatiale couleur de l'eau représente un outil précieux pour décrire de manière synoptique la variabilité biogéochimique de ces écosystèmes à des résolutions spatiales et temporelles suffisantes pour décrire également des variations locales ou épisodiques. Cependant, l'application de cet outil dans des eaux optiquement complexes telles que celles de la Guyane Française nécessite l'utilisation 1) de méthodes d'inversion adaptées pour fournir des informations précieuses sur les descripteurs biogéochimiques clés et 2) d'approches statistiques adaptées pour extraire des informations sur la dynamique spatio-temporelle des masses d'eau.

Cette thèse a été construite dans ce contexte a pour objectifs principaux de 1) développer un ensemble de produits de couleur de l'océan (Chlorophylle a, Chl-a, particules en suspension, SPM, Matière Organique Dissoute Colorée, CDOM, carbone organique particulaire et dissous, POC et DOC, respectivement) pour surveiller la qualité de l'eau en Guyane française, 2) décrire la dynamique biogéochimique à l'échelle régionale afin d'évaluer l'impact des principaux forçages environnementaux et de définir les descripteurs biogéochimiques clés à surveiller à l'échelle régionale, et 3) proposer une partition des masses d'eau afin de soutenir le développement de politiques de suivi.

Le Chapitre 1 fournit des informations sur l'état de l'art alors que le Chapitre 2 présente les données et les approches statistiques utilisées dans ce doctorat. Le Chapitre 3 présente les développements méthodologiques réalisés pour améliorer un ensemble d'algorithmes d'inversion à l'échelle régionale pour diverses capteurs à haute (Sentinel-2) et moyenne résolution spatiale (MERIS, Sentinel-3). Les modèles d'inversion les plus adaptés pour fournir des informations sur le phytoplancton, les matières particulaires et dissoutes ont été définis à partir d'exercices d'optimisation/validation régionaux. Un cadre général basé sur la classification optique pour combiner différents modèles afin d'estimer ce paramètre dans les eaux côtières est également proposé à l'échelle globale. Le Chapitre 4 décrit la variabilité spatio-temporelle des paramètres biogéochimiques considérés via des analyses des séries temporelles réalisées sur les archives de la couleur de l'océan générées permettant notamment de caractériser l'impact de l'Amazone sur les eaux Guyanaises. Nos

résultats ne montrent aucun changement significatif à long terme, à l'exception de ceux liés à la migration des bancs de vase le long de la côte. Il est également suggéré que le rapport POC/SPM pourrait être un descripteur approprié pour surveiller la qualité des eaux côtières de Guyane française. Le Chapitre 5 se concentre sur la partition des masses d'eau de Guyane en considérant différentes approches (i.e., classification optique et temporelle). En particulier, une classification optique de ces masses d'eau est proposée afin de fournir une vue globale et dynamique de la distribution des masses d'eau marines de la Guyane française. Une illustration du potentiel offert par les classifications basées sur les variations temporelles est également présentée. De telles partitions des eaux de Guyane peuvent représenter un cadre pertinent pour évaluer l'état de référence, développer des programmes de surveillance in situ de ces écosystèmes et évaluer l'impact potentiel des changements environnementaux.

Mots-clés: Couleur de l'océan, dynamique biogéochimique, qualité des eaux côtières, chlorophylle-a, classification optique.

remote sensing

MDPI

Article

Band Ratios Combination for Estimating Chlorophyll-a from Sentinel-2 and Sentinel-3 in Coastal Waters

Manh Duy Tran [1,*], Vincent Vantrepotte [1], Hubert Loisel [1], Eduardo N. Oliveira [2], Kien Trung Tran [1], Daniel Jorge [1], Xavier Mériaux [1] and Rodolfo Paranhos [3]

[1] Univ. Littoral Côte d'Opale, CNRS, Univ. Lille, IRD, UMR 8187-LOG-Laboratoire d'Océanologie et de Géosciences, F-62930 Wimereux, France
[2] Faculdade de Oceanografia, Rio de Janeiro State University, Rua São Francisco Xavier, 524, Maracanã, CEP 20550-013, RJ, Brazil
[3] Institute of Biology, Rio de Janeiro Federal University, Avenue Prof. Rodolpho Rocco 211, sl. A1-071, CEP 20551-030, RJ, Brazil
* Correspondence: manh.tran-duy@univ-littoral.fr

Abstract: Chlorophyll-a concentration (Chl-a) is a crucial parameter for monitoring the water quality in coastal waters. The principal aim of this study is to evaluate the performance of existing Chl-a band ratio inversion models for estimating Chl-a from Sentinel2-MSI and Sentinel3-OLCI observation. This was performed using an extensive in situ R_{rs}-Chl-a dataset covering contrasted coastal waters (N = 1244, Chl-a (0.03–555.99) μg/L), which has been clustered into five optical water types (OWTs). Our results show that the blue/green inversion models are suitable to derive Chl-a over clear to medium turbid waters (OWTs 1, 2, and 3) while red/NIR models are adapted to retrieve Chl-a in turbid/high-Chl-a environments. As they exhibited the optimal performance considering these two groups of OWTs, MuBR (multiple band ratio) and NDCI (Normalized Difference Chlorophyll-a Index)-based models were merged using the probability values of the defined OWTs as the blending coefficients. Such a combination provides a reliable Chl-a prediction over the vast majority of the global coastal turbid waters (94%), as evidenced by a good performance on the validation dataset (e.g., MAPD = 21.64%). However, our study further illustrated that none of the evaluated algorithms yield satisfying Chl-a estimates in ultra-turbid waters, which are mainly associated with turbid river plumes (OWT 5). This finding highlights the limitation of multispectral ocean color observation in such optically extreme environments and also implies the interest to better explore hyperspectral Rrs information to predict Chl-a.

Keywords: chlorophyll-a; coastal waters; ocean color remote sensing; optical water types

Citation: Tran, M.D.; Vantrepotte, V.; Loisel, H.; Oliveira, E.N.; Tran, K.T.; Jorge, D.; Mériaux, X.; Paranhos, R. Band Ratios Combination for Estimating Chlorophyll-a from Sentinel-2 and Sentinel-3 in Coastal Waters. *Remote Sens.* **2023**, *15*, 1653. https://doi.org/10.3390/rs15061653

Academic Editor: Xiaofeng Yang

Received: 15 February 2023
Revised: 16 March 2023
Accepted: 17 March 2023
Published: 18 March 2023

1. Introduction

Phytoplankton biomass, estimated through the Chlorophyll-a (Chl-a) concentration, represents a key parameter for monitoring the response of the coastal domain to environmental changes of natural or anthropogenic origins. The evaluation of human impacts on coastal ecosystems' structure and functioning leading for instance to eutrophication processes (e.g., [1]) represents a crucial scientific and societal objective, which strongly relies on the availability of long-lasting consistent Chl-a times series. Satellite ocean observation represents in this context a relevant tool since it provides a continuous synoptic view of the coastal waters over more than two decades. At the same time, the spatial and temporal resolutions of ocean color observations are fine enough for allowing local studies or capturing episodic events advantageously complementing classical in situ monitoring. Recent ocean color sensors onboard satellites from the ESA Sentinel constellation (i.e., Sentinel2-MSI and Sentinel3-OLCI) have further increased the availability of ocean satellite data. These satellite archives are now considered an essential observation tool for

supporting the development of sustainable environmental policies (EU Water Framework Directive and Marine Strategy Framework Directive, [2,3]).

While Chl-a concentration represents the pioneer product of ocean color observation, efforts are still required for improving the accuracy of Chl-a estimation in optically complex waters [4,5]. Chl-a inversion algorithms have indeed been first dedicated to the oceanic (Case-1) waters where the variability of optical properties is mainly driven by phytoplankton [6]. The ocean color (OC) chlorophyll-a models and related offspring algorithms [7,8] are typically based on the use of a maximum band ratio in the blue–green domain of the visible spectrum. Such algorithms have been widely validated over clear environments and are now operationally used for deriving Chl-a in open ocean waters (e.g., [9–11]). Estimating Chl-a from space still, however, represents a challenging task in coastal waters (Case-2 waters, [5,12]). This is related to the high optical diversity of these environments [13] where water optical properties are diversely driven by a variable contribution of phytoplankton, suspended particulate matter (SPM), and colored dissolved organic matter (CDOM). In high-CDOM and/or -SPM phytoplankton conditions, the co-occurrence of different water constituents presents impacts on the reflectance signal, especially at the shortest wavelengths of the visible range. This feature tends to impair the performance of classical blue/green ratio-based inversion models [14–16].

For this reason and considering the crucial need to monitor Chl-a over turbid coastal environments, specific Chl-a algorithms have been developed taking advantage of the impacts of phytoplankton on the water optical properties in the red and near-infrared (NIR) regions. These models rely on the negligible impacts of CDOM and SPM absorption as well as the optical signature of phytoplankton absorption or chlorophyll fluorescence over the red–NIR domain of the electromagnetic spectrum (e.g., [17–20]). Such red–NIR approaches are, however, failing in clear waters, where the phytoplankton signal can be masked in relationships to the high contribution of pure water absorption at higher wavelengths [21,22].

Regional inversion models have been considered to be a convenient way for optimizing ocean color products over a defined coastal area. Such approaches present, however, numerous limitations being dependent on the representativeness of the dataset used and are intrinsically limited in terms of spatial applicability [23]. Alternative approaches based on the applications of a defined model on a pixel-per-pixel basis according to the water optical characteristics have been shown to represent a valuable alternative for combining different algorithms for estimating ocean color satellite products in coastal waters [23–25]. An extensive study by Neil et al. [26] has further illustrated the interest in an adaptive framework for dynamically selecting and optimizing Chl-a inversion models in inland waters based on optical water types (OWTs). With the main objective to provide ocean color data users a simple way to evaluate the reliability of the Chl-a estimates derived from blue/green and red/NIR inversion models, Lavigne et al. [12] developed quality control tests for improving MERIS and OLCI Chl-a estimates in coastal waters. In addition to these recent studies, new alternative approaches that rely on machine learning, which may be more computing-time-consuming than standard reflectance ratios, are now developed for deriving Chl-a over a large range of Chl-a contents and considering a variety of bio-optical regimes in inland and coastal waters [27]. Although there were numerous efforts performed during the last decades for accurately estimating Chl-a concentration from the remote sensing reflectance using adapted inversion, there is still no consensus on the algorithm or the set of algorithms to be applied for deriving Chl-a for large-scale applications in coastal waters.

This study contributes to ongoing efforts to optimize the retrieval of Chl-a from ocean color observations in coastal waters, with a specific focus on Sentinel-2/MSI and Sentinel-3/OLCI observations. A comprehensive global in situ remote sensing reflectance (R_{rs})–Chl-a dataset (N = 1244) of samples collected in contrasted environments has been gathered. This dataset was classified into five OWTs ranging from clear to ultra-turbid waters. Using OWTs as a general framework, this work first aims at illustrating the limitations of

historical band-ratio-based algorithms for deriving Chl-a and selecting the most appropriate inversion models by evaluating novel formulations and state-of-the-art algorithms adapted for different OWTs considered. This study further presents the interest and requirements (e.g., compatibility of inversion algorithms to provide accurate Chl-a estimates, discontinuities in the map when merging Chl-a models) of band-ratio-based blending approaches to provide reliable Chl-a across diverse coastal environments. The applicability of band-ratio-based approaches at a global scale, as well as possible future improvements in Chl-a retrieval, especially in ultra-turbid environments, by exploiting the potential of upcoming hyperspectral observations, is specifically discussed.

2. Materials and Methods

An overview of the study process, including the performed development and processing, can be seen in the flow chart (Figure 1).

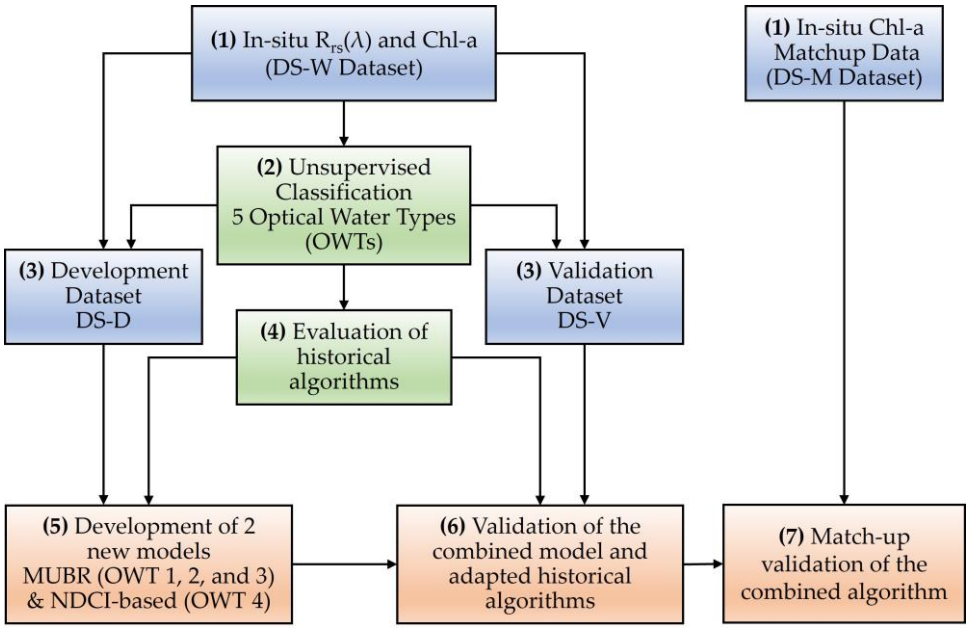

Figure 1. Flow chart of the present study illustrating the general methodology for development and validation of the combined Chl-a model.

2.1. In Situ Dataset

The in situ dataset (DS-W, N = 1244, mean Chl-a = 12.14 μg/L) combines concomitant measurements of Chl-a and remote sensing reflectance (R_{rs}) collected between 1997 and 2016 in the frame of diverse worldwide distributed field campaigns in contrasted coastal areas (European coastal waters [28–31], French Guiana [23,32], Eastern Viet Nam Sea [15,33], South Shetland Islands, the US coastal waters, The Sea of Japan [34], Beaufort Sea North Canada [35], and Brazil (Guanabara Bay, Rio de Janeiro) [36]) (Figure 2). This dataset covers a wide range of Chl-a concentrations with values ranging over 4 orders of magnitude (0.03–555.99 μg/L, Table 1) from oligotrophic waters (e.g., Mediterranean Sea, clear polar waters) to ultra-eutrophic environments (Guanabara Bay, Rio de Janeiro; [36]). The DS-W was further randomly split into a development dataset (DS-D, N = 831, mean Chl-a = 13.63 μg/L) and a validation dataset (DS-V, N = 356, mean Chl-a = 9.45 μg/L), representing 70 and 30% of the DS-W, respectively; these three datasets follow a similar distribution (Figure 3). It is worth noting that the proportion of DS-D/DS-V partition was performed excluding the points corresponding to OWT5 (N = 57), for which no band-ratio-based model development has been performed (see Sections 3.2.1 and 3.3.1).

The Chl-a/SPM ratio has been calculated for the whole dataset for providing rough information on the relative importance of the Chl-a signal associated with the different

water masses considered in this study. Considering that the SPM concentration was not available for all the in situ samples in the DS-W, SPM was estimated from the $R_{rs}(665)$ using the model by Han et al. [37], which has had a reliable performance illustrated from various former studies in contrasted coastal waters (e.g., [38,39]).

Table 1. Description of the in situ dataset of Chl-a (µg/L) considered in the frame of this study: number of samples (N), minimum (Min), maximum (Max), mean (Mean), and standard deviation (StdDev).

Region	Temporal Coverage	N	Min	Max	Mean	StdDev	Reference
Vietnam	2011–2014	43	0.66	17.45	4.63	3.75	[15,33]
French Guiana	2006–2016	108	0.41	22.65	6.40	5.45	[23,32]
Guanabara Bay (Brazil)	2012–2015	161	1.03	555.99	76.06	101.46	[36]
Beaufort Sea	2014	40	0.03	3.52	0.32	0.64	[35]
Sea of Japan	1999–2001	41	0.13	2.89	0.73	0.64	[34]
USA	1999–2007	498	0.08	28.46	1.71	2.79	[34]
South Shetland Islands	2000–2007	82	0.03	4.01	0.86	0.81	[34]
Europe	1997–2012	271	0.05	33.33	3.69	5.42	[28–31]
Total	1997–2016	1244	0.03	555.99	12.14	44.13	

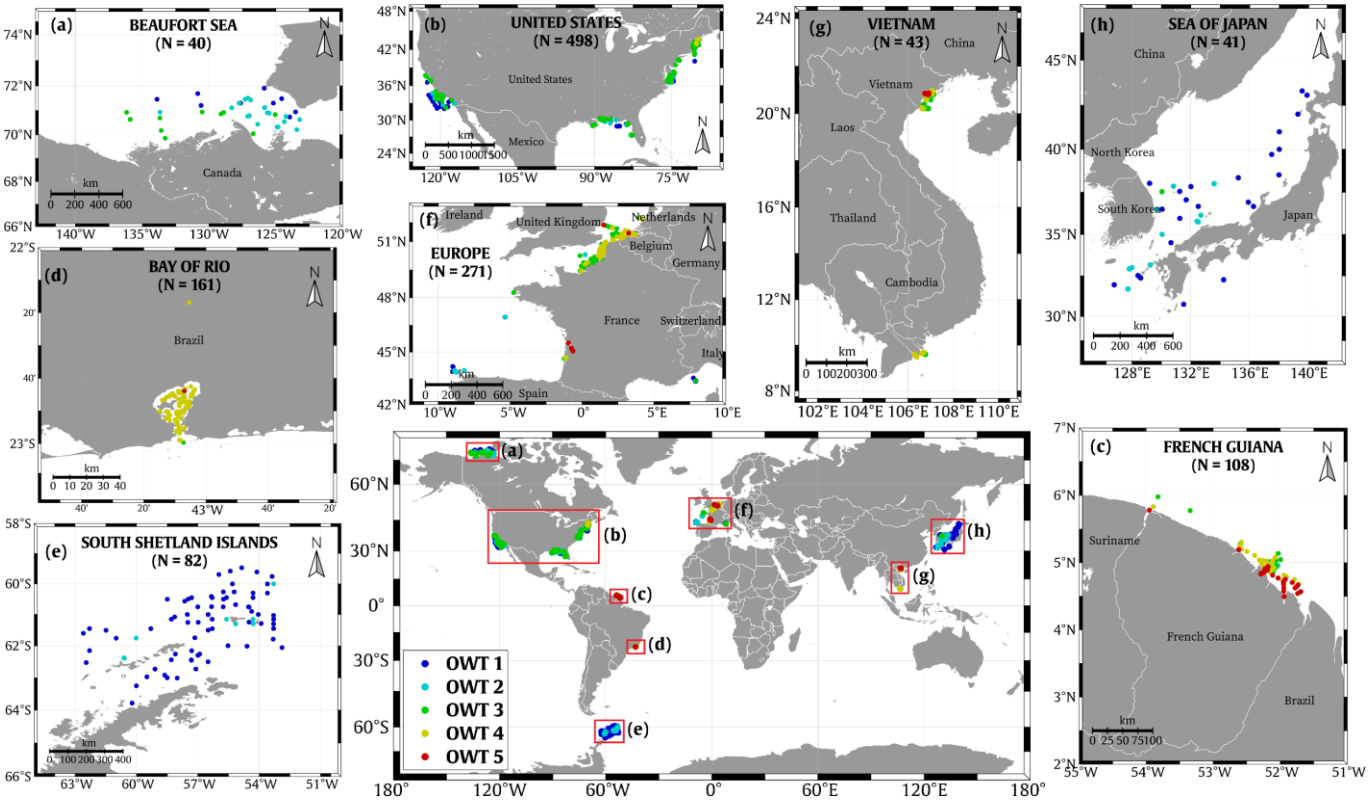

Figure 2. Spatial distribution of in situ R_{rs}-Chl-a measurements gathered within the DS–W dataset (N = 1244) collected in (**a**) the Beaufort Sea, (**b**) the United States coastal waters, (**c**) the French Guiana coastal waters, (**d**) Guanabara Bay, (**e**) the South Shetland Islands, (**f**) European coastal waters, (**g**) Vietnamese coastal waters, and (**h**) the Sea of Japan: colors indicate the optical water types each in situ sample is associated with (see Section 2.3).

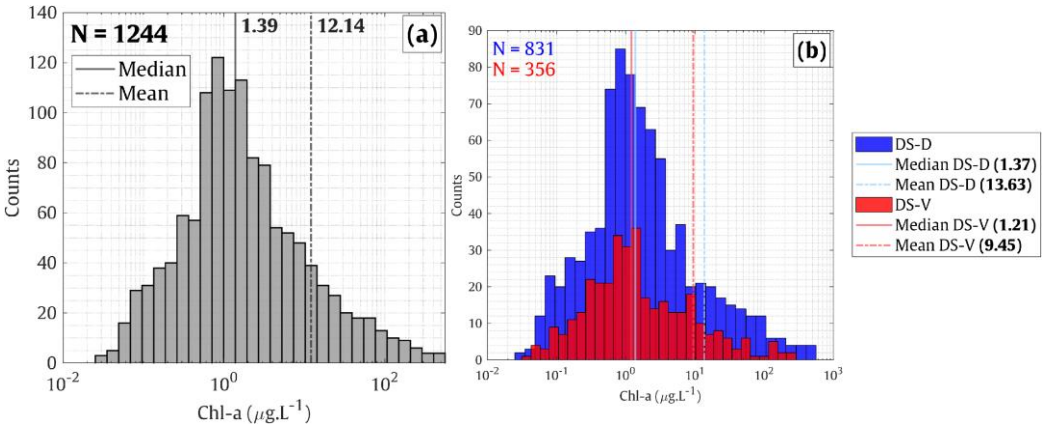

Figure 3. Chl-a absolute frequency distribution for (**a**) the whole in situ dataset DS−W (N = 1244), (**b**) the development dataset (DS−D, N = 831), and the validation dataset (DS−V, N = 356). The number of data points corresponding to OWT 5 is not considered in the DS−D and DS−V.

2.2. Satellite and Matchup Dataset

Data in the DS-W have been acquired before the S2 and S3 time period (from June 2015 and February 2016, respectively). An external and independent in situ dataset, which encompasses only Chl-a measurements, has been therefore considered in addition to the DS-W for validation purposes (Figure 4). In practice, Chl-a samples collected along the French coast are in the frame of the SOMLIT (Coastal Environment Observation Service, https://www.somlit.fr/, accessed on 15 June 2021) and REPHY (Observation and Monitoring Network for Phytoplankton and Hydrology in coastal waters, https://www.seanoe.org/data/00361/47248/, accessed on 15 June 2021) French national survey programs. These long-lasting in situ datasets (e.g., continuous monthly data since 1997 for SOMLIT) present the advantage of being acquired following a standardized protocol.

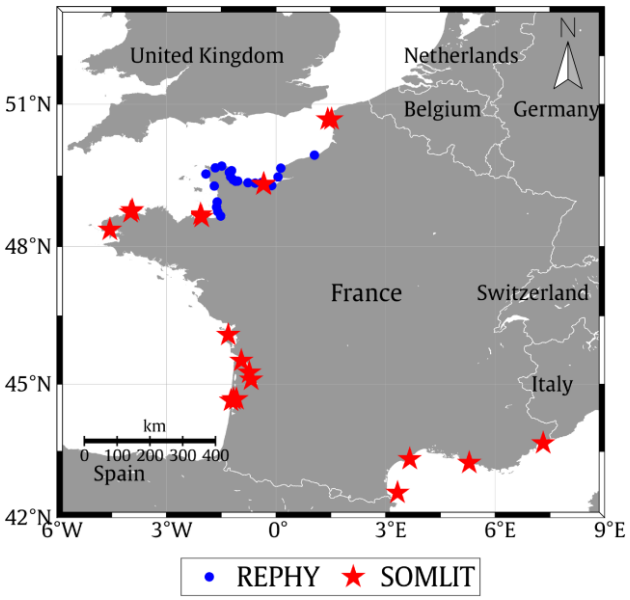

Figure 4. Distribution of the REPHY and SOMLIT stations considered in the matchup dataset DS−M.

In practice, Satellite Sentinel2-MSI A/B (60 m resolution) and Sentinel3-OLCI A/B (300 m resolution) R_{rs} data have been extracted for both SOMLIT and REPHY Chl-a samples over the time periods from 7 September 2015 to 19 March 2021 and from 24 May 2016 to 7 April 2021 for MSI and OLCI, respectively). Specifically, top-of-atmosphere Level 1 products have been processed considering three atmospheric correction schemes

including POLYMER (version 4.13, [40]), C2RCC [41], and ACOLITE [42]. The matchup extraction was performed considering a 3 × 3 window around each in situ sampling point. Several quality control criteria were then applied [43] considering the following: (1) the number of valid pixels (at least 5 valid pixels among the 9 pixels extracted), (2) the spatial homogeneity of the matchup subsets assessed from the variation coefficient within the subset window (CV = standard deviation/mean. 100 < 30%), and (3) the time difference between in situ and satellite measurements (lower than 3 h).

After the application of all these criteria, the final matchup dataset (DS-M) is then composed of a maximal number of 194 matchup points for MSI and 362 for OLCI with Chl-a concentrations ranging between 0.19 and 34.12 µg/L (mean = 2.48 µg/L, standard deviation = 3.79 µg/L) and 0.05 and 52.93 µg/L (mean = 2.52 µg/L, standard deviation = 3.7 µg/L), respectively. The Chl-a statistic of the DS-M is further illustrated in Figure 5.

In addition to the Sentinel2 and Sentinel3 matchup dataset, the global MERIS GlobColour dataset (monthly 1 km spatial resolution, [15,33]) was further considered for illustrating and discussing the potential applicability of the models selected with the frame of this study with a global-scale perspective.

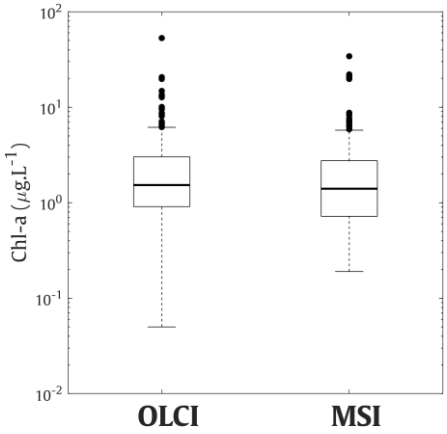

Figure 5. Box plot showing Chl-a range of the final matchup dataset (DS–M) regarding OLCI and MSI sensors.

2.3. Optical Classification

2.3.1. Optical Water Types Definition

Optical water types (OWTs) were defined using the procedure defined in [23] applied to the DS-W R_{rs} dataset. In practice, normalized R_{rs} data were considered to cluster the reflectance data focusing on the shape of the spectra. The normalization was applied to multispectral R_{rs} data considering 6 wavelengths in the visible part of the spectrum (412, 443, 490, 510, 560, and 665 nm) centered on the OLCI bands. The normalized R_{rs} was determined by the ratio between its original value and the surface below the spectral shape as follows:

$$R_{rs}^{norm} = \frac{R_{rs}(\lambda)}{\int_{\lambda_1}^{\lambda_2} R_{rs}(\lambda) d\lambda} \quad (1)$$

where R_{rs}^{norm} represents the normalized remote sensing reflectance.

An unsupervised classification was then applied to the R_{rs}^{norm} dataset using Ward's clustering method [44], which presents the advantage of being less sensitive to outliers compared to other approaches [23].

This classification led to the definition of 5 optical water types showing different R_{rs} spectral shapes (Figure 6a). OWTs 1 and 2 (N = 269 and 185, respectively) are associated with clear oligotrophic to mesotrophic waters (mean Chl-a = 0.38 ± 0.36 and 0.96 ± 0.74 µg/L, respectively) with R_{rs} spectra typically peaking in the blue part of the visible

spectrum. OWT 3 samples correspond to mesotrophic waters characterized by high R_{rs} in the green part of the visible spectrum with an R_{rs} plateau ranging between 490 and 560 nm (N = 426, mean Chl-a = 2.33 ± 3.09 µg/L). The Chl-a/SPM ratio for these 3 OWTs increases from OWT 1 (2.25×10^{-3}) to OWT 3 (4.04×10^{-3}).

OWTs 4 and 5 are associated with highly turbid/eutrophic coastal waters. OWT 4 corresponds to high-Chl-a waters with an R_{rs} peak at 560 nm (N = 307, mean Chl-a = 43.72 ± 80.89 µg/L) and shows the maximal Chl-a/SPM ratio among the different OWTs (Chl-a/SPM = 13×10^{-3}) related to ultra-eutrophic for these samples. Conversely, OWT 5 samples (N = 57) are more likely associated with turbid waters showing a higher proportion of non-algal particles (sediments and detritus) when compared to OWT 4 as emphasized from the lower average Chl-a (7.15 ± 10.46 µg/L) and the lowest Chl-a/SPM ratio (1.43×10^{-3}) found for these samples (Figure 6c).

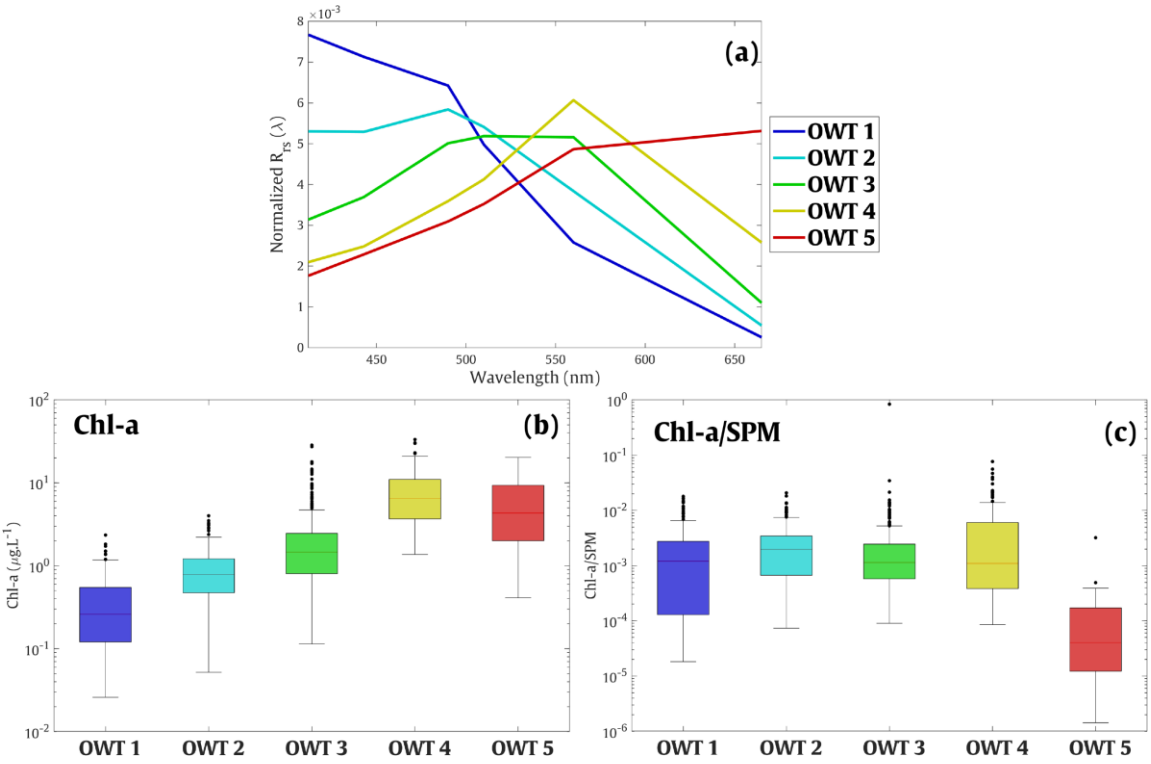

Figure 6. (**a**) Average R_{rs}^{norm} spectra corresponding to the optical water types defined from the DS−W dataset (N = 1244); box plots illustrating the distribution of Chl-a (**b**) and Chl-a/SPM ratio (**c**) associated with each optical class. While all the samples considered in DS−W are available for all the visible wavelengths corresponding to Sentinel2−MSI and Sentinel3−OLCI bands, it is worth noticing that the spectral coverage of the R_{rs} in situ dataset in the NIR part of the spectrum is unequal. For most of the samples associated with OWTs 1, 2, and 3, little information was available in the NIR (12.8% for OWTs 1, 2, and 3, respectively) while this information was present for most (98%) of the samples associated with OWTs 4 and 5, for which red and NIR algorithms are devoted (see Section 2.4).

2.3.2. Satellite Pixel Optical OWT Labeling, OWT Membership Calculation

The five OWTs defined in the previous section were used for labeling the satellite R_{rs} spectra. This labeling consists of computing the OWT membership of an input R_{rs} spectrum (e.g., satellite R_{rs}) to each of the OWTs defined from the in situ dataset, which are characterized by specific mean (µ) and covariance (Σ) matrices [23,25]. The Mahalanobis distance Δ^2 applied to the log-transformed R_{rs}^{norm} is then used to estimate the distance between input spectrum x and a given OWT i_c as follows:

$$\Delta^2_{ic}(x) = (x - \mu_{ic})^T \Sigma^{-1}_{ic} (x - \mu_{ic}) \quad (2)$$

where T indicates the matrix transpose.

The OWT membership of satellite pixels to each of the defined OWTs was then estimated as in [23]. The probability density function (PDF), corresponding to each targeted pixel associated with $x = \log(R_{rs})$, is calculated based on its Mahalanobis distance (Δ_M^2) to the distribution of OWT i_c and can be expressed as below:

$$P_{ic}(x) = \frac{1}{(2\pi)^{d/2}|\Sigma|^{1/2}} \exp\left[-\frac{1}{2}\Delta_{ic}^2(x)\right] \quad (3)$$

The computed probability values are then normalized (p*) so that the sum of OWT memberships equals 1 by taking the ratio between P for ic OWT and the total P for all OWTs considering such as follows [13]:

$$p_{ic}^* = \frac{P_{ic}}{\sum_{ic=1}^{Nc} P_{ic}} \quad (4)$$

2.4. Chl-a Candidate Inversion Algorithms

A variety of empirical band-ratio-based bio-optical algorithms have been developed for estimating Chl-a concentration from satellite ocean remote sensing observation. Here, a selection of "standard" models based on different input R_{rs} data and formulations have been performed among the number of different methods available considering models whose performances have already been shown to be relevant to the diverse types of coastal environments taking into account results provided from recent extensive intercomparison exercises (e.g., [26]). In practice, historical models considered here can be split into two categories: blue/green(Red) ratio-based models more likely adapted to clear to moderately turbid waters ([8,45]) and red/NIR ratio-based methods specifically developed for turbid environments [17,18,21,46].

It is important to mention that all the considered models (except the model OC5, [45]) have been considered in their original and tuned versions fitting the different formulations to the DS-D data corresponding to the optical water types they have been designed for (see Sections 3.2 and 3.3). These coefficients are here provided for each original model.

2.4.1. Blue/Green (Red) Band-Ratio-Based Models

Considering the radiometric resolution of Sentinel2-MSI and Sentinel3-OLCI sensors, two models have been selected for clear to medium turbid waters. These models correspond to the empirical NASA OC-family algorithms developed from the NOMAD dataset extensively used to produce standard Chl-a products from satellite observation.

(1) OC6

This recent algorithm OC6 [8] corresponds to an adaptation of the OC4 model [7], which includes additional bands at 412 and 665 nm to extend the applicability of this approach, typically applied to open ocean waters, towards coastal waters. This model can be described as follow:

$$\text{Chl-a} = 10^{\,a_0 + a_1 \times R + a_2 \times R^2 + a_3 \times R^3 + a_4 \times R^4} \quad (5)$$

where

$$R = \log_{10}\left\{\frac{\max\left[R_{rs}(412), R_{rs}(443), R_{rs}(490), R_{rs}(510)\right]}{\text{mean}\left[R_{rs}(560), R_{rs}(665)\right]}\right\} \quad (6)$$

The original coefficients for this model are $a_0 = 0.2424$, $a_1 = -2.2146$, $a_2 = 1.5193$, $a_3 = -0.7702$, and $a_4 = -0.4291$

(2) OC3

The main equation of the OC3 model to compute Chl-a remains the same as in Equation (5). However, this algorithm uses a different blue/green ratio input that is established

by 3 spectral bands in the visible part of the spectrum [8]. Such a ratio can be expressed as below:

$$R = \log_{10}\left\{\frac{\max[(490), R_{rs}(490)]}{R_{rs}(560)]}\right\} \quad (7)$$

and the coefficients are a_0 = 0.41712, a_1 = −2.56402, a_2 = 1.22219, a_3 = 1.02751, and a_4 = −1.56804.

(3) OC5—Gohin

The five channels model by Gohin et al. [45] was developed in order to correct the overestimation of the Chl-a estimated from the OC4 model in coastal waters presenting moderate turbidity levels and highCDOM loads, based on sensor-specific LUTs empirically developed from an extensive in situ dataset. It has been considered here using the LUTs defined for MERIS.

2.4.2. Red–NIR Algorithms

(1) Gurlin11

The empirical model developed by Gurlin et al. [17] consists of a second-order polynomial function based on the $R_{rs}(709)/R_{rs}(665)$ band ratio:

$$\text{Chl-a} = a\times\left[\frac{R_{rs}(709)}{R_{rs}(665)}\right]^2 + b\times\left[\frac{R_{rs}(709)}{R_{rs}(665)}\right] + c \quad (8)$$

where a = 25.28; b = 14.85; c = −15.18

(2) Gilerson10

The model proposed for MERIS by Gilerson et al. [18] is based on a linear relationship between in situ Chl-a and the NIR/red ratio of MERIS, such as the following:

$$\text{Chl-a} = a\times\left[\frac{R_{rs}(709)}{R_{rs}(665)}\right] + b \quad (9)$$

where a = 35.745; b = −19.295; c = 1.124

(3) Gons08

The Chl-a inversion algorithm developed by Gons et al. [47] for turbid environments is a semi-analytical approach considering IOPs information along with the red–NIR reflectance ratio and the reflectance at 779 nm. The version proposed in [21] is considered here and is expressed as follows:

$$\text{Chl-a} = \frac{\left\{\left[\frac{R_{rs}(709)}{R_{rs}(665)}\right]\times\left[a_w(709)+b_b\text{-}a_w(665)\text{-}b_b^p\right]\right\}}{a^*_{phy}(665)} \quad (10)$$

where $a_w(709)$ and $a_w(665)$, the water absorption coefficients at 709 nm and 665 nm, were estimated as 0.7 m^{-1} and 0.4 m^{-1}, respectively [48]. $a^*_{phy}(665)$ is the chlorophyll-specific absorption that was defined as 0.016 m^2 mg^{-1}. The calculation of the back-scattering coefficient b_b is estimated from the water-leaving reflectance at 779 nm as follows:

$$b_b = \frac{1.61\times R_w(779)}{0.082\text{-}0.6R_w(779)} \quad (11)$$

where R_w (779) is the water-leaving reflectance ($R_w = R_{rs}\times$ pi)

(4) Mishra12

The model proposed by Mishra and Mishra [46] is an empirical model developed for application in estuarine and coastal waters. It is based on the calculation of the Normalized Difference Chlorophyll Index (NDCI) as an input variable to derive Chl-a:

$$NDCI = \frac{R_{rs}(709)-R_{rs}(665)}{R_{rs}(709)+R_{rs}(665)} \quad (12)$$

$$Chl\text{-}a = a + b \times NDCI + c \times NDCI^2 \quad (13)$$

where a = 42.197; b = 236.5; c = 314.97

2.5. Statistical Indicators for Algorithm Performance Assessment

The performance of the considered Chl-a models was evaluated considering a set of statistical descriptors including the following:

$$RMSD = \left\{ \sum_{i=1}^{N} \frac{\left[\log_{10}\left(Chl\text{-}a_i^{mod}\right)-\log_{10}\left(Chl\text{-}a_i^{obs}\right)\right]^2}{N} \right\}^{\frac{1}{2}} \quad (14)$$

$$MAPD = \text{median}\left[\frac{\left|\log_{10}\left(Chl\text{-}a_i^{mod}\right)-\log_{10}\left(Chl\text{-}a_i^{obs}\right)\right|}{\log_{10}\left(Chl\text{-}a_i^{obs}\right)} \right] \times 100\% \quad (15)$$

$$MRAD = \frac{1}{N} \times \sum_{i=1}^{N} \frac{\left|Chl\text{-}a_i^{mod}-Chl\text{-}a_i^{obs}\right|}{Chl\text{-}a_i^{obs}} \times 100\% \quad (16)$$

$$MB = \frac{1}{N} \times \sum_{i=1}^{N} \left|\log_{10}\left(Chl\text{-}a_i^{mod}\right)-\log_{10}\left(Chl\text{-}a_i^{obs}\right)\right| \quad (17)$$

$$\log_{10}\left(Chl\text{-}a^{mod}\right) = m \times \log_{10}\left(Chl\text{-}a^{obs}\right) + c \quad (18)$$

where $Chl\text{-}a^{obs}$ represents the in situ Chl-a observations and $Chl\text{-}a^{mod}$ the Rrs-based Chl-a estimates.

In addition, a linear regression between $Chl\text{-}a^{obs}$ and $Chl\text{-}a^{mod}$ was performed for each considered model leading to the estimation of a slope and coefficient of determination (R^2) as additional statistical descriptors.

Radar charts have been further used to compare the performance of the Chl-a inversion algorithms. This graphical display allows the representation of multiple statistical parameters summarized in the form of a two-dimensional chart [49]. Here, an overview of the normalized MAPD, RMSD, MRAD, MB, slope, and R^2 (Equations (14)–(18)) is provided, and the normalization is computed as follows:

$$RMSD^{norm}(j) = \frac{RMSD(j)}{\max(RMSD(j), j = 1, k)} \quad (19)$$

$$MAPD^{norm}(j) = \frac{MAPD(j)}{\max(MAPD(j), j = 1, k)} \quad (20)$$

$$MRAD^{norm}(j) = \frac{MRAD(j)}{\max(MRAD(j), j = 1, k)} \quad (21)$$

$$MB^{norm}(j) = \frac{MB(j)}{\max(MB(j), j = 1, k)} \quad (22)$$

$$Slope^{norm}(j) = \frac{\left|1\text{-}Slope(j)\right|}{\max(\left|1\text{-}Slope(j)\right|, j = 1, k)} \quad (23)$$

$$R^{2^{norm}}(j) = \frac{\min(R^2(j), j = 1, k)}{R^2(j)} \quad (24)$$

where j represents each individual Chl-a model considered in a defined intercomparison exercise.

In addition to a synthetic visual examination, radar plots were also used to compute a unique statistical indicator outlining the general performance of the considered Chl-a inversion methods. This consists in practice to compute the area associated with the polygons linking the normalized indicators indicated from (19) to (24) as below:

$$\begin{aligned} Area = \frac{1}{2} \times \frac{\pi}{6} \times [&RMSD^{norm}(j) \times MAPD^{norm}(j) + MAPD^{norm}(j) \times MRAD^{norm}(j) + MRAD^{norm}(j) \times \\ &MB^{norm}(j) + MB^{norm}(j) \times Slope^{norm}(j) + Slope^{norm}(j) \times R^{2^{norm}}(j) + R^{2^{norm}}(j) \times RMSD^{norm}(j)] \end{aligned} \quad (25)$$

3. Results

3.1. Performances of Historical Models

The performances of the historical models described in Section 2.4 in their original version were first illustrated considering the whole dataset (DS-W, Figures 7 and 8) gathering a maximum of 1244 values considering the R_{rs} input wavelengths for the OC3, OC5, and OC6 models (i.e., R_{rs} at 412, 443, 490, 510, 560, and 665 nm) and 470 values for the one used in Gurlin11, Gilerson10, Mishra12, and Gons08 (i.e., R_{rs} at 665, 709, and 779 nm).

As already documented, models based on the use of the band ratios in the visible part of the spectrum (OC6, OC3, and OC5, Figure 7a–c) provide reliable Chl-a estimates for clear to medium turbid waters (OWTs 1, 2, and 3) with R^2 values of 0.59, 0.61, and 0.57, respectively (Figure 8). The models, however, show limitations for estimating Chl-a in the most turbid environments (OWTs 4 and 5) as illustrated by the high scattering found in Figure 7 as well as by the low R^2 (<0.28) found for the OWT 4 samples when applying these models (Figure 8). The OC5 model, which has been designed for moderately coastal waters providing a correction of the overestimation generally provided from the OC4 algorithm, also shows clear limitations for the OWT 4 (Figure 7) in agreement with the previous studies [12,15]. Loisel et al. [15], for instance, documented an exponential increase in the uncertainties related to OC5-derived Chl-a with increasing turbidity (i.e., SPM concentration > 60 $mg.L^{-1}$). As expected, the OC3, OC4, and OC5 models (not based on the NIR band) are totally saturated over the whole range of Chl-a for the OWT 5 samples generating quasi-invariant Chl-a estimates.

Red–NIR-based approaches (Gurlin11, Gilerson10, Mishra12, and Gons08; Figure 7d–g) are conversely showing poor performances for OWT 1, 2, and 3 samples with the R^2 remaining below 0.1 (see Figure 8) for these waters whatever the model considered. These models have, however, not been developed for these waters with a relatively low level of turbidity. A general better performance is, however, found for Gilerson10, Gurlin11, Mishra12, and Gons08 models for the OWT 4 samples. This confirms the reliable applicability of the latter methods for estimating Chl-a over highly turbid and high-Chl-a waters [26]. These models, in their original formulations, still, however, show limitations, more likely related to the data range they have been developed. This is emphasized, for instance, by the saturation pattern found for the lower-end Chl-a values for Mishra12 (Figure 7f) already pointed out by previous studies [46]. The model of Gons08 while providing relatively good Chl-a estimates for high Chl-a values (>10 $g.L^{-1}$) tends to fail for low Chl-a for the OWT 4 samples, highly underestimating the Chl-a value (Figure 7g), and further generates negative Chl-a (N = 287 vs. N = 299, 298, and 300 for Gurlin11, Gilerson10, and Mishra12, respectively) in agreement with former studies (e.g., [12,21]).

None of the red–NIR models evaluated are able to produce reliable Chl-a estimates for the ultra-turbid waters represented by the OWT 5 samples, due to the very low impact of the Chl-a on the reflectance signal for these waters [12]. A clear saturation is found for

Gilerson10, Gurlin11, and Mishra12 (Figure 7d–f) and low R^2 values were obtained for these models (Figure 8), emphasizing the limitation of these red–NIR-based methods towards ultra-turbid waters. The model by Gons et al. [21] is globally able to reproduce the Chl-a gradient found in OWT 5 data although it has an overall high uncertainty level as illustrated by the scattering in Figure 7d for these samples. As previously mentioned for OWT 4, this model tends to produce negative Chl-a values as illustrated by the lower estimated Chl-a for the Gons08 model when compared to Gurlin11, Gilerson10, and Mishra12 algorithms for OWT 5 (N = 35 and 57, 57, and 57, respectively).

These results are confirming the relative limitations of the different band-ratio formulations usually considered for estimating Chl-a over contrasted coastal environments. Considering the performance of the considered models in their original formulations, an optimization of historical models as well a development of a new formulation was further performed, subsetting the in situ dataset into two groups: (1) one gathering oligotrophic to mesotrophic waters (OWTs 1, 2, 3) for which visible wavelengths have been considered and (2) one gathering highly turbid/high-Chl-a samples corresponding to OWT 4.

Further considering that all the band-ratio-based evaluated methods were failing for OWT 5 samples, no adaptation of these existing methods was performed for the corresponding samples.

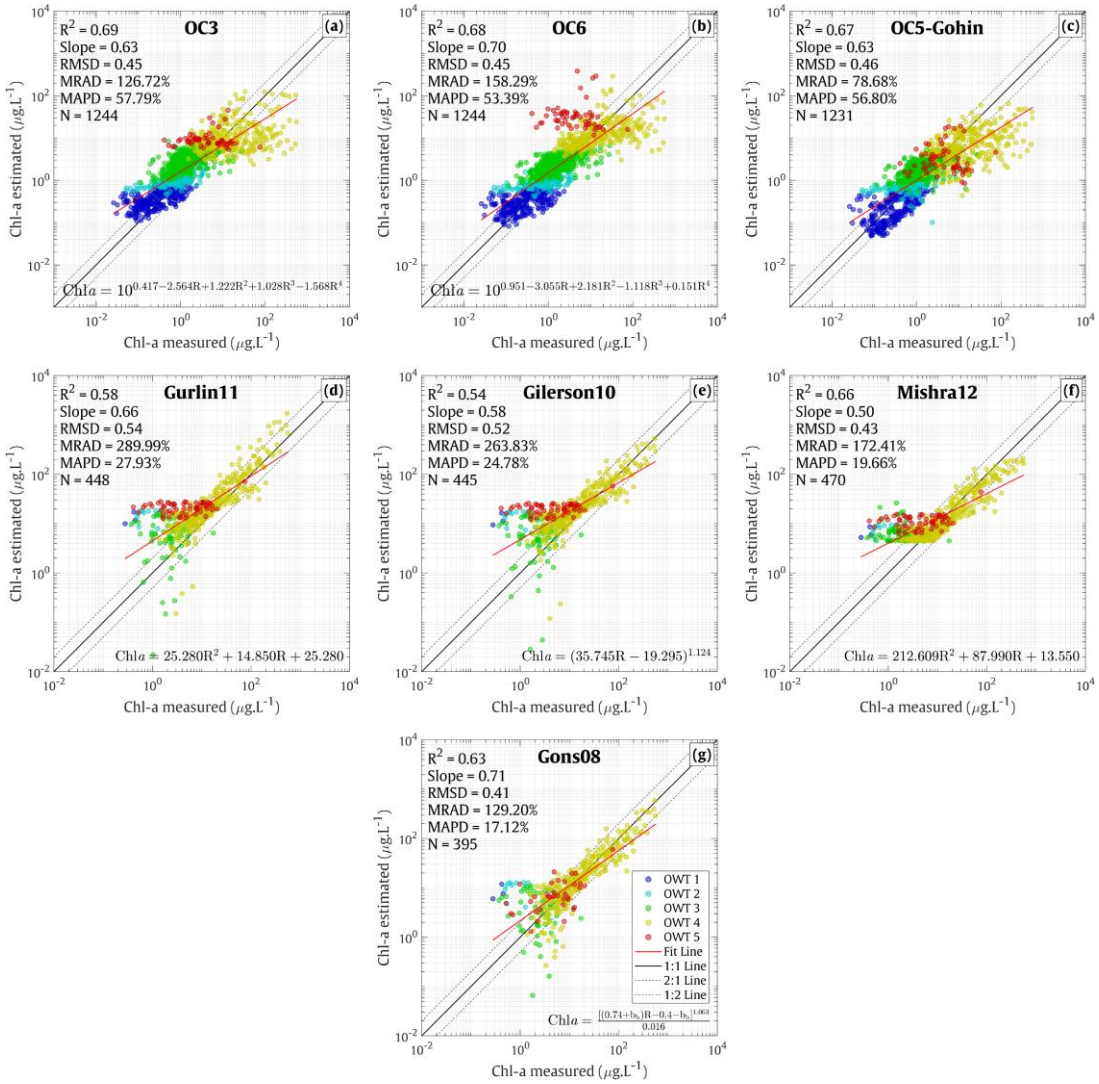

Figure 7. Scatterplot (log–log scale) of the in situ Chl-a (DS–W) vs. the Chl-a estimated from the different historical band-ratio-based models (**a**) OC3, (**b**) OC6, (**c**) OC5–Gohin, (**d**) Gurlin11, (**e**) Gilerson10, (**f**) Mishra12, and (**g**) Gons08 considered in their original formulations (see Section 2.4).

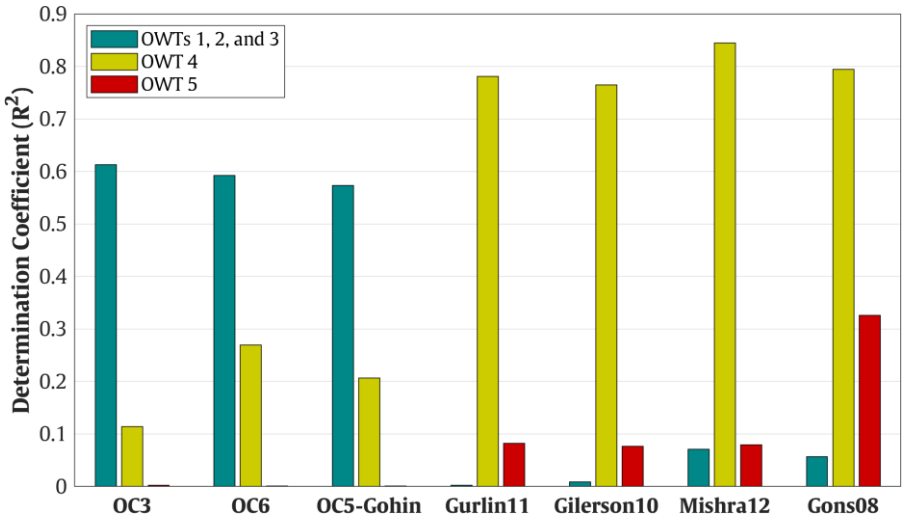

Figure 8. Determination coefficient (R^2) of the linear relationships between the in situ Chl-a and the estimated Chl-a corresponding to each OWT subset in DS−W (Figure 6) for the different band-ratio-based historical models considered in the frame of this study in their original versions (Section 2.4).

3.2. Chl-a Estimates for Clear to Medium Turbid Waters

3.2.1. Development of a New Algorithm for OWTs 1, 2, and 3

Considering the previous results, OC3 and OC6 models (OC3-Tuned and OC6-Tuned), which are the most adapted for clear to medium turbid waters (OWTs 1, 2, and 3), have been optimized on the DS-D dataset (N = 617, Table 2) using the QR decomposition method where the input matrix of the regression problem can be presented as a product of the orthogonal matrix (Q) and a triangular matrix (R). This optimization approach is available as the "fitlm" function in Matlab.

Table 2. Coefficients of the OC3 and OC6 models adapted to the DS-D dataset for OWTs 1, 2, and 3 (N = 617).

Models	Tuned Coefficients	Equations	R^2
OC3	$a_0 = 0.289$; $a_1 = -2.997$; $a_2 = 1.956$; $a_3 = 2.189$; $a_4 = -3.773$	(5), (6)	0.63
OC6	$a_0 = 0.931$; $a1 = -2.710$; $a_2 = -2.715$; $a_3 = 8.873$; $a_4 = -5.340$	(5), (7)	0.60

In addition to these adapted historical formulations, an alternative model for oligotrophic to mesotrophic waters was developed by exploiting the DS-D dataset. This model named MUBR is based on a combination of multiple band ratios, which have been shown to provide the best performance for estimating Chl-a from DS-D (Figure 9). It is worth noticing that the $R_{rs}(412)$ was not considered in the development of the MUBR model considering that this wavelength is not available for MSI and that this band is susceptible to be affected by large uncertainties related to the atmospheric correction processes ([50]). The MUBR algorithm is in practice based on the combination of three band ratios using four visible bands from the blue to the red available for both Sentinel2-MSI and Sentinel3-OLCI. This formulation is expressed as follows:

$$Chl_{MuBR} = 10^{a_0 + a_1 R1 + a_2 R2 + a_3 R3} \quad (26)$$

where

$$R1 = \log_{10}\left[\frac{R_{rs}(490)}{R_{rs}(443)}\right] \quad (27)$$

$$R2 = \log_{10}\left[\frac{R_{rs}(560)}{R_{rs}(490)}\right] \quad (28)$$

$$R3 = \log_{10}\left[\frac{R_{rs}(665)}{R_{rs}(560)}\right] \quad (29)$$

and where $a_0 = 0.665$, $a_1 = -3.506$, $a_2 = 3.590$, and $a_3 = -0.019$.

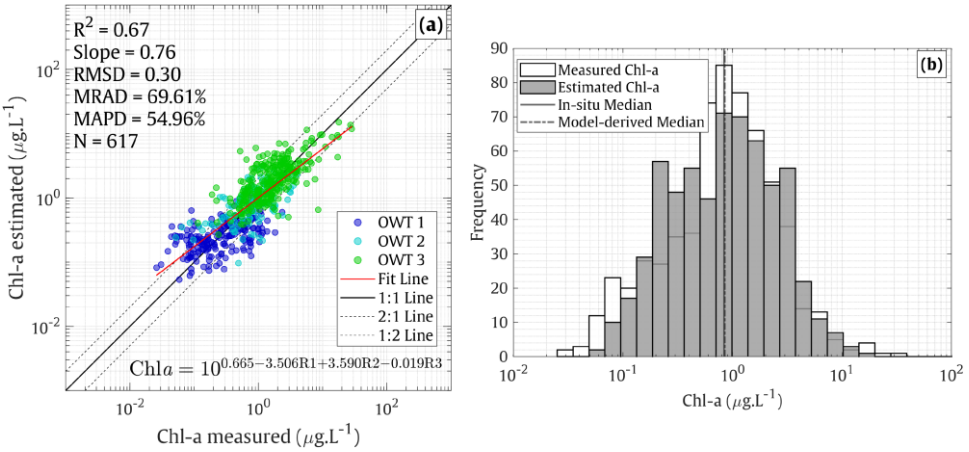

Figure 9. (**a**) Relationship between the in situ vs. estimated Chl-a from the MUBR model developed on the samples corresponding to OWTs 1, 2, and 3 in the DS–D dataset (N = 617). (**b**) Histograms of distribution of the Chl-a values corresponding to OWT 1, 2, and 3 samples in DS–D and for the Chl-a values estimated from the MUBR model.

3.2.2. Model Selection for Clear to Medium Turbid Waters

The intercomparison on the performance of the Chl-a estimates on clear to medium turbid waters (OWTs 1, 2, and 3) was performed on the independent validation dataset DS-V (N = 263) considering, in addition to the MUBR, classical clear waters band-ratio models adapted on DS-D (OC3-Tuned and OC6-Tuned) as well as considering the model OC5 in its original version. The results in Figure 10a–c show that the MUBR model provides the best performance considering our validation dataset when compared to OC3-Tuned and OC6-Tuned models with an overall lower dispersion (e.g., MRAD = 66.72% vs. 97.12% and 86.24%, respectively) as well as with a general better estimation of Chl-a value over the whole range of Chl-a for the considered subset (e.g., slope = 0.76 vs. 0.69 and 0.64, respectively). We observed a similar performance of the OC5 original model in the clear to medium turbid waters on the validation dataset (Figure 10c) to that obtained for OC3 (e.g., area of 2.109). The better performance for the MUBR model is further underlined in the radar plot provided in Figure 10d where the area found for the MUBR, representing a summary of the statistical parameters considered, is lower (1.24) than that for the other three methods considering both their original and adapted versions (OC3-Tuned: 2.45 and 2.09, respectively; OC6-Tuned: 2.45 and 2.05, respectively). The lower performance of the OC3 and OC6 methods on the DS-V subset for OWTs 1, 2, and 3 can be explained by an overestimation of the very low Chl-a values as well as by a saturation of the Chl-a estimated for the highest Chl-a values (Figure 10).

Our results, therefore, tend to indicate that the model MUBR represents a valuable alternative for estimating Chl-a focusing on the clear to moderate turbid waters gathered using the dataset considered in the frame of the present study (OWTs 1, 2, and 3 data).

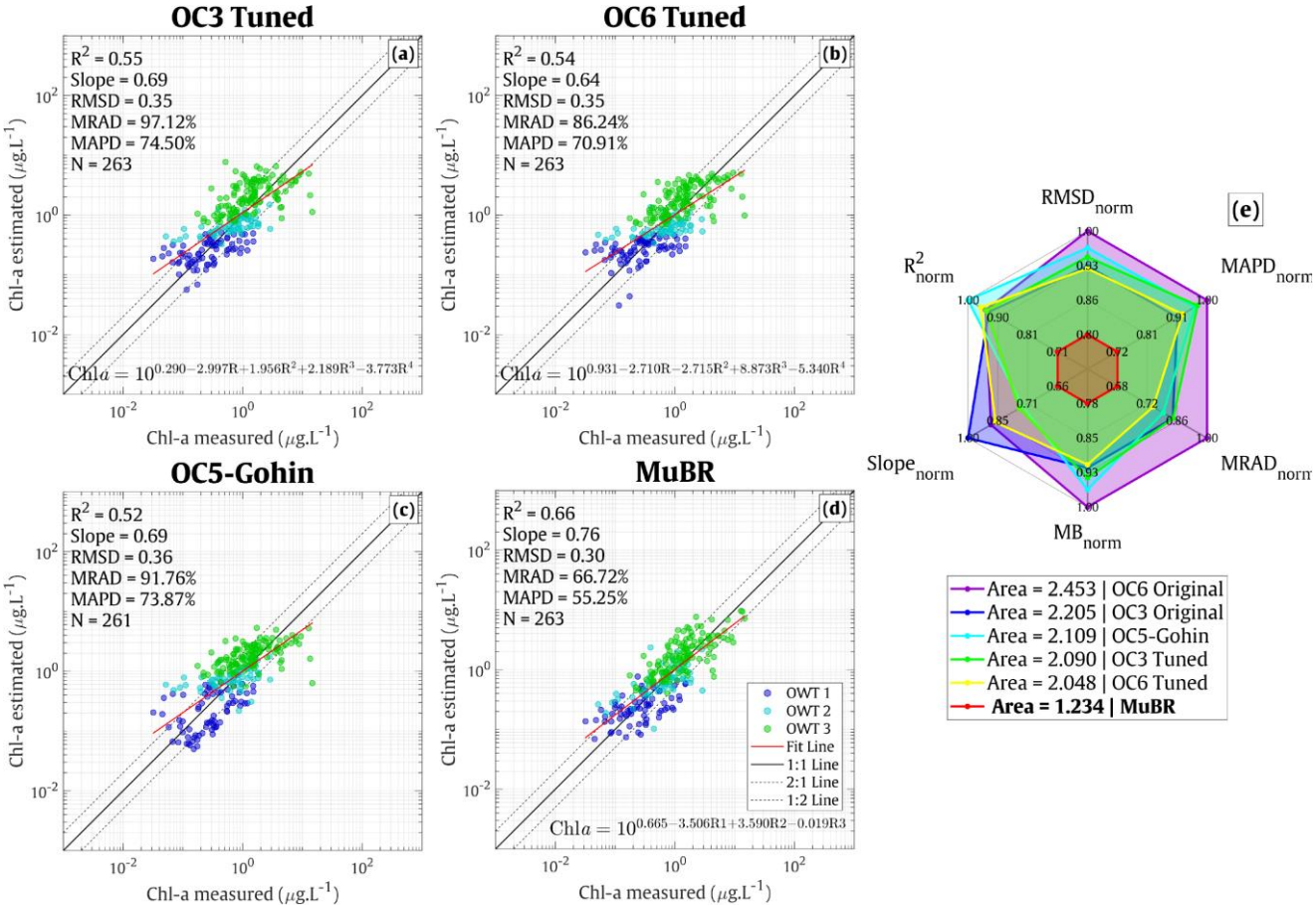

Figure 10. Intercomparison of the performance of the Chl-a inversion models for the OWT 1, 2, and 3 samples in the in situ validation dataset DS−V (N = 263): relationships between in situ vs. estimated Chl-a applying (**a**–**c**) the OC3, OC6, and OC5−Gohin models adapted to the development dataset DV−D and (**d**) for the MUBR model; (**e**) summary of the performance of the Chl-a inversion models where the lowest area of the polygon associated with each model represented in the radar plot corresponds to the best model. Note that the statistics for the original versions of OC3 and OC6 are also shown for completeness.

3.3. Chl-a Estimation in Turbid/high-Chl-a Waters (OWT 4)

3.3.1. Development of a New Algorithm

Considering the results of the previous section, a focus was performed to define the model most adapted for estimating Chl-a over highly turbid/high-Chl-a waters corresponding to OWT 4 samples only. This is also due to the fact that none of the adapted models has been found to provide accurate Chl-a retrieval for OWT 5 samples (not shown). In practice, the Red-NIR-based models by Gurlin11, Gilerson10, Mishra12, and Gons08 were adapted to our dataset defining new coefficients for each model refitting the corresponding formulation on the DS-D samples (not shown, Table 3).

Table 3. The tuned coefficients for the Gurlin10, Gilerson11, Gons08, and Mishra12 models adapted to the DS-D dataset for OWT 4 (N = 210).

Models	Tuned Coefficients	Equations	R^2
Gurlin11	a = 0.83; b = −11.398; c = 24.923	(8)	0.80
Gilerson10	a = 13.328; b = −6.373; c = 1.393	(9)	0.80
Gons08	$a^*_{phy}(665)$ = 0.0139; p = 1.0752	(10), (11)	0.79
Mishra12	a = 13.801; b = 111.673; c = 354.095	(12), (13)	0.82

In addition, a new formulation (referred to as the NDCI-based model) was developed for OWT 4 samples (Figure 11) considering the saturation pattern towards low Chl-a values already reported for models using the NDCI parameter as an input value [26,46,51] and is expressed as follows:

$$\text{Chl-a} = 10^{a_0 + a_1\text{NDCI} + a_2\text{NDCI}^2} \quad (30)$$

where $a_0 = 1.179$, $a_1 = 2.689$, and $a_2 = -1.083$

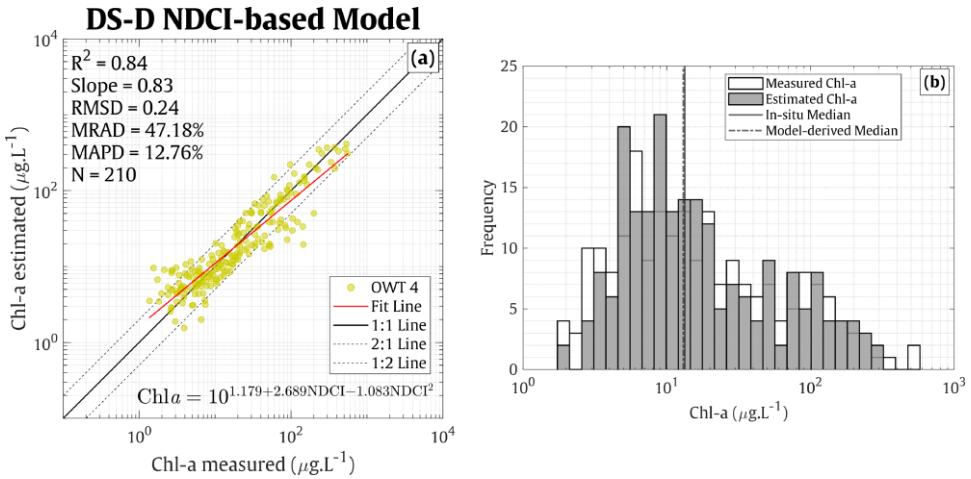

Figure 11. (**a**) Relationship between the in situ vs. estimated Chl-a from the NDCI-based model developed on the OWT 4 samples in the DS–D dataset (N = 210). (**b**) Histograms of distribution of the OWT 4 Chl-a in DS–D and for the Chl-a values estimated from the NDCI-based model.

3.3.2. Model Selection for Highly Turbid/High-Chl-a Waters

The relative performances of these red–NIR models were then evaluated on the DS-V dataset for OWT 4 ($N_{max} = 90$, Figure 12). Although very similar statistics are found for all the tuned versions of the models evaluated, the new NDCI-based model presents the best performances (area = 0.472, Figure 12f). As previously pointed out from the DS-W dataset (Figure 7g), Gons08 tends to generate an underestimation of the lower-end Chl-a concentration (i.e., Chl-a < 5 µg/L) in OWT 4, potentially leading to the generation of negative values (Figure 12c, N = 86 for the original and tuned versions vs. N = 90 for the other models). It is worth mentioning that the tuned version of Gons08 does not provide better estimates than the original one, which is probably related to the difference in the Chl-a range presented in our development dataset (1.37–556 µg/L) and the one in [21] (0.37–131 µg/L) as the adapted coefficients and the performances corresponding to different inversion models in the DS-V might vary according to Chl-a level. The tuned versions of Gilerson10 and Gurlin11 (Figure 12a,b) globally show satisfactory performances (area = 0.602 and 0.577, respectively), confirming the effectiveness of these models to derive Chl-a in turbid environments [26]. Interestingly the tuned version of Mirshra12 (Figure 12d), although exhibiting a generally reliable performance, still shows a saturation pattern towards the smallest Chl-a for the OWT 4 samples (<5 µg/L). Such a saturation pattern is not found when applying the modification of this model corresponding to the NDCI-based formulation proposed here (Figure 12e).

This intercomparison exercise thus suggests that the NDCI-based model represents the most adapted model for estimating Chl-a over highly turbid/high-Chl-a (OWT 4) waters gathered in our in situ dataset.

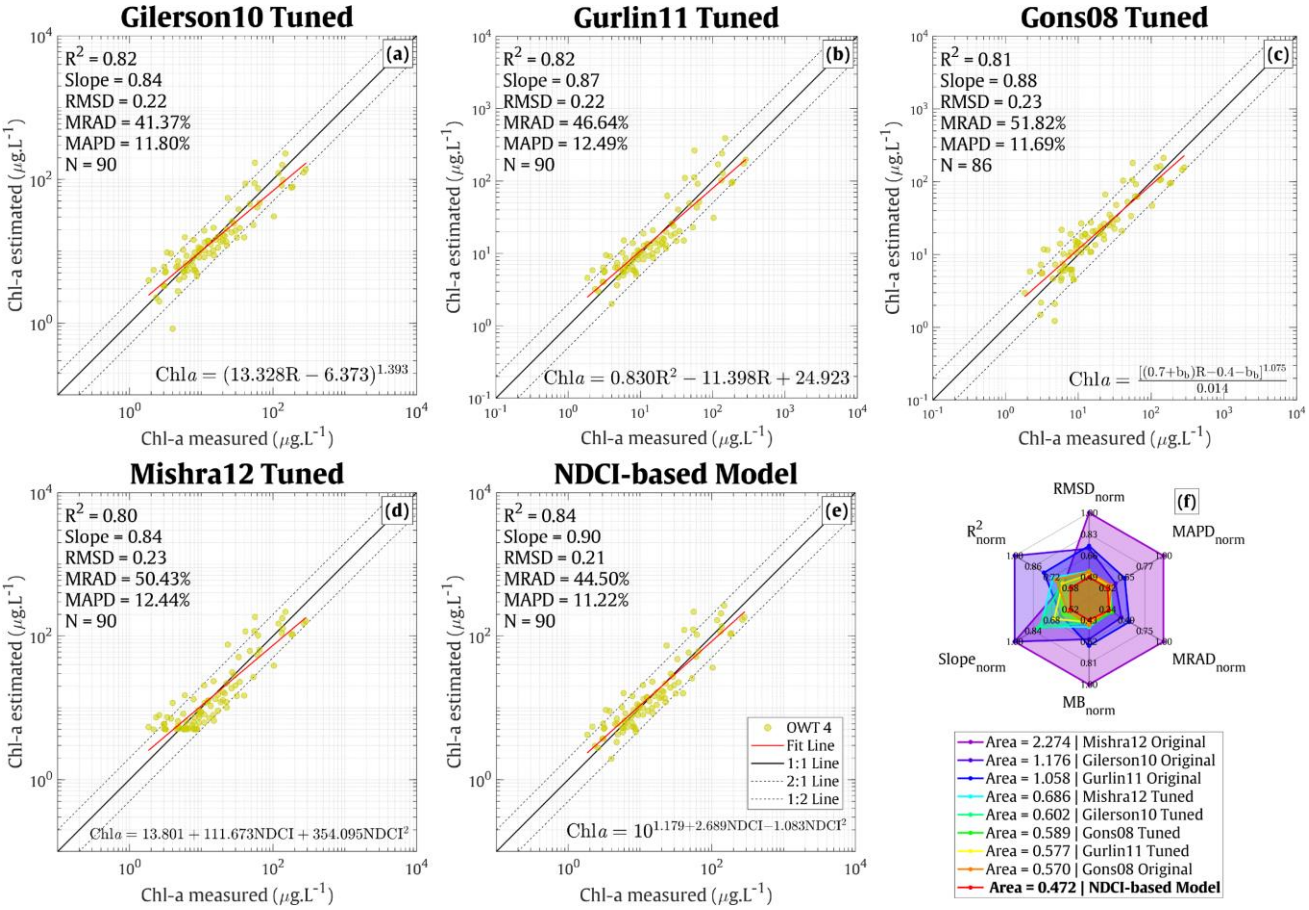

Figure 12. Intercomparison of the performance of the adapted versions of Red-NIR model on highly turbid/high-Chl-a validation data corresponding to the OWT 4 samples in DS−V (N = 90): scatterplots of the in situ Chl-a vs. the Chl-a estimated from (**a**) Gilerson10, (**b**) Gurlin11, (**c**) Gons08, (**d**) Mishra12, and (**e**) NDCI-based models; a summary of the performance of the considered model for estimating Chl-a is provided in the radar plot (**f**) where the performance of both original and tuned versions of these 4 models is also provided for completeness.

3.4. Class-Based Combination of Multiple Chl-a Models for OWTs 1, 2, 3, and 4

The previous algorithm evaluation exercises clearly confirm the inability for a unique simple band ratio to deliver reliable estimates over the whole range of Chl-a values found in coastal waters [12,15,26]. We further illustrate the use of two band-ratio formulations considering a first model combining band ratios in the visible domain for clear to medium turbid waters (MUBR for OWTs 1, 2, 3) and a red–NIR model (NDCI-based) for highly turbid/high-Chl-a waters (OWT 4).

Different methods can be used for producing Chl-a maps by applying different bio-optical algorithms on a pixel-per-pixel basis. Diverse former studies have, for instance, illustrated the interest of using a weighted average to provide smooth Chl-a gradients in transition areas between different inversion algorithms. Such weighting approaches were diversely based on the use of Chl-a values [52] or on the exploitation of the optical characteristics of the water masses provided from optical water types defined from the reflectance spectra [25,26,53].

Such an optical-based weighted approach was considered in the frame of this study using weights based on the belonging probability of each sampling point (in situ sample or satellite pixel) to each optical group of optical water types to which a specific Chl-a model should be applied (i.e., MUBR for OWTs 1, 2, and 3 and Mishra12-Tuned for OWT 4). The combination of algorithms from two groups of OWTs was performed following the equation [23]:

$$\text{Chl-a} = (p_1^* + p_2^* + p_3^*) \times \text{Chl-a}_{123} + p_4^* \times \text{Chl-a}_4 \quad (31)$$

where the terms are defined as follows:

- p_1^*, p_2^*, p_3^*, and p_4^* correspond to the normalized probability for OWTs 1, 2, 3, and 4, respectively (Equation (4), [13]).
- Chl-a_{123} is the Chl-a estimated from MuBR designed for OWTs 1, 2, and 3. Chl_4 is the Chl-a estimated by using red/NIR models designed for OWT 4. The tuned coefficients are used for the calculation of Chl-a_{123} and Chl-a_4 (Equations (26) and (30)).

The evaluation of this weighted combination is provided in Figure 13. It is worth mentioning that the number of points presented in Figure 13 (N = 147) corresponds to the maximal number of points in DS-V with available information from the visible to the NIR for samples corresponding to OWTs 1, 2, 3, and 4. An overall good performance is found for the MUBR-NDCI-based combination (MAPD = 21.64%, RMSD = 0.25).

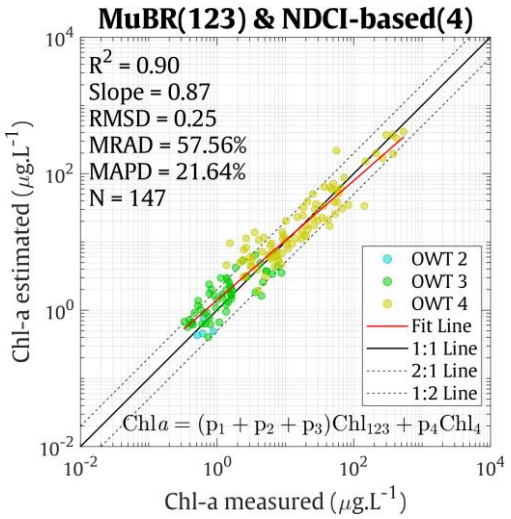

Figure 13. Performance of the combined model between the MUBR model for clear/moderate turbid waters (OWTs 1, 2, and 3) and the NDCI-based model on the DS–V (N = 147).

3.5. Matchup Exercise

The validation of the Chl-a estimates performed using the MUBR-NDCI-based combination proposed in this study was performed through a matchup exercise based on the DS-M dataset for both OLCI and MSI (Section 2.2). Our results emphasize a general expected degradation in the accuracy of the Chl-a estimates for these two sensors (Figure 14) when compared to the performance of the Chl-a inversion performed using the in situ validation dataset (Figure 13). Globally, the best performance is here found when applying the MUBR-NDCI-based combination using satellite $R_{rs}(\lambda)$ derived from the POLYMER processing for both sensors. The Chl-a derived with POLYMER yields the highest number of valid matchups for both OLCI (N = 358 vs. N = 184 and 225 for ACOLITE and C2RCC, respectively) and MSI (N = 188 vs. N = 138 and 143 for ACOLITE and C2RCC, respectively). This result is in agreement with former intercomparison exercises (e.g., [54]). Although it has an overall high scattering level in the matchups, POLYMER globally provides better estimates from the clear to the highly turbid waters with a better performance found for OLCI when compared to MSI (Figure 14b,e). For both sensors, ACOLITE processing tends to generate an overestimation of the retrieved Chl-a also found for C2RCC, especially for the OWT 4 samples, suggesting the probable need to improve atmospheric correction in the NIR domain. The patterns depicted in Figure 13 remain globally valid when considering the common matchup points (not shown) for the three atmospheric correction schemes applied to both sensors. A general better performance in retrieving Chl-a is still found when applying the MUBR-NCDI-based

combination to POLYMER data to OLCI (e.g., MAPD = 114, 172, and 116% for POLYMER, ACOLITE, and C2RCC, respectively; N = 214) and MSI (e.g., MAPD = 68, 149, and 148% for POLYMER, ACOLITE, and C2RCC, respectively; N = 99) $R_{rs}(\lambda)$.

Our results therefore relatively differ from previous works [54] where POLYMER was not found to provide the best performance when evaluating different atmospheric correction schemes (and Chl-a models) for Landsat-8 and Sentinel-2 applications over lakes, rivers, and coastal waters. However, this better performance might be related to the general good performance of POLYMER when considering band ratios as illustrated from former studies in coastal waters [50,55,56]. This might also be explained by the fact that the current matchup dataset (DS-M) does not contain many very highly turbid or high-Chl-a waters (max Chl-a = 34.12 µg/L and 52.93 µg/L for MSI and OLCI, respectively) underlining the need to perform additional matchup exercises on a larger dataset. Investigating in more detail the relative impact of the considered atmospheric correction schemes is out of the scope of this study considering that the matchup dataset DS-D contains Chl-a data only. However, it should be mentioned that up to now no consensual atmospheric correction scheme is currently recommended for Sentinel2-MSI and Sentinel3-OLCI applications in coastal waters, as the performance of the different approaches is susceptible to vary widely according to the wavelength as well as according to the water type considered [50,54,57].

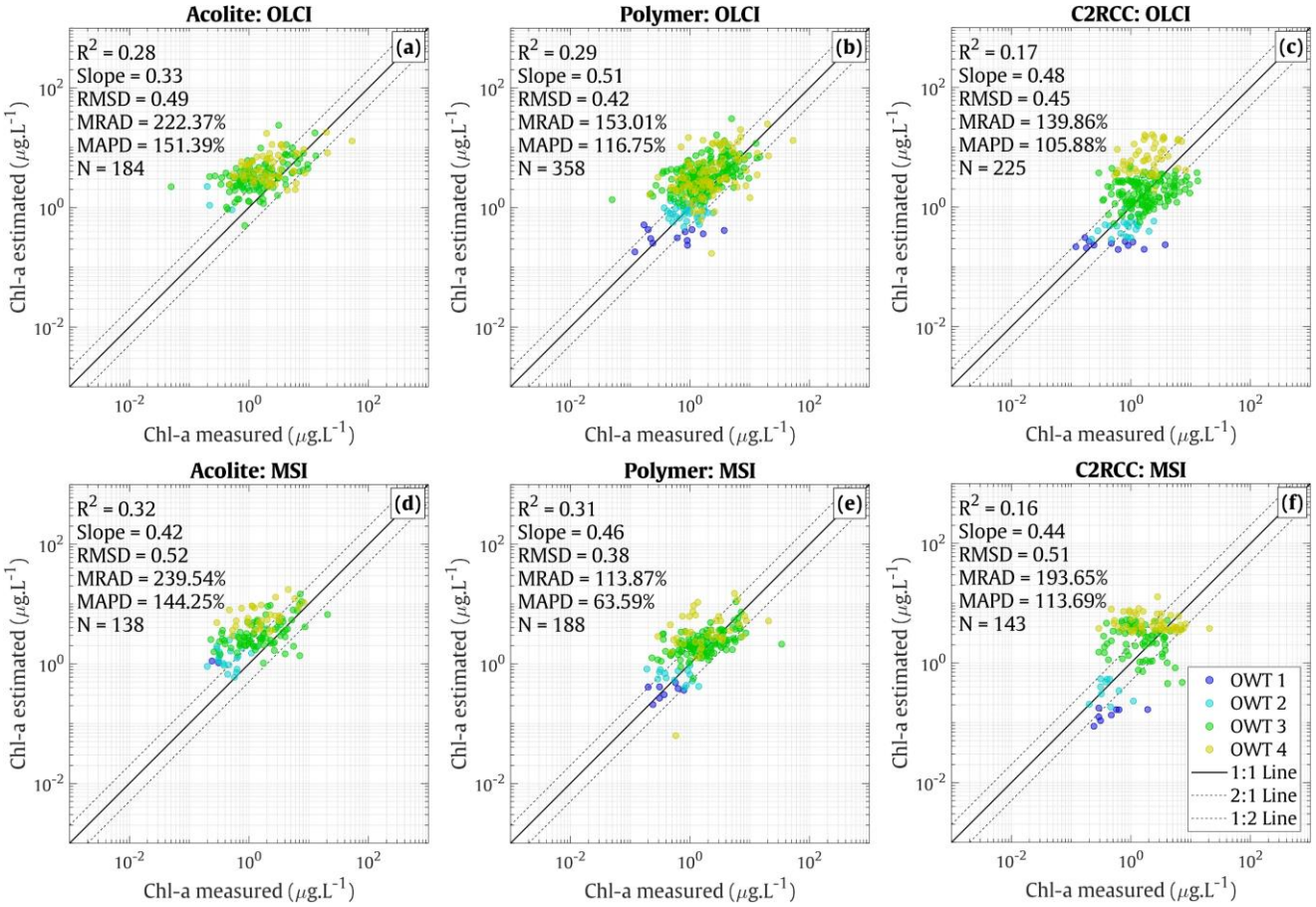

Figure 14. Chl-a matchup validation (DS−M dataset, Section 2.2) computed applying the MUBR-Mishra12-Tuned combination (Section 3.4) on the $R_{rs}(\lambda)$ generated applying three atmospheric corrections schemes (ACOLITE, POLYMER, and C2RCC) for Sentinel3−OLCI (**a**–**c**) and Sentinel2−MSI (**d**–**f**), respectively.

4. Discussion

4.1. Chl-a Algorithms Combination

The results obtained in the previous sections have illustrated that the red–NIR formulations globally demonstrated their ability to retrieve Chl-a values in highly turbid/high-Chl-a waters with a satisfying accuracy (Figure 13). Our results further emphasize the necessity to consider compatible models when applying weighting approaches, such as the one depicted in Section 3.4, taking care of the applicability of the approaches to be merged especially in transition areas. A limitation was, for instance, found for the formulation by Gons et al. [21], which tends to generate negative Chl-a values for the low Chl-a levels (<5 μg/L) for the OWT 4 waters. Such limitations might represent an issue when merging multiple algorithms on a pixel-per-pixel basis. As a matter of fact, the application of a combination based on MUBR and Gons08 will lead to a generation of bias or even create negative Chl-a in the transition area between OWT 3 and OWT 4 (not shown) where pixels can show relatively high OWT membership values for both OWTs.

To avoid such issues; a possible way would consist of considering other approaches than the one based on the weighting methods based on pixel OWT membership (Equation (31)) for combining multiple bio-optical models. Lavigne et al. [12], for instance, recently proposed pixel-per-pixel-based quality control tests (diversely based on the Chl-a as well as on thresholds applied on different MERIS $R_{rs}(\lambda)$) for selecting the most appropriate models for estimating Chl-a [8,21,45]. As mentioned by these authors, the main objective of such a quality-control-based approach is more likely to provide the users with a way to evaluate the reliability of the models applied to a defined area. These authors further illustrate the possibility to use this selection procedure to eventually merge multiple algorithms although such an approach might generate discontinuity in the Chl-a maps when switching from one algorithm to another.

The interest of using the OWT membership information to merge the two inversion models considered here was further illustrated from a Sentinel2-MSI map in the Vietnamese coastal waters close to the Mekong River and Nha Be River estuaries (East Vietnam Sea, Figure 15a), which shows contrasted water masses ranging from clear (OWT 2) to ultra-turbid (OWT 5) waters (Figure 15c). The MUBR-NDCI-based combination was here applied considering for each pixel the best model according to the pixel OWT (i.e., without weighting the models, not shown) as well as applying the weighing approach described in Equation (31) (Figure 15d). The need to consider the pixel OWT membership to combine MUBR- and NDCI-based models is illustrated in Figure 15e where the relative difference between the Chl-a map produced without and with a weighting function is shown. It appears that the simple juxtaposition of the most pertinent model can generate significant discontinuities in the final Chl-a estimates. As a matter of fact, maximum differences reaching 10% are observed in the transition areas between OWTs 3 and 4. Such possible spatial artifacts induced using an unweighted function can represent a significant issue when using high-spatial-resolution data, such as from Sentinel2-MSI (or Landsat8-OLI), which are susceptible to capturing fine-scale transition gradients in coastal waters [12,23].

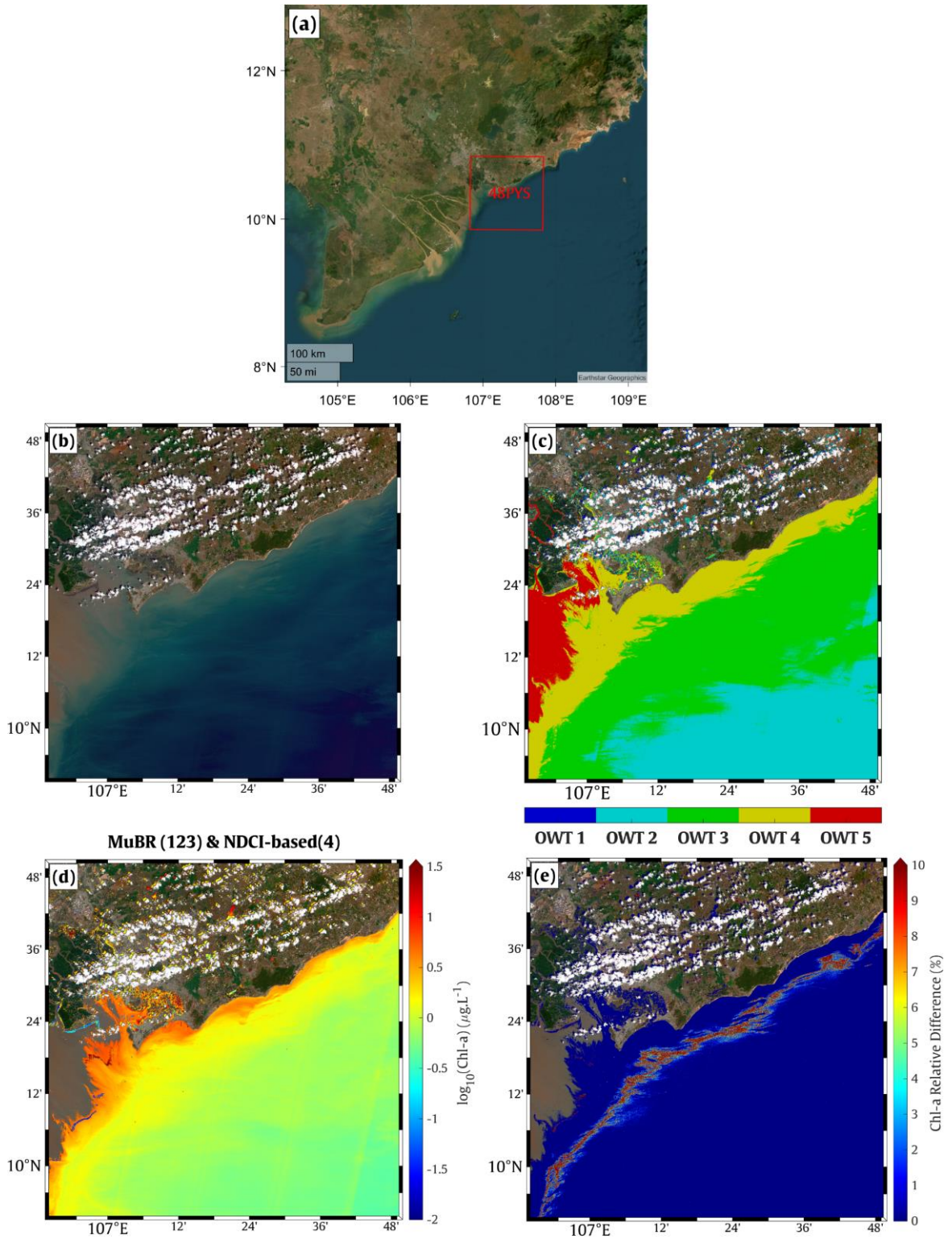

Figure 15. Illustration of the interest of using a weighting function based on the OWT membership probability for blending multiple Chl-a from a Sentinel2–MSI (60 m, POLYMER processing) image capturing the Vietnamese coastal waters: (**a**) Location of the Sentinel2 (Tile 48PYS) (**b**) true color image; (**c**) optical water types distribution; (**d**) Chl-a estimated from the MUBR-NDCI-based combination where masked gray areas are those belonging to OWT 5; (**e**) relative difference (%) in the Chl-a estimated from the MUBR-NDCI-based combination with and without using pixel OWT belonging probability as a weighting function (see Equation (31)).

4.2. Applicability of Band-Ratio-Based Chl-a Models at Global Scale and Current Limitations and Perspectives

To summarize the results developed in the previous sections regarding the relative performance of the different Chl-a inversion methods selected for the different optical OWTs defined in the frame of this study, global monthly MERIS 1 km R_{rs} data were associated with the five optical OWTs defined in this work. Figure 16 shows the most frequent OWTs observed for each pixel over the MERIS time period. The coastal domain was here defined considering a global mask proposed by Mélin and Vantrepotte [13] for characterizing the optical diversity of coastal waters, which is based on the combination of criteria based on bathymetry and distance to the coast. It appears that pixels corresponding to OWTs 1, 2, and 3 represent 63, 21, and 14% of the considered coastal domain, meaning that the MUBR model can be applied in the vast majority (98%) of the considered waters. OWT 4 pixels, where the use of red/NIR models such as the NDCI-based model defined here are the most suitable, represent only 2% of the whole domain, often corresponding to coastal margins impacted by the dilution of terrestrial inputs, including waters offshore river plume or mangrove areas, for instance. The OWT 5 waters, for which none of the tested band-ratio-based Chl-a inversion methods provide accurate Chl-a estimates, represent 1% of the global domain here considered. Focusing on moderate to ultra-turbid waters (OWTs 3, 4, and 5), our results indicate that Chl-a can be estimated with a satisfying accuracy (OWTs 3 and 4) over 94% of the coastal margins and shelf waters.

The main limitations in estimating Chl-a from ocean color observation are therefore related to ultra-turbid waters corresponding to OWT 5, mainly associated with the proximal part of most of the large rivers. Despite the restricted spatial extension of OWT-5 regions, an accurate monitoring of the recent evolution of the biogeochemical quality of these water masses is, however, essential considering their vulnerability to environmental changes of a natural and anthropic origin impacting the transfer of matter along the land–sea continuum [1]. Our results, however, clearly question the pertinence of considering Chl-a concentration as a relevant indicator for monitoring from satellite ocean color observation such environments where the phytoplankton signal on the marine reflectance seems to be too low for being detected considering band-ratio-based methods on both visible and NIR wavelengths.

The present study only allows the pixels for which Chl-a estimates are not reliable, considering the evaluated models to be dynamically identified using optical water types information to potentially mask the corresponding areas. A possible way to overcome this issue could consist of adopting alternative methods, for instance, taking advantage of the new potential offered by upcoming hyperspectral satellite sensors (e.g., the NASA PACE mission). Cheng et al. [58], for instance, documented the interest of an R_{rs} derivative-based approach for estimating Chl-a in turbid inland waters. More specifically, these authors demonstrated that the first R_{rs} derivative at 699 nm was a good proxy for estimating Chl-a in turbid lakes. The pertinence of this approach was evaluated on the OWT 5 dataset testing the best combination considering wavelengths ranging from 412 to 740 nm [58]. Our preliminary results show that the highest correlation with Chl-a ($R^2 = 0.40$, $N = 57$) is obtained when using the second derivative at 671 nm ($R''_{rs}(671)$); using $R_{rs}(l)$ measurements at X and Y nm, these two parameters follow a linear relationship indicated in Figure 17.

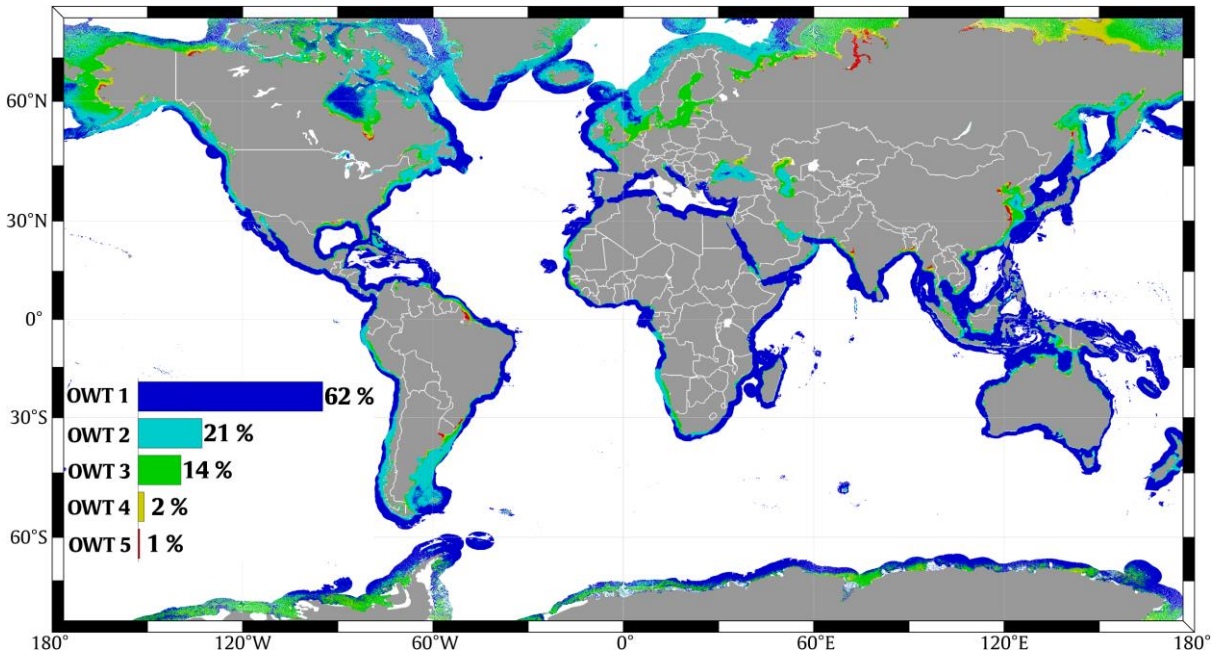

Figure 16. Global distribution of the most frequent optical water type among the 5 optical water types considered in the frame of this study observed from the monthly MERIS 1 km observation between 2002 and 2012. The histogram chart provides an illustration of the relative spatial coverage (in %) associated with each optical water type over the whole domain considered here.

The derivative-based approach, although it has potential interest, will not fully allow for the solving of the issue represented by the Chl-a inversion in ultra-turbid OWT 5 waters (Figure 17). Indeed, a clear overestimation of the Chl-a concentration is observed for the low Chl-a samples in OWT 5 (<1 µg/L), for which the data correspond to samples showing extremely to fairly low values for the Chl-a/SPM ratio (<3.9×10^{-5}). However, the performance of this latter model has proven a significant improvement in retrieving Chl-a over such optically complex water when comparing the R^2 value to that of the traditional approaches (see Figure 8). It is also important to recognize that additional in situ observations are required to further confirm the latter statement and deliver more robust information on the current limitations of ocean-color-based observation for depicting Chl-a in such ultra-turbid environments.

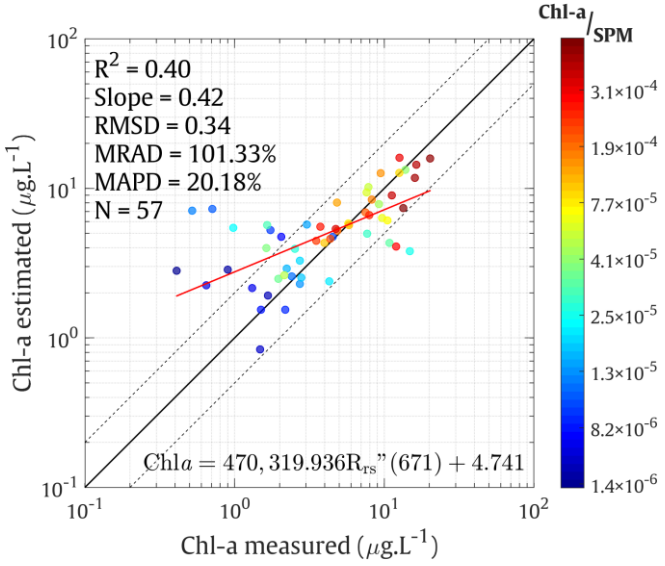

Figure 17. Illustration of the potential of an $R_{rs}(671)$ second derivative-based model for estimating Chl-a concentration in ultra-turbid waters (OWT 5).

5. Conclusions

This work aimed at evaluating the performance of band-ratio-based algorithms for estimating Chl-a in coastal waters from Sentinel2-MSI and Sentinel3-OLCI observation from an extensive in situ dataset covering a large spectrum of coastal environments in terms of optical characteristics (from clear to ultra-turbid waters) and trophic status (from oligotrophic to ultra-eutrophic environments). The best combination found from our dataset consists of mixing a visible band-ratio model (MUBR) for clear to medium turbid waters (OWTs 1, 2, and 3) and an adapted version of the red–NIR model (NDCI-based) for highly turbid/high-Chl-a waters. Such a combination can provide relevant Chl-a estimates covering four orders of magnitude from oligotrophic to ultra-eutrophic waters covering the vast part of the coastal domain. From our dataset, POLYMER processing was the most adapted to derive Chl-a from the proposed approach although additional match-ups should be performed considering more data, especially towards higher turbidity/Chl-a levels. While the methodology proposed in this work can be transposed to other sensors (e.g., MERIS), future works should be performed for other sensors (e.g., MODIS) for which less information is available in the NIR domain, which is, however, crucial for coastal waters applications. Finally, classical band-ratio-based methods show clear limitations, failing, whatever the model considered, for delivering Chl-a in ultra-turbid environments (e.g., proximal part of main river plumes). While optical water types information could allow for the dynamic flagging of the corresponding pixels, this work further emphasizes the necessity to develop specific approaches for these waters (e.g., exploiting the potential offered by future hyperspectral missions).

Author Contributions: Conceptualization, M.D.T. and V.V.; methodology, M.D.T., V.V. and H.L.; formal analysis, M.D.T. and V.V.; in situ data collection: E.N.O., R.P. and X.M.; satellite data processing: M.D.T., K.T.T. and D.J.; writing—original draft preparation, V.V., M.D.T. and H.L.; supervision, V.V. and H.L.; project administration, V.V.; funding acquisition, V.V. All authors have read and agreed to the published version of the manuscript.

Funding: This research was funded by the Office de l'eau Guyane, OFB and DEAL M.T PhD support, as well as by the ANR-FAPESP COCOBRAZ (ANR-21-CE01-0026) and the CNES-TOSCA OSYNICO projects. Guanabara Bay sampling and analyses were funded by CNPq (PELD-BG) and FAPERJ (several projects).

Data Availability Statement: The database used in this study encompasses the SeaBASS dataset (https://seabass.gsfc.nasa.gov/wiki/NOMAD), the LOG's dataset (included in GLORIA dataset: https://doi.org/10.1038/s41597-023-01973-y), and the dataset collected in Guanabara Bay, Brazil (only available for specific requests).

Acknowledgments: This work has benefited of the CNRS International Research Project VELITROP research projects for gathering parts of the in situ dataset.

Conflicts of Interest: The authors declare no conflict of interest about the work presented here.

References

1. Abril, G.; Cotovicz, L.C., Jr.; Nepomuceno, A.; Erbas, T.; Costa, S.; Ramos, V.V.; Moser, G.; Fernandes, A.; Negri, E.; Knoppers, B.A.; et al. Spreading Eutrophication and Changing CO_2 Fluxes in the Tropical Coastal Ocean: A few lessons from Rio de Janeiro Propagação da Eutrofização e Mudanças Nos Fluxos de CO_2 No Oceano Costeiro Tropical: Algumas Lições Do Rio de Janeiro. *Espec. Labomar* **2022**, *55*, 461–476. https://doi.org/10.32360/78518.
2. Papathanasopoulou, E.; Simis, S.G.H.; Alikas, K.; Ansper, A.; Anttila, S.; Jenni, A.; Barillé, A.-L.; Barillé, L.; Brando, V.; Bresciani, M.; et al. Satellite-Assisted Monitoring of Water Quality to Support the Implementation of the Water Framework Directive. *EOMORES White Pap.* **2019**, *28 pp* https://doi.org/10.5281/zenodo.3463050.
3. Gohin, F.; Van der Zande, D.; Tilstone, G.; Eleveld, M.A.; Lefebvre, A.; Andrieux-Loyer, F.; Blauw, A.N.; Bryère, P.; Devreker, D.; Garnesson, P.; et al. Twenty Years of Satellite and in Situ Observations of Surface Chlorophyll-a from the Northern Bay of Biscay to the Eastern English Channel. Is the Water Quality Improving? *Remote Sens. Environ.* **2019**, *233*, 111343. https://doi.org/10.1016/j.rse.2019.111343.
4. Loisel, H.; Vantrepotte, V.; Jamet, C.; Dinh Ngoc, D. Challenges and New Advances in Ocean Color Remote Sensing of Coastal Waters. In *Topics in Oceanography*; IntechOpen: Rijeka, Croatia, 2013; ISBN 978-953-51-1179-5.

5. Groom, S.; Sathyendranath, S.; Ban, Y.; Bernard, S.; Brewin, R.; Brotas, V.; Brockmann, C.; Chauhan, P.; Choi, J.; Chuprin, A. Satellite Ocean Colour: Current Status and Future Perspective. *Front. Mar. Sci.* **2019**, *6*, 485.
6. Morel, A.; Prieur, L. Analysis of Variations in Ocean Color. *Limnol. Oceanogr.* **1977**, *22*, 709–722. https://doi.org/10.4319/lo.1977.22.4.0709.
7. O'Reilly, J.E.; Maritorena, S.; Mitchell, B.G.; Siegel, D.A.; Carder, K.L.; Garver, S.A.; Kahru, M.; McClain, C. Ocean Color Chlorophyll Algorithms for SeaWiFS. *J. Geophys. Res. Oceans* **1998**, *103*, 24937–24953. https://doi.org/10.1029/98JC02160.
8. O'Reilly, J.E.; Werdell, P.J. Chlorophyll Algorithms for Ocean Color Sensors - OC4, OC5 & OC6. *Remote Sens. Environ.* **2019**, *229*, 32–47. https://doi.org/10.1016/j.rse.2019.04.021.
9. Ford, D.; Barciela, R. Global Marine Biogeochemical Reanalyses Assimilating Two Different Sets of Merged Ocean Colour Products. *Remote Sens. Environ.* **2017**, *203*, 40–54. https://doi.org/10.1016/j.rse.2017.03.040.
10. Garnesson, P.; Mangin, A.; D'Andon, O.F.; Demaria, J.; Bretagnon, M. The CMEMS GlobColour Chlorophyll a Product Based on Satellite Observation: Multi-Sensor Merging and Flagging Strategies. *Ocean Sci.* **2019**, *15*, 819–830. https://doi.org/10.5194/os-15-819-2019.
11. Xi, H.; Losa, S.N.; Mangin, A.; Soppa, M.A.; Garnesson, P.; Demaria, J.; Liu, Y.; d'Andon, O.H.F.; Bracher, A. Global Retrieval of Phytoplankton Functional Types Based on Empirical Orthogonal Functions Using CMEMS GlobColour Merged Products and Further Extension to OLCI Data. *Remote Sens. Environ.* **2020**, *240*, 111704. https://doi.org/10.1016/j.rse.2020.111704.
12. Lavigne, H.; Zande, D.; Ruddick, K.; Santos, J.; Gohin, F.; Brotas, V.; Kratzer, S. Quality-Control Tests for OC4, OC5 and NIR-Red Satellite Chlorophyll-a Algorithms Applied to Coastal Waters. *Remote Sens. Environ.* **2021**, *255*, 112237. https://doi.org/10.1016/j.rse.2020.112237.
13. Mélin, F.; Vantrepotte, V. How Optically Diverse Is the Coastal Ocean? *Remote Sens. Environ.* **2015**, *160*, 235–251. https://doi.org/10.1016/j.rse.2015.01.023.
14. Yang, M.M.; Ishizaka, J.; Goes, J.I.; Gomes, H. do R.; Maúre, E. de R.; Hayashi, M.; Katano, T.; Fujii, N.; Saitoh, K.; Mine, T.; et al. Improved MODIS-Aqua Chlorophyll-a Retrievals in the Turbid Semi-Enclosed Ariake Bay, Japan. *Remote Sens.* **2018**, *10*, 1335. https://doi.org/10.3390/rs10091335.
15. Loisel, H.; Vantrepotte, V.; Ouillon, S.; Ngoc, D.D.; Herrmann, M.; Tran, V.; Mériaux, X.; Dessailly, D.; Jamet, C.; Duhaut, T.; et al. Assessment and Analysis of the Chlorophyll-a Concentration Variability over the Vietnamese Coastal Waters from the MERIS Ocean Color Sensor (2002–2012). *Remote Sens. Environ.* **2017**, *190*, 217–232. https://doi.org/10.1016/j.rse.2016.12.016.
16. Freitas, F.H.; Dierssen, H.M. Evaluating the Seasonal and Decadal Performance of Red Band Difference Algorithms for Chlorophyll in an Optically Complex Estuary with Winter and Summer Blooms. *Remote Sens. Environ.* **2019**, *231*, 111228.
17. Gurlin, D.; Gitelson, A.A.; Moses, W.J. Remote Estimation of Chl-a Concentration in Turbid Productive Waters—Return to a Simple Two-Band NIR-Red Model? *Remote Sens. Environ.* **2011**, *115*, 3479–3490. https://doi.org/10.1016/j.rse.2011.08.011.
18. Gilerson, A.A.; Gitelson, A.A.; Zhou, J.; Gurlin, D.; Moses, W.; Ioannou, I.; Ahmed, S.A. Algorithms for Remote Estimation of Chlorophyll-a in Coastal and Inland Waters Using Red and near Infrared Bands. *Opt. Express* **2010**, *18*, 24109. https://doi.org/10.1364/OE.18.024109.
19. Gower, J.; King, S.; Borstad, G.; Brown, L. Detection of Intense Plankton Blooms Using the 709 Nm Band of the MERIS Imaging Spectrometer. *Int. J. Remote Sens.* **2005**, *26*, 2005–2012.
20. Gower, S.T.; Kucharik, C.J.; Norman, J.M. Direct and Indirect Estimation of Leaf Area Index, FAPAR, and Net Primary Production of Terrestrial Ecosystems. *Remote Sens. Environ.* **1999**, *70*, 29–51.
21. Gons, H.J.; Auer, M.T.; Effler, S.W. MERIS Satellite Chlorophyll Mapping of Oligotrophic and Eutrophic Waters in the Laurentian Great Lakes. *Remote Sens. Environ.* **2008**, *112*, 4098–4106. https://doi.org/10.1016/j.rse.2007.06.029.
22. Odermatt, D.; Gitelson, A.; Brando, V.E.; Schaepman, M. Review of Constituent Retrieval in Optically Deep and Complex Waters from Satellite Imagery. *Remote Sens. Environ.* **2012**, *118*, 116–126.
23. Vantrepotte, V.; Loisel, H.; Dessailly, D.; Mériaux, X. Optical Classification of Contrasted Coastal Waters. *Remote Sens. Environ.* **2012**, *123*, 306–323. https://doi.org/10.1016/j.rse.2012.03.004.
24. D'Alimonte, D.; Zibordi, G. Phytoplankton Determination in an Optically Complex Coastal Region Using a Multilayer Perceptron Neural Network. *IEEE Trans. Geosci. Remote Sens.* **2003**, *41*, 2861–2868.
25. Mélin, F.; Vantrepotte, V.; Clerici, M.; D'Alimonte, D.; Zibordi, G.; Berthon, J.-F.; Canuti, E. Multi-Sensor Satellite Time Series of Optical Properties and Chlorophyll-a Concentration in the Adriatic Sea. *Prog. Oceanogr.* **2011**, *91*, 229–244.
26. Neil, C.; Spyrakos, E.; Hunter, P.D.; Tyler, A.N. A Global Approach for Chlorophyll-a Retrieval across Optically Complex Inland Waters Based on Optical Water Types. *Remote Sens. Environ.* **2019**, *229*, 159–178. https://doi.org/10.1016/j.rse.2019.04.027.
27. Pahlevan, N.; Smith, B.; Schalles, J.; Binding, C.; Cao, Z.; Ma, R.; Alikas, K.; Kangro, K.; Gurlin, D.; Hà, N.; et al. Seamless Retrievals of Chlorophyll-a from Sentinel-2 (MSI) and Sentinel-3 (OLCI) in Inland and Coastal Waters: A Machine-Learning Approach. *Remote Sens. Environ.* **2020**, *240*, 111604. https://doi.org/10.1016/j.rse.2019.111604.
28. Babin, M.; Stramski, D.; Ferrari, G.M.; Claustre, H.; Bricaud, A.; Obolensky, G.; Hoepffner, N. Variations in the Light Absorption Coefficients of Phytoplankton, Nonalgal Particles, and Dissolved Organic Matter in Coastal Waters around Europe. *J. Geophys. Res. Oceans* **2003**, *108(C7)*, 3211. https://doi.org/10.1029/2001jc000882.
29. Lubac, B.; Loisel, H.; Guiselin, N.; Astoreca, R.; Artigas, L.F.; Mériaux, X. Hyperspectral and Multispectral Ocean Color Inversions to Detect Phaeocystis Globosa Blooms in Coastal Waters. *J. Geophys. Res. Oceans* **2008**, *113*, C06026. https://doi.org/10.1029/2007JC004451.

30. Lubac, B.; Loisel, H. Variability and Classification of Remote Sensing Reflectance Spectra in the Eastern English Channel and Southern North Sea. *Remote Sens. Environ.* **2007**, *110*, 45–58. https://doi.org/10.1016/j.rse.2007.02.012.
31. Neukermans, G.; Ruddick, K.; Loisel, H.; Roose, P. Optimization and Quality Control of Suspended Particulate Matter Concentration Measurement Using Turbidity Measurements. *Limnol. Oceanogr. Methods* **2012**, *10*, 1011–1023. https://doi.org/10.4319/lom.2012.10.1011.
32. Vantrepotte, V.; Danhiez, F.-P.; Loisel, H.; Ouillon, S.; Mériaux, X.; Cauvin, A.; Dessailly, D. CDOM-DOC Relationship in Contrasted Coastal Waters: Implication for DOC Retrieval from Ocean Color Remote Sensing Observation. *Opt. Express* **2015**, *23*, 33. https://doi.org/10.1364/oe.23.000033.
33. Loisel, H.; Mangin, A.; Vantrepotte, V.; Dessailly, D.; Ngoc Dinh, D.; Garnesson, P.; Ouillon, S.; Lefebvre, J.P.; Mériaux, X.; Minh Phan, T. Variability of Suspended Particulate Matter Concentration in Coastal Waters under the Mekong's Influence from Ocean Color (MERIS) Remote Sensing over the Last Decade. *Remote Sens. Environ.* **2014**, *150*, 218–230. https://doi.org/10.1016/j.rse.2014.05.006.
34. Bailey, S.W. An Improved Bio-Optical Data Set for Ocean Color Algorithm Development and Satellite Data Product Variation. *Remote Sens. Environ.* **2005**, *98*, 122–140.
35. Be, S.; Babin, M.; Larouche, P.; Seas, N. An Empirical Ocean Color Algorithm for Estimating the Contribution of Chromophoric Dissolved Organic Matter to Total Light Absorption in Optically Complex Waters. *J. Geophys. Res. Oceans* **2008**, *113*, 1–14. https://doi.org/10.1029/2007JC004436.
36. Oliveira, E.N.; Fernandes, A.M.; Kampel, M.; Cordeiro, R.C.; Brandini, N.; Vinzon, S.B.; Grassi, R.M.; Pinto, F.N.; Fillipo, A.M.; Paranhos, R. Assessment of Remotely Sensed Chlorophyll- a Concentration in Guanabara Bay, Brazil. *J. Appl. Remote Sens.* **2016**, *10*, 026003. https://doi.org/10.1117/1.jrs.10.026003.
37. Han, B.; Loisel, H.; Vantrepotte, V.; Mériaux, X.; Bryère, P.; Ouillon, S.; Dessailly, D.; Xing, Q.; Zhu, J. Development of a Semi-Analytical Algorithm for the Retrieval of Suspended Particulate Matter from Remote Sensing over Clear to Very Turbid Waters. *Remote Sens.* **2016**, *8*, 211. https://doi.org/10.3390/rs8030211.
38. Gensac, E.; Martinez, J.M.; Vantrepotte, V.; Anthony, E.J. Seasonal and Inter-Annual Dynamics of Suspended Sediment at the Mouth of the Amazon River: The Role of Continental and Oceanic Forcing, and Implications for Coastal Geomorphology and Mud Bank Formation. *Cont. Shelf Res.* **2016**, *118*, 49–62. https://doi.org/10.1016/j.csr.2016.02.009.
39. Zorrilla, N.A.; Vantrepotte, V.; Ngoc, D.D.; Huybrechts, N.; Gardel, A. Automated SWIR Based Empirical Sun Glint Correction of Landsat 8-OLI Data over Coastal Turbid Water. *Opt. Express* **2019**, *27*, A294–A318.
40. Steinmetz, F.; Deschamps, P.-Y.; Ramon, D. Atmospheric Correction in Presence of Sun Glint: Application to MERIS. *Opt. Express* **2011**, *19*, 9783. https://doi.org/10.1364/oe.19.009783.
41. Brockmann, C.; Doerffer, R.; Peters, M.; Kerstin, S.; Embacher, S.; Ruescas, A. Evolution of the C2RCC Neural Network for Sentinel 2 and 3 for the Retrieval of Ocean Colour Products in Normal and Extreme Optically Complex Waters. In Proceedings of the Living Planet Symposium, Prague, Czech Republic, 9–13 May 2016; Volume 740, p. 54.
42. Vanhellemont, Q. Adaptation of the Dark Spectrum Fitting Atmospheric Correction for Aquatic Applications of the Landsat and Sentinel-2 Archives. *Remote Sens. Environ.* **2019**, *225*, 175–192. https://doi.org/10.1016/j.rse.2019.03.010.
43. Werdell, P.J.; Bailey, S.W.; Franz, B.A.; Harding Jr, L.W.; Feldman, G.C.; McClain, C.R. Regional and Seasonal Variability of Chlorophyll-a in Chesapeake Bay as Observed by SeaWiFS and MODIS-Aqua. *Remote Sens. Environ.* **2009**, *113*, 1319–1330.
44. Ward, J.H. Hierarchical Grouping to Optimize an Objective Function. *J. Am. Stat. Assoc.* **1963**, *58*, 236. https://doi.org/10.2307/2282967.
45. Gohin, F.; Druon, J.N.; Lampert, L. A Five Channel Chlorophyll Concentration Algorithm Applied to SeaWiFS Data Processed by SeaDAS in Coastal Waters. *Int. J. Remote Sens.* **2002**, *23*, 1639–1661. https://doi.org/10.1080/01431160110071879.
46. Mishra, S.; Mishra, D.R. Normalized Difference Chlorophyll Index: A Novel Model for Remote Estimation of Chlorophyll-a Concentration in Turbid Productive Waters. *Remote Sens. Environ.* **2012**, *117*, 394–406. https://doi.org/10.1016/j.rse.2011.10.016.
47. Gons, H.J. A Chlorophyll-Retrieval Algorithm for Satellite Imagery (Medium Resolution Imaging Spectrometer) of Inland and Coastal Waters. *J. Plankton Res.* **2002**, *24*, 947–951. https://doi.org/10.1093/plankt/24.9.947.
48. Pope, R.M.; Fry, E.S. Absorption Spectrum (380–700 Nm) of Pure Water. II. Integrating Cavity Measurements. *Appl. Opt.* **1997**, *36*, 8710–8723.
49. Tran, T.K.; Duforět-Gaurier, L.; Vantrepotte, V.; Ferreira Jorge, D.S.; Mériaux, X.; Cauvin, A.; d'Andon, F.; Loisel, H. Deriving Particulate Organic Carbon in Coastal Waters from Remote Sensing: Inter-Comparison Exercise and Development of a Maximum Band-Ratio Approach. *Remote Sens.* **2019**, *11*, 2849. https://doi.org/10.3390/rs11232849.
50. Mograne, M.; Jamet, C.; Loisel, H.; Vantrepotte, V.; Mériaux, X.; Cauvin, A. Evaluation of Five Atmospheric Correction Algorithms over French Optically-Complex Waters for the Sentinel-3A OLCI Ocean Color Sensor. *Remote Sens.* **2019**, *11*, 668. https://doi.org/10.3390/rs11060668.
51. Bi, S.; Li, Y.; Liu, G.; Song, K.; Xu, J.; Dong, X.; Cai, X.; Mu, M.; Miao, S.; Lyu, H. Assessment of Algorithms for Estimating Chlorophyll-a Concentration in Inland Waters: A Round-Robin Scoring Method Based on the Optically Fuzzy Clustering. *IEEE Trans. Geosci. Remote Sens.* **2022**, *60*, 1–17. https://doi.org/10.1109/TGRS.2021.3058556.
52. Smith, M.E.; Lain, L.R.; Bernard, S. An Optimized Chlorophyll a Switching Algorithm for MERIS and OLCI in Phytoplankton-Dominated Waters. *Remote Sens. Environ.* **2018**, *215*, 217–227.
53. Hieronymi, M.; Müller, D.; Doerffer, R. The OLCI Neural Network Swarm (ONNS): A Bio-Geo-Optical Algorithm for Open Ocean and Coastal Waters. *Front. Mar. Sci.* **2017**, *4*, 140.

54. Pahlevan, N.; Mangin, A.; Balasubramanian, S.V.; Smith, B.; Alikas, K.; Arai, K.; Barbosa, C.; Bélanger, S.; Binding, C.; Bresciani, M.; et al. ACIX-Aqua: A Global Assessment of Atmospheric Correction Methods for Landsat-8 and Sentinel-2 over Lakes, Rivers, and Coastal Waters. *Remote Sens. Environ.* **2021**, *258*, 112366. https://doi.org/10.1016/j.rse.2021.112366.
55. Li, Q.; Jiang, L.; Chen, Y.; Wang, L.; Wang, L. Evaluation of Seven Atmospheric Correction Algorithms for OLCI Images over the Coastal Waters of Qinhuangdao in Bohai Sea. *Reg. Stud. Mar. Sci.* **2022**, *56*, 102711.
56. Warren, M.A.; Simis, S.G.H.; Martinez-Vicente, V.; Poser, K.; Bresciani, M.; Alikas, K.; Spyrakos, E.; Giardino, C.; Ansper, A. Assessment of Atmospheric Correction Algorithms for the Sentinel-2A MultiSpectral Imager over Coastal and Inland Waters. *Remote Sens. Environ.* **2019**, *225*, 267–289. https://doi.org/10.1016/j.rse.2019.03.018.
57. Bui, Q.-T.; Jamet, C.; Vantrepotte, V.; Mériaux, X.; Cauvin, A.; Mograne, M.A. Evaluation of Sentinel-2/MSI Atmospheric Correction Algorithms over Two Contrasted French Coastal Waters. *Remote Sens.* **2022**, *14*, 1099.
58. Cheng, C.; Wei, Y.; Sun, X.; Zhou, Y. Estimation of Chlorophyll-a Concentration in Turbid Lake Using Spectral Smoothing and Derivative Analysis. *Int. J. Environ. Res. Public Health* **2013**, *10*, 2979–2994. https://doi.org/10.3390/ijerph10072979.